NMR investigations of ionic host polymer systems

Thesis

NMR INVESTIGATIONS OF IONIC HOST POLYMER SYSTEMS

A thesis submitted to the Open University

for the degree of Doctor of Philosophy

Martin Alexander Keith Williams B.Sc.

Chemistry Discipline

April, 1994.

THE CARTOON AT THE BEGINNING OF CHAPTER 3 HAS NOT BEEN SCANNED ON INSTRUCTION FROM THE UNIVERSITY

Abstract

NMR studies of the archetypal ionic host polymer system, in which polyethylene oxide (PEO) forms the polymer host, and lithium trifluoromethanesulphonate ($LiCF_3SO_3$) is the guest ionic salt, are reported. The work is primarily concerned with the ability of the polymer host to incorporate the guest salt within its structure.

Studies of pure PEO, $LiCF_3SO_3$ itself, and ionic host polymer systems of O:Li ratios of 3.5:1 and 9:1 are reported in detail. A key experimental approach is the use of spin-lattice relaxation time measurements (^1H, ^7Li and ^{19}F) to act as a probe of structure and dynamics.

^{19}F spin-lattice relaxation time investigations in $LiCF_3SO_3$ and $PEO/LiCF_3SO_3$ systems are interpreted in terms of a mechanism in which the hindered reorientation of CF_3 groups plays a key role. Cross-correlations are shown to be responsible for non-exponentiality in nuclear magnetization recoveries. The problem of defining and measuring spin-lattice relaxation times in these circumstances is considered in some detail. In the ionic host polymer systems an additional spin-lattice relaxation mechanism is that due to ^{19}F-^1H cross-relaxation. A model is developed to simulate the key features that can be observed experimentally for this type of mechanism. ^7Li spin-lattice relaxation time studies in $LiCF_3SO_3$ and $PEO/LiCF_3SO_3$ systems are also reported. In the salt a heteronuclear dipolar coupled ^7Li-^{19}F spin-lattice relaxation mechanism is shown to be dominant. The predicted relaxation behaviour is calculated in detail from a proposed crystal structure. ^1H lineshape and spin-lattice relaxation time measurements are reported in PEO and $PEO/LiCF_3SO_3$ systems.

Overall, no evidence is found for the existence of the $CF_3SO_3^-$ anion in the amorphous phase of the $PEO/LiCF_3SO_3$ systems studied. Hindered reorientation of the CF_3 group also occurs in these systems, with a similar activation energy to that found in the salt itself. However, there is evidence that the $^7Li^+$ cation can move between crystalline and amorphous regions.

Acknowledgements

I would like to thank my supervisors Dr E A Moore and Dr M Mortimer for their continued support and many interesting discussions. Special thanks to Mike for schooling me in the arts of debugging, free-fall soldering, universal earthing and paper wedge noise reduction techniques.

Thanks go to all those in the OU Chemistry Department who have helped me, particularly to Professor F J Berry for allowing me to continue my work into a third year, and to Mrs S Foster for turning my scribblings into typewritten form.

Special thanks to Gordon Oates for all his help, particularly on the experimental and computational side, not to mention on the "does the fly stop the train" question and numerous other Tuesday afternoon discussions, scientific and otherwise.

Thanks to Brandon, Darren, Rob, et al for subsidising my leisure activities during my final year at the OU. Thanks to Steve 'Captain' Picken and the other lads from Macclesfield for buying me breakfast in Wales, a brave act and how I needed those extra few pounds.

Thanks to my Dad for helping to support me when I needed it, and to Mandy Topham, for everything. Finally, to all my friends, old and new.....I thank you all.

CONTENTS

CHAPTER 1

INTRODUCTION

Chen said "Dr Seldon, you disturb the peace of the Emperor's realm. None of the quadrillions living now among all the stars of the Galaxy will be living a century from now. Why then should we concern ourselves with events of five centuries distance?"
"I shall not be alive half a decade hence," said Seldon, "and yet it is of overpowering concern to me. Call it idealism. Call it an identification of myself with that of mystical generalization to which we refer by the term, 'man'."

Isaac Asimov, Foundation.

Introduction

This thesis is concerned with the study of ionic host polymer systems using nuclear magnetic resonance (n.m.r.) spectroscopy. The aim of the work is to investigate the structure and dynamics of these systems. In particular, the archetypal ionic host polymer system has been studied, where the ion-coordinating macromolecule is polyethylene oxide (PEO) and the 'dissolved' metal salt is lithium trifluromethanesulphonate ($LiCF_3SO_3$). The study has concentrated on the spin $I = \frac{1}{2}$ nuclei, ^{19}F and ^{1}H, which are particularly suited to study by the n.m.r. technique, as well as the spin $I = \frac{3}{2}$ nucleus, ^{7}Li. In particular the PEO/$LiCF_3SO_3$ systems with O:Li ratios given by 3.5:1 and 9:1 have been investigated. It has been suggested that the 3.5:1 system forms a stoichiometric complex, and thus it is of particular interest in the study of ion-polymer interactions. In the course of this thesis arguments are developed to suggest that the system ratio at which the crystalline stoichimetric complex is formed is, in fact, slightly less than 3.5:1. This would be consistent with recent publications which suggest a 3:1 ratio. By way of a contrast, the phase behaviour in the 9:1 system is more complicated, although it will be suggested that, in essence, this system consists of a stoichiometric complex with the remainder of the system being uncoordinated PEO. Spin-lattice relaxation behaviour has been studied in detail. This provides a powerful probe of the local motional environment of the resonant nuclei.

It was apparent at the outset that to obtain a useful interpretation of the experimental results, an initial study of the constituents of the ionic host polymer system was required. In particular a detailed understanding of the ^{19}F spin-lattice relaxation behaviour in polycrystalline $LiCF_3SO_3$ is essential to the unambiguous determination of behaviour in the PEO/$LiCF_3SO_3$ systems; this is because of the influence of cross-correlation effects. These are inherently responsible for introducing non-exponentiality into nuclear magnetization

recoveries. An understanding of this behaviour is crucial to the separation of the effects of independent sources of non-exponential nuclear magnetization recovery. In the PEO/$LiCF_3SO_3$ systems, non-exponential spin-lattice relaxation behaviour was found to result from

(i) cross-correlation of reorientating internuclear vectors in the trifluoromethyl group,

(ii) cross-relaxation where the return of nuclear magnetization to one spin population (^1H) is influenced by the population of another spin type (^{19}F), and

(iii) the presence of distinct phases, where the nuclear magnetization recovery reflects a multi exponential decay in which each distinct spin-lattice relaxation time is associated with a different spatial or interfacial region of the sample.

The thesis is divided into seven chapters following this one. Chapter 2 reviews the basic theoretical framework that is used throughout the rest of the thesis. Particular attention is given to basic notation and conventions. The relevant Hamiltonians are discussed, both in the form of a vector interaction where the coupling information is contained in a cartesian second rank tensor and that of irreducible tensor operators. In particular the dipolar Hamiltonian is considered in detail and is used to demonstrate the equivalence of the two theoretical approaches. Further theory, required for a particular application, is introduced later, as needed.

Chapter 3 describes the experimental apparatus used in the work, and includes a discussion of the preparation and characterization of samples. The n.m.r. spectrometer is based on a commercial single-channel solid-state instrument. Also described are the computational methods used.

The next chapter (4) presents a literature review of ionic host polymer systems with particular reference to the PEO/$LiCF_3SO_3$ system. This deals with areas

that are now well understood and those which remain contentious, and seeks to place the current work in a wider context.

Chapter 5 is the first chapter to deal with experimental results and describes a detailed ^{19}F spin-lattice relaxation study of polycrystalline $LiCF_3SO_3$. Non-exponential nuclear magnetization recoveries are interpreted as due to the effects of cross-correlation, and a model spin system, consisting of three spin $I = \frac{1}{2}$ nuclei at the corners of an equilateral triangle, is considered in detail. This model is used to define a spin-lattice relaxation time in such systems that is independent of the effects of cross-correlation, and it is shown how such spin-lattice relaxation times can be measured experimentally. The approach adopted in the chapter allows motional parameters relating to the hindered reorientation of the CF_3 group to be determined.

The first part of Chapter 6 is concerned with the ionic host polymer system samples themselves and their characterization. The results of a ^{19}F spin-lattice relaxation study in the PEO/$LiCF_3SO_3$ systems are then presented. The values of spin-lattice relaxation time were necessarily obtained using the methods developed in Chapter 5. It is suggested that the observed double minimum in the ^{19}F spin-lattice relaxation time behaviour is due to cross-relaxation with ^1H nuclei in the PEO backbone. Consequently a dynamic model is proposed involving the general treatment of two unlike dipolar coupled, spin $I = \frac{1}{2}$ nuclei. This model is examined in detail and is used extensively in the simulation of the expected spin-lattice relaxation behaviours in an I-S system. The motional parameters relating to the reorientation of the CF_3 group extracted from experimental data are found, perhaps surprisingly, to be similar to those obtained in polycrystalline $LiCF_3SO_3$.

In Chapter 7, the ^{7}Li spin-lattice relaxation is investigated in polycrystalline $LiCF_3SO_3$ and in the PEO/$LiCF_3SO_3$ systems. The ^{7}Li motional environment is found to be markedly different in the pure salt and the ionic host polymer systems. A dynamic model based on a ^{7}Li-^{19}F dipolar coupled spin-lattice relaxation mechanism is developed and the spin-lattice relaxation behaviour is calculated explicitly for the pure salt, using a proposed crystal structure for $LiCF_3SO_3$ and the CF_3 group motional parameters found in Chapter 5. The ^{7}Li spin-lattice relaxation mechanism in the PEO/$LiCF_3SO_3$ systems has a substantially reduced activation energy and it is suggested that this may be because of an exchange process.

The final chapter deals with ^{1}H lineshape and spin-lattice relaxation studies, both in polycrystalline PEO and the 3.5:1 and 9:1 PEO/$LiCF_3SO_3$ systems. The discussion is less quantative than that in the previous chapters. This is because the ^{1}H nucleus does not act as a distinctive spin label, but rather reflects the complexity, both in structural and motional terms, of the behaviour of the PEO molecule. A key feature in the discussion of the results is the presence of both amorphous and crystalline PEO phases in the systems studied.

CHAPTER 2

THEORETICAL INTRODUCTION

"Your eyes speak invitation..."

King's X, Gretchen goes to Nebraska

CONTENTS

2.1 Introduction

This chapter outlines basic n.m.r. theory. The fundamentals are dealt with in a number of texts on the subject[1-7]. The objective is to establish a working picture of the interactions that affect nuclei in a magnetic field during an n.m.r. experiment. Most of the work described in this thesis uses pulsed n.m.r. techniques[8] to examine solid state systems. Many of the experimental results are involved with the measurement of spin-lattice relaxation behaviour, and so a detailed discussion of this area of n.m.r. is given.

The chapter is designed to provide sufficient theoretical background to the work that has been undertaken. In addition it also aims to bring some clarity to the extensive literature on the subject, irrespective of the many variations in convention and notation.

A comment on notation is important at the outset. In this chapter, operators will be denoted by italics, and vector operators by bold italics. Vector quantities are denoted by bold Roman characters and all other quantities by Roman characters, unless otherwise stated.

2.2 Basic Theory

The idea of spin angular momentum was postulated to explain the result of the Stern-Gerlach[9] experiment. Previously, to account for the fine structure of some spectral lines, Uhlenbeck and Goudsmit had, in 1925, introduced a fourth quantum number, but had not speculated on its origin. This turned out to be the electron spin quantum number. Similarly nuclei possess spin. Pauli had actually postulated the existence of nuclear spin in 1924, and later Dirac showed how spin was a natural consequence of relativistic quantum mechanics.

The spin angular momentum of a nucleus is quantized, so that

$$P = \hbar[I(I + 1)]^{\frac{1}{2}} \qquad (2.1)$$

where P is the magnitude of the spin angular momentum vector, $\hbar = h/2\pi$ (h is Planks constant), and I is the appropriate quantum number. The direction of the spin angular momentum vector is defined as that of a conventional spinning body; viewed along the vector it twists in the same sense as a right-handed screw. The spin angular momentum vector defines direction as well as magnitude, and this direction too must be quantized. This is achieved by specifying the z component of the spin angular momentum vector (z taken in a right handed cartesian frame) according to

$$P_z = \hbar m \qquad (2.2)$$

There are (2I + 1) allowed values of m given by

$$m = I, I-1 \ldots . -I \qquad (2.3)$$

A circulating charge in a magnetic field possesses a magnetic moment as described by classical electromagnetism. For nuclei with spin angular momentum **P** the magnetic moment is given by

$$\boldsymbol{\mu} = \gamma \mathbf{P} \qquad (2.4)$$

where $\boldsymbol{\mu}$ is the magnetic moment, **P** is the spin angular momentum and γ is the gyromagnetic ratio of the nucleus in question. It follows that

$$\mu_z = \gamma\hbar m \qquad (2.5)$$

and

$$\mu = \gamma\hbar[I(I + 1)]^{\frac{1}{2}} \qquad (2.6)$$

where μ and μ_z are the magnitudes of the appropriate vectorial quantities. The allowed values of the magnetic moment for a spin $I = \frac{1}{2}$ nucleus are shown in Figure 2.1.

In the absence of a magnetic field the 2I + 1 energy levels defined by the 2I + 1 values of the magnetic spin quantum number, m, are degenerate. This is equivalent to the fact that in zero magnetic field the energy of a magnet is independent of its orientation. However, in the presence of a magnetic field $\mathbf{B}_0$ applied in a defined z direction, a magnetic moment will have an interaction energy classically given by

$$E = -\boldsymbol{\mu} \cdot \mathbf{B}_0 = -\mu_z B_z \qquad (2.7)$$

so that

$$E = -\gamma \hbar m B_z \qquad (2.8)$$

The degeneracy of the 2I + 1 levels is lifted by the magnetic field. Transitions may be induced between the energy levels by electromagnetic radiation of the appropriate frequency; that is

$$h\nu = \gamma \hbar B_0 \qquad (2.9)$$

so that

$$\nu = (\gamma/2\pi)B_0 \qquad (2.10)$$

and

$$\omega = \gamma B_0 \qquad (2.11)$$

where ν is the frequency of the radiation and ω is the corresponding angular frequency.

In practice, n.m.r. experiments are carried out on samples which contain an ensemble of many spins. These spins are distributed among the available (2I + 1) energy levels defined by m. Although it is impossible to establish the position of an individual spin, the equilibrium distribution of spins among the energy levels will be Boltzmann[10], and dependent on temperature. For $I = \frac{1}{2}$ the two allowed energy levels are characterized by $m = \frac{1}{2}$ and $-\frac{1}{2}$, and are often called α and β. For a particular temperature

$$\frac{n_\alpha}{n_\beta} = \frac{\exp(-E_\alpha/kT)}{\exp(-E_\beta/kT)} = \exp((E_\beta - E_\alpha)/kT \qquad (2.12)$$

where n_α and n_β are the populations of the α and β levels, E_α and E_β are their respective energies, k is the Boltzmann constant and T is temperature in Kelvin.

2.3 Angular Momentum Operators

The wavefunctions corresponding to each permitted nuclear spin state are characterized by the quantum numbers I and m. These wavefunctions can be written in Dirac notation[11], $|I\ m>$. No spatial information is considered here, only spin variables. The measurement of the magnitude of the spin angular momentum vector, or its z component, collapses the appropriate wavefunction to an eigenstate and the result of the measurement is the corresponding eigenvalue. Mathematically this is described by operation on the wavefunction by an operator corresponding to the measured observable, for example

$$I_z |I,m> = m |I,m> \qquad (2.13)$$

where I_z is the operator corresponding to the z component of angular momentum and $|I,m>$ is an eigenfunction with eigenvalue m. Similarly,

$$I^2 |I,m> = I(I + 1) |I,m> \qquad (2.14)$$

so that the eigenvalue of I^2 is I(I + 1).

The raising and lowering operators are defined as

$$I_+ = I_x + iI_y$$

$$I_- = I_x - iI_y \qquad (2.15)$$

so that operation on $|I, m>$ gives

$$I_\pm |I, m> = [I(I + 1) - m(m \pm 1)]^{\frac{1}{2}} |I, m \pm 1> \qquad (2.16)$$

The commutator of two operators A and B is defined to be

$$[A,B] = A\,B - B\,A \tag{2.17}$$

so that when $[A,B] = 0$, the operators are said to commute. This has the significance that the physical quantities corresponding to the operators in question may be measured simultaneously. The commutator is equivalent to the Poission bracket of classical mechanics. Commutators can be derived by performing the appropriate operations on an arbitrary wavefunction. Some examples for spin angular momentum operators are as follows

$$\begin{aligned} [I_x, I_y] &= iI_z \\ [I_x, I_z] &= iI_x \\ [I_z, I_x] &= iI_y \end{aligned} \tag{2.18}$$

$$[I^2, I_z] = 0 \tag{2.19}$$

$$\begin{aligned} [I_+, I_z] &= -iI_+ \\ [I_-, I_z] &= I_- \\ [I_x, I_-] &= 2I_z \end{aligned} \tag{2.20}$$

2.4 Time-Dependent Perturbation Theory[5,11]

The measurement of the energy of a system corresponds to operation on the wavefunction describing the system, by the Hamiltonian operator, that is

$$\mathcal{H}\phi_n(t) = E_n\,\phi_n(t) \tag{2.21}$$

where $\mathcal{H}$ is the Hamiltonian of the system and $\phi_n(t)$ is an eigenfunction with eigenvalue E_n. Generally the wavefunction is a function of a number of variables, not just time. The Schrödinger equation is the basic equation that governs the time development of the probability amplitudes of quantum mechanical systems. In operator form

$$i\hbar\frac{d}{dt}\phi(t) = \mathcal{H}\phi(t) \tag{2.22}$$

When $\mathcal{H}$ is a time-independent operator, time dependent solutions of equation (2.21) can be found using equation (2.22); that is, the equation

$$i\hbar\frac{d}{dt}\phi_n(t) = E_n\,\phi_n(t) \tag{2.23}$$

can be solved by separation of variables to give

$$\phi_n(t) = \phi_n(0)\exp(-iE_nt/\hbar) \tag{2.24}$$

where $\phi_n(0)$ is the eigenfunction of the Hamiltonian at $t = 0$. Hamiltonians for particular quantum mechanical systems can be expressed explicitly. The classical expression for the interaction energy of a system can yield the Hamiltonian by replacing variables in the expression by their quantum mechanical operator analogues.

Time-dependent perturbation theory deals with the case where the total Hamiltonian of a system can be expressed in two parts, $\mathcal{H}_1$, an operator of the type discussed above and $\mathcal{H}_2$, with much smaller, time-dependent eigenvalues,

$$(\mathcal{H}_1 + \mathcal{H}_2)\,\psi(t) = i\hbar\frac{d}{dt}\psi(t) \tag{2.25}$$

Any wavefunction can be expanded as a set of eigenfunctions of the Hamiltonian. At a particular time the coefficients a_n of the eigenfunctions ϕ_n may vary as the wavefunction does;

$$\psi(t) = \sum_n a_n(t)\phi_n(t) \tag{2.26}$$

This idea is analagous to that of Fourier series. As with Fourier series the basis functions, here the eigenfunctions, form a complete orthonormal set. The orthonormality relation gives

$$\int \phi_m^*\phi_n\,dv = \delta_{mn} \tag{2.27}$$

where $\delta_{mn} = 1$ when n = m, and zero otherwise. Using this expansion to rewrite equation (2.25) gives

$$\sum_n (\mathcal{H}_1 + \mathcal{H}_2)\, a_n(t)\, \phi_n(t) = i\hbar \sum_n \frac{d}{dt}\, a_n(t)\phi_n(t)$$

$$\sum_n a_n(t)\, \mathcal{H}_1 \phi_n(t) + \sum_n a_n(t)\mathcal{H}_2(t)\, \phi_n(t) = i\hbar \sum_n a_n(t)\, \frac{d}{dt}\, \phi_n(t) + i\hbar \sum_n \frac{da_n}{dt}(t)\, \phi_n(t) \qquad (2.28)$$

With reference to equation (2.22) the first terms on both sides cancel, leaving

$$\sum_n a_n(t)\, \mathcal{H}_2(t)\, \phi_n(t) = i\hbar \sum_n \frac{da_n(t)}{dt}\, \phi_n(t) \qquad (2.29)$$

Multiplication of both sides by ϕ_f^* and integration over dv, followed by simplification using equation (2.27) gives

$$\sum_n a_n(t) \int \phi_f^*\, \mathcal{H}(t)\phi_n(t)dv = i\hbar \frac{da_f(t)}{dt} \qquad (2.30)$$

so that substitution of equation (2.24) now gives

$$\frac{d}{dt}\, a_f(t) = \frac{1}{i\hbar} \sum_n a_n(t) \int \phi_f^*(0)\, \mathcal{H}_2(t)\, \phi_n(0) \exp(-i(E_n - E_f)t/\hbar)\, dv \qquad (2.31)$$

Representation of the intitial state (t = 0) by an eigenfunction φ_i of energy E_i gives $a_i = 1$ $a_{n \neq i} = 0$ and integration of equation (2.31) now gives

$$a_{if}(t) = \frac{1}{i\hbar} \int_0^t < f \mid \mathcal{H}_2 \mid i > \exp(-i(E_i - E_f)t`/\hbar)\, dt` \qquad (2.32)$$

where

$$< f \mid \mathcal{H}_2 \mid i > = \int \phi_f^*(0) \mathcal{H}_2\, (t`)\, \phi_i(0)\, dv$$

The probability of finding a quantum mechanical system in a state described by eigenfunction $\varphi_f(0)$ at time t is given by

$$W_{if} = a_{if}^*\, a_{if} \qquad (2.33)$$

where a_{if} is given by equation (2.32). The derivation inherently contains the condition that the system is described at time zero by eigenfunction ϕ_i. The probability W_{if} is therefore the probability of transition between eigenfunctions ϕ_i and ϕ_f with energies E_i and E_f respectively.

2.5 Coordinate Systems

The complete Hamiltonian of systems of interest can be split into a spin part and a spatial part. This is the essence of semi-classical treatments of spin systems where the spin operators are quantum mechanical but the space variables are treated classically. It is usual for spin parts to be referred to a laboratory system (x, y, z) where the z direction is defined by the applied static magnetic field. However, it is important to realise that like all frames of reference it is arbitrary. Appropriate transformations allow another frame of reference to be selected and in some cases this can be beneficial, particularly when the rotation of molecular groups is involved. The reference frames that are most likely to be used are:

1 A crystal based system where (x_c, y_c, z_c) are based on suitably chosen crystal axes.

2 A molecular based system where (x_m, y_m, z_m) are based on the relative positions of atoms within a molecule and usually reflect the symmetry of the molecule. This is important when considering intramolecular interactions,

3 A principal axis system (PAS), where X, Y, Z are based on a frame of reference where the second rank irreducible coupling tensor (Section 2.6) is diagonal for the spin interactions of interest.

4 A rotating frame where (x`, y`, z) are based on the laboratory coordinates x, y rotating about the fixed z direction with some angular velocity ω_R. This is the spectrometer frame of reference.

All coordinate systems are orthogonal and in principle transformations from one general coordinate system to another can be achieved by rotation using three operations.

2.5.1 Rotation of Axes and Euler Angles

Rotations are of particular importance in n.m.r. theory. In general, rotations can be described by two complimentary methods. In an active rotation the coordinates of an object change with respect to some fixed axis. In a passive rotation, the coordinate system axes move relative to a fixed object so that the object is now described by new coordinates.

When an orthogonal axis system (x, y, z) is rotated to become (x`, y`, z`), this change of frame can be performed by three rotations. The Euler angles (α, β, γ) give the magnitude of each stage of rotation about a defined axis. Rotations are defined in a positive sense in a right handed screw system, so that the process is described by

START	ROTATION	FINISH
(x, y, z)	Angle α about z direction	(x_1, y_1, z)
(x_1, y_1, z)	Angle β about y_1 direction	(x_1`, $y_1$, z`)
(x_1`, $y_1$, z`)	Angle γ about z` direction	(x`, y`, z`)

This is shown in Figure 2.2.

The operator that performs this sequence is given by[12]

$$\mathcal{D}(\alpha,\beta,\gamma) = \exp(-i\gamma I z`)\ \exp(-i\beta I y_1)\ \exp(-i\alpha I_z) \qquad (2.34)$$

For rotations about the original z and y axes equation (2.34) becomes

$$\mathcal{D}(\alpha,\beta,\gamma) = \exp(-i\alpha I_z)\ \exp(-i\beta I_y)\ \exp(-i\gamma I_z) \qquad (2.35)$$

Defining $\mathcal{D}^{\dagger}(\alpha,\beta,\gamma)$ to be the adjoint of $\mathcal{D}(\alpha,\beta,\gamma)$ (the complex conjugate of the tranpose) gives

$$\mathcal{D}^{\dagger}(\alpha,\beta,\gamma) = \mathcal{D}^{-1}(\alpha,\beta,\gamma) = \mathcal{D}(-\alpha, -\beta, -\gamma) \tag{2.36}$$

so that

$$\mathcal{D}^{\dagger}\mathcal{D} = \mathcal{D}\mathcal{D}^{\dagger} = 1 \tag{2.37}$$

This is the definition of a unitary operator. An alternative and often useful form of the rotation operator is given by

$$\mathcal{D}(\alpha,\beta,\gamma) = \begin{pmatrix} \cos\alpha\cos\beta\cos\gamma - \sin\alpha\sin\gamma & \sin\alpha\cos\beta\cos\gamma + \cos\alpha\sin\gamma & -\sin\beta\cos\gamma \\ -\cos\alpha\cos\beta\sin\gamma - \cos\alpha\cos\gamma & -\sin\alpha\cos\beta\sin\gamma + \cos\alpha\cos\gamma & \sin\beta\sin\gamma \\ \cos\alpha\sin\beta & \sin\alpha\sin\beta & \cos\beta \end{pmatrix} \tag{2.38}$$

An operator A in one frame can now be transformed to an operator $A`$ in another frame by

$$A` = \mathcal{D}(\alpha\beta\gamma) A \mathcal{D}^{-1}(\alpha\beta\gamma) \tag{2.39}$$

2.6 Tensor Operators and Irreducible Notation

A tensor[6,13] is a mathematical object that contains information about the coupling of quantities. Tensors of different rank are defined which transform in different ways under coordinate transformations. The n^L components of tensor operators; where n is the dimension and L is the rank; form a group. According to group theory these components have an irreducible representation. This representation has particularly useful symmetry properties. A tensor operator of rank L in 3 dimensions can be represented by L+1 irreducible tensor operators

$$T_0^0 + \sum_{M=-1}^{M=1} T_M^1 + \sum_{M=-2}^{M=2} T_M^2 + \text{- - - -} \sum_{M=-L}^{M=L} T_M^L \tag{2.40}$$

Number of Terms	1	3	5	2L + 1

A tensor operator of rank 2, which has 9 components, can be written as the sum of three irreducible tensor operators with 1, 3 and 5 components respectively. The irreducible tensor operators have straightforward simple transformation properties under unitary transformations and the rotation operator is a unitary operator as shown in Section 2.5.1. An irreducible tensor operator of rank L has (2L + 1) components, labelled by M, which transform according to

$$\mathcal{D}(\alpha\beta\gamma)\, T^{L}_{M}\, \mathcal{D}^{-1}(\alpha\beta\gamma) = \sum_{M`=-L}^{M=L} T^{L}_{M`}\, \mathcal{D}^{L}_{M`M}(\alpha\beta\gamma) \qquad (2.41)$$

$\mathcal{D}^{L}_{M`M}(\alpha\beta\gamma)$ are components of the Wigner rotation matrices, calculated explicitly in many texts on group theory[12,14,15] (Appendix 1). The irreducible $T^{L}_{M}$ transform under rotation into linear combinations of $T^{L}_{M`}$, in exactly the same way as the spherical harmonics Y^{L}_{M} transform into linear combinations of $Y^{L}_{M`}$. Hence, the irreducible form of a vector operator $\boldsymbol{I}$ is the form in which the components $T^{1}_{m}$, transform into linear combinations of the components $T^{1}_{m`}$ under rotation. It can hence be shown that the irreducible representation of $\boldsymbol{I}$ is not I_x, I_y, I_z, but $I^{1}_{\pm1}$, and I^{1}_{0}, where

$$I^{1}_{\pm1} = \mp(1/\sqrt{2})\ (I_x \pm iI_y) \qquad (2.42)$$

and

$$I^{1}_{0} = I_z$$

so that, I_x, I_y and I_z can be related to the irreducible representation of $\boldsymbol{I}$ by

$$I_x = -(1/\sqrt{2})\ (I^{1}_{+1} - I^{1}_{-1})$$

$$I_y = -(1/\sqrt{2}i)\ (I^{1}_{+1} + I^{1}_{-1}) \qquad (2.43)$$

$$I_z = I^{1}_{0}$$

The irreducible components of the vector operator $\boldsymbol{I}$ are closely related to the raising and lowering operators described in Section 2.3. It turns out that

$$I^{1}_{\pm1} = \mp(1/\sqrt{2})\ I_{\pm} \qquad (2.44)$$

Irreducible tensorial components can be used to construct components of higher rank irreducible tensors, using the Clebsch-Gordan coefficients (these are derived from a transformation between an uncoupled and coupled representation of two coupled angular momenta[12,16]). In the cases of interest here, components of the second rank coupling tensor containing information about the coupling of $\boldsymbol{I}$ to some other quantity, for example **B**, can be constructed from the irreducible components of $\boldsymbol{I}$ and **B**. In general, for two vectors **I** and **V**, the nine components of the second rank coupling tensor T^L_M are given in Table 2.1.

Table 2.1 Components of the second rank tensor, T^L_M, constructed from the irreducible component of two vectors **I** and **V**.

T^L_M	Irreducible components	Cartesian Representation
$T^0_0 =$	$-I^1_{+1}V^1_- - I^1_- V^1_+ + I^1_0 V^1_0$	$I_x V_x + I_y I_y + I_z V_z$
$T^1_0 =$	$\frac{1}{\sqrt{2}}(I^1_{+1}V^1_{-1} - I^1_{-1}V^1_{+1})$	$\frac{1}{\sqrt{2}}(I_xV_y - I_y V_x)$
$T^1_{\pm1} =$	$\frac{1}{\sqrt{2}} \pm (I^1_{\pm1}V^1_0 \mp I^1_0 V^1_{\pm1})$	$\frac{1}{2}[-(I_x \pm iV_y)V_z + I_z(V_x \pm iV_y)]$
$T^2_0 =$	$\frac{1}{\sqrt{6}}(I^1_{+1}V^1_{-1} + I^1_{-1}V+^1_{+1} + 2I^1_0 V^1_0)$	$\frac{1}{\sqrt{6}}[-I_xV_z - I_y V_y - I_z V_z + 3I_zV_z]$
$T^2_{\pm1} =$	$\frac{1}{\sqrt{2}}(I^1_{\pm1}V^1_0 + I^1_0V^1_{\pm1})$	$\frac{1}{2}[\mp V_x \pm iV_y) \mp (I_x \pm iI_y) V_z]$.
$T^2_{\pm2} =$	$I^1_{\pm1}V^1_{\pm1}$	$[I_xV_x - I_yV_y \pm i(I_xV_y + I_yV_x)]$

Any second rank cartesian tensor can be expressed in terms of a scalar, an antisymmetric first rank tensor and a symmetric traceless second rank tensor;

$$\begin{pmatrix} A_{xx} & A_{xy} & A_{xz} \\ A_{yx} & A_{xy} & A_{yz} \\ A_{zx} & A_{zy} & A_{zz} \end{pmatrix} = \begin{pmatrix} \frac{1}{3}(A_{xx}+A_{yy}+A_{zz}) & 0 & 0 \\ 0 & \frac{1}{3}(A_{xx}+A_{yy}+A_{zz}) & 0 \\ 0 & 0 & \frac{1}{3}(A_{xx}+A_{yy}+A_{zz}) \end{pmatrix}$$

$$+ \begin{pmatrix} 0 & \frac{1}{2}(A_{xy}-A_{yx}) & \frac{1}{2}(A_{xz}-A_{zx}), \\ \frac{1}{2}(A_{yx}-A_{xy}) & 0 & \frac{1}{2}(A_{yz}-A_{zy}) \\ \frac{1}{2}(A_{zx}-A_{xz}) & \frac{1}{2}(A_{zy}-A_{yz}) & 0 \end{pmatrix}$$

$$+\begin{pmatrix} A_{xx}-\frac{1}{3}(A_{xx}+A_{yy}+A_{zz}) & \frac{1}{2}(A_{xy}+A_{yx}) & \frac{1}{2}(A_{xz}+A_{zx}) \\ \frac{1}{2}(A_{yx}+A_{xy}) & A_{yy}-\frac{1}{3}(A_{xx}+A_{yy}+A_{zz}) & \frac{1}{2}(A_{yz}+A_{zy}) \\ \frac{1}{2}(A_{zx}+A_{xz}) & \frac{1}{2}(A_{zy}+A_{yz}) & A_{zz}-\frac{1}{3}(A_{xx}+A_{yy}+A_{zz}) \end{pmatrix}$$

$$= R^{(0)} + R^{(1)} + R^{(2)} \tag{2.45}$$

For $R^{(2)}$ there is a PAS, such that the matrix is diagonal. This system can be obtained by a unitary rotation; that is

$$R^{(2)} = \mathcal{D}(\alpha\beta\gamma)\, \rho^{(2)}\, \mathcal{D}^{-1}(\alpha\beta\gamma) \tag{2.46}$$

where $\rho^{(2)}$ is diagonal. The complete tensor can be rotated into this frame. The off-diagonal elements of $\rho^{(2)}$ being zero gives $\rho_{xy} = -\rho_{yx}$, $\rho_{xz} = -\rho_{zx}$, and $\rho_{zy} = -\rho_{yz}$ in the PAS of $R^{(2)}$; giving $\rho^{(1)}$ in a new form, and $\rho^{(0)}$ is invariant under coordinate transformations, so that

$$A_{ij} = R\begin{pmatrix}1&0&0\\0&1&0\\0&0&1\end{pmatrix} + \begin{pmatrix} 0 & \rho_{xy} & \rho_{xz} \\ -\rho_{xy} & 0 & \rho_{yz} \\ -\rho_{xz} & -\rho_{xz} & 0 \end{pmatrix} + \begin{pmatrix} \rho_{xx} & 0 & 0 \\ 0 & \rho_{yy} & 0 \\ 0 & 0 & \rho_{zz} \end{pmatrix} \tag{2.47}$$

$$= \quad \rho^{(o)} \quad + \quad \rho^{(1)} \quad + \quad \rho^{(2)}$$

where

$$R = \tfrac{1}{3}(A_{xx} + A_{yy} + A_{zz}).$$

If the axes of the PAS are labelled according to

$$|\rho_{zz}| \geq |\rho_{xx}| \geq |\rho_{yy}| \tag{2.48}$$

and an asymmetry parameter is defined as

$$\eta = \frac{\rho_{yy} - \rho_{xx}}{\delta};\ \delta = \rho_{zz} \tag{2.49}$$

then $\rho^{(2)}$ being traceless, imposes limits, $0 \leq \eta \leq 1$, and gives

$$\begin{pmatrix} \rho_{xx} & 0 & 0 \\ 0 & \rho_{yy} & 0 \\ 0 & 0 & \rho_{zz} \end{pmatrix} = \delta \begin{pmatrix} -\frac{1}{2}(1+\eta) & 0 & 0 \\ 0 & -\frac{1}{2}(1-\eta) & 0 \\ 0 & 0 & 1 \end{pmatrix}$$

Equation (2.47) can now be rewritten as

$$A_{ij} = R \begin{pmatrix} 1 & 0 & 0 \\ 0 & 1 & 0 \\ 0 & 0 & 1 \end{pmatrix} + \begin{pmatrix} 0 & \rho_{xy} & \rho_{xz} \\ -\rho_{xy} & 0 & \rho_{yz} \\ -\rho_{xz} & -\rho_{yz} & 0 \end{pmatrix} + \delta \begin{pmatrix} -\frac{1}{2}(1+\eta) & 0 & 0 \\ 0 & -\frac{1}{2}(1-\eta) & 0 \\ 0 & 0 & 1 \end{pmatrix} \quad (2.50)$$

$$= \quad \rho^{(0)} \quad + \quad \rho^{(1)} \quad + \quad \rho^{(2)}$$

Substitution of this form of $\rho^{(2)}$ into equation (2.46) and use of the matrix form of $\mathcal{D}(\alpha\beta\gamma)$, given by equation (2.38), gives the principal elements of the original, traceless, symmetric second rank tensor as

$$R_{xx}^{(2)} = \frac{\delta}{2}(-1+3\sin^2\beta\cos^2\gamma - \eta[\cos2\alpha(\cos^2\beta\cos^2\gamma-\sin^2\gamma) - \sin2\alpha\sin2\gamma\cos\beta])$$

$$R_{yy}^{(2)} = \frac{\delta}{2}(-1+3\sin^2\beta\sin\gamma - \eta[\cos2\alpha(\cos^2\beta\sin^2\gamma-\cos^2\gamma) + \sin2\alpha\sin2\gamma\cos\beta]) \quad (2.51)$$

$$R_{zz}^{(2)} = \frac{\delta}{2}(3\cos^2\beta - 1 - \eta\sin^2\beta\cos2\alpha)$$

A similar rotation can be performed to give the original $R^{(1)}$ components[6]. The zz component of the symmetric traceless second rank tensor differs from the zz component of the original second rank coupling tensor by the scalar R; $R_{zz}^{(2)} = A_{zz}^{(2)} - R$, as can be deduced from equation (2.45).

2.7 The Basic Hamiltonians

The energy of a system characterized by the stationary wavefunction $|\psi>$ is the eigenvalue of the operation of the appropriate Hamiltonian,

$$\mathcal{H}|\psi> = E|\psi> \quad (2.52)$$

The total Hamiltonian for a nucleus in an external magnetic field is the sum of Hamiltonians corresponding to all possible interactions. In general for a hetronuclear system

$\mathcal{H} = \mathcal{H}^{Z} + \mathcal{H}^{RF}$ (External influences applied by experimental conditions, field and pulse).

$+ \mathcal{H}^{D,II} + \mathcal{H}^{D,IS} + \mathcal{H}^{D,SS}$ (Internal pairwise dipolar interaction present between nuclei type I and S)

$+ \mathcal{H}^{CS}$ (Internal chemical shielding interactions)

$+ \mathcal{H}^{Q}$ (Internal quadrupolar interactions; only for $I > \frac{1}{2}$)

$+ \mathcal{H}^{L}$ (Internal direct coupling to lattice-phonon or phonon-electron) (2.53)

The Hamiltonian operator can be described in two ways – each with its particular merit. The two complimentary descriptions are outlined below.

The Interaction Written in the Form of a Second Rank Cartesian Tensor

The operator expresses the coupling between the nuclear spin vector and another vectorial quantity, either another spin vector or an applied field. The information about the coupling of one element with another is contained in a second rank cartesian tensor, A^{λ}, where λ = Z, RF, D, CS,Q, L, corresponding to the particular interaction being considered.

Generally, for the coupling of two vector operators in angular frequency units[4]

$$\mathcal{H} = \boldsymbol{I}.A^{\lambda}.\boldsymbol{V} \qquad (2.54)$$

The advantage of this approach is that it gives a straightforward picture of the physical relationship between the two vectorial quantities involved.

An Irreducible Tensor Approach

The operator can be written in terms of irreducible tensor operators

$$\mathcal{H} = C^{\lambda} \sum_{L=0}^{2} \sum_{M=-L}^{M=L} (-1)^{M} R_{M}^{L\lambda} T_{-M}^{L\lambda} \quad (IV) \tag{2.55}$$

This representation is of particular benefit when dealing with problems which involve the rotation of molecular groups. The $T_{-M}^{L\lambda}$ refer only to spin variables and the $R_{M}^{L\lambda}$ contain only spatial information. The $R_{M}^{L\lambda}$ are related to the coupling tensor A^{λ}.

Cartesian tensors can be transformed into irreducible spherical harmonic tensors as follows. The irreducible representation of equation (2.54) in the PAS of $\rho^{(2)}$, using equation (2.50) and dropping λ, gives, for two general vectors

$$\mathcal{H} = (I_x\, I_y\, I_z)R \begin{pmatrix} 1 & 0 & 0 \\ 0 & 1 & 0 \\ 0 & 0 & 1 \end{pmatrix} \begin{pmatrix} V_x \\ V_y \\ V_z \end{pmatrix} + (I_x I_y\, I_z) \begin{pmatrix} 0 & \rho_{xy} & \rho_{xz} \\ -\rho_{xy} & 0 & \rho_{yz} \\ -\rho_{xz} & -\rho_{yz} & 0 \end{pmatrix} \begin{pmatrix} V_x \\ V_y \\ V_z \end{pmatrix} +$$

$$(I_x\, I_y\, I_z)\, \delta \begin{pmatrix} -\frac{1}{2}(1+\eta) & 0 & 0 \\ 0 & -\frac{1}{2}(1-\eta) & 0 \\ 0 & 0 & 1 \end{pmatrix} \begin{pmatrix} V_x \\ V_y \\ V_z \end{pmatrix} \tag{2.56}$$

which can be multiplied out to give

$$\mathcal{H}^{(0)} = R(I_x V_x + I_y V_y + I_z V_z)$$

$$\mathcal{H}^{(1)} = (I_x V_y - I_y V_x)\rho_{xy} + (I_x V_z - I_z V_x)\rho_{xz} + (I_y V_z - I_z V_y)\rho_{yz} \tag{2.57}$$

$$\mathcal{H}^{(2)} = \tfrac{1}{2}\delta(1+\eta)\, I_x V_x - \tfrac{1}{2}\delta(1-\eta) I_y V_y + I_z V_z$$

$$= \tfrac{1}{2}\delta(-I_x V_x - I_y V_y - I_z V_z + 3 I_z V_z) + \tfrac{1}{2}\delta\eta(-I_x V_z + I_y V_y)$$

Equation (2.55) in the PAS, again dropping λ for convenience, gives, for two general vectors

$$\mathcal{H} = \sum_{L=0}^{2} \sum_{M=-L}^{M=L} (-1)^M \rho_M^L T_{-M}^L \ (\mathbf{IV}) \qquad (2.58)$$

Simultaneous substitution of $\mathcal{H}(0)$ with the corresponding T_0^0; $\mathcal{H}(1)$ with the corresponding T_0^1, $T_{\pm 1}^1$; and $\mathcal{H}(2)$ with the corresponding T_0^2, $T_{\pm 1}^2$, and $T_{\pm 2}^2$, gives the ρ_M^L by comparison of the appropriate **I** and **V** component combinations on either side of equation (2.58). These are

$$\rho_0^0 = R$$

$$\rho_0^1 = -\frac{i}{\sqrt{2}} \rho_{xy}$$

$$\rho_{\pm 1}^1 = \rho_{xz} + i\rho_{yz} \qquad (2.59)$$

$$\rho_0^2 = \sqrt{\tfrac{3}{2}}\, \delta$$

$$\rho_{\pm 1}^2 = 0$$

$$\rho_{\pm 2}^2 = -\tfrac{1}{2}\, \delta\eta$$

In the following chapter, the irreducible tensor operator description is demonstrated in detail for the dipolar Hamiltonian, by way of an example; otherwise the Hamiltonians are simply stated in both forms of representation.

2.71 The Zeeman Hamiltonian

In the presence of a magnetic field **B**, the energy of a 'bare' nucleus possessing spin I is determined by the Zeeman Interaction

$$\mathcal{H}^z = \mathbf{B}.A^z.I \qquad (2.60)$$

Usually the applied static magnetic field is taken to be along the cartesian z axis, and in this case only has a z component. The LAB frame is equivalent to the PAS frame.

$$\mathcal{H}_Z = -\gamma(0 \;\; 0 \;\; B_Z)\begin{pmatrix}1 & 0 & 0\\ 0 & 1 & 0\\ 0 & 0 & 1\end{pmatrix}\begin{pmatrix}I_x\\ I_y\\ I_z\end{pmatrix}$$

$$\mathcal{H}^Z = -\gamma B_Z I_Z \tag{2.61}$$

Alternatively, in irreducible tensor notation

$$\mathcal{H}^z = C^z \sum_{L=0}^{2} \sum_{M=-L}^{M=L} (-1)^M R_M^{LZ} T_{-M}^{L\,Z}\,(\boldsymbol{I}\mathbf{B}) \tag{2.62}$$

2.7.2 The RF Hamiltonian

During an n.m.r. experiment transitions are induced between the nuclear spin states. These transitions are of energy ΔE, where

$$\Delta E = h\nu$$

The radiant energy is supplied by photons of electromagnetic radiation in the radiofrequency region. In a continuous wave experiment, the frequency is swept and resonance is found at a particular frequency corresponding to the resonant frequency of one nuclear species in one environment. In pulsed Fourier transform n.m.r. the selected frequency is the carrier frequency of a pulse. The pulse is short, typically of the order of microseconds and the sample is irradiated by a large band of Fourier frequency components. This is discussed further in Chapter 3.

The coupling between the nuclear spin system and the applied r.f radiation is identical to that described by the Zeeman Hamiltonian with the magnetic field vector described by the magnetic field component of the radiation. The form of the radiofrequency Hamiltonian is

$$\mathcal{H}^{RF} = \mathbf{B}_1 . A^{RF} . \boldsymbol{I} \tag{2.63}$$

$$\mathcal{H}^{RF} = \gamma(0 \;\; B_{1y}(t) \;\; 0)\cos(\omega_R t)\begin{pmatrix}1 & 0 & 0\\ 0 & 1 & 0\\ 0 & 0 & 1\end{pmatrix}\begin{pmatrix}I_x\\ I_y\\ I_z\end{pmatrix} \tag{2.64}$$

$$\mathcal{H}^{RF} = \gamma B_{1y}(t)\cos\omega_R t I_y \tag{2.65}$$

Alternatively in irreducible tensor notation

$$\mathcal{H}^{RF} = C^{RF} \sum_{L=0}^{2} \sum_{M=-L}^{M=L} (-1)^M R_M^{L\,RF}\, T_{-M}^{L\,RF}(\boldsymbol{I}\boldsymbol{B}_1) \tag{2.66}$$

2.7.3 The Dipolar Hamiltonian

The dipolar interaction is composed of two distinct couplings: a direct through space vector coupling of magnetic moments and a scalar coupling via electrons. Isotropic molecular tumbling will average the vector coupling to zero. This is seen in solution state experiments. In the solid state this is not the case and usually the direct vector coupling is orders of magnitude larger than the scalar term. The direct coupling is examined here. Classically, the interaction energy of two magnetic dipoles, with magnetic moments $\boldsymbol{\mu}_1$ and $\boldsymbol{\mu}_2$ respectively, is given by

$$E = \frac{\boldsymbol{\mu}_1.\boldsymbol{\mu}_2}{r^3} - 3\frac{(\boldsymbol{\mu}_1.\mathbf{r})(\boldsymbol{\mu}_2.\mathbf{r})}{r^5} \tag{2.67}$$

The dipolar Hamiltonian can be obtained by replacing the classical quantities by the appropriate quantum mechanical operators

$$\boldsymbol{\mu}_1 = \gamma_1 \hbar \boldsymbol{I}_1$$

$$\boldsymbol{\mu}_2 = \gamma_2 \hbar \boldsymbol{I}_2$$

For a macroscopic sample in which pairwise interactions can be summed, the Hamiltonian is given by

$$\mathcal{H}^D = \frac{1}{2}\sum_{j=1}^{N}\sum_{k=1}^{N} \frac{\mu_0}{4\pi}\frac{\gamma_1\gamma_2\hbar}{r_{jk}^3}\left\{\boldsymbol{I}_j.\boldsymbol{I}_k - 3\frac{(\boldsymbol{I}_j.\mathbf{r})(\boldsymbol{I}_k.\mathbf{r})}{r_{jk}^2}\right\} \tag{2.68}$$

The $\frac{1}{2}$ is required as the notation $\sum_{j=1}^{N}\sum_{k=1}^{N}$ counts each spin pair twice: $\sum_{j<k}$ is an equivalent notation. Equation (2.68) can be written in a more familiar and useful

way by a transformation to spherical polar coordinates and vector operator components I_+, I_- (the raising and lowering operators) and I_z. That is

$$\mathcal{H}^D = \tfrac{1}{2} \sum_{j=1}^{N} \sum_{k=1}^{N} \frac{\mu_0}{4\pi} \frac{\gamma_j \gamma_k \hbar}{r_{jk}^3} \, [A+B+C+D+E+F] \tag{2.69}$$

where

$$A = I_z^{(1)} I_z^{(2)} (1-3\cos^2\theta)$$

$$B = -\tfrac{1}{4} (I_+^{(1)} I_-^{(2)} + I_-^{(1)} I_+^{(2)}) (1-3\cos^2\theta)$$

$$C = -\tfrac{3}{2} (I_z^{(1)} I_+^{(2)} + I_z^{(2)} I_+^{(1)}) \sin\theta\cos\theta\exp(-i\varphi)$$

$$D = -\tfrac{3}{2} (I_z^{(1)} I_-^{(2)} + I_z^{(2)} I_-^{(1)}) \sin\theta\cos\theta\exp(i\varphi)$$

$$E = -\tfrac{3}{4} I_+^{(1)} I_+^{(2)} \sin^2\theta\exp(-2i\varphi)$$

$$F = -\tfrac{3}{4} I_-^{(1)} I_-^{(2)} \sin^2\theta\exp(+2i\varphi)$$

The terms of this equation, A-F, are referred to as the dipolar alphabet. A simple physical interpretation of these terms is discussed later. Equation (2.69) can be presented in a notation consistent with equation (2.54), so that for a pair of spins

$$\mathcal{H}^D = \boldsymbol{I}^{(1)} . A^D . \boldsymbol{I}^{(2)} \tag{2.70}$$

Alternatively the irreducible spherical tensor operator notation can be used to describe the Hamiltonian. There are no terms with L=0 or L=1 as the coupling tensor is symmetric and traceless, giving restrictions on possible ρ_M^L (from equation (2.59); so that

$$\mathcal{H}^D = \sum_{j<k} C_{jk}^D \sum_{M=-2}^{M=2} (-1)^M \, R_{M,jk}^2 \, T_{-M,jk}^2 \, (\boldsymbol{I}_j \boldsymbol{I}_k) \tag{2.71}$$

The dipolar Hamiltonian provides a good example for demonstrating the equivalence between the cartesian and irreducible tensor notations. For a pair of spins, equation (2.68) gives

$$\mathcal{H}^D = \frac{\mu_0}{4\pi} \frac{\gamma_1 \gamma_2}{r^5} \hbar \{ (\boldsymbol{I}^{(1)} . \boldsymbol{I}^{(2)}) r^2 - 3 (\boldsymbol{I}^{(1)} . \mathbf{r}) (\boldsymbol{I}^{(2)} . \mathbf{r}) \}$$

where the (1) and (2) signify the two distinct spins. It is straightforward to expand products in terms of I_x, I_y, I_z and r_x, r_y, r_z. The irreducible tensor components can then be substituted, as described in equations (2.43) giving

$$I_x = -\frac{1}{\sqrt{2}}(I_{+1}^1 - I_{-1}^1);\ I_y = -\frac{1}{\sqrt{2i}}(I_{+1}^1 + I_{-1}^1);\ I_z = I_0^1$$

and

$$r_x = -\frac{1}{\sqrt{2}}(r_{+1}^1 - r_{-1}^1);\ r_y = -\frac{1}{\sqrt{2i}}(r_{+1}^1 + r_{-1}^1);\ r_z = r_0^1$$

so that

$$\begin{aligned}\mathcal{H}^D = \frac{\mu_0}{4\pi}\frac{\gamma_1\gamma_2\hbar}{r^5}\ \{&(-I_{+1}^{1(1)}I_{-1}^{1(2)} + I_0^{1(1)}I_0^{1(2)} - I_{-1}^{1(1)}I_{+1}^{1(2)})(-2r_{-1}^1 r_{+1}^1 + (r_0^1)^2)\\ &- 3[I_{-1}^{1(1)}I_{-1}^{1(2)}(r_{+1}^1)^2 + I_{+1}^{1(1)}I_{+1}^{1(2)}(r_{-1}^1)^2 - (I_{-1}^{1(1)}I_0^{1(2)} + I_0^{1(1)}I_{-1}^{1(2)})r_{+1}^1 r_0^1\\ &- (I_{+1}^{1(1)}I_0^{1(2)} + I_0^{1(1)}I_{+1}^{1(2)})r_{-1}^1 r_0^1 + (I_{-1}^{1(1)}I_{+1}^{1(2)} + I_{+1}^{1(1)}I_{-1}^{1(2)})r_{+1}^1 r_0^1\\ &+ I_0^{1(1)}I_0^{1(2)}(r_0^1)^2]\}\end{aligned} \tag{2.72}$$

The rearrangement of this equation and comparison with the irreducible components given in Table 2.1 gives

$$\begin{aligned}\mathcal{H}^D = \frac{\mu_0}{4\pi}\frac{\gamma_1\gamma_2\hbar}{r^5}\ \{&-3[T_{-2}^2 R_2^2 + T_{+2}^2 R_{-2}^2 - T_{-1}^2 R_1^2 - T_1^2 R_{-1}^2] - (I^1{}_{-1}{}^{(1)} I^1{}_{+1}{}^{(2)} +\\ &I^1{}_{+1}{}^{(1)} I^1{}_{-1}{}^{(2)})r^1{}_{+1}\, r^1{}_{-1} - 2I^1{}_0{}^{(1)} I^1{}_0{}^{(2)}(r_0^1)^2 - 2I^1{}_0{}^{(1)} I^1{}_0{}^{(2)}\, r^1{}_{+1} r^1{}_{-1} -\\ &(I^1{}_{+1}{}^{(1)} I_{-1}^{1(2)} + I_{-1}^{1(1)} I_{+1}^{1(2)})(r_0^1)^2\}\end{aligned} \tag{2.73}$$

$$\mathcal{H}^D = -3\frac{\mu_0}{4\pi}\frac{\gamma_1\gamma_2\hbar}{r^5}\sum_{M=-2}^{2}(-1)^M R_M^2 T_{-M}^2 \tag{2.74}$$

which summed over all spin pairs, is equivalent to equation (2.71)

The explicit expression for the dipolar Hamiltonian can be calculated using the irreducible tensor notation. In this case the PAS is not the LAB frame and so the R_M^2 are not equivalent to the calculated ρ_M^2 given in equation (2.59), but are

related to them by a rotation parameterized by the Euler angles (Section 2.5.1). Under rotation, irreducible spherical tensor components transform, as given in equation (2.41), according to

$$R^L_M = \sum_{M'} \rho^L_{M'} \mathcal{D}^L_{M'M}(\alpha\beta\gamma) \tag{2.75}$$

where $\mathcal{D}^L_{M'M}(\alpha\beta\gamma)$ is an element of the Wigner rotation matrix,

$$\mathcal{D}^L_{M'M}(\alpha\beta\gamma) = \exp(-i(M'\alpha + M\gamma))\, d^L_{M'M}(\beta) \tag{2.76}$$

and $d^L_{M'M}$ are real and calculated explicitly, as given in Appendix 1. The asymmetry parameter of the coupling tensor given in equation (2.70) is zero, giving only ρ^2_0 as non-zero, from equations (2.59), so that equation (2.71) simplifies to

$$\mathcal{H}^D = C^D \sum_{M=-2}^{2} (-1)^M \mathcal{D}^2_{0M}(\alpha\beta\gamma)\, \rho^2_0\, T^2_M \tag{2.77}$$

for a single pair of spins. The corresponding T^L_M are obtained from Table 2.1:

$$T^2_0 = \frac{1}{\sqrt{6}} (I^1{}_{-1}{}^{(1)} I^1{}_{+1}{}^{(2)} + I^1{}_{+1}{}^{(1)} I^1{}_{-1}{}^{(2)} + 2I^1{}_0{}^{(1)} I^1{}_0{}^{(2)})$$

$$T^2_{\pm1} = \frac{1}{\sqrt{2}} (I^1{}_{\pm1}{}^{(1)} I^1{}_0{}^{(2)} + I^1{}_0{}^{(1)} I^1{}_{\pm1}{}^{(2)}) \tag{2.78}$$

$$T^2_{\pm2} = I^1{}_{\pm1}{}^{(1)} I^1{}_{\pm1}{}^{(2)}$$

$$\rho^2_0 = \sqrt{\tfrac{3}{2}}\,\delta = \sqrt{\tfrac{3}{2}}\, r^{-3}$$

The corresponding elements of $\mathcal{D}^2_{0-M}$ are given by

$$\mathcal{D}^2_{0-2} = \exp(2i\gamma) \sqrt{\tfrac{3}{8}} \sin^2\theta$$

$$\mathcal{D}^2_{0-1} = -\exp(i\gamma) \sqrt{\tfrac{3}{2}} \sin\theta\cos\theta$$

$$\mathcal{D}^2_{00} = \tfrac{1}{2}(3\cos^2\theta - 1) \tag{2.79}$$

$$\mathcal{D}^2_{01} = \exp(-i\gamma)\sqrt{\tfrac{3}{2}}\sin\theta\cos\theta$$

$$\mathcal{D}^2_{02} = \exp(-2i\gamma)\sqrt{\tfrac{3}{8}}\sin^2\theta$$

Substitution of these explicit expressions into equation (2.77) gives

$$\begin{aligned}\mathcal{H}^D = C^D\sqrt{\tfrac{3}{2}}r^{-3}\{&\tfrac{1}{\sqrt{6}}(I^1{}_{+1}{}^{(1)}\,I^1{}_{-1}{}^{(2)} + I^1{}_{-}{}^{(1)}\,I_{+1}{}^{(2)} + 2I^1{}_0{}^{(1)}\,I^1{}_0{}^{(2)})\,\tfrac{1}{2}(3\cos^2\theta-1)\\ &-\tfrac{1}{\sqrt{2}}(I^1{}_{+1}{}^{(2)}\,I^1{}_0{}^{(2)} + I^1{}_0{}^{(1)}\,I^1{}_{+1}{}^{(2)})\,(\exp(-i\gamma))\sqrt{\tfrac{3}{2}}\sin\theta\cos\theta\\ &-\tfrac{1}{\sqrt{2}}(I^1{}_{-1}{}^{(1)}\,I^1{}_0{}^{(2)} + I^1{}_0{}^{(1)}\,I^1{}_{-1}{}^{(2)})\,(-\exp(i\gamma))\sqrt{\tfrac{3}{2}}\sin\theta\cos\theta\\ &+I^1{}_{+1}{}^{(1)}\,I^1{}_{+1}{}^{(2)}\,(\exp(-2i\gamma))\sqrt{\tfrac{3}{8}}\sin^2\theta\\ &+I^1{}_{-1}{}^{(1)}\,I^1{}_{-1}{}^{(2)}\,(\exp(2i\gamma))\sqrt{\tfrac{3}{8}}\sin^2\theta\}\end{aligned} \qquad (2.80)$$

This equation can be written in terms of the raising and lowering operators which are related to the irreducible components, as described in Section 2.6, by $I^1{}_{\pm1} = \mp\frac{1}{\sqrt{2}}I_{\pm}$, and $I^1{}_0 = I_z$, so that

$$\begin{aligned}\mathcal{H}^D = C^D\,r^{-3}\{&\tfrac{1}{8}(-I_+{}^{(1)}\,I_-{}^{(2)} - I_-{}^{(1)}\,I_+{}^{(2)} + 4I_z{}^{(1)}\,I_z{}^{(2)})(3\cos^2\theta-1)\\ &-\tfrac{3}{4}(I_+{}^{(1)}\,I_z{}^{(2)} + I_z{}^{(1)}\,I_+{}^{(2)})\sin\theta\cos\theta\exp(i\gamma)\\ &-\tfrac{3}{2}(I_-{}^{(1)}\,I_0{}^{(2)} + I_0{}^{(1)}\,I_-{}^{(2)})\sin\theta\cos\theta\exp(i\gamma)\\ &-\tfrac{3}{8}I_+{}^{(1)}\,I_+{}^{(2)}\sin^2\theta\,\exp(2i\gamma)\\ &-\tfrac{3}{8}I_+{}^{(1)}\,I_-{}^{(2)}\sin^2\theta\,\exp(2i\gamma)\}\end{aligned} \qquad (2.81)$$

Putting $C^D = -2\gamma_1\gamma_2\hbar\mu_0/4\pi$ and summing over all spin pairs gives the Hamiltonian expressed in terms of the dipolar alphabet, identical to equation (2.69)

The frequency spectrum for two dipolar coupled spin $I = \frac{1}{2}$ nuclei consists of two lines separated by $\Delta\omega = \frac{3}{2}\gamma^2\hbar\frac{1}{r^3}(1 - 3\cos^2\theta)$ where θ is the angle between the applied field and the internuclear vector. For an isotropically orientated distribution of dipolar vectors, the frequency spectrum of non-interacting spin $I = \frac{1}{2}$ pairs is shown in Figure 2.3. This was first calculated by Pake[16].

The spin operator components in each term of the dipolar alphabet are associated with specific transitions. In a homonuclear two spin system the terms of the dipolar alphabet connect states as shown in Table 2.2.

Table 2.2: States connected by the terms of the dipolar alphabet.

Spin State	$\|\beta\beta\rangle$	$\|\alpha\beta\rangle$	$\|\beta\alpha\rangle$	$\|\alpha\alpha\rangle$
$\|\beta\beta\rangle$	A	D	D	F
$\|\alpha\beta\rangle$	C	A	B	D
$\|\beta\alpha\rangle$	C	B	A	D
$\|\alpha\alpha\rangle$	E	C	C	A

When $|\alpha\beta\rangle$ and $|\beta\alpha\rangle$ are degenerate (only for a homonuclear system) both terms A and B conserve energy; they are secular and commute with the Zeeman Hamiltonian. Term A simply expresses the interaction energy of the magnetic dipoles due to their respective alignments in the field. Term B can be said to simultaneously flip one spin up and another one down and is known as the flip-flop term. The fact that this term is non-diagonal in the representation shown in Table 2.2 shows that the states used in the table are not true basis states and Term B therefore plays an important role in determining these true basis states (as shown in Chapter 8). Terms C-F all express interactions where energy is emitted or absorbed. They are non-secular. Terms C and D each flip one spin only and connect states that differ in energy by $\hbar\omega$, where as terms E and F flip both spins up or both spins down, connecting states that differ by $2\hbar\omega$. They are important as they permit otherwise forbidden transitions, but will contribute to the spectrum with an intensity ratio $(B_0/B)^2 \sim 10^{-8}$. It is usually a good

approximation to drop terms C⟶F when calculating the spectrum, leaving the secular dipolar Hamiltonian, often referred to as the dipolar term.

2.7.4 The Chemical Shielding Hamiltonian

The movement of electrons around a nucleus constitutes a current. When a static magnetic field, $\mathbf{B}_0$, is applied, the electrons are subject to a force, and this in turn generates a local magnetic magnetic field. This local magnetic field will be opposed to $\mathbf{B}_0$ and the effect is to shield the nucleus from it. The nucleus experiences an effective field given by

$$\mathbf{B}_{eff} = \mathbf{B}_0(1-\sigma) \tag{2.82}$$

where σ is the chemical shielding tensor usually measured in parts per million (ppm) and,

$$\mathcal{H}^{CS} = \boldsymbol{I}.\mathrm{A}^{CS}.\mathbf{B}_0 \tag{2.96}$$

In the case of isolated atoms electrons are free to circulate and the shielding is positive and isotropic. When the electronic environment of a given nucleus of an atom in a molecule is not symmetric, anisotropic shielding occurs and the second rank coupling tensor need not be symmetric or traceless. In general, for the applied field along the cartesian z axis, the Hamiltonian is given by

$$\mathcal{H}^{CS} = \gamma(I_x\, I_y\, I_z)\begin{pmatrix}\sigma_{xx} & \sigma_{xy} & \sigma_{xz}\\ \sigma_{yx} & \sigma_{yy} & \sigma_{yz}\\ \sigma_{zx} & \sigma_{zy} & \sigma_{zz}\end{pmatrix}\begin{pmatrix}0\\0\\B_z\end{pmatrix} \tag{2.83}$$

The interaction tensor can be written in irreducible notation in the PAS of $\rho^{(2)}$ in accordance with equation (2.50). The first rank antisymmetric component is negligible or zero for systems of interest in this work; this is discussed in some detail by Haeberlen[7]. In the PAS of $\rho^{(2)}$ then;

$$\mathcal{H}^{CS} = (I_x I_y I_z)\gamma\bar{\sigma}\begin{pmatrix}1&0&0\\0&1&0\\0&0&1\end{pmatrix}\begin{pmatrix}0\\0\\Bz\end{pmatrix} + (I_x I_y I_z)\gamma\delta\begin{pmatrix}-\frac{1}{2}(1+\eta)&0&0\\0&-\frac{1}{2}(1-\eta)&0\\0&0&1\end{pmatrix}\begin{pmatrix}0\\0\\B_z\end{pmatrix} \tag{2.84}$$

where

$$\bar{\sigma} = \tfrac{1}{3}(\sigma_{xx} + \sigma_{yy} + \sigma_{zz}),\ \eta = \frac{\rho_{yy}-\rho_{xx}}{\delta},\ \delta = \rho_{zz}^{(2)}$$

so that

$$\mathcal{H}^{CS} = \gamma I_z B_z\,\bar{\sigma} + \gamma I_z B_z \rho_{zz}^{(2)} \tag{2.85}$$

A transformation to the LAB frame can be carried out by

$$\mathcal{H}^{CS} = \gamma I_z B_z\,[\mathcal{D}(\alpha\beta\gamma)\,\bar{\sigma}\,\mathcal{D}^{-1}(\alpha\beta\gamma) + \mathcal{D}(\alpha\beta\gamma)\,\rho_{zz}^{(2)}\mathcal{D}^{-1}(\alpha\beta\gamma)] \tag{2.86}$$

so that according to equation (2.46)

$$\mathcal{H}^{CS} = \gamma I_z B_z[\bar{\sigma} + R_{zz}^{(2)}] \tag{2.87}$$

This simplifies, using equation (2.62) to

$$\mathcal{H}^{CS} = \gamma I_z B_z\,\sigma_{zz} \tag{2.88}$$

or, substituting the expression for $R_{zz}^{(2)}$, given in equation (2.51), to

$$\mathcal{H}^{CS} = \gamma I_z B_z[\bar{\sigma} + \frac{\delta}{2}(3\cos^2\beta - 1 - \eta\sin^2\beta\cos 2\alpha)] \tag{2.89}$$

where $\bar{\sigma}$, η and δ are experimental parameters. The orientation of the PAS to the LAB frame is only available from single crystal studies. In some cases the orientation can be determined simply from molecular geometry. The calculated spectrum for chemical shielding interactions in a polycrystalline sample with a large anisotropy is shown in Figure 2.4.

Alternatively the Hamiltonian can be written using the irreducible tensor notation

$$\mathcal{H}^{CS} = C^{CS} \sum_{L=0}^{2} \sum_{M=-L}^{L} (-1)^M R^L_M T^L_{-M} \quad (\boldsymbol{IB}) \qquad (2.90)$$

2.75 The Quadrupolar Hamiltonian

In general the electric quadrupole moment is one of a series of multipole moments which can be used to describe the distribution of electric charge over a body. In simplistic terms it can be regarded as an arrangement of two positive and two negative charges which has no net charge and no net dipole moment. Quadrupole moments will interact with an electric field gradient (e.f.g.). Only nuclei with $I \geq \frac{1}{2}$ possess a nuclear electric quadrupole moment In the absence of an applied magnetic field, the orientation of the nucleus and the splitting of the energy levels are determined by the e.f.gs. These can be investigated by nuclear quadrupole resonance (NQR). In n.m.r experiments with nuclei $I > \frac{1}{2}$, when the applied magnetic field is large the quadrupolar interaction will perturb the Zeeman energy levels. The origin of the coupling is the interaction between the charge distribution of the nuclei, density ρ, and an external potential V. Classically, the energy of such an interaction is given by

$$E = \int \rho(r)\, V(r)\, dr^3 \qquad (2.91)$$

Expanding V(r) as a Taylor series about the origin, chosen to be the mass centre of the nucleus, and using Laplaces equation, $\nabla^2 V = 0$, the quadrupolar term can be written as

$$E^{(Q)} = \frac{1}{6} \sum_{\alpha\beta} V_{\alpha\beta} Q_{\alpha\beta} \qquad (2.92)$$

where

$$Q_{\alpha\beta} = \int [3x_\alpha x_\beta - \delta_{\alpha\beta} r^2] d\tau \qquad (2.93)$$

The substitution of the appropriate quantum mechanical operators for their classical counterparts gives

$$\mathcal{H}_Q = \frac{1}{6}\sum_{\alpha\beta} V_{\alpha\beta}\, Q_{\alpha\beta} \tag{2.94}$$

where

$$Q_{\alpha\beta} = e\sum_{\kappa}(3x_{\alpha k}x_{\beta k} - \delta_{\alpha\beta}r_k^2) \tag{2.95}$$

and κ is the sum over nuclear particles.

The matrix elements of the operator $Q_{\alpha\beta}$ can be evaluated using the Wigner-Eckart Theorem[11] to change operator variables and then symmetrizing the expression, so that equation (2.94) becomes

$$\mathcal{H}_Q = \frac{1}{6}\sum_{\alpha\beta} V_{\alpha\beta}\frac{eQ}{I(2I-1)}[\tfrac{3}{2}(I_{\alpha\beta} + I_{\beta\alpha}) - \delta_{\alpha\beta}I^2] \tag{2.96}$$

where

$$eQ = (II|e\sum_k[3z_k^2 - r_k^2]|II) \tag{2.97}$$

In a PAS in which $V_{\alpha\beta}$ is diagonal, this can be rewritten, using Laplace's equation as

$$\mathcal{H}_Q = \frac{eQ}{4I(2I-1)}[V_{zz}(3I_z^2 - I^2) + (V_{xx} - V_{yy})(I_x^2 - I_y^2)] \tag{2.98}$$

When axial symmetry of the potential is a good approximation, this reduces to

$$\mathcal{H}_Q = \frac{e^2q_{zz}Q}{4I(2I-1)}(3I_z^2 - I^2) \tag{2.99}$$

where

$$eq_{zz} = V_{zz} = \frac{d^2V}{dz^2} \tag{2.100}$$

So, when the applied magnetic field is large, the energy eigenvalues in first order are given by

$$E_m = -\gamma B_z m + \frac{e^2qQ}{8I(2I-1)} (3\cos^2\theta - 1)[3m^2 - I(I+1)] \qquad (2.101)$$

The effect of first order quadrupole coupling is shown in Figure 2.5 for a $I = \frac{3}{2}$ nucleus.

2.8 The Density Matrix

For a homonuclear spin system in a large applied magnetic field of strength B_z applied along the z axis, a measurement of macroscopic nuclear magnetization will produce a value given by

$$M_z = \chi B_z \qquad (2.102)$$

where χ is the static nuclear susceptibility parallel to the field. Measurements at right angles to the field give $M_x = M_y = 0$. These values are macroscopic observations of the properties of the ensemble of spins.

In a quantum mechanical description any wavefunction can be expanded as a set of its orthonormal eigenfunctions (Section 2.4).

$$\psi = \sum_n c_n \phi_n$$

where ϕ_n are the eigenfunctions and c_n are the corresponding coefficients. Any state can thus be described by the terms $c_j^* c_k$, which can be conveniently arranged as elements of a matrix p_{jk} so that the expectation value of a general operator A is given by

$$\begin{aligned} \langle A \rangle &= \langle \psi | A | \psi \rangle \\ &= \langle \sum_j c_j^* \phi_j | A | \sum_k c_k \phi_k \rangle \\ &= \sum_{jk} c_j^* c_k \langle \phi_j | A | \phi_k \rangle \\ \langle A \rangle &= \sum_{jk} p_{jk} \langle \phi_j | A | \phi_k \rangle \end{aligned} \qquad (2.103)$$

It is convenient to express the matrix elements, as defining the representation of an operator P

$$<\phi_k | P | \phi_j > = c_k c_j^* = P_{kj} \tag{2.104}$$

and now equation (2.103) can be written as

$$<A> = \sum_{jk} <\phi_k | P | \phi_j > < \phi_j | A | \phi_k >$$

$$= \sum_{k} < \phi_k | PA | \phi_j >$$

that is,

$$<A> = \mathrm{Tr}\{P\, A\} \tag{2.105}$$

However, it is clear that for a quantum mechanical description to be consistent with the observables of a macroscopic system the terms of interest are the average of the crossproducts $c_j^* c_k$. If this was not the case then the macroscopic observations $M_x = M_y = 0$ could only be consistent with a quantum description for the case of complete polarization. Replacement of P by ρ, the ensemble average density matrix operator gives[17]

$$<\bar{A}> = \mathrm{Tr}\{\rho\, A\} \tag{2.106}$$

In general this treatment introduces statistical operations twice. Firstly, in the quantum mechanical expectation values. This is connected with the perturbation of the system during measurement and is inherent to the interpreation of quantum mechanics. Secondly, in the averaging of expectation values with statistical weights inherent in replacing P by ρ.

The time dependence of the ensemble average density matrix operator is given by the Liouville-von Neumann equation:

$$\frac{d\rho}{dt} = \frac{i}{\hbar} [\rho, \mathcal{H}] \tag{2.107}$$

When $\mathcal{H}$ is time independent, the solution of this equation is given by

$$\rho(t) = \exp(-(i/\hbar)\,\mathcal{H}\,t)\,\rho(0)\,\exp((i/\hbar)\,\mathcal{H}\,t) \qquad (2.108)$$

For a system that is initially in thermal equilibrium $\rho(0)$ can be determined. The populations of the states will depend on the Boltzman distribution (Section 2.2). The probability of a system being in a state with energy, E_n is given by

$$P(E_n) = \frac{\exp(-E_n/kT)}{Z} \qquad (2.109)$$

where Z is the partition function, defined to be $Z = \sum_n \exp(-E_n/kT)$, and equivalent to the sum over all states. The expectation value for the energy of the system, E_n, is expressed by equation (2.106). For this to be consistent with equation (2.109), then

$$\rho(0) = \frac{\exp(-\mathcal{H}/kT)}{Tr\{\exp(-\mathcal{H}/kT)\}} \qquad (2.110)$$

The exponential terms can be expanded as a power series, and in a high temperature approximation only the first two terms of the numerator are kept so that

$$\rho(0) \approx \frac{1-(\mathcal{H}/kT)}{Tr\{\exp(-\mathcal{H}/kT)\}} \qquad (2.111)$$

For an n.m.r. sample at thermal equilibrium in a strong static field, the Zeeman Hamiltonian is given by equation (2.61),

$$\mathcal{H} = -\gamma B_z I_z$$

If the $Tr\{A\}$, (A being the operator on which $\rho(0)$ operates at t = 0), is zero, then the first term of equation (2.111) can be ignored. This is true for I_x, I_y and I_z; so that for systems of interest here,

$$\rho(0) \approx \frac{\gamma B_z I_z}{Tr\{1\}\,kT} \qquad (2.112)$$

The average expectation value of a general operator A, over an ensemble, can now be calculated at any time under these conditions, using equations (2.106), (2.108) and (2.111); so that

$$\langle \bar{A} \rangle = \frac{\gamma B_z}{\mathrm{Tr}\{1\}kT} \mathrm{Tr}\{\exp(-(i/\hbar)\,\mathcal{H}(t))\, I_z \exp((i/\hbar)\,\mathcal{H}(t))\, A\} \qquad (2.113)$$

The value of M_z under static conditions (no time dependent interactions) can be calculated using this method;

$$\langle \bar{M}_z \rangle = \frac{\gamma B_z}{\mathrm{Tr}\{1\}kT} \mathrm{Tr}\{I_z M_z\} \qquad (2.114)$$

giving

$$\langle \bar{M}_z \rangle = \frac{N\gamma^2 B_z \hbar}{\mathrm{Tr}\{1\}kT} \mathrm{Tr}\{I_z^2\} \qquad (2.115)$$

The evaluation of the trace in equation (2.115) involves the sum of a series

$$\mathrm{Tr}\{I_z^2\} = \sum_{m=-I}^{m=I} m^2 = 2\sum_{m=1}^{m=I} m^2 \qquad (2.116)$$

and

$$\sum_{m=-I}^{m=I} m^2 = \frac{I(I+1)(2I+1)}{3} \qquad (2.117)$$

Substituting this into equation (2.115), and also noting that,

$$\mathrm{Tr}\{1\} = \sum_{m=-I}^{m=I} 1 = 2I + 1 \qquad (2.118)$$

gives

$$\langle \bar{M}_z \rangle = \frac{N\gamma^2 B_z \hbar I(I+1)}{3kT} \qquad (2.119)$$

which is Curie's Law for magnetization.

2.8.1 Transient NMR signals

The time evolution of the n.m.r. signal following an applied r.f pulse is called the free induction decay (f.i.d.). In general to calculate this f.i.d. requires the evaluation of $\langle I_x(t) \rangle$. Using the density matrix formalism developed in Section 2.8, and writing the Hamiltonian in frequency units, gives

$$\langle I_x(t) \rangle = \mathrm{Tr}\{\exp(-i\,\mathcal{H}\,t)\,\rho(0)\exp(i\,\mathcal{H}\,t)\,I_x\} \tag{2.120}$$

For the system initially in thermal equilibrium, equation (2.112) gives

$$\rho(0) = cI_z \tag{2.121}$$

where c is a constant, so that equation (2.120) becomes

$$\langle I_x(0) \rangle = c\mathrm{Tr}\{I_z I_x\} \tag{2.122}$$

A trace is invariant under coordinate rotation and hence a rotation of coordinate system by π about the x axis gives $\mathrm{Tr}\{I_z I_x\} = \mathrm{Tr}\{-I_z I_x\}$. This only holds for $\mathrm{Tr}\{I_z I_x\} = 0$, giving $\langle I_x(0) \rangle = 0$.

For a hard r.f. pulse it can be assumed that,

$$\| \mathcal{H}^{RF} \| >> \sum_i \| \mathcal{H}_i \| \tag{2.123}$$

where $\mathcal{H}_i$ denotes any other interaction, and

$$\| \mathcal{H} \| = \{\mathrm{Tr}[\mathcal{H}^2]\}^{\frac{1}{2}} \tag{2.124}$$

The application of such an r.f pulse, length τ, produces $\rho(\tau)$ of the form

$$\rho(\tau) = \exp(-i\mathcal{H}^{RF}\tau)\; cI_z \exp(i\mathcal{H}^{RF}\tau) \tag{2.125}$$

or, using equation (2.65)

$$\rho(\tau) = c\,\exp(-i\omega\tau I_y)\,I_z\,\exp(i\omega\tau I_y) \tag{2.126}$$

This is equivalent to rotation of the operator. Expressions for the rotation of any spin coordinate about any axis can be derived by cycling x, y and z (preserving the right handedness of the system) in the expression:

$$\exp(i\alpha I_j)I_k\exp(-i\alpha I_j) = I_k\cos\alpha - I_l\sin(\alpha e_{jkl}) \qquad (2.127)$$

where $e_{jkl} = 0$ if any indices are equivalent, 1 if indices in cyclic order, and -1 if indices are in anticyclic order. So that equation (2.126) becomes

$$\rho(\tau) = c(I_z\cos\omega\tau + I_x\sin\omega\tau) \qquad (2.128)$$

or when τ is selected to give $\omega\tau = 90°$

$$\rho(\tau) = cI_x \qquad (2.129)$$

giving

$$<I_x(\tau)> = cTr\{I_x^2\} \qquad (2.130)$$

This equation shows that the magnetization has been rotated onto the x axis. The total Hamiltonian governing the evolution of the system from time τ can be written as $\mathcal{H}^D + \mathcal{H}^{OTH}$, where $\mathcal{H}^{OTH} = \mathcal{H}^Z + \mathcal{H}^{CS} + \mathcal{H}^Q + \mathcal{H}^L$. For a non-quadrupolar spin system, and where $\mathcal{H}^L$ is negligible, equations (2.61) and (2.88) give

$$\mathcal{H}^{OTH} = \Delta\omega I_z \qquad (2.131)$$

where

$$\Delta\omega = -\gamma B_z(1 + \sigma_{zz})$$

Substitution of these Hamiltonians into equation (2.120) gives the signal at time t after a 90° pulse, which can be normalised using equation (2.130), as

$$<I_x(t)> = \frac{Tr\{\exp(-i(\mathcal{H}^D + \mathcal{H}^{OTH})t)\, cI_x\exp(i(\mathcal{H}^D + \mathcal{H}^{OTH})t)\, I_x\}}{cTr\{I_x^2\}} \qquad (2.132)$$

It can be shown that when $[\mathcal{H}^D, \mathcal{H}^{OTH}] = 0$, then this simplifies to

$$<I_x(t)> = \frac{\cos\Delta\omega t \; Tr\{\exp(-i\mathcal{H}^D t) I_x \exp(i\mathcal{H}^D t) I_x\}}{Tr\{I_x^2\}} \qquad (2.133)$$

This is a LAB frame expression, where $\Delta\omega$ depends on spectrometer offset and chemical shift. An analytical solution is not always possible, since elements of the Hamiltonian do not in general commute amongst themselves.

2.10 The Method of Moments

The moments of a spectral line characterize its shape. To completely describe a line shape all moments must be obtained. However, for broad featureless lines the important information is contained in the first few moments. This is the case for spectra broadened by dipolar interactions. The method of moments, developed by Van Vleck[18] can provide important information about a sample. The nth moment, M_n, of a spectral line in the frequency domain is defined, about ω_o to be

$$M_n = \frac{\int_{-\infty}^{\infty} (\omega-\omega_o)^n f(\omega) d\omega}{\int_{-\infty}^{\infty} f(\omega)\, d\omega} \qquad (2.134)$$

The denominator is the zeroth moment and is equivalent to the area under the spectrum. This constant will not affect the lineshape and generally will be normalized giving

$$M_n = \int_{-\infty}^{\infty} (\omega-\omega_0)^n f(\omega) d\omega \qquad (2.135)$$

If $f(\omega)$ is an even function centred on ω_o, then all odd moments will be zero. For odd functions, it is always possible to choose an ω_o such that the first moment will be zero (this will be the centre of gravity of the shape). The second moment

is analogous to the moment of inertia of the lineshape about ω_o, and in principle can be determined experimentally.

A dipolar broadened n.m.r. signal, typical of a solid, can often be approximated by a Gaussian function in both the time and frequency domains (the Gaussian function is its own Fourier transform). The Gaussian assumption is in general, reasonable, when $M_4/(M_2)^2$ is the order of 3. For this case the normalized lineshape of the frequency spectrum is given by

$$f(\omega) = \frac{1}{\sigma\sqrt{2\pi}} \exp\left(\frac{(-\omega-\omega_o)^2}{2\sigma^2}\right) \qquad (2.136)$$

where σ is a number characteristic of a particular spectrum. Using equation (2.135), with reference to standard mathematical integrals, gives the result

$$M_2 = \sigma^2 \qquad (2.137)$$

and more generally

$$M_{2n} = (2n-1)(\sigma^2)^n \qquad (2.138)$$

In this case only one parameter is needed to completely describe the lineshape. Manipulation of equation (2.136) gives a second moment expression in terms of the half width at half height, δ, of the lineshape function; that is

$$M_2 = \delta^2/(2\ln 2) \qquad (2.139)$$

where

$$\delta = \sqrt{2\ln 2}\,\sigma \sim 1.18\sigma \qquad (2.140)$$

Theoretical expressions for M_2 can be derived, related to structural and dynamical properties of a system.

In the time domain, the n^{th} moment of the resonance line is defined as

$$M_n = (-i)^n \frac{d^n}{dt^n} G(t) \Big|_{t=0} / M_o \tag{2.141}$$

where M_o is defined to be the area under the absorption spectrum. In general the f.i.d., G(t), can be expressed as an infinite time series

$$G(t) = \left\{ \sum_{n=0}^{\infty} M_n \frac{t^n}{n!} \right\} M_0 \tag{2.142}$$

and can in principle be obained from equation (2.133). The time expansion

$$\exp(-iQt)P\exp(iQt) = P - it[P,Q] + \frac{t^2}{2}[Q,[Q,P]] \text{ ------} \tag{2.143}$$

is particularly useful under conditions in which the Hamiltonian components of the evolving system do not commute. Using this expansion the form of G(t) becomes

$$G(t) = \frac{1}{Tr\{I_x^2\}} Tr\{(1 + i[\mathcal{H},I_x]t + i^2[\mathcal{H},[\mathcal{H},I_x]] \frac{t^2}{2!} + ..)I_x\} \tag{2.144}$$

so that the expressions for the nth moments are

$$M_n = \frac{1}{Tr\{I_x^2\}} Tr\{[\mathcal{H},[\text{---} [\mathcal{H},I_x]\text{---}]]I_x\} \tag{2.145}$$

$$\longleftarrow \text{ n times } \longrightarrow$$

and in particular

$$M_2 = \frac{1}{Tr\{I_x^2\}} Tr\{[\mathcal{H},[\mathcal{H},I_x]]I_x\} \tag{2.146}$$

The form of the f.i.d. using this time expansion now becomes

$$\langle I_x(t) \rangle = \frac{\cos\Delta\omega t}{Tr\{I_x^2\}} Tr\{(1 + i[\mathcal{H},I_x]t + i^2[\mathcal{H}[\mathcal{H},I_x]]\frac{t^2}{2!}...)I_x\} \tag{2.147}$$

which is equivalent to

$$\langle I_x(t) \rangle = \cos\Delta\omega t[1 - \frac{M_2t^2}{2!} + \frac{M_4t^4}{4!} - \frac{M_6t^6}{6!} + ...] \tag{2.148}$$

The reason for the Gaussian lineshape approximation now becomes clear. The Gaussian function $\exp(-\frac{1}{2}M_2t^2)$ has the expansion

$$\exp(-\tfrac{1}{2}M_2t^2) = \cos\Delta\omega t[1 - \frac{M_2t^2}{2!} + \frac{3M_2^2t^4}{4!} - \frac{15M_2^3t^6}{6!} + ...] \qquad (2.149)$$

which is identical in second order with equation (2.148). An approximate model for the system is therefore given by

$$\langle I_x(t)\rangle \approx \exp(-\tfrac{1}{2}M_2t^2) \qquad (2.150)$$

How good a model this is will depend on the relative sizes of M_4 and $3M_2^2$; M_6 and $15M_2^2$ etc.

Explicit evaluation of the second moment involves equation (2.146), simplified by the associative properties of commutators with respect to diagonal elements, to

$$M_2 = -\frac{Tr\{[\mathcal{H},I_x]^2\}}{Tr\{I_x^2\}} \qquad (2.151)$$

It can be shown that this expression yields, for a homonuclear system;

$$M_2 = \frac{3}{4}\left(\frac{\mu_0}{4\pi}\right)^2\gamma^4\hbar^2I(I+1)\sum_j\frac{(1-3\cos^2\theta_{jk})^2}{r_{jk}^6} \qquad (2.152)$$

For a polycrystalline powder composed of randomly oriented crystals, it is necessary to average over all possible orientations of the crystallites, which gives

$$M_2 = \frac{3}{5}(\frac{\mu_0}{4\pi})^2\gamma^4\hbar^2I(I+1)\sum_j\frac{1}{r_{jk}^6} \qquad (2.153)$$

The second moment due to interactions between unlike spins can be similarly calculated using the secular part of the hetronuclear dipolar Hamiltonian. The result differs by a factor, given by

$$M_2^{IS} = M_2^{II}\frac{4}{9}(\frac{\gamma_S}{\gamma_I})^2\frac{S(S+1)}{I(I+1)} \qquad (2.154)$$

The total second moment of a system containing both homonuclear and heteronuclear interactions will be the sum $M_2^{II} + M_2^{IS}$. These second moments are defined as 'rigid-lattice' values since they are derived assuming no motion. The main advantage of this method is that moments can be calculated without knowledge of the Hamiltonian eigenstates. The main difficulty with the method is the experimental determination of moments; that is, where to truncate the frequency domain spectra.

Studies of moments can give dynamical information. It can be shown that, for rotational motion of a particular molecular group, more rapid than the static linewidth, the angular dependent quantity involved in calculating second moments is given by

$$\langle(1-3\cos^2\theta)^2\rangle = \tfrac{1}{4}(3\cos^2\beta-1)^2(3\cos^2\chi-1)^2 \qquad (2.155)$$

where β is the angle between the internuclear vector and the applied field, and χ is the angle between the internuclear vector and the axis of rotation. For a polycrystalline sample the averaging is averaged over the angle β_{jk}, as previously described for θ_{jk}. It can be seen that for a rapidly rotating molecular group. M_2 is scaled by $\frac{1}{4}(3\cos^2\chi-1)^2$. It is exactly this fact that is exploited by magic angle spinning n.m.r. experiments. When $\chi = 54.7°$, $\frac{1}{4}(3\cos^2\chi-1)^2 = 0$ and broad solid lines are narrowed to produce high resolution spectra.

2.10 Spin Relaxation

An ensemble of spins placed in a magnetic field will populate available energy levels according to a statistical equilibrium. The time evolution of the system from a prepared state, to equilibrium, is the process of relaxation. The total system consists of two coupled systems; the spin system consisting of all degrees of freedom dependent on the spin operators, and the lattice, consisting of all other degrees of freedom appropriate to the sample; for example molecular

motions. The relaxation process defined by the interaction of these systems is spin-lattice relaxation. The lattice is taken to be large in the sense that its own thermal equilibrium is not affected by the exchange of energy between systems. Macroscopically, at thermal equilibrium with the lattice, the population difference of the energy states of the spin system gives rise to a nuclear magnetization M_z. The components of the nuclear magnetization M_x and M_y are zero (Section 2.8). The decrease of these transverse nuclear magnetization components does not involve direct energy exchange with the lattice. Bloch produced empirical equations assuming exponential evolution towards equilibrium[20]

$$\frac{d}{dt}M_z = -\frac{1}{T_1}(M_z - M_0) \tag{2.156}$$

$$\frac{d}{dt}M_{x,y} = -\frac{1}{T_2}M_{x,y} \tag{2.157}$$

where T_1 and T_2 are the characteristic time constants for longitudinal (spin-lattice) relaxation, and transverse (spin-spin) relaxation respectively.

Explicit expressions for T_1 and T_2, for defined motional processes can be obtained using the density matrix formalism (Section 2.8) [1,6,21,22]. The starting point for the derivation of relaxation rates in this manner is the master equation,

$$\frac{d}{dt}\rho_R = -\int_0^\infty <[\mathcal{H}_R^\lambda(t), [\mathcal{H}_R^\lambda(t-\tau), \rho_R(t)]] > d\tau \tag{2.158}$$

where R denotes the rotating frame, λ denotes the interaction, and $\mathcal{H}_R^\lambda(t)$ are the spin Hamiltonians, now rendered time dependent. This can result from two mechanisms; $R_M^\lambda \longrightarrow R_M^\lambda(t)$ or $T_M^\lambda \longrightarrow T_M^\lambda(t)$. The latter is important in just two cases, where the time dependency results from; (i) Fluctuating angular velocity of the molecules due to a spin rotation interaction (ii) scalar interactions between two nuclei where one has a shortened relaxation time due to another interaction. In all other cases the coupling operators that depend on space

variables become time dependent due to molecular motion. It is this time dependence that determines the spin-lattice relaxation rate encountered when the spin Hamiltonian is dipolar, quadrupolar or chemical shielding in nature.

The foundations of the quantum theory of n.m.r. were layed down by Bloembergen, Purcell and Pound[23]. This treatment involves the use of time-dependent perturbation theory. Each spin experiences, superimposed on the applied field, a small field due to its interactions, the amplitude and orientation of which change suddenly and randomly at random time intervals of mean value τ_c, which is referred to as the correlation time.

2.10.1 Correlation Functions and Spectral Density

The idea of correlation functions is an element of the theory of random processes. For a random variable X, $\bar{P}(x)$ is the probability that a measurement of X will produce x. If the total number of measurements made of X is N then,

$$N = \int \bar{P}(x)dx \tag{2.159}$$

The normalized probability density is defined as

$$P(x) = \frac{1}{N}\bar{P}(x) \tag{2.160}$$

such that

$$1 = \int P(x)\ dx$$

and

$$< X > = \int xP(x)dx \tag{2.161}$$

In many physical situations pairs of random variables are encountered. These may or may not be interdependent to some degree. The interdependency can be examined in a quantitive way. For random variables X (set of measurements x_i)

and Y (set of measurements y_i) a set of x_iy_i can be calculated, these correspond to measurements of a new random variable XY. The mean value of XY can be expressed in two equivalant ways.

$$<XY> = \iint xyP(x,y)dxdy$$

or

$$<XY> = \iint xyP(x)P(x/y)dxdy \qquad (2.162)$$

where P(x,y) is the probability density of the appearance of the pair x,y, and P(x/y) is the probability density of y (the result of a measurement of Y) appearing together with x, known as the conditional probability density. Particular conditions give:

$$<XY> = \int xP(x)dx \int yP(y)dy = <X><Y> \qquad (2.163)$$

(X and Y are independent) and

$$<XY> = <xf(x)> \qquad (2.164)$$

(X and Y are interdependent)

That is, the quantity $<XY>$ is a measure of the correlation between X and Y.

A random function of time is an important concept in the theory of nuclear magnetic relaxation. In general, the random functions of time encountered are themselves of time independent character. Such functional forms are known as stationary. From a set of measurements of a random function F(t) at two arbitrary times t and $t+\tau$, a set of the products of the random function $F(t)F(t+\tau)$ can be calculated so that equation (2.162) gives

$$< F(t)F(t+\tau) > = \int xyP(x)P(x/y,\tau)\, dxdy = R(\tau) \qquad (2.165)$$

The mean is only a function of τ, and is known as the autocorrelation function.

Random functions may have complex values and hence $F(t+\tau)$ is replaced by $F^*(t+\tau)$, ensuring that autocorrelation function is stationary $F(t)$. When t and $t+\tau$ are very far apart then the measurements are independent so that

$$R(\tau) = \langle F(t)F^*(t+\tau) \rangle = \langle F(t) \rangle \langle F^*(t+\tau) \rangle = |\langle F(t) \rangle|^2 \qquad (2.166)$$

When t and $t+\tau$ are very close then the measurements are not independent so that now

$$R(\tau) = \langle F(t)F^*(t+\tau) \rangle = \langle |F(t)|^2 \rangle \qquad (2.167)$$

The investigation of the limits of $R(\tau)$ set by equations (2.166) and (2.167) shows that

$$|\langle F(t) \rangle|^2 < R(\tau) < \langle |F(t)|^2 \rangle \qquad (2.168)$$

For random motions $\langle F(t) \rangle = 0$ and accordingly

$$0 < R(\tau) < \langle |F(t)|^2 \rangle \qquad (2.169)$$

It can be shown that for stationary random functions of time

$$R(\tau) = \langle |F(t)|^2 | \rangle \exp(-|\tau|/\tau_c) \qquad (2.170)$$

where τ_c is the correlation time. It is a positive number which describes the relationship between values of a random function and the values at a previous or later time (the correlation function is symmetric with respect to time). It describes the extent to which the system has a memory of its previous state.

The Fourier transform of an autocorrelation function is known as the spectral density, $J(\omega)$. For an autocorrelation function of the form described in equation (2.170), this is given by

$$J(\omega) = \int_{-\infty}^{\infty} \langle |F(t)|^2 \rangle \exp(-(|\tau/\tau_c)) \exp(-i\omega\tau)\, d\tau \qquad (2.171)$$

This integral is solved by rewriting $\exp(-i\omega\tau)$ in the standard trigonometric way and integrating twice by parts, to give

$$J(\omega) = <|F(t)|^2> \frac{2\tau_c}{1 + \omega^2\tau_c^2} \qquad (2.172)$$

This is the spectral density function corresponding to diffusive motion.

2.10.2 Spin-lattice Relaxation in a Two Spin System

The eigenfunctions of the Zeeman Hamiltonian for a pair of isolated spin $I = \frac{1}{2}$ nuclei are denoted by $\alpha\alpha$, $\alpha\beta$, $\beta\alpha$, $\beta\beta$. The populations of these levels for an ensemble of isolated pairs are $N_{\alpha\alpha}$, $N_{\alpha\beta}$, $N_{\beta\alpha}$ and $N_{\beta\beta}$, where the sum of these terms is the total number of pairs N. Probabilities of a transition occurring between one level and another are denoted by w_0, w_1, w_1' and w_2, a number of transitions per pair per second, as shown below in Table 2.3.

Table 2.3: Probabilities of transitions between states in a two spin system

Spin State	$\|\beta\beta>$	$\|\beta\alpha>$	$\|\alpha\beta>$	$\|\alpha\alpha>$
$\|\beta\beta>$	–	w_1'	w_1	w_2
$\|\beta\alpha>$	w_1'	–	w_0	w_1
$\|\alpha\beta>$	w_1	w_0	–	w_1'
$\|\alpha\alpha>$	w_2	w_1	w_1'	–

The probability of transition from $|\alpha\beta> \longrightarrow |\alpha\alpha>$, is the same as $|\beta\beta> \longrightarrow |\beta\alpha>$, as both transitions only involve the second spin. Similarly the transition probability $|\beta\alpha> \longrightarrow |\alpha\alpha>$ is identical to that of $|\beta\beta> \longrightarrow |\alpha\beta>$. The number of transitions per second from $|\alpha\alpha> \longrightarrow |\alpha\beta>$, for example, is given by $N_{\alpha\alpha} W_1'$.

By writing the rate of change of populations in terms of these transitions, for example

$$\frac{dN_{\alpha\alpha}}{dt} = + w_2 N_{\beta\beta} + w_1 N_{\beta\alpha} + w_1' N_{\alpha\beta} - (w_1 + w_1' + w_2) N_{\alpha\alpha} + c_1 \qquad (2.173)$$

where c_1 corresponds to spontaneous emission; and the expectation value of I_z in terms of the difference between the populations of states of the relevant spin, that is, for example:

$$K < I_z^{(1)} > = (N_{\alpha\alpha} + N_{\alpha\beta}) - (N_{\beta\alpha} + N_{\beta\beta}) \tag{2.174}$$

it can be shown that the time dependence of $< I_z^{(1)} >$ and $< I_z^{(2)} >$ can be described by the two coupled differential equations given by

$$\frac{d}{dt} <I_z^{(1)}> = -(w_0 + 2w_1 + w_2)\ (<I_z^{(1)}> - I_\infty^{(1)}) - (w_2 - w_0)(<I_z^{(2)}> - I_\infty^{(2)}) \tag{2.175}$$

$$\frac{d}{dt} <I_z^{(2)}> = -(w_0 + 2\grave{w_1} + w_2))\ (<I_z^{(2)}> - I_\infty^{(2)}) - (w_2 - w_0)(<I_z^{(1)}> - I_\infty^{(1)}) \tag{2.176}$$

In a homonuclear system $\gamma_1 = \gamma_2$, $w_1 = \grave{w_1}$, and $<I_z> = <I_z^{(1)}> + <I_z^{(2)}>$ with $I_\infty = I_\infty^{(1)} + I_\infty^{(2)}$. Under these conditions, the addition of equations (2.175) and (2.176) gives

$$\frac{d}{dt} <I_z> = -2(w_2 + w_1)(<I_z> - I_\infty) \tag{2.177}$$

which can be solved by separation of variables to give

$$<I_z> - I_\infty, = A\exp(-2(w_2 + w_1)t) \tag{2.178}$$

When $t = 0$, $<I_z>_{t=0} = A + I_\infty$ so that

$$A = <I_z>_{t=0} - I_\infty \tag{2.179}$$

and equation (2.178) becomes

$$<I_z> = (<I_z>_{t=0} - I_\infty)\ \exp(-t/T_1) + I_\infty \tag{2.180}$$

where

$$T_1 = 1/2(w_2 + w_1) \tag{2.181}$$

In a heteronuclear system, in which one of the spins $I^{(2)}$ relaxes via a strong interaction with the environment with a fast spin-lattice relaxation time and does not depend on the other spin $I^{(1)}$ then, $<I_z^{(2)}> = I_\infty^{(2)}$, and equation (2.175) becomes

$$\frac{d}{dt}<I_z^{(1)}> = -(w_0 + 2w_1 + w_2)(<I_z^{(1)}> - I_\infty^{(1)}) \tag{2.182}$$

which again can be solved by separation of variables, giving

$$<I_z^{(1)}> = (<I_z^{(1)}>_{t=0} - I_\infty^{(1)})\ \exp(-t/T_1) + I_\infty^{(1)} \tag{2.183}$$

where

$$T_1 = 1/(w_0 + 2w_1 + w_2) \tag{2.184}$$

This is the case when, say, spin $I^{(2)}$ belongs to a nucleus with a large quadrupole moment, where interactions with electric field gradients gives rise to very efficient spin-lattice relaxation.

The calculation of spin-spin relaxation rates can be performed in a similar manner. This relaxation is taken to be in terms of quantum transitions between the eigenstates of the I_x operator (the identical arguments apply to the I_y operator). The solutions are similar to equations (2.180) and (2.184) with T_1 replaced by T_2 and the important distinction that the equilibrium values of the transverse components of nuclear magnetization are zero.

2.10.3 General Calculation of Spin-lattice Relaxation Time Behaviour

Consider spins $I^{(1)}$ and $I^{(2)}$, which belong to the same molecule such that the internuclear vector r is a constant. When the molecules are undergoing thermal motions, the polar angles θ and φ (see the dipolar alphabet) are random functions

eigenfunction $|n>$ at time zero, will, under the influence of perturbing Hamiltonian, $\mathcal{H}'(t)$ be described by $|m>$ at time t can be calculated using time-dependent perturbation theory as described in Section 2.4,

$$w_{nm} = a_{nm}\, a^*_{nm} \tag{2.185}$$

where

$$a_{nm} = \frac{1}{i\hbar}\int_0^t <m|\mathcal{H}'(t')|n> \exp(-i\omega_{nm}t')dt' \tag{2.186}$$

and ω_{nm} is the angular frequency corresponding to the energy difference of the states ($\omega_{nm} = (E_n - E_m)/\hbar$). The peturbing Hamiltonian will contain composite random functions of time, and generally each spin, or pair of spins, will have a different ω_{nm}. The average value of the particular transition probability over the sample will determine the experimentally accessable bulk properties

$$<w_{nm}> = \frac{1}{t}\int_0^t w_{nm}\, dt \tag{2.187}$$

so that,

$$\frac{d}{dt}<w_{nm}> = \frac{1}{t}\int_0^t \frac{d}{dt} w_{nm}\, dt$$

from which it follows that w_{nm}, the transition probability per unit time is given by

$$w_{nm} = \frac{d}{dt}<w_{nm}> \tag{2.188}$$

Substituting from equation (2.185) this becomes

$$w_{nm} = \frac{d}{dt}<a_{nm}a^*_{nm}>$$

$$W_{nm} = <a_{nm}^*\frac{d}{dt}a_{nm}> + <a_{nm}\frac{d}{dt}a^*_{nm}> \tag{2.189}$$

$$W_{nm} = \langle a_{nm}^* \frac{d}{dt} a_{nm} \rangle + \langle a_{nm} \frac{d}{dt} a^*_{nm} \rangle \qquad (2.189)$$

For the dipolar interaction between two nuclei, the perturbing Hamiltonian, as described in Section 2.7.3, is given by

$$\mathcal{H}^D(t) = \frac{\mu_0 \gamma_1 \gamma_2 \hbar^2}{4\pi r^3} [A(t) + B(t) + C(t) + D(t) + E(t) + F(t)]$$

where $A(t) = I_z^{(1)} I_z^{(2)} (1 - 3\cos^2\theta(t))$

$B(t) = -(1/4)(I_+^{(1)} I_-^{(2)} + I_-^{(1)} I_+^{(2)})(1 - 3\cos^2\theta(t))$

$C(t) = -(3/2)(I_z^{(1)} I_+^{(2)} + I_z^{(2)} I_+^{(1)}) \sin\theta(t) \cos\theta(t) \exp(-i\varphi(t))$

$D(t) = -(3/2)(I_z^{(1)} I_-^{(2)} + I_z^{(2)} I_-^{(1)}) \sin\theta\cos\theta \exp(+i\varphi(t))$

$E(t) = -(3/4) I_+^{(1)} I_+^{(2)} \sin^2\theta \exp(-2i\varphi(t))$

$F(t) = -(3/4) I_-^{(1)} I_-^{(2)} \sin^2\theta \exp(+2i\varphi(t))$

So that, the probability w_0 of a transition between $|\beta\alpha\rangle$ and $|\alpha\beta\rangle$, is given according to equation (2.185); where

$$a_{\beta\alpha,\alpha\beta} = \frac{1}{i\hbar} \int_0^t \langle +- | \mathcal{H}'(t') | -+ \rangle \exp(i(\omega_1 - \omega_2)t')dt' \qquad (2.190)$$

which only involves the term B(t) of the perturbing Hamiltonian, giving

$$a_{\beta\alpha,\alpha\beta} = \frac{1}{i\hbar} \int_0^t -\frac{d}{4}(1 - 3\cos^2\theta) \exp(i(\omega_1 - \omega_2)t')dt' \qquad (2.191)$$

and

$$a_{\beta\alpha,\alpha\beta}^* = \frac{1}{i\hbar} \int_0^t (-\frac{d}{4}(1 - 3\cos^2\theta))^* \exp(-i(\omega_1 - \omega_2)t')dt' \qquad (2.192)$$

where $d = (\mu_0 \gamma_1 \gamma_2 \hbar^2 / 4\pi r^3)$. The differentiation of equations (2.191) and (2.192) and subsequent substitution of expressions into equation (2.189) gives

$$w_0 = \frac{1}{16\hbar^2}\int_0^t < d^2(1-3\cos^2\theta(t`))^*(1-3\cos^2 t)) > \exp(i(\omega_1 - \omega_2)(t - t`))\, dt`$$

$$+ \frac{1}{16\hbar^2}\int_0^t < d^2(1-3\cos^2\theta(t`))(1-3\cos^2\theta(t))^* > \exp(i(\omega_1 - \omega_2)(t - t`))\, dt` \qquad (2.193)$$

These averaged terms, < >, are functions of time and can be recognized as autocorrelation functions discussed in Section 2.10.1. If these terms are random functions of time and have the form of equation (2.170), then it can be shown that, the solution to equation (2.194) is of the form

$$w_0 = \frac{1}{8\hbar^2} <|F_0(t)|^2> \frac{\tau_c}{1 + (\omega_1 - \omega_2)^2\tau_c^2} \qquad (2.194)$$

That is, the transition probability is proportional to the spectral density of the correlation function of the perturbation at the frequency of the transition. It can be shown, for the case under consideration, where

$$< |F_0(t)|^2 > = < d^2(1\text{-}3\cos^2\theta(t))(1-3\cos^2\theta(t)) > \qquad (2.195)$$

that for random isotropic motion

$$< |F_0(t)|^2 > = (4/5)d^2 \qquad (2.196)$$

The other probabilities can be calculated in an identical manner. It is possible then to substitute these expressions, evaluated for particular motional processes, into equations such as (2.181) and (2.184) to obtain explicit spin-lattice relaxation expressions. For example; for a dipolar coupled homonuclear two spin system, where $\gamma_1 = \gamma_2$, and $\omega_1 = \omega_2 = \omega$, substituting expressions for w_1 and w_2 evaluated for random isotropic motional processes, into eqution (2.181) gives

$$\frac{1}{T_1} = \frac{3}{10}\left(\frac{\mu_0}{4\pi}\right)^2 \frac{\gamma^4\hbar^2}{r^6}\left[\frac{\tau_c}{1+\omega^2\tau_c^2} + \frac{4\tau_c}{1+4\omega^2\tau_c^2}\right] \qquad (2.197)$$

The detailed calculations of spin-lattice relaxation time behaviour in the systems under study in this thesis are included in the relevant chapters.

APPENDIX 1 THE WIGNER ROTATION MATRICES[12,14]

$$\mathcal{D}^{L}_{MM}(\alpha\beta\gamma)^* = (-1)^{M`-M}\,\mathcal{D}^{L}_{-M`,-M}(\alpha\beta\gamma) = \mathcal{D}^{L}_{MM`}(-\gamma, -\beta, -\alpha)$$

$$\int_0^{2\pi}\int_0^{\pi}\int_0^{2\pi} \mathcal{D}^{L}_{M`M}(\alpha\beta\gamma)^*\mathcal{D}^{L`}_{N`N}d\alpha\sin\beta d\beta d\gamma = \frac{8\pi^2}{2L+1}\,\delta_{LL`}\delta_{MN}\delta_{M`N`}$$

Reduced Wigner Rotation matrix elements for L = 2, $d^{L}_{M`M}(\beta)$

M`/M	2	1	0	−1	−2
2	$\cos^4(\beta/2)$	$-\frac{1}{2}\sin\beta(\cos\beta+1)$	$\sqrt{\frac{3}{8}}\sin^2\beta$	$\frac{1}{2}\sin\beta(\cos\beta-1)$	$\sin^4(\beta/2)$
1	$\frac{1}{2}\sin\beta(\cos\beta+1)$	$(\frac{1}{2}\ 2\cos\beta-1)(1+\cos\beta)$	$-\sqrt{\frac{3}{2}}\sin\beta\cos\beta$	$\frac{1}{2}(2\cos\beta+1)(1-\cos\beta)$	$\frac{1}{2}\sin\beta(\cos\beta-1)$
O	$\sqrt{\frac{3}{8}}\sin^2\beta$	$\sqrt{\frac{3}{2}}\sin\beta\cos\beta$	$\frac{1}{2}(3\cos^2\beta-1)$	$-\sqrt{\frac{3}{2}}\sin\beta\cos\beta$	$\sqrt{\frac{3}{8}}\sin^2\beta$
−1	$-\frac{1}{2}\sin\beta(\cos\beta-1)$	$\frac{1}{2}(2\cos\beta+1)(1-\cos\beta)$	$\sqrt{\frac{3}{2}}\sin\beta\cos\beta$	$\frac{1}{2}(2\cos\beta-1)(1+\cos\beta)$	$-\frac{1}{2}\sin\beta(\cos\beta+1)$
−2	$\sin^4(\beta/2)$	$-\frac{1}{2}\sin\beta(\cos\beta-1)$	$\sqrt{\frac{3}{8}}\sin^2\beta$	$\frac{1}{2}\sin\beta(\cos\beta+1)$	$\cos^4(\beta/2)$

$$\mathcal{D}^{L}_{MO}(\alpha,\beta,0) = \sqrt{\frac{4\pi}{2l+1}}\,Y^{m}_{l}{}^*(\beta,\alpha)$$

REFERENCES

1 A Abragam
Principles of Nuclear Magnetism
Clarendon Press, Oxford, 1962.

2 C P Slichter
Principles of Magnetic Resonance (2nd edition)
Springer-Verlag, Berlin, 1980.

3 R K Harris
Nuclear Magnetic Resonance Spectroscopy
Longman, Harlow, 1986.

4 M Mehring
High Resolution NMR Spectroscopy in Solids (2nd edition)
Springer-Verlag, Berlin, 1983.

5 J W Hennel and J Klinowski
Fundamentals of Nuclear Magnetic Resonance
Longman Group U K Limited, Harlow, 1993.

6 A Steigel and H W Spiess
Dynamic NMR Spectroscopy
Springer-Verlag, Berlin, 1978.

7 U Haeberlen
High Resolution NMR in Solids
Academic Press, New York, 1976.

8 T C Farrar and E D Becker
Pulse and Fourier Transform NMR, Introduction to Theory and Methods,
Academic Press, New York, 1971.

9 O Stern and W Gerlach

Z. Phys., 8,110, 1922.

10 C J Adkins

An Introduction to Thermal Physics,

Cambridge University Press, Cambridge, 1976.

11 A D Dars and C Melissinos

Quantum Mechanics A Modern Introduction

Gordon and Breach Science Publishers S A, New York, 1986.

12 D M Brink and G R Satchler

Angular Momentum,

Oxford University Press, Oxford, 1971.

13 B L Silver

Irreducible tensor methods,

Academic Press, New York, 1976.

14 M E Rose

Elementary Theory of Angular Momentum

John Wiley & Sons Inc., New York, 1967.

15 R N Zare

Angular Momentum - Understanding Spatial Aspects in Chemistry and Physics

John Wiley & Sons, New York, 1988.

16 G E Pake

J. Chem. Phys., 16, 327, 1948.

17 K Blum

Density Matrix Theory and Applications

Plenum Press, New York, 1981.

18 J H Van Vleck

Phys. Rev., 74, 1168, 1948.

19 E R Andrew and R G Eades

Proc. R. Soc. Lond., 218, 537, 1953.

20 F Bloch

Phys. Rev., 69, 127, 1946.

21 A G Redfield

IBM J. Res. Develop., 1, 19, 1957.

22 P S Allen

J. Phys C. Solid State Phys., 6, 3174, 1973.

23 N Bloembergen, E M Purcell and R V Pound

Phys. Rev., 73, 679, 1948.

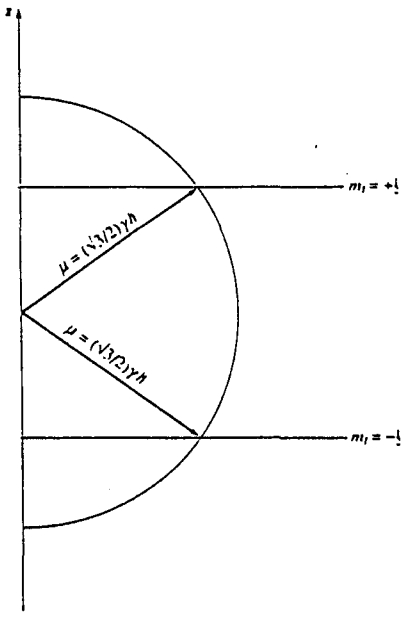

Figure 2.1 A schematic diagram of the allowed orientations of the nuclear magnetic moment of a nucleus with spin $I = \frac{1}{2}$

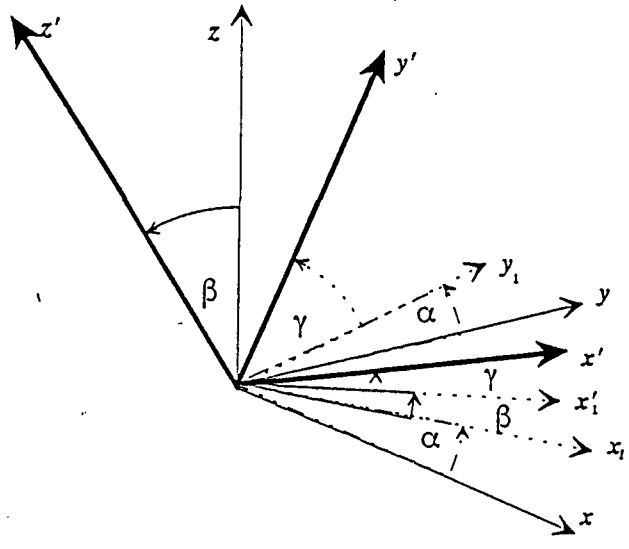

Figure 2.2 A rotation defined in terms of the Euler angles.

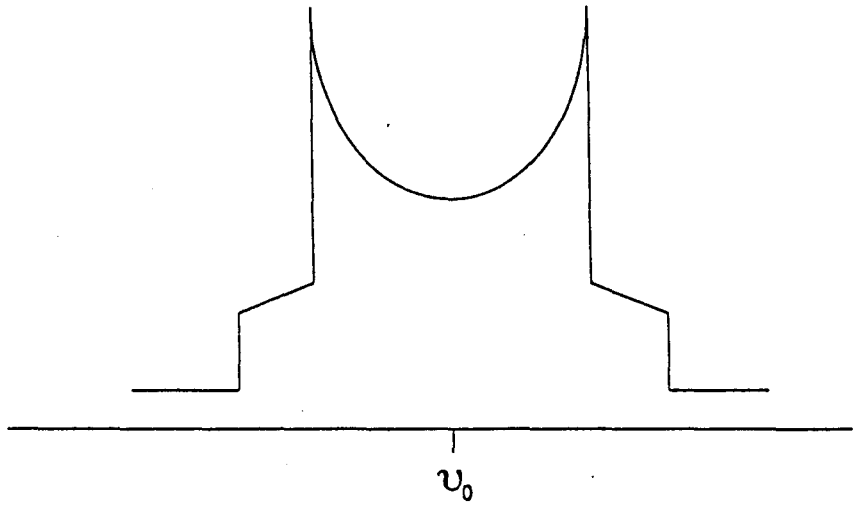

Figure 2.3 A dipolar broadened spectrum of a polycrystalline sample containing homonuclear spin I = ½ pairs.

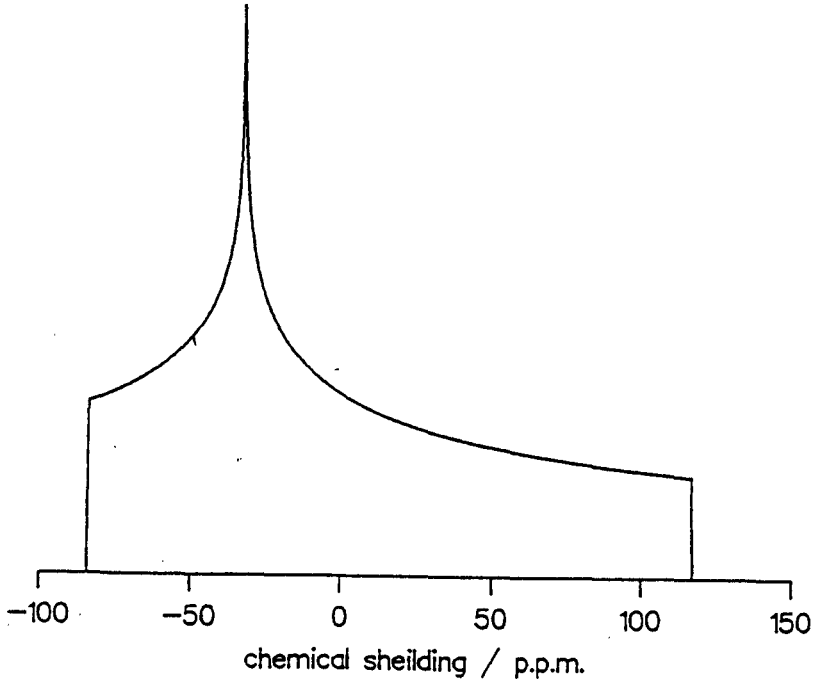

Figure 2.4 A calculated chemical shielding spectrum for an isotropic orientational distribution of equivalent spin I = ½ nuclei (δ = 117 ppm, η = 0.4).

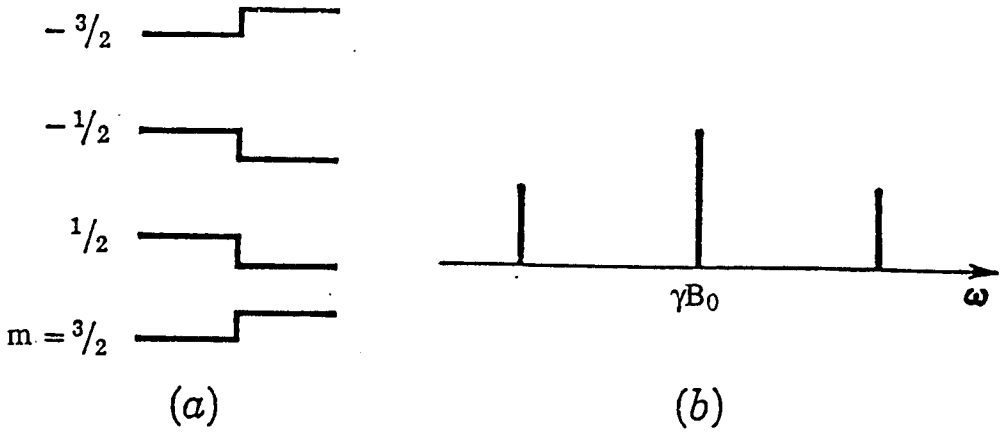

Figure 2.5 (a) Effect of a quadrupole coupling in first order for an $I = \frac{3}{2}$ nucleus; (b) spectral absorption corresponding to the energy levels of (a).

CHAPTER 3

EXPERIMENTAL AND COMPUTATIONAL METHODS

CONTENTS

3.1 Introduction

The aim of this chapter is to outline the experimental and computational methods which have been used in this thesis. It also describes the preparation and characterization of the samples that have been investigated. The main characterization techniques used were differential scanning calorimetry (DSC), and powder x-ray diffraction (XRD). Although strictly not used for characterization purposes, ^{7}Li n.m.r. studies, using a high-resolution n.m.r. spectrometer, are also included in the discussion.

3.2 The NMR Experiment

In a typical n.m.r. experiment there are many key areas. These are discussed in this section.

The Spectrometer

The n.m.r. spectrometer used for all the measurements described in this thesis was the Bruker CXP100b. This instrument is a pulse spectrometer designed specifically for pulsed n.m.r. experiments on solid samples. The operating frequency of the spectrometer is the carrier frequency of a radio frequency pulse, with a duration typically of microseconds. In this way, a single pulse can irradiate over a broad frequency band, which is determined by the Fourier components of the time domain pulse. As many frequencies are irradiated simultaneously, the pulse is required to be of high power. The present spectrometer has a 1 kW amplifier and gives peak to peak pulses of 900 V at maximum output. The n.m.r. spectrometer is shown in schematic form in Figure 3.1

All samples studied were sealed in evacuated pyrex glass n.m.r. tubes of 10mm outside diameter. The sample preparation is discussed further in Section 3.6. The tubes were placed inside a home-built probe head solenoid, in a magnetic field. The applied static magnetic field was provided by either of two permanent

magnets, with field strengths of 1.4T and 0.6T respectively. Applied r.f pulses were controlled by a microprocessor-controlled pulse programmer. The n.m.r. signal was detected by the same solenoid, as an oscillating voltage, generated by the sample nuclei, as described by Faraday's law of electromagnetic induction. The signal was then amplified and, for different resonance frequencies, the reactance of electronic components were matched to give the maximum signal and minimum distortion. The time domain n.m.r. signal was detected using phase sensitive detection (PSD). Diode detection was also available and was useful in preliminary tuning of the spectrometer. A bandwidth filter, (1MHz – 25 kHz), was also available. The bandwidth used for all experiments described in this thesis was 1MHz. However, it was sometimes useful to reduce this while tuning on a noisy signal.

Receiver Sensitivity

The final amplitude of the signal was determined by a sensitivity control. The setting of this control, in decibels, corresponds to an attenuation of the signal. For the same initial signal, before the sensitivity control, two final signals recorded at two different sensitivity settings, are related by:

$$\mathrm{Amp}(2) = \mathrm{Amp}(1)\ 10^{\left(\frac{\mathrm{dB}(1) - \mathrm{dB}(2)}{20}\right)} \qquad (3.1)$$

where Amp(1) is the amplitude of the signal measured at setting dB(1), and similarly for Amp(2) and setting dB(2); Amp(1) > Amp(2) corresponds to dB(2) > dB(1). The relationship given in equation (3.1) was checked experimentally, to ensure there was no bias to the attenuation. Deviations might be expected at low decibel values, but equation (3.1) was found to hold for the whole experimental range.

N.m.r. Probeheads

The probeheads were home-built and optimized for the detection of a particular resonant nuclei in a particular field. The ^{19}F and ^{1}H probe heads were constructed from aluminium for both frequencies; 25.56 MHz and 59.45 MHz for ^{1}H, and 24.05 MHz and 55.93 MHz for ^{19}F; corresponding to 0.6T and 1.4T respectively. The solenoids were wound around PTFE formers for ^{1}H, and nylon formers for ^{19}F. In this way extraneous signals from the n.m.r. probe assembly were eliminated. A ^{7}Li probehead was constructed for use at 23.17 MHz, corresponding to 1.4T. The initial ^{7}Li probehead was also aluminium but problems were encountered with magnetoacoustic ringing[1]. Replacement of this initial aluminium probehead by a brass one gave far superior results[2] reducing the deadtime from ~50 μs to ~13 μs. It was this brass probehead that was used for the investigations in this thesis.

The simple solenoids within the probeheads were made from tinned copper. The solenoids are grounded to earth through a variable high wattage resistance. All resistors are carbon to limit unwanted inductance. This resistance was optimized, for each resonant frequency and each probehead. The larger the resistance, the more the quality factor (Q) of the system drops, and the more the dead-time is reduced. However, the signal amplitude also drops as the resistance is increased. The approximate optimized characteristics of each probehead are shown in Table 3.1.

Table 3.1 The optimized characteristics for the probeheads used for investigations in this thesis

Resonant Nuclei	Field/T	Frequency /MHz	Probe Head Material	Solenoid Former Material	Solenoid Number of Turns in 3cm	Resistance/Ω (In Parallel)	~Dead-time /μs
^{1}H	0.6	25.56	Aluminium	PTFE	17	1.65 (2×3.3)	11
^{1}H	1.4	59.45	Aluminium	PTFE	8	0.54 (5×2.7)	13
^{19}F	0.6	24.05	Aluminium	Nylon	17	1.65	11
^{19}F	1.4	55.93	Aluminium	Nylon	8	0.54	13
^{7}Li	1.4	23.17	Brass	PTFE	15	zero	13

Signal Acquisition

The output signal from the phase sensitive detector was captured using a Data Laboratories DL912 transient recorder. The data collection was triggered by a command issued by the Bruker pulse programmer. The signal was digitized to 4096 data values. Each value has an 8-bit resolution. The maximum resolution in time was 0.05 μs per point. Programs were written and run on a Research Machines Nimbus microcomputer which read the transient analyser data set. The data transfer used an IEEE interface.

Signal to Noise Ratio

The signal-to-noise ratio is an important experimental consideration, and optimization of components and techniques used in n.m.r. measurements which can produce an improvement are of interest. Hoult and Richards[3] have demonstrated how the signal-to-noise ratio can be calculated for a variety of receiving coil configurations. The simplest way of improving the signal-to-noise ratio is to average out random noise by repeating the process of data accumulation and adding appropriate data arrays. For a dataset of n values, where each value is subject to random deviations from the mean[4], then

$$\bar{x} = \frac{1}{n}\sum_{i=1}^{n} x_i = \frac{1}{n}(nX \pm \sigma\sqrt{n}) \qquad (3.2)$$

where $\bar{x}$ is the mean, x_i is a general dataset element, σ is the standard deviation of the dataset, and X would have been the value of the mean in the absence of random deviations. There is a 68% probability that the mean value of the dataset is within $\pm \sigma/\sqrt{n}$ of the true value of X. A set of n points, corresponding to n successive measurements of the amplitude value of a certain point in the n.m.r. signal, is an example of such a dataset. It is clear that a one hundred fold increase in the number of measurements averaged, for example one hundred

scans of the experimental signal by the computer, as opposed to a single scan will lead to a ten fold improvement in the precision of the data value, and a ten fold improvement in the signal-to-noise ratio.

Spectrometer Tuning

The tuning of the spectrometer system was carried out using the general pulse program described in Appendix 1. The method was based on the work of Boden et al[5] on pulse echo experiments. The solid echo is discussed further in Section 3.3. The tuning process used is presented in list form for clarity.

1. The spectrometer was tuned in a standard way, using a sample containing a concentrated source of the resonant nuclei under investigation. These are shown in Table 3.2.

Table 3.2 Samples used in initial spectrometer tuning for each nuclei investigated

Nucleus	Concentrated Source for Initial Tuning	Molar Ratio
^{19}F	CsF/H_2O	R=5
^{7}Li	$LiCl/D_2O$	R=4
^{1}H	H_2O	

2. A 180° pulse length was obtained, by varying the pulse length until a null signal was obtained.

3. A solid 90° pulse length was obtained, after replacing the initial samples with the appropriate solid sample under investigation. A $P_x(\theta)$-τ-$P_x(\theta)$-t' pulse sequence was applied to the sample, with $\tau \sim 200$ μs and the angle θ less than 90° (typically 1.5 μs). To obtain a 90° pulse, the pulse duration was slowly varied until a signal minimum was observed. This pulse length was usually slightly less than half the 180° pulse length.

4. The frequency was tuned. With the pulse length set to 90°, τ was reduced to about 20 μs, and the frequency was adjusted to obtain a minimum signal.

5. Other τ spacings in the range 12-40 μs were used and the signal was checked to ensure it remained at a null. If it did not the above process was repeated.

6. With both the frequency and pulse length set, a $P_x(90)$–τ–$P_y(90)$-t' sequence was applied with $\tau \sim 15$ μs, to produce a solid echo. The reference phase was then adjusted to maximize the echo amplitude.

3.3 Signal Acquisition and The Measurement of Lineshapes

A straightforward f.i.d. can be produced by a single r.f pulse applied along the x axis, followed by the triggering of data acquisition. A $P_x(90°)$ pulse will give the maximum amplitude signal. Before the system is pulsed again it is usual to wait approximately 5 spin-lattice relaxation times, by which time more than 99% of the nuclear magnetization will have returned to the z direction (Equation (3.3)). In this way the next pulse also produces a maximum signal. If the system is pulsed again more quickly, the signal is saturated and a lower amplitude signal results. This is discussed further below. The functional form of the f.i.d. is unchanged by saturation of the signal, at least for the samples studied in this thesis. The signal-to-noise ratio can be improved by sampling the signal a number of times (Section 3.2) and so by repeating the pulse sequence while saturating the signal, more samples of the f.i.d. can be taken in a fixed time. However, each dataset taken will be of reduced amplitude and worse signal-to-noise ratio. The optimum pulse repetition rate that will maximise the signal-to-noise ratio can be calculated as shown below. The longitudinal nuclear magnetization is given in Chapter 2, by

$$\frac{dM_z}{dt} = \frac{-(M_z - M_0)}{T_1}$$

which has the solution

$$M_z = M_0(1 - \exp(-t/T_1)) \tag{3.3}$$

The logitudinal nuclear magnetization, at the initiation of a following pulse is found by setting $t = T_{SEQ}$, where T_{SEQ} is the pulse repetition time. The magnitude of the longitudinal nuclear magnetization, following subsequent pulses is given in Table 3.3.

Table 3.3 The longitudinal nuclear magnetization immediately before the application of 90° pulses, where the time between pulses is T_{SEQ}.

Time	Longitudinal Nuclear Magnetization	Nuclear Magnetization Still to Return to the z-direction
0	M_0	0
T_{SEQ}	$M_0(1\text{-}\exp(-T_{SEQ}/T_1))$	$M_0\exp(-T_{SEQ}/T_1)$
$2T_{SEQ}$	$M_0(1\text{-}\exp(-T_{SEQ}/T_1))(1\text{-}\exp(-T_{SEQ}/T_1))$ + $M_0\exp(-T_{SEQ}/T_1)$ $(1-\exp(-T_{SEQ}/T_1))$ = $M_0(1\text{-}\exp(-T_{SEQ}/T_1))$	$M_0(1\text{-}\exp(-T_{SEQ}/T_1))\exp(-T_{SEQ}/T_1)$ = $M_0\exp(-T_{SEQ}/T_1)$

It can be seen from Table 3.3 that, for a system obeying equation (3.3), the constant signal magnitude due to a train of sequential pulses, is given by

$$\text{Constant Signal} = M_0(1-\exp(-T_{SEQ}/T_1)) \tag{3.4}$$

During a fixed period T, the number of scans of the f.i.d. that can be obtained, n, is T/T_{SEQ}. The total signal over this time interval will be given by

$$\text{Total Signal} = n \times \text{Signal} = \frac{T}{T_{SEQ}} M_0(1\text{-}\exp(\text{-}T_{SEQ}/T_1)) \tag{3.5}$$

With reference to equation (3.2) the total noise over this time interval will be given by

$$\text{Total Noise} = \sqrt{n} \times \text{constant} = \sqrt{\frac{T}{T_{SEQ}}}\, K \tag{3.6}$$

where K is a constant; so that the signal-to-noise ratio is given by

$$\frac{S}{N} = \frac{1}{K}\sqrt{\frac{T}{T_{SEQ}}}\, M_0(1-\exp(-T_{SEQ}/T_1)) \qquad (3.7)$$

Thus, the signal-to-noise ratio increases as the data collection time increases, as expected. However, for a given value of finite collection time there will be a value of T_{SEQ} for which the signal-to-noise ratio is a maximum. Differentiation of equation (3.7) gives

$$\frac{d(S/N)}{dT_{SEQ}} = \frac{\sqrt{T}}{2K} M_0 (T_{SEQ})^{-\frac{3}{2}} (\exp(-T_{SEQ}/T_1))\ (1+2T_{SEQ}/T_1 - \exp(T_{SEQ}/T_1)) \qquad (3.8)$$

When the signal-to-noise ratio is maximum, equation (3.8) is equal to zero. There is one non-trivial solution to equation (3.8) when equated to zero, given by

$$1 + (2T_{SEQ}/T_1) - \exp(T_{SEQ}/T_1) = 0 \qquad (3.9)$$

Equation (3.9) has no analytical solution but can be solved by the Newton-Raphson method[6]. The solution was found to be $T_{SEQ} = 1.26\ T_1$. Similar discussions are reported in the literature[7,8].

Data Collection System

The data collection was triggered by a command issued from the pulse programmer, immediately after the pulse. A f.i.d. acquisition BASIC program was used to take data digitized by the transient analyser into an array. The signals from the subsequent pulses were 'fast-added' to the data array, and the process was continued for a user defined number of scans. The final averaged signal was plotted on the screen and could be stored on file, in the form of a column of 4096 data points with a six value pre-amble indicating the experimental conditions. Use of a simple BASIC program reformatted the data files, discarding the preamble and producing two adjacent columns; signal amplitudes and corresponding time values. These files were transferred to the VAX cluster through an Ethernet and are compatible with the UNIGRAPH package. UNIGRAPH was then be used to manipulate and plot experimental data. Figure

3.2 shows a typical ^1H f.i.d measured at 59.45 MHz and 293 K from polycrystalline PEO.

Data recordings were started at a minimum of 0.05 μs after the end of the pulse. Due to the recovery of electronic components after the overload of the applied r.f pulse, there was a dead time of ~13μs during which no reliable data was taken. (See Figure 3.2). This varied slightly for the different probeheads, as shown in Table 3.1. The applied pulses were not δ functions, but had a finite width. It has been shown that n.m.r. transient signals can be assumed to start at the centre of an r.f pulse[9]. Distortions due to both the receiver band width of the r.f coil and the spectrometer circuits have previously been shown to be small enough to be neglected[10,11].

Spin Echoes in Solids

The standard pulse sequence, $P_x(90°)–\tau–P_y(90°)–t'$, was used throughout the investigations described in this thesis, as a read of the longitudinal nuclear magnetization. τ was usually of the order of 15 μs. A typical spin echo (often called a 'solid echo') is shown in Figure 3.3, measured at 59.45 MHz and 293 K, in the 3.5:1 PEO/$LiCF_3SO_3$ system. The reason for the partial refocussing of nuclear magnetization by this pulse sequence is not straightforward and cannot be explained by a simple vector model, as commonly applied to spin echoes in liquids. However, the basic principle can be demonstrated by density matrix operator methods, described in Chapter 2.

For a system in thermal equilibrium the spin density matrix operator is given by

$$\rho(0) = cI_z \qquad (3.10)$$

The application of a $P_x(90)$ pulse, of length T, where T is small, gives

$$\rho(T) \sim \rho(0) = cI_x \qquad (3.11)$$

The system then evolves for a time τ. The density matrix is now given, in frequency units, by

$$\rho(\tau) = \exp(-i\mathcal{H}t)\, cI_x\, \exp(i\mathcal{H}t) \tag{3.12}$$

where $\mathcal{H}$ is the total interaction Hamiltonian under which the system evolves. The application of a $P_y(90)$ pulse can be written as a rotation operator, giving

$$\rho(\tau+T)\sim\rho(\tau) = \exp(-\omega TI_x)[\exp(-i\mathcal{H}\tau)\, cI_x\exp(i\mathcal{H}\tau)]\exp(i\omega TI_x) \tag{3.13}$$

where T is such that $\omega T = 90°$. Following the second pulse the system again evolves under the influence of $\mathcal{H}$, and assuming $\mathcal{H}$ to be time independent, this gives

$$\rho(\tau+t') = \exp(-i\mathcal{H}t')\exp(-i\omega TI_x)[\exp(-i\mathcal{H}\tau)cI_x\exp(i\mathcal{H}\tau)]$$
$$\exp(i\omega TI_x)\exp(i\mathcal{H}t') \tag{3.14}$$

Equation (3.14) can be written in terms of t from the start of the pulse sequence, by substitution of $t' = t - \tau$, so that

$$\rho(t) = \exp(-i\mathcal{H}(t-\tau))\, \exp(-\omega TI_x)[\exp(-i\mathcal{H}\tau)cI_x\exp(i\mathcal{H}\tau)]\exp(i\omega TI_x)$$
$$\exp(i\mathcal{H}(t-\tau)) \tag{3.15}$$

Insight can be gained by calculating the expectation value of $I_z(t)$ is given by

$$< I_z(t) > = \mathrm{Tr}\{\rho(t)I_z\}$$

and substitution of equation (3.15) gives

$$< I_z(t) > = \mathrm{Tr}\{\exp(-i\mathcal{H}(t-\tau))\exp(-i\omega TI_x)[\exp(-$$
$$i\mathcal{H}\tau)cI_x\exp(i\mathcal{H}\tau)]\exp(i\omega TI_x)\exp(i\mathcal{H}(t-\tau))\, I_z\} \tag{3.16}$$

Taking advantage of the fact that the trace is invariant to cyclic changes in the order of terms, (3.16) becomes

$$< I_z(t) > = \mathrm{Tr}\{\exp(i\mathcal{H}\tau)cI_x\exp(i\mathcal{H}\tau)\exp(i\omega TI_x)\exp(i\mathcal{H}(t-\tau))I_z$$
$$\exp(-i\mathcal{H}(t-\tau))\exp(-i\omega TI_x)\} \qquad (3.17)$$

and further, if I_x and $\mathcal{H}(t-\tau)$ commute, then

$$\exp(i\omega TI_x)\exp(i\mathcal{H}(t-\tau))I_z\exp(-i\mathcal{H}(t-\tau))\exp(-\omega TI_x)$$
$$= \exp(i\mathcal{H}(t-\tau))\exp(\omega TI_x)I_z\exp(-i\omega TI_x)\exp(-i\mathcal{H}(t-\tau))$$
$$= \exp(-i\mathcal{H}(t-\tau))\exp(-i\omega TI_x)I_z\exp(i\omega TI_x)\exp(i\mathcal{H}(t-\tau))$$
$$= \exp(-i\mathcal{H}(t-\tau))I_y\exp(i\mathcal{H}(t-\tau)) \qquad (3.18)$$

so that equation (3.17) can now be written as

$$< I_z(t) > = \mathrm{Tr}\{\exp(-i\mathcal{H}(t-\tau))cI_x\exp(i\mathcal{H}(t-\tau))\exp(-i\mathcal{H}(t-\tau))I_y\exp(i\mathcal{H}(t-\tau))\} \qquad (3.19)$$

when $t = 2\tau$, equation (3.19) becomes

$$< I_z(2\tau) > = \mathrm{Tr}\{\exp(-i\mathcal{H}\tau)cI_x\exp(i\mathcal{H}\tau)\ \exp(-i\mathcal{H}\tau)I_y\exp(i\mathcal{H}\tau)\} \qquad (3.20)$$

or

$$< I_z(2\tau) > = \mathrm{Tr}\{A\ B\}$$

where

$$A = \exp(-i\mathcal{H}\tau)cI_x\exp(i\mathcal{H}\tau) \text{ and } B = \exp(-i\mathcal{H}\tau)I_y\ \exp(i\mathcal{H}\tau)$$

It is clear that terms A and B are orthogonal. A rotation of π about the y axis produces

$$< I_z(2\tau) > = \mathrm{Tr}\{-A\ B\} \qquad (3.21)$$

However, the trace is invariant under the rotation of axis so that

$$< I_z(2\tau\ ) > = \mathrm{Tr}\{A\ B\} \qquad (3.22)$$

It is clear that equations (3.21) and (3.22) are only consistent when $\mathrm{Tr}\{A\ B\} = 0$, so that

$$\langle I_z(2\tau) \rangle = 0 \qquad (3.23)$$

For the solid echo, at $t = 2\tau$, the entire nuclear magnetization vector is back in the x-y plane and the signal is refocussed. However, in practice the refocussing is only partial. Complete refocussing demonstrated by equation (3.23) depends on the total interaction Hamiltonian being time independent, and more importantly the commutability of I_x and $\mathcal{H}$, and of all components of $\mathcal{H}$ with each other. This is not realistic for real systems.

Using similar methods an expression for $\langle I_x(t) \rangle$ following a $P_x(90)-\tau-P_y(90)-t'$ pulse sequence can be derived. This is commonly expanded as a power series, using the time expansion described in Chapter 2. The result of the expansion, for a homonuclear spin system is given by[12]

$$\langle I_x(t) \rangle = \cos\Delta\omega t[1-M_2\frac{(t-2\tau)^2}{2!} + M_4\frac{(t-2\tau)^4}{4!} + \frac{1}{4}M_{4\varepsilon}\tau^2(t-\tau)^2...] \qquad (3.24)$$

where $M_{4\varepsilon}$ is an error term up to the fourth power in time and is 'a measure of the irreversibility of the transverse decay'[12]. All other quantities are defined in Chapter 2. The basic functional form of equation (3.24) can easily be seen. As t increases from 0 to 2τ the signal increases, as the second negative term decreases. There will be a maximum at about 2τ, the exact time being determined by the size of $M_{4\varepsilon}$ and higher order terms. At times larger than 2τ the signal then decreases as the second negative term increases. The time expansion equivalent of equation (3.24) for hetronuclear solids has also been developed[12,13].

Early work on homonuclear solids[14,15] suggested that the solid echo following a $P_x(90°)-\tau-P_y(90)-t'$ pulse sequence had the same half shape as the f.i.d. at short τ spacings. This provided a method of overcoming the problems of spectrometer dead time, which obscures the first part of the f.i.d. A similar method has been used to obtain spectra of deuterium containing compounds, where the quadrupolar interaction leads primarily to the formation of an echo[16].

Lineshape Studies and Second Moment Measurements

In lineshape studies and second moment measurements, described in Chapter 8, f.i.ds were Fourier transformed to produce frequency domain spectra. To enable a Fourier transform to be performed, an estimate of the dead time signal is required. Approximations of dead time signals have previously been made by applying a quadratic expansion of the signal, back to zero time[17] (taken to be in the centre of a pulse of finite duration). Bessel functions[18] have also been used in a similar way to fit the signal back to zero time[19]. However, the use of solid echoes overcomes this problem, as previously mentioned, and this technique was used in all measurements reported in this thesis.

The solid echo signal was captured and stored on a RM Nimbus as discussed previously. The signal could then be manipulated for Fourier transformation and analysis. A BASIC program was used to find the echo maximum, employing a search over a user defined number of points either side of the theoretical echo maximum at time 2τ. The time values corresponding to the amplitudes were then calculated with t=0 set to correspond to the maximum amplitude. To keep the same number of data values the end of the signal was zero filled. An exponential apodization function was used. The operation of a FORTRAN fast Fourier transform program produced spectra in the frequency domain.

The manipulated, pre-transformed, f.i.d was also transferred to the VAX cluster through an Ethernet and was formatted to be compatible with UNIGRAPH. A FORTRAN fitting program written in the VAX environment was employed in carrying out comparisons of this experimental data with theoretical simulations. NAG library routines[20] were available and were used where appropriate, particularly in the evaluation of the Fresnel integrals[21], involved in the explicit calculation of f.i.ds (Further discussed in Chapter 8).

Software was also developed to calculate theoretical second moments, both rigid lattice and motionally averaged. Proposed crystal structure data was used to calculate the involved lattice sums, and, in general, it was found that the values obtained from summing over all spins within a sphere of fixed radius about a reference nucleus, approached an asymptotic value for a radius of about 1.5 nm. This has also been shown to be the case in similar studies[21]. This is discussed further in the relevant chapters.

3.4 The Measurement of Spin-lattice Relaxation Times

There are many established methods for the measurement of spin-lattice relaxation time. These include saturation recovery, inversion recovery and modified fast inversion recovery[22]. Saturation recovery was employed in spin-lattice relaxation time studies detailed in this thesis. The pulse sequence used was $P_x(90)$-t-$P_x(90)$-τ-$P_y(90)$–t´ (the pulse program is documented in Appendix 2), where t is a variable time interval, and τ was typically 15 μs. The standard solid echo sequence $P_x(90)$-τ-$P_y(90)$ is described in Section 3.3.

The essence of the technique is the variable time interval between the two $P_x(90)$ pulses. The amplitude of the signal refocussed by the echo, is dependent on the nuclear magnetization in the x-y plane immediately after the second pulse. This depends on the nuclear magnetization in the z direction immediately before this pulse. This nuclear magnetization is, in turn, dependent on the time elapsed since the first $P_x(90)$ pulse initially tipped the nuclear magnetization into the x-y plane. The longer the time interval, t, the greater the value of the nuclear magnetization in the z direction that the second pulse tips back into the x-y plane for refocussing. Any nuclear magnetization left in the x-y plane after time t, consists of dephased spin isochromats and will not contribute to the signal. In this way signal amplitudes and corresponding time intervals were recorded. The

equilibrium longitudinal nuclear magnetization, M_0 was measured in a separate experiment with $t > 5T_1$, corresponding to no saturation of signal.

For a well behaved signal, the values of M_z versus time interval describe an exponential function according to equation (3.3). However, even for simple systems this is not always the case (see Chapter 5). Many studies have employed direct non-linear 3 parameter fitting to the nuclear magnetization versus time interval data[24-26]. Similar fits are also documented involving the explicit consideration of a pulse angle parameter, for non-ideal pulses[23,27-29]. It has been shown that a non-linear total least squares fit of n.m.r. spectra to analytical expressions produces minimum variance estimates of spectral parameters[30] in liquid systems where frequency domain spectra are well resolved. In a similar way another method of extracting relaxation rates is suggested in the literature for such systems, where a simultaneous fit to all spectra in a relaxation experiment (the Fourier transforms of each echo, corresponding to different pulse intervals) is carried out and an analytical expression that includes an exponential function is used to fit the variation of signal intensities[31].

The simplest way to analyse the data from a solid is to carry out a linear least squares fit to the logarithm of nuclear magnetization versus time interval data[27,32]. Although in this treatment the estimate of precision is considerably more complex (except where M_0 is known exactly) than in a simultaneous three parameter fit, the method is common and lends itself to easy graphical solutions. For the work in this thesis the logarithmic estimation method was used.

The pulse programmer did have the facility to cycle a spin-lattice relaxation time experiment, for example; 100 scans with time interval t_1, 100 scans with time interval t_2, 100 scans with time interval t_3, etc, automatically. This could be arranged for any number of values of time interval, but the values all had to be

equally spaced. However, considering an exponential function of time (an example of a well behaved nuclear magnetization recovery) it is clear that the amplitude does not decrease in a regular manner within equally spaced in intervals of time. This is shown in Figure 3.4. For small values of time, f(a)-f(b) is relatively large, compared with longer values of time, where f(c)-f(d) is small. If the amplitude of the function in Figure 3.4 was sampled at regularly spaced intervals of time, then ; for small intervals of time between sampling, amplitudes at long times contain little information; for large intervals of time between sampling, information about the amplitude variation at short times would be lost. In the studies described in this thesis, the nuclear magnetization was sampled at time intervals which correspond to drops in amplitude, usually chosen to be approximately 5%. These time intervals are spaced exponentially in time and are determined from equation (3.3) by substituting an initial guess of spin-lattice relaxation time, and ratios of (M_Z/M_0). These calculated time intervals had to be entered manually. A better approach would be to have an automatic system which could change the pulse intervals used in the pulse sequence in a user defined way. This would require the pulse programmer to be interfaced with a PC and software to be developed.

In a typical spin-lattice relaxation time experiment the maximum amplitude of the echo and corresponding pulse interval were recorded by software operating on the RM Nimbus. The program recorded the amplitude as an average over the top of the echo, using a user defined number of points about the maximum value, with a baseline subtraction. The baseline was determined from the last 800 data points of the echo signal. For each value of pulse interval, the echo signal was recorded a selected number of times to improve signal-to-noise ratio as discussed in Section 3.3. After the last pulse interval, the amplitude and pulse interval data were stored, and a graph of $\ln(M_0-M_Z)$ versus time was plotted on the screen. The best fit line to the data, calculated by a linear least squares fit, was also

was also plotted along with the value of spin-lattice relaxation time; given by the inverse of the gradient of this line. BASIC programs manipulated the data files to produce UNIGRAPH compatible spin-lattice relaxation data files which could be transferred to the VAX.

3.5 The Temperature System

The temperature range for the studies described in this thesis was 200 K to 350 K. Temperature values within this range were taken to have an uncertainty of ± 1 K. The temperature control system consisted of a nitrogen gas flow through a simple heat exchanger, set against a heating element. The heat exchanger was a simple coil of copper tubing immersed in icewater for ambient and higher temperatures, and liquid nitrogen for low temperatures. A thermocouple is mounted in the probe head, with its tip just below the base of a sample tube. This thermocouple provided the feedback signal to control the heater input power. The control unit was a DTC2, supplied by Oxford Instruments. This unit incorporates proportional control with differentiation and integration operational amplifier arrangements. The differentiating operational amplifier circuit monitors the rate of change of the error signal. The integrating operational amplifier circuit records the area under the error signal with respect to time. These functions can both be adjusted, along with the droop value for the proportional control, to produce feedback signals of varying character for input to the heater control. The variable characteristics include rise time, oscillation and overshoot behaviour. Typical values used in this thesis were; proportional droop 2%, integration contribution 4%, differentiation contribution 0%.

In any given experiment the required temperature was set and the system set running. A sample tube containing glycerol and a copper-copper-nickel thermocouple was inserted into the usual sample position in the probe head. This thermocouple output was monitored using a digital voltmeter and a chart recorder.

The chart recorder signal displayed the temperature variation and allowed adjustment of the control system feedback signal, and set temperature, to stabilise the temperature at that required, as given by standard international thermocouple data[33] for the digital voltmeter reading. Thermal equilibrium was usually reached within 10-15 minutes. At low temperatures the 1.4T magnet, which was uninsulated, exhibited significant field drift. This was suggested to be due to uneven cooling of the magnet. A study to monitor the resonance frequency drift of a standard sample in this magnet at low temperature, over long times, suggested that after two hours the drift was stabilising. A typical dataset is shown in Table 3.4.

Table 3.4 The resonance frequency of ^{7}Li in $LiCl/D_2O$(R=4) at 210 K, measured at various times after the sample was introduced into the applied field.

Time/min	Resonance Frequency/Hz	Δ Frequency/Hz
0	23102775	
15	23102475	300
30	23102175	300
45	23101975	200
60	23101845	130
75	23101545	300
90	23101545	0
105	23101455	90
120	23101355	100
135	23101285	80
150	23101235	50

The pulse programs used for data acquisition also incorporated facilities for retuning, in case of observable drift problems.

3.6 Sample Preparation

The main samples that are the subject of studies in this thesis are PEO, $LiCF_3SO_3$ and PEO/$LiCF_3SO_3$ systems of ratios 3.5:1 and 9:1. This ratio refers to monomeric units of PEO to salt, often written as O:Li. The PEO was of average molecular weight 900 000. It was obtained from Aldrich and was 99% pure. $LiCF_3SO_3$ was obtained from Aldrich (97% purity) and Fluorochem (99% purity). This sample is hygroscopic, and accordingly opened sample bottles were kept sealed in a desiccator and handled with care at all times. ^1H n.m.r. was used to study different $LiCF_3SO_3$ samples which had been kept for different times, to examine the process of water absorption from the atmosphere and carefully handled samples were found to contain a negligible quantity of ^1H nuclei.

The production of PEO/$LiCF_3SO_3$ systems is described in the literature by two basic methods. (1) A solvent free, ball mill method can be used[34-36], in which the polymer and salt are ground by stainless balls at 77 K and annealed at elevated temperatures. (2) A solvent evaporation method can also be used, in which the polymer and salts are co-dissolved in a solvent, which is then mixed. The solvent is evaporated off, casting the sample. The conditions reported differ widely, as shown in Table 3.5.

Table 3.5 Conditions reported in the synthesis of ionic host polymer systems

Solvent	Mixing	Evaporation	Cast	Ref
Dry Acetonitrile	36 hours in dry box	In glovebox for 2 days, room temp	PTFE	37
Dry Acetonitrile	Argon dry box	In partial vacuum, circulating Argon	PTFE	38
Dry Acetonitrile		In partial vacuum, circulating Argon	PTFE	39
Dry Methanol		At 283 K for a few days	PTFE	40
Dry Acetonitrile		At 10^{-3} Tor at 25 °C for 24 hrs	PTFE	41
Dry Methanol		Heating under vacuum	PTFE	42
Dry Acetonitrile		At 10^{-3}Tor at 110 °C for 48 hrs	PTFE	43
Dry Acetonitrile	24 hrs at room temp	Doctor-blade method	PTFE	44
Dry Acetonitrile		Covered, left for slow evaporation	Silicon Paper	45
Dry Acetonitrile		In vacuum with heating for 24 hrs	Glass	46

The solvent evaporation method was adopted for the production of samples in this work. All of the above references reported systems with negligible solvent and

water content. Negligible water content is important and can be crucial; conductivity measurements are particularly sensitive to this [47]. In this work the correct ratios of masses of PEO and $LiCF_3SO_3$ to produce the selected system ratios were co-dissolved in dry acetonitrile and mixed with a magnetic stirrer for 24 hours. The solution was then cast in a teflon dish and the acetonitrile was left to evaporate under nitrogen. Discs of ~8mm diameter were punched out of the cast film and these were placed in a n.m.r. tube of 10mm outside diameter. The sample tube was evacuated on a vacuum line to 10^{-3} Tor for 24 hours to remove traces of solvent and water. The tube was then sealed on the line. Initial n.m.r. signals showed no dependence on sample orientation, indicating there was no preferred direction of molecular orientations within the discs.

In an attempt to obtain a crystal structure of $LiCF_3SO_3$ work was undertaken to produce single crystals of the compound. Initial attempts involved recrystallization of $LiCF_3SO_3$ from solutions of acetonitrile, saturated at elevated temperatures. These temperatures of around 340 K, were produced by a simple waterbath. THF was also tried as a solvent in this experimental procedure. Layering techniques were also attempted. A 10 mm n.m.r. tube had a near saturated solution of $LiCF_3SO_3$ placed in the bottom. Toluene, in which the salt is insoluble, was layered on top. As the solvents slowly mixed, crystals were formed at the interface. The best results were obtained by recrystallization from acetonitrile, although initial studies carried out with a Weissenberg camera indicated the majority of the crystals were twinned. The best samples were sent to Professor M Hursthouse at the University of Swansea, but attempting to solve the structure was complicated by the presence of solvent molecules. A crystal structure has now been proposed for polycrystalline $LiCF_3SO_3$ determined by Rietveld analysis of powder diffraction data in conjunction with maximum entropy and likelihood considerations. This is discussed further in Chapter 5.

3.7 Characterization of Samples

Molecular weight measurement, DSC, FT-IR, and ESCA studies have all been used in the characterization of ionic host polymer system films prepared from PEO with $LiCF_3SO_3$ by evaporation methods[48]. In this work both DSC, and powder XRD were used.

DSC

DSC studies have previously been used to analyse PEO/$LiCF_3SO_3$ systems produced by different experimental procedures[37,39].For the studies described in this thesis the thermal analysis was initially carried out at the University of Nottingham, over a temperature range −193 K to 533 K. Later analysis was carried out at the Open University over a range 293 K to 423 K, using a Polymer Laboratories Thermal Science Division PL-DSC interfaced with an OPUS PCSX 386X.

A differential scanning calorimeter measures changes in heat flow as a function of time or temperature. Typically samples were of the order of milligrams and temperatures were controlled by the flow of Argon gas.

XRD

Powder diffraction has long been used in the study of crystal structure and since the work of Rietveld[49,50], techniques and applications of powder methods for obtaining detailed crystal structure parameters, are constantly being developed[51]. Obtaining experimental results capable of being analyzed to produce detailed structural parameters, however, requires very stringent conditions[52].

X-ray diffraction patterns for PEO/$LiCF_3SO_3$ systems have previously been reported[38]. In the studies described in this thesis the objective was the

qualitative comparison of samples. A Siemens D500 diffractometer was used, which was computer controlled. Films were placed directly onto sample holders and raised to the correct level, corresponding to the surface of a powder sample, (using blu-tack). An important test was to compare a PEO powder pattern with that of a PEO film cast from acetonitrile. The results are shown in Figure 3.5. The powder pattern of $LiCF_3SO_3$ was also recorded. This sample was placed in the sample holder and covered with parafilm to minimise moisture absorption during the spectrum collection. Control spectra of parafilm and blu-tack were collected under identical experimental conditions. Menu driven software implemented on the diffractometer computer, was used for data manipulation.

3.8 High Resolution NMR

^7Li high resolution n.m.r. spectroscopy was used to investigate ^7Li lineshapes. The spectrometer was a JEOL JNM-EX400, with a superconducting magnet of field 9.4T, corresponding to a 400 MHz ^1H resonance. A programmable multi pulser (PGX300) controls the pulse sequences and is initially programmed with many standard sequences. The system is provided with a data system which consists of a host computer (PEC ISI11/73) and a data processing computer. Using the operating system, (RSX11M), data processing, plotting, menu file creation etc. can be performed in parallel with spectrum measurement. The spectrometer system incorporates a NM-EVT33 variable temperature system. The working limits for the probe specifications are 173 K to 423 K. The temperature stability is quoted at ± 1 K. For temperatures between 324 K and 423 K, air from a compressor is sent to the probe heater. Air heated to the desired temperature is obtained by controlling the power of the probe heater. The sample is heated to the set temperature by the hot air. For temperatures between 222 K and 324 K, the heating of liquid nitrogen in the metal dewar generates a fixed amount of nitrogen gas which passes through the probe heater

and is supplied to the probe. The control of the power of the heater, controls the temperature of the sample.

The samples of $LiCF_3SO_3$ and the PEO/$LiCF_3SO_3$ systems were sealed in 5 mm outside diameter pyrex sample tubes. There was initially concern that a high resolution machine, designed basically for solution state work, would not produce reliable results on solid systems. A ^7Li investigation was carried out to study the behaviour of amplitude of the the n.m.r. signal with variation in the length of a single pulse. The response of a LiCl solution and polycrystalline $LiCF_3SO_3$ are shown in Figure 3.6. The system responded well in both cases giving a variation close to a trigonometric function with the maximum value corresponding to a $P_x(90)$ pulse. The technique proved useful for lineshape comparison, and is discussed further in Chapter 7.

APPENDIX 1

A general pulse program written on the Bruker CXP100 pulse programmer. The four columns are; address; duration; condition; branch. The address is in hexadecimal

0 3 0 0	- W	Trigger, duration D3
1 2 0 0		Wait, D2
2 1 0 0	+X	Pulse along z axis, duration D1
3 0 F 0		End
4 1 0 0	+X	Pulse along x axis, duration D1
5 2 0 0		Wait, D2
6 1 0 0	+X	Pulse along x axis, duration D1
7 3 0 0	- W	Trigger, duration D3
8 0 F0		End
9 1 0 0	+X	Pulse along x axis, duration D1
A 2 0 0		Wait, D2
B 1 0 0	+Y	Pulse along y axis, duration D1
C 3 0 0	- W	Trigger, duration D3
D 0 F0		End

APPENDIX 2

The pulse program written for the Bruker CXP100 pulse programmer, used for spin-lattice relaxation time measurement

0 1 0 0	+X	Pulse along x axis, duration D1
1 2 0 0		Wait, D2
2 1 0 0	+X	Pulse along x axis, duration D1
3 4 0 0		Wait, D4
4 1 0 0	+Y	Pulse along y axis, duration D1
5 3 0 0	- W	Trigger, duration D3
6 0 F 0		End
7 1 0 0	+X	Pulse along x axis, duration D1
8 2 0 0	- W	Trigger, duration D3]
9 1 0 0	+X	Pulse along x axis, duration D1
A 3 0 0	- W	Trigger, duration D3
B 0 F 0		End

The program section initiated at starting address 7 can be used as a check on the spectrometer tuning.

REFERENCES

1 M L Buess and G L Peterson
Rev. Sci. Instrum., 49, 1151, 1978.

2 E Fukushima and S B W Roeder
Experimental Pulse NMR: A Nuts and Bolts Approach
Addison-Welsey Publishing, Massachusetts, 1981.

3 D I Hoult and R E Richards
J. Mag. Res., 24, 71, 1976.

4 I G Parrat
Probability and Experimental Errors in Science
Longman, London, 1961.

5 N Boden, P Kahol, A Mee, M Mortimer and G N Peterson
J. Mag. Res., 54, 419, 1983.

6 G Stephenson
Mathematical Methods for Science Students
Longman, London, 1973.

7 R Dupree and M E Smith
J. Mag. Res., 75, 153, 1987.

8 M J Forster
J. Mag. Res., 84, 580, 1989.

9 D E Barnaal and I J Lowe
Phys. Rev., 148, 328, 1966.

10 E A Moore, M Mortimer, N F Peirson and G Oates
Chem. Phys. Lett., 151, 213, 1988.

11 D C Apperley
PhD Thesis
The Open University, 1986.

12 P Mansfield
Phys. Rev., 137, 961, 1965.

13 M Engelsberg and R E Norberg
Phys. Rev. B., 5, 3395, 1972.

14 J G Powles and P Mansfield
Phys. Lett., 2, 58, 1962.

15 J G Powles and J H Strange
Proc. Phys. Soc., 82, 6, 1963.

16 N Boden, S M Hanlon, Y K Levine and M Mortimer
Mol. Phys., 36, 519, 1978.

17 E E Burnell, A J Mackay, R C Roe and A G Marshall
J. Mag. Res., 45, 344, 1981.

18 M Abrammowitz and I A Stegun
Hand Book of Mathematic Functions
Dover Publications, 1965.

19 G N Peterson
PhD Thesis
Leeds University, 1980.

20 Numerical Algorithms Group
NAG Fortran Library Manual, Mark 11
Oxford, 1983.

21 N F Peirson
PhD Thesis
Open University, Feb 1992.

22 R K Gupta, J A Ferrelli, E D Becker and G H Weiss
J. Mag. Res., 38, 447, 1980.

23 G H Weiss and J A Ferretti
J. Mag. Res., 61, 499, 1985.

24 G H Weiss, R K Gupta, J A Ferretti and E D Becker
J. Mag. Res., 37, 369, 1980.

25 H Hanssum, W Maurer and H Rüterjans
J. Mag. Res., 31, 231, 1978.

26 H Hanssum and H Rüterjans
J. Mag. Res., 39, 65, 1980.

27 G H Weiss and J A Ferretti
J. Mag. Res., 61, 490, 1985.

28 H Hanssum
J. Mag. Res., 45, 461, 1981.

29 J Grand
J. Mag. Res., 53, 386, 1983.

30 F Abildgaard, H Gesmar and J J Led
J. Mag. Res., 79, 78, 1988.

31 F. Abildgaard, G O Soresen and J J Led
J. Mag. Res., 91, 371, 1982.

32 R Crouch, S Hurlbert and A Ragouzeos
J. Mag. Res., 49, 371, 1982.

33 International Standard Thermocouple Tables
Chesterfield, England.

34 F M Gray, J R MacCallum and C A Vincent
Solid State Ion., 18/19, 282, 1986.

35 D P Tunstall, A S Tomlin, J R MacCallum and C A Vincent
J. Phys. Chem. Solid State Phys., 21, 1039, 1988.

36 D P Tunstall, A S Tomlin, F M Gray, J R MacCallum, C A Vincent
J. Phys., 1, 4035, 1989.

37 S M Zahurak, M L Kaplan, E A Rietmas, D W Murphy and R J Cava
Macromol., 21, 654, 1988.

38 C Berthier, W Gorecki, M Minier, M B Armand, J M Chubagno, P Rigand
Solid State Ion., 11, 91, 1983.

39 M Minier, C Berthier and W Gorecki
J. Physique, 45, 739, 1984.

40 P J Bannister, G R Davies, I M Ward and J E McIntyre
Polymer, 25, 1291, 1984.

41 B L Papke, M A Ratner and D F Shriver
J. Electrochem. Soc., Electrochem. Sci. ad Tech., (July), 1434, July 1982.

42 B L Papke, M A Ratner and D F Shriver
J. Phys. Chem. Solids, 42, 493, 1981.

43 S Bhattaharja, S W Smoot and D M Whitmore
Solid State Ion., 18 and 19, 306, 1986.

44 CAC Sequeiro, J M North and A Hooper
Solid State Ion., 13, 175, 1984.

45 R Neat, M Glasse, R Linford and A Hooper
Solid State Ion., 18 and 19, 1088, 1986.

46 P R Sorensen and T Jacobson
Solid State Ion., 9 and 10, 1147, 1983.

47 R D Armstrong and M D Clarke
Solid State Ion., 11, 305, 1984.

48 Y Ita, K Miyanchi and T Kudo
J. Chem. Phys. Solids, 48(2), 161, 1987.

49 H M Rietveld
Acta Crystallogr., 22, 151, 1967.

50 H M Rietveld
J. Appl. Crystallogr., 2, 65, 1969.

51 A K Cheetham and J C Taylor
J. Solid State Chem., 21, 253, 1977.

52 J C Taylor
Aust. J. Phys., 38, 519, 1985.

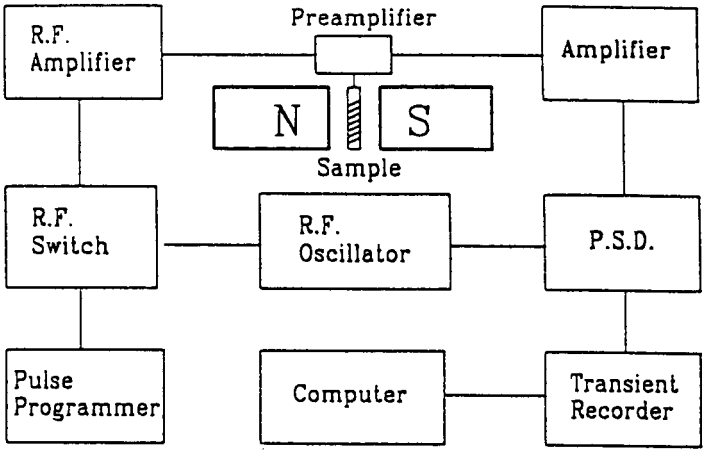

Figure 3.1 The n.m.r. spectrometer system used for the experiments described in this thesis. The system is shown in block diagrammatic form.

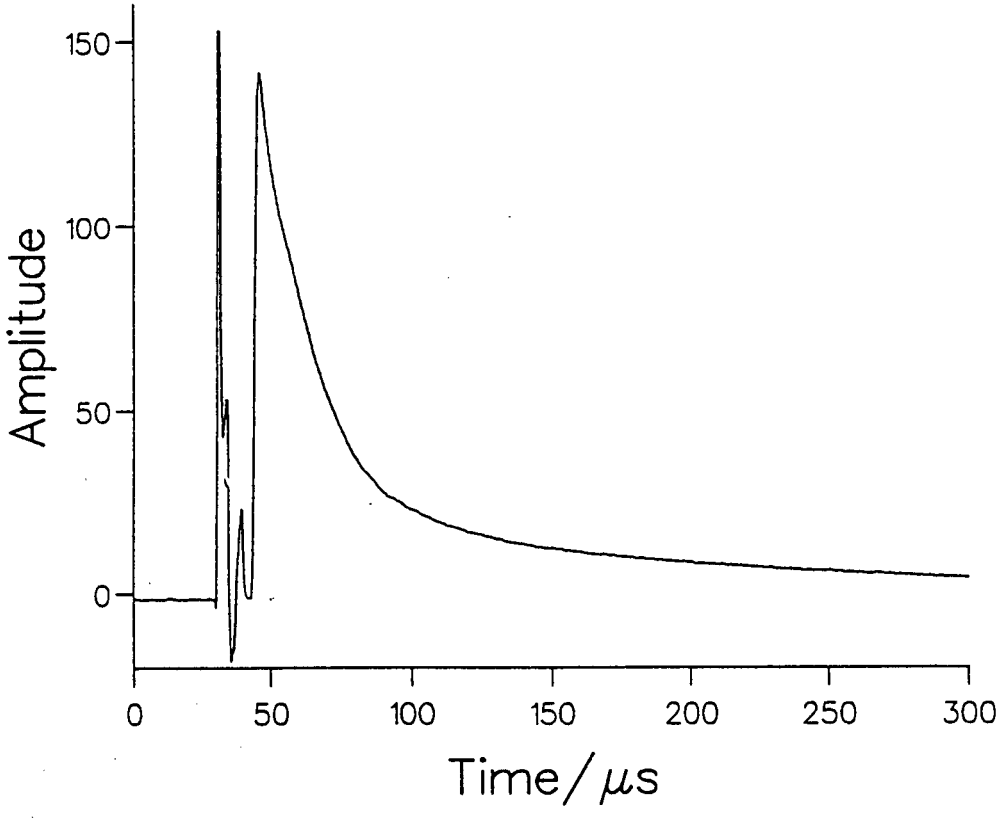

Figure 3.2 A typical ^1H f.i.d measured at 59.45 MHz and 293 K, in polycrystalline PEO. For clarity there is a 30 μs delay before application of the pulse.

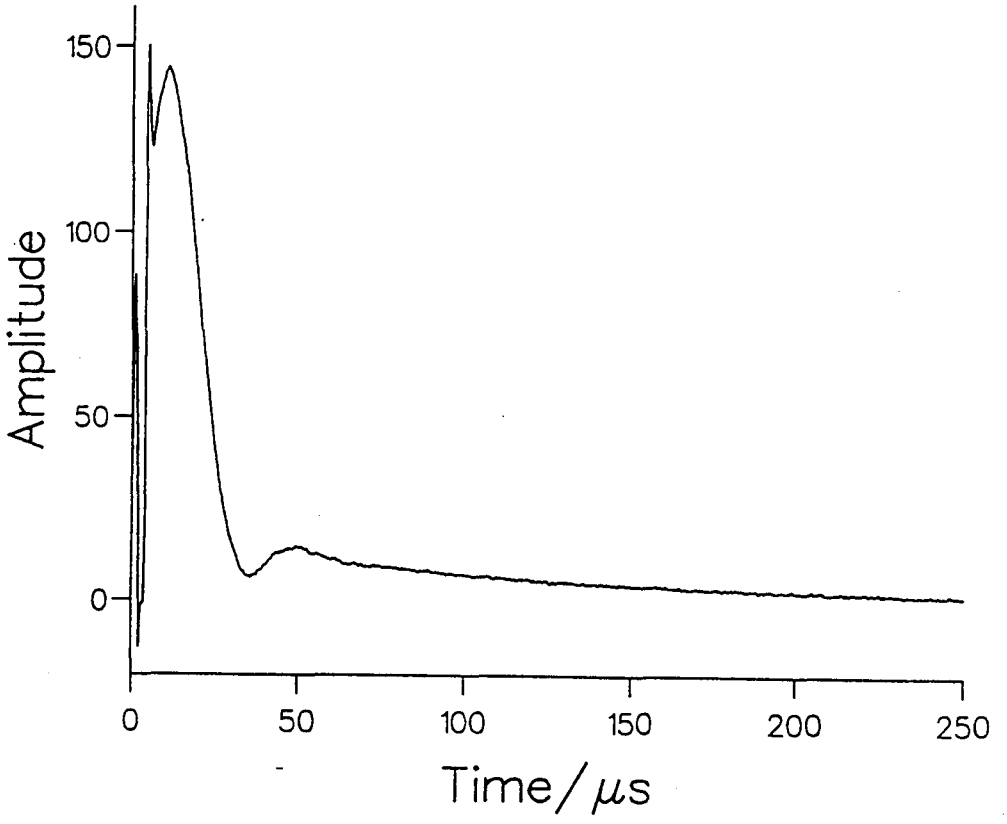

Figure 3.3 A typical ^1H spin echo measured at 59.45 MHz and 293 K in the 3.5:1 PEO/$LiCF_3SO_3$ system. The signal is triggered after the application of the final pulse.

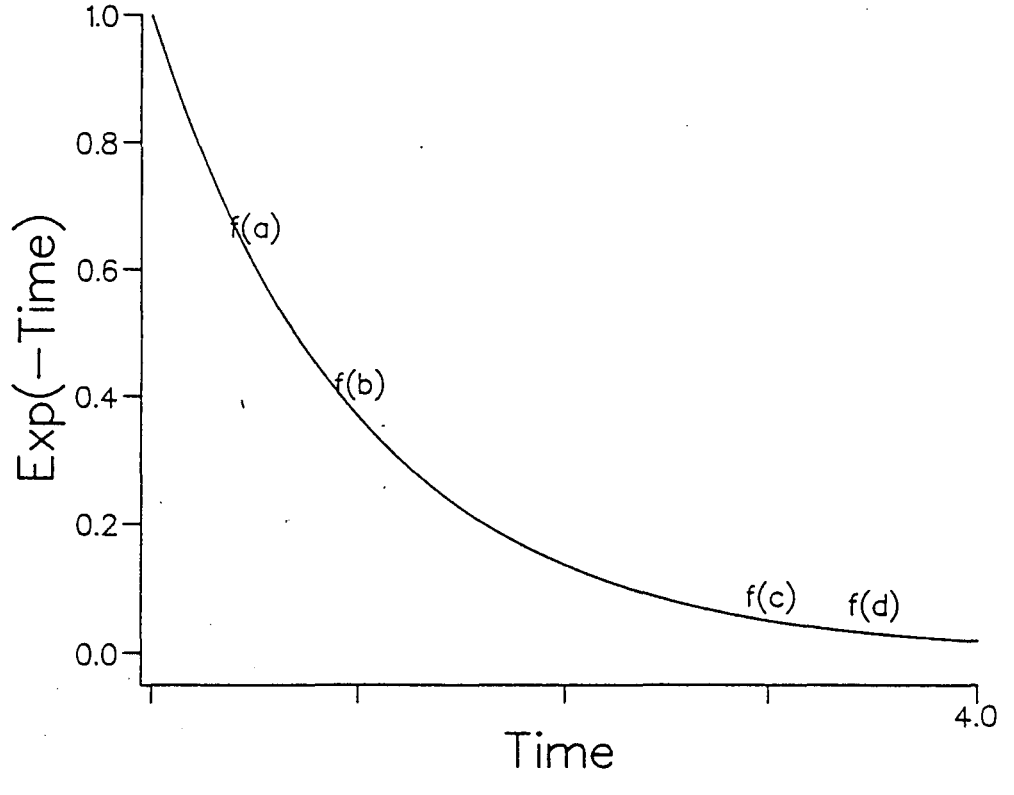

Figure 3.4 An exponential function of time, f(a...d) represent the amplitude of the function at times a...d, where b-a = d-c. It is apparent that sampling the amplitude of an exponential function in increments of a regular time interval is not efficient.

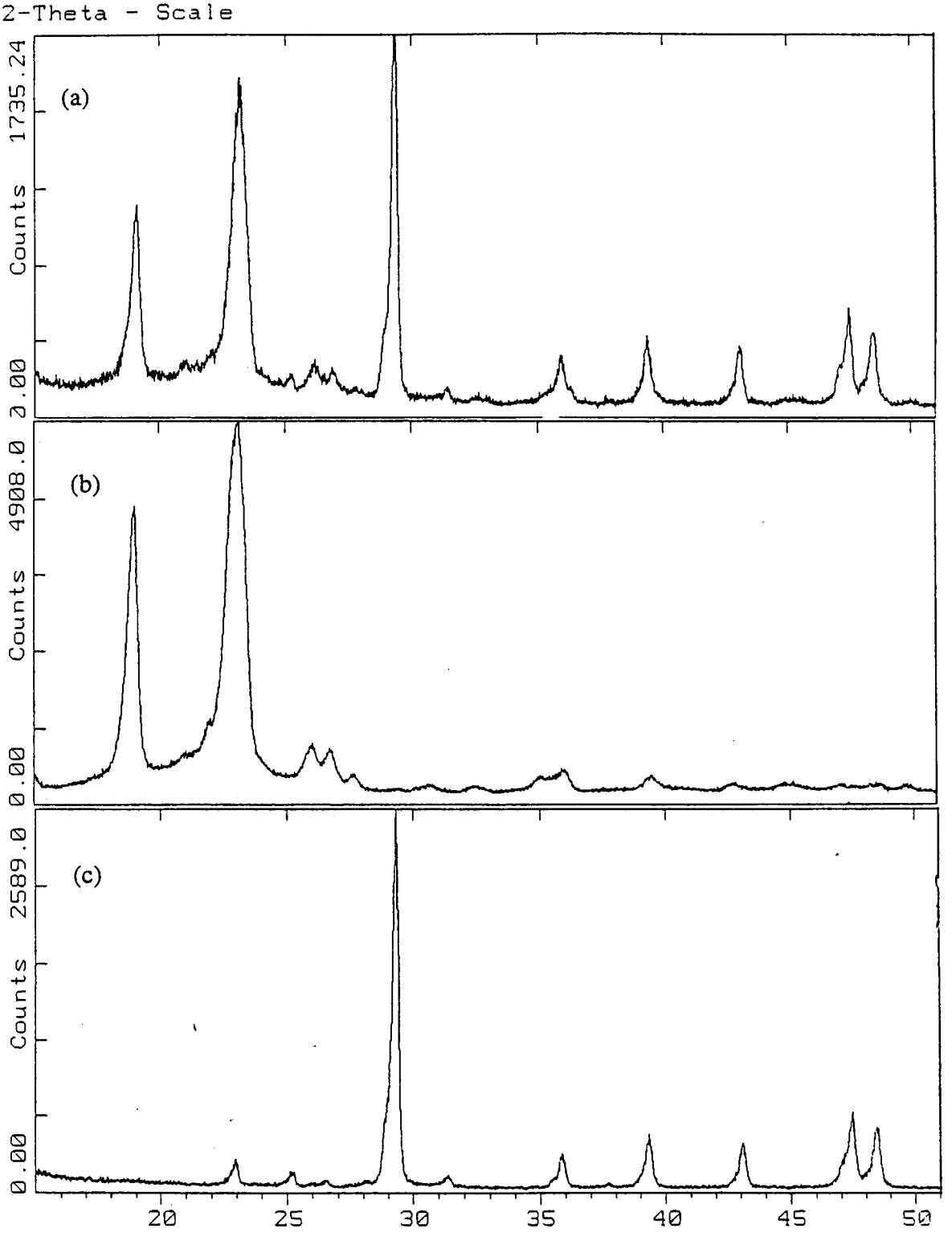

Figure 3.5 XRD spectra measured at room temperature, of (a) a PEO film cast from acetonitrile, (b) polycrystalline PEO, and (c) blu-tack. It can be seen by comparison of the control blu-tack spectra with that obtained for the cast PEO, that both the polycrystalline PEO and the cast sample produce identical patterns.

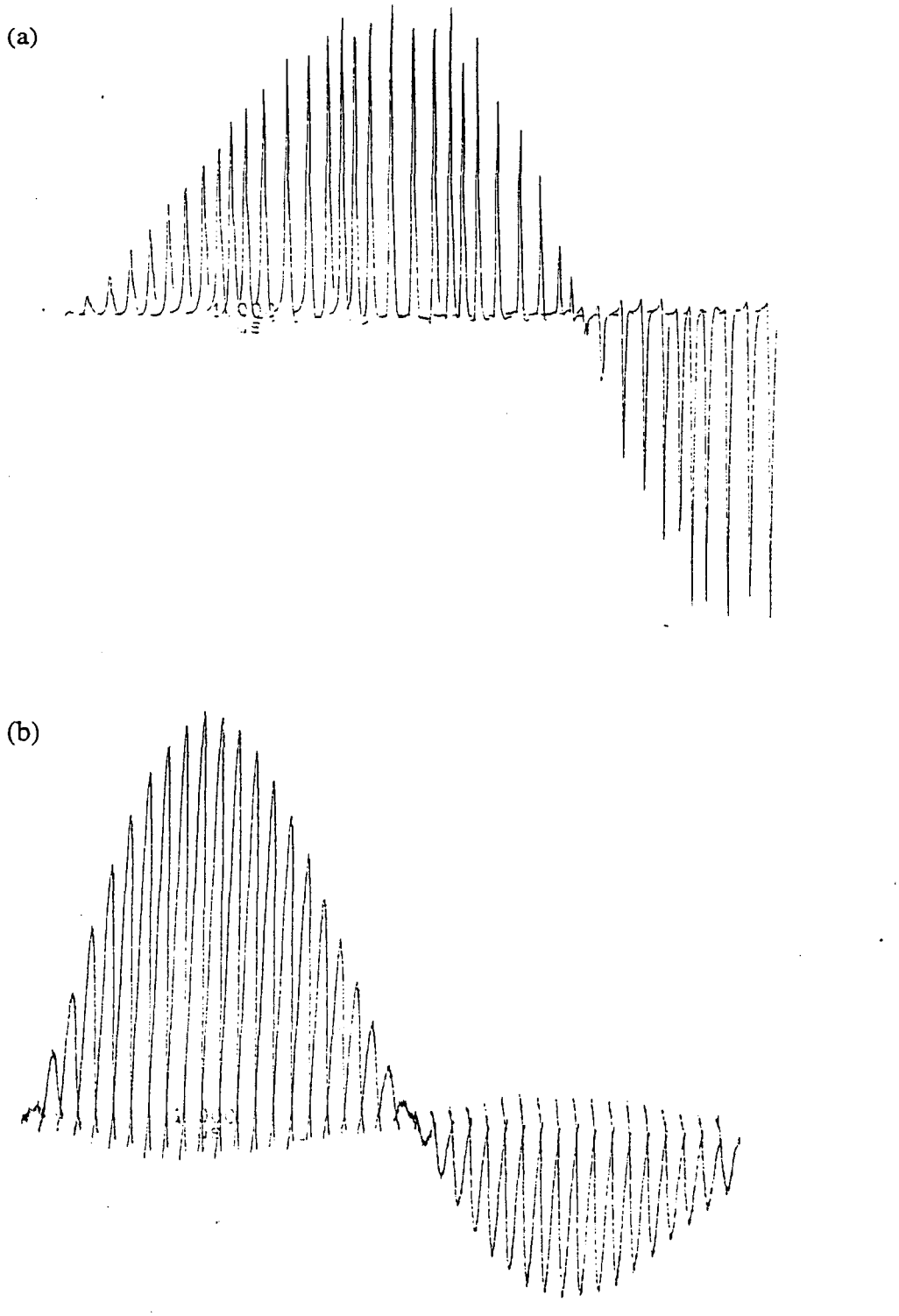

Figure 3.6 The maximum amplitude of the ^{7}Li n.m.r. signal measured at 400 MHz and 293 K, as a function of pulse length (increments of 1 μs), (a) in LiCl solution, and (b) in polycrystalline $LiCF_3SO_3$.

CHAPTER 4

LITERATURE REVIEW

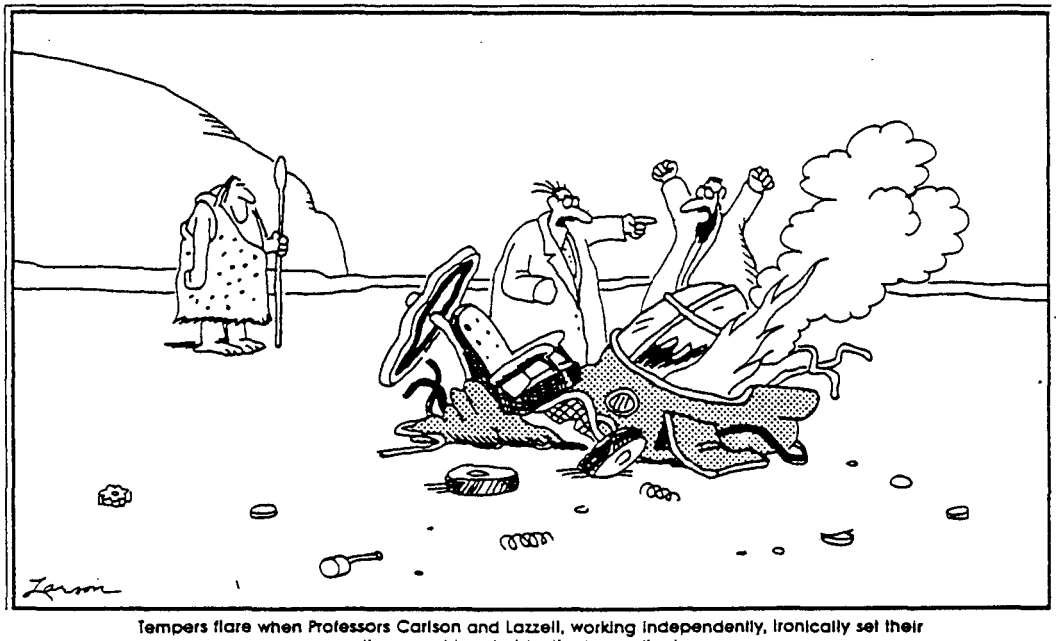

Tempers flare when Professors Carlson and Lazzell, working independently, ironically set their time machines to identical coordinates.

CONTENTS

4.1 Introduction and the Scope of the Review

It is well-known that adducts can be formed between ion-coordinating macromolecules such as polyethers, and simple metal salts. The polymeric compounds in these systems essentially act as solvents for the metal salts. The overall process is known as intercalation, although in some cases specific stoichiometric complexes are formed.

The potential for ionic host polymer systems to be developed as solid polymer electrolytes was first recognised in 1978 by Armand[1] who proposed practical applications in the area of high energy density batteries. These systems possess a number of properties which make them preferable to standard electrochemical cells; discussed further in Section 4.7. It should be noted, however, that Wright[2-3] was carrying out the preparation of PEO/MSCN and PEO/MI systems with M = Na and K, as early as 1973. In these initial studies a polarizing microscope was used to observe the formation of spherulitic complexes with a ratio of ~4:1, and IR spectra indicated the association of the cation with the PEO oxygen sites.

In recent years, environmental issues have become more highly regarded by society, and are more widely reported by worldwide media. With petroleum powered vehicles being associated with atmospheric pollution[4], acid rain[5], and even global climate change[6], the prospect of electric transport powered by a the solid polymer electrolyte fuel cell is a particularly attractive idea.[7-9].

The majority of the research activity conducted on ionic host polymer systems, to date, has been aimed at understanding

(i) the interactions involved in the formation of distinct system phases,

(ii) the mechanism of ion transport and conductivity,

(iii) the parameters which are important in the empirical optimization of bulk electrical, chemical and mechanical properties, and

(iv) the behaviour of the materials when they are incorporated into a working electrochemical cell.

A good deal of progress has been made in basic understanding, and various models have been proposed with varying degrees of success. The aim of this chapter is to present a literature review for ionic host polymer systems, with particular reference to investigations relating to the PEO/$LiCF_3SO_3$ system. This will deal both with areas which are now well understood and those which remain contentious. The review is also intended to place the current work in a wider context. Much of the research in the area of ionic host polymer systems is concentrated on increasing the conductivity of polymer electrolytes. Although the stoichiometric crystalline complexes do not contribute significantly to ionic conductivity, the study of their structure provides valuable information on ion-polymer interactions, and as such, the 3.5:1 PEO/$LiCF_3SO_3$ system examined in this thesis is of considerable interest.

The review presented here is by no means intended to be comprehensive. Other reviews are available in the literature[10-13].

4.2 Ionic Host Polymer Systems Investigated and their Basic Structure

A wide variety of ionic host polymer systems have been studied.

The homopolymers that have been used as solvents include: PEO, polypropylene glycol (PPG), polypropylene oxide, (PPO), polyethylene succinate, polyaziridine, poly N-methyl aziridine, polymethyl sulfide, polyethylene adipate, polyoligoxyethylenemethacrylate and polypropiolactone. The majority of work has involved the metal salts $LiClO_4$ and $LiCF_3SO_3$ as solutes, although recent work has been carried out with PEO systems formed with $Cu(ClO_4)_2$[14] and

$Zn(CF_3SO_3)_2$[15]. A large number of investigations have focussed on PEO as the polymer component. This is because it is readily obtained in a number of molecular weights, has favourable mechanical properties, and has a simple well known, crystal structure[16]. At room temperature approximately 85% of the polymer is crystalline (for high molecular weights), with the remaining fraction amorphous in nature[12]. The possibilities of complex formation between PEO and metal salts as determined in experimental investigations are summarised in Table 4.1.

Table 4.1 Complex formation between PEO and metal salts: (✓) denotes the formation of a complex for that anion/cation combination; (x) denotes no complex formation

	Li^+	Na^+	K^+	Rb^+	Cs^+	NH_4^+
F^-	X	X	X	X	X	X
Cl^-	✓	X	X	X	X	X
Br^-	✓	✓	X	X	X	X
I^-	✓	✓	✓	✓	✓	✓
SCN^-	✓	✓	✓	✓	✓	✓
ClO_4^-	✓	✓	✓	✓	✓	✓
$CF_3SO_3^-$	✓	✓	✓	✓	✓	✓
AsF_6^-	✓	✓	✓	✓	✓	✓
BF_4^-	✓	✓	✓	✓	✓	✓

To improve bulk electrical and mechanical properties host polymer systems can be created by networking, blending, mixing and grafting co-polymers[17]. This is discussed further in Section 4.6.

The molar ratio of the host polymer to metal salt in an ionic host polymer system is an important variable and can have a marked effect on system properties. The ratio can be as small as 3:1. This corresponds to an ultraconcentrated solution. In the PEO/$LiCF_3SO_3$ system (the system of interest in this thesis) it has been suggested that at a ratio of 3.5:1 a stiochiometric complex is formed. Recent

investigations may indicate that this complex is formed at a lower ratio of 3:1. This is discussed further in Chapter 6.

In contrast to ionic host polymer systems a recently published paper[18] describes studies on systems of lithium salts, $LiClO_4$–LiI–LiOAc, mixed with small quantities of PPO and PEO with molar ratios of ~1:16; that is, a polymer in salt mixture. Interestingly these systems are rubbery at room temperature while exhibiting good Li^+ conductivities and high electrochemical stabilities. There is considerable scope to investigate these novel mixtures further.

Thermal measurements, XRD, NMR, conductivity studies and optical microscopy have all been used to construct phase diagrams of ionic host polymer systems. A schematic phase diagram is shown in Figure 4.1. Most systems, as with PEO/$LiCF_3SO_3$, are generally considered to have a single stoichiometric crystalline phase, with other phases consisting of amorphous ionic host polymer complex, host polymer and pure salt. The host polymer is often taken to be crystalline as an initial approximation, although in reality it contains amorphous regions co-existing with the crystalline phase, even at temperatures below the melting point of the polymer. An experimentally determined phase diagram for PEO/$LiCF_3SO_3$ is given in Chapter 6, in Figure 6.2.

In an amorphous polymer the molecules have fast internal modes of segmental motion. The bulk properties of the material are solid-like, but, at the microscopic level, liquid-like degrees of freedom exist, influencing local relaxation processes. It is now widely accepted that significant ionic conductivity in polymer electrolytes is dependent on the existence of amorphous regions in the systems, and crystalline phases do not significantly contribute[19]. However, the relationship between localized motion and larger scale ionic conductivity remains unclear. Structural relaxation may simply provide time-dependent sites for ions, or may actively facilitate ionic transport. Models of ionic transport are discussed further

in Section 4.5. A more detailed assessment of proposed structures and adduct formation is described in Section 4.4.

4.3 Experimental Techniques

The purpose of this section is to comment on the wide spectrum of experimental methods that are used in the study of ionic host polymer systems. Some of these techniques are also used in this thesis. Each of the methods tends to have been used to investigate different features of the systems; each is highlighted below.

A major aspect of ionic host polymer systems that is a source of much research is their microscopic structure. This is not straightforward due to the complex phase behaviour of the systems, shown in Figure 4.1. Stoichiometric complexes that are formed are highly crystalline and have been subject to structural investigations using x-ray diffraction[20,21]. The structure of the complexes however, can be difficult to obtain from single crystal studies as unit cells are often large with low symmetry. Powder x-ray data has recently been analysed using Rietveld methods with soft chemical constraints and the crystal structure of the complexes formed between PEO and $NaClO_4$ (3:1)[22], and PEO and $LiCF_3SO_3$[23] (3:1) have been determined.

However, the systems that are of interest as polymer electrolytes are predominantly amorphous, and are usually PPO based at room temperature, or PEO-based at elevated temperatures of ~373 K. For these cases XRD techniques are not useful. Optical microscopy[24] and DSC[25] have been used for the identification and classification of dominant phase regions, but these techniques give no insight into actual microscopic structure.

Extended x-ray absorption fine structure spectroscopic investigations (EXAFS) can be used to probe local structural environments irrespective of morphology and are therefore potentially very useful. EXAFS spectroscopy uses the fact that

oscillations present on the high-energy side of x-ray spectra absorption edges in condensed materials contain information on the local environment of the absorbing atoms. This is shown schematically in Figure 4.2. The oscillations are due to interference of the ejected photoelectrons, and a fraction of these backscattered by neighbouring atoms[26]. At present the technique has been applied only scarcely to probe local structure in ionic host polymer systems, although it is ideal for yielding values of radii and number and distance of coordinated neighbours in amorphous solids. A recent near edge x-ray absorption fine structure spectroscopy investigation of PEO/KI complexes[27] concluded that on heating the complex the oxygen co-ordination number of the K^+ ion decreased, perhaps being responsible for the higher ionic conductivity at higher temperatures. PEO/ZnX_2 ionic host polymer systems have also been the subject of EXAFS studies[28,29]. The anion and cation were found to be close in this system, indicating that ion-pairing, suggested from Zn diffusion studies, is indeed likely. At present, information from this technique is fairly qualitative, and there is no available data for the PEO/$LiCF_3SO_3$ system. This may be difficult to obtain due to Li being relatively 'light' in terms of being a diffraction centre for the photoelectrons.

Information on cation-oxygen interactions in a range of polyethylene oxide alkali metal salt systems has been obtained from infrared and Raman spectroscopic studies conducted on solvent free systems[30]. The Raman spectra of PEO/$LiBF_4$ systems show vibrational bands attributed to metal-oxygen stretches, with the cation symmetrically surrounded by oxygen atoms. This suggests that the cation is probably in the crystalline phase. The solution spectra of $CF_3SO_3^-$ anions clearly show a distinction between free ions and ions in clusters and this technique has been used to identify $CF_3SO_3^- - Li^+ - {}^-O_3SCF_3$ triplet ions in low concentration (~50:1) PEO/$LiCF_3SO_3$ systems[13].

N.m.r. techniques are well known as probes of local environment and structure, and of dynamical processes occurring at the molecular level. The structural

aspects of ionic host polymer systems were first studied using n.m.r. methods by Berthier et al[31]. This group studied PEO/$LiCF_3SO_3$ mixtures and assigned ^1H and ^{19}F n.m.r. signals to crystalline or amorphous phases based on the transverse nuclear magnetic relaxation time T_2. Long T_2 components of both signals were associated with the amorphous fraction. The results are shown in Figure 4.3. The fractions of nuclei predicted by this technique to be in each phase agrees well with DSC data. However, a later study[32] suggested that at elevated temperatures segmental motions in the crystalline PEO chains, even at ratios of 4:1 would be of a high enough frequency to narrow the spectral lineshape and increase T_2.

N.m.r. linewidths for the cation nuclei, usually ^7Li or ^{23}Na, have also been studied with a view to extracting diffusion coefficients, by relating diffusion to narrowing of the lineshape. This was first attempted for ^7Li in the PEO/$LiCF_3SO_3$ 4:1 system[33], and assuming that line narrowing observed from 243 K to 373 K was solely due to lithium ion diffusion a value of $D = 10^{-11}$ cm^2 s^{-1} was estimated. This is in agreement with the order of magnitude obtained from pulsed field gradient n.m.r. measurements, discussed next, although theoretically there is a problem of relating n.m.r. parameters to diffusion coefficients[12]. Furthermore ^7Li and ^{23}Na are quadrupolar nuclei, so interpretation is not straightforward. Many of the studies also include complementary spin-lattice relaxation time measurements.

In the case of motional investigations at a molecular level, n.m.r. methods are particularly useful, as they are nuclei selective and capable of studying a wide range of motional frequencies. In addition to T_1 and T_2, slower molecular motions can be probed by measuring relaxation times in the rotating frame, $T_{1\rho}$, and the local dipole field T_{1D}, as shown in Figure 4.4. Diffusion coefficients can be measured directly by a pulsed field gradient (p.f.g) n.m.r. technique. In a p.f.g experiment a large field gradient is applied to the sample for a short duration, after

a 90° pulse and before a refocussing pulse. The same field gradient is applied at an identical time after the refocussing pulse as shown in Figure 4.5.

If diffusion of the selected nuclei has occurred between the applications of the field gradient, a particular nucleus will not experience the same external field in which it was initially dephased and so the echo will be attenuated by far more than would be expected in a normal T_2 measurement. This method is applicable to crystalline or amorphous solids, and gives n.m.r. determined diffusion coefficients. The diffusion coefficients for both Li^+ and $CF_3SO_3^-$ ions in the 8:1 PEO/$LiCF_3SO_3$ system have been measured by this technique[34,35]. These are shown in Figure 4.6. The cation and anion have comparable mobility over the studied temperature range.

Another technique for measuring diffusion, is that of radiotracer measurements. These are widely applicable to the study of diffusion in solids. The method consists of monitoring the progress of isotopically labelled molecules through a solid. The most reliable diffusion method is radiotracer serial sectioning, in which a penetration profile is obtained directly. Theoretically, the tracer concentration at a distance x from the surface, after time t, where the active layer of activity Cs is deposited at t = 0, and D is the tracer diffusion coefficient, is given by the solution to Fick's Law with appropriate boundary conditions;

$$C(x,t) = \frac{Cs}{(\pi\, Dt)^{\frac{1}{2}}} \exp(-x^2/4Dt) \qquad (4.1)$$

Results at several temperatures can be fitted to an Arrhenius law. Self diffusion measurements have been carried out for Na^+ and SCN^- ions in the PEO/NaSCN system[36]. The tracer studies clearly show that both anions and cations are mobile in this system. They are consistent with conductivity data, if it assumed that mobile ions are in the amorphous phase. There is at present no data for this type of study in the PEO/$LiCF_3SO_3$ system.

The characterization of the electrical properties of polymer electrolytes involves investigation of the total conductivity as a function of temperature, and identification of the charged species contributing with corresponding transport numbers. Although the systems under study are hetrogeneous, containing different phase regions, electrical measurements are usually interpreted in terms of two models, one in which only one ionic species is mobile, and one in which anions and cations are equally mobile.

The most straightforward method of investigating electrical properties of a system is a simple direct current conductivity measurement. Two terminal cells, however, have the problem that the electrode resistances add to that of the electrolyte. This can be overcome by the use of a four electrode cell. With this type of measurement it is often difficult to obtain sufficiently reversible electrodes that are stable over a large temperature range, and alternating current techniques are often favoured. These techniques are well established in the investigation of electrochemical systems. In a typical experiment there are two parameters relating the flow of current through the sample to an applied voltage, these are the ratio of the voltage and current maxima, and the phase difference between the voltage and current. The combination of these parameters gives the impedance which is represented on a vector diagram, analogous to the Argand diagram representation of a complex number. The distance from the origin corresponds to the magnitude of the impedance, |Z| and the angle formed with the x-axis corresponds to the phase difference between voltage and current. The impedance of an electrochemical cell is a function of applied frequency and can be represented by a separate point at each frequency on the vector diagram, as shown in Figure 4.7.

In simple cases the response of an electrochemical system can be compared to an equivalent circuit. The exact nature of the equivalent model circuit impedance plot will however depend on the electrolyte model, and on the type of the electrode,

blocking or non-blocking, (mobile species in the electrolyte do not participate in electrode reactions for blocking electrodes). In theory, the magnitude of all the fundamental electrical properties of a cell are obtainable from complete impedance data. The a.c response of polymer/salt complexes between electrodes which are non-blocking towards one of the mobile ions have proved to be of considerable interest[37]. The a.c response of real polymer electrolyte cells show departure from the ideal, with semicircles broadened and spikes non-vertical. A typical example for the PEO/$LiCF_3SO_3$ 16:1 system is shown in Figure 4.8.

The non-ideal behaviour can be due to many factors. In particular, surface layers on electrodes need to be considered. This is thought to be important for PEO/$LiCF_3SO_3$ systems. When in contact with Li metal electrodes, a thin layer forms between the electrode and the ionic-host polymer system which is permeable to Li^+ ions[38]. The resistivity and capacitance of a thin layer will be large and so the interface will dominate the a.c response. Interactions between ions are also likely to contribute to distorted impedance semicircles. Such interactions will hinder the migration of ions in an electric field. Alternating current measurements do have advantages, for example, blocking electrodes (Au, and Pt) are stable over large temperature ranges, and information on charge migration and polarisation within the electrolyte, and at the electrodes, can be obtained. However, relatively sophisticated equipment is required, great care must be taken over the elimination of cable impedances, and interpretation of results is not straightforward.

Transport numbers can be determined by comparison of the distorted semicircle impedance plot at low frequency, with the bulk resistance. The interpretation of such measurements should be undertaken with caution as the diffusion process responsible for the low frequency behaviour may take place in the passivating film and not in the electrolyte. Transport numbers for a binary polymer electrolyte may be determined by measuring the d.c conductivity of a two terminal cell, the

electrodes of which are non-blocking towards one of the mobile ions. On application of a d.c potential, an initial current flows due to migration of cations and anions. With time a salt concentration profile builds up across the cell. If the rate of anion diffusion becomes exactly opposite to that of the rate of anion migration due to the applied potential, then at this situation the current is due to the cations only. In this case the difference between initial and final currents can give the cation transport number. A similar method is the Tunandt method where the salt concentration profile is examined by weighing sections of the cell before and after the passage of a known quantity of change. Tubandt measurements have been carried out in the PEO/$LiCF_3SO_3$ 24:1 system in the range 343 K to 393 K, and give a Li^+ transport number of 0.2[39]. The p.f.g. measurements discussed in Section 4.3[34,35] found a temperature dependent transport number, but extrapolation to 393 K also gives a value of Li^+ transport number of ~0.2. However, an electrochemical method which makes allowance for passivating layers has determined a value of Li^+ transport number of ~0.5[10].

The results of transport number measurements still show considerable variation. This may be due in part to the complication of the distribution of charge. Electrochemically determined transference numbers include simple ions, triple ions and higher charged aggregates, while p.f.g. n.m.r. determined transference numbers may be complicated by neutral ion pairs and higher aggregates. Conductivity measurements are discussed further in Section 4.5.

4.4 Ion-Polymer and Ion-Ion Interactions

It is well known that the existence of ion-ion interactions have important consequences for the ionic transport behaviour in ionic host polymer systems. Indeed, the formation of an ionic host system polymer and its subsequent structure depend intimately on ion-ion, as well as ion-polymer interactions. These types of interactions were of interest in systems consisting of polyethers in

the presence of simple salts, long before the electrical conductance properties were examined. Systems consisting of both high and low molecular weight PPO with up to 25% $LiClO_4$ were studied as early as 1965.[40]. The authors measured specific volume, damping constants and shear moduli and interpreted the results in terms of the superposition of free polyether segment behaviour and the behaviour of segments which were nearest neighbours of $LiClO_4$ ion pairs. A change in mechanical properties above 5% $LiClO_4$ composition was attributed to the depletion of free segments.

A salt will dissolve in a solvent only when the enthalpy and entropy changes involved result in an overall decrease in the free energy of the system. These changes are the difference between the initial crystal lattice state values and those with the ions at equilibrium in solution. Lattice energy is compensated for by exothermic ion-solvent interactions. Entropy is gained by the disordering of the lattice, but short range ion-solvent interactions can cause an ordering of solvent molecules. Indeed, some amorphous ionic host polymer systems precipitate salt as the temperature is raised, indicating a negative entropy of solution; this is not observed in the PEO/$LiCF_3SO_3$ system. Generally, in systems with a polymer solvent, the loss of translational entropy will be small, especially when the ion is solvated by neighbouring coordination sites on a polymer chain. Evaluation of the thermodynamic properties of an ionic host polymer system will involve consideration of; the energy of cavity formation within the solvent host; short range interactions between ions and solvating groups; and long range electrostatic forces.

Salt concentrations proposed for Li-PEO batteries, and indeed those of the most frequently studied systems, are concentrated or ultraconcentrated. However, valuable insights into ion-polymer interactions have been gained from studies of low concentration liquid solutions. NMR methods have been used to study the complexes of Na^+ with polyethers in CH_3CN[41], and the solvation of Na^+, K^+ and

Cs^+ ions with PEO in nitromethane solutions[42]. These studies concluded that the complexing ability of the alkali metal ions decreased monotonically with increasing ionic radii, and that the solvation shell involved 6-12 monomeric CH_2CH_2O units depending on the cation. This work showed that specific interactions were active, in addition to normal electrostatic forces, which bound a fraction of the anions to the PEO cation complex.

Ion-ion interactions have also been the subject of study in low concentration systems. The interpretation of results assumes the solvent to be a homogeneous continuum. In such a system, bringing a mole of anions and a mole of cations from infinity to form a mole of isolated ion pairs of separation r, will result in a decrease in potential energy given by

$$\Delta U = Le^2/4\pi\varepsilon_o\varepsilon_r\, r \qquad (4.2)$$

The quantity ε_o is the permitivity of free space, ε_r is the relative permitivity of the solvent, L is Avogradro's constant and e is electronic charge. When the electrostatic attractive energy becomes greater than the energy of thermal motion the ions no longer behave independently. This will occur when r is such that $\Delta U/L > 2kT$. The relative concentration of ion pairs can be predicted for a system if certain fundamental properties are known. If the solvation of free ions and ion pairs, exhibited approximately the same energy change which is small relative to the electrostatic energy involved in the formation of an ion pair, then the total energy of ion pair formation can be given by equation 4.2. Potential energy and statistical entropy terms have been developed for ion pairs, and also for larger aggregates, specifically triplet, quartet and sextet clusters. Specific calculations for the PEO/$LiCF_3SO_3$ system, or any real ionic host polymer system are difficult, as the proportion of different ion clusters is difficult to establish. The determination of which aggregates are involved in conductance is important in polymer electrolytes. The conductance is given by

$$\sigma = \sum_i n_i(Z_i e)u_i \qquad (4.3)$$

where n_i is the number of carriers of type i, $z_i e$ is the net charge on the ith type of carrier, and u_i is the corresponding mobility in unit field. The mobility can be calculated from the Nernst-Einstein equation,

$$u_i = (z_i e)D_i/kT \qquad (4.4)$$

where D_i is the diffusion coefficient. This is discussed further in Section 4.5. Much attention has been given to relating the diffusion coefficient to bulk properties while the carrier profile has not been extensively investigated. Transport number measurements, which, as discussed in Section 4.3, can be unreliable, only give information on the sum of fluxes and not on the carrier distribution. There is evidence to suggest that for systems of moderate electrolyte concentration a simplification can be achieved by assuming all uncharged species are ion pairs and all charged species are simple ions or triplets[43]. Taking this assumption it has been shown how to obtain the fraction of the total electrolytic system existing in each state, from experimental plots involving the conductivity and concentration[12]. Studies on $LiClO_4$ and $LiCF_3SO_3$ in PEO (400), have concluded that above a salt concentration of about 0.01 mol dm^{-3}, the majority of current is carried by triple ions. However, it is doubtful that these conclusions are valid in systems of practical importance as polymer electrolytes, where concentrations are much higher (1:8 to 1:50) and continuum models are unlikely to be applicable.

While insight has been gained into ion-polymer interactions through comparison with low concentration liquid solutions, there is a fundamental difference between these systems and polymer electrolytes. That is, the coordinating groups of a polymer solvent are incapable of independent motion. It has proved useful to study macromolecular species which also exhibit this structural characteristic.

Ionomers, (linear organic polymers in which 20% of the monomeric units have been substituted by an acid group and subsequently a salt), have been shown by small angle x-ray diffraction to exhibit clustering of ion pairs[44]. Two main models of ion-pair aggregation have been proposed, distorted lattice[45], and spherical shell-core[46].

Similarly, there are two basic models for the structure of ionic host polymer systems. (1) A structure has been proposed in which the salt occupies a paracrystalline array, with the PEO chains as a containing matrix[47]. (2) A spherulitic structure has also been proposed, and is generally favoured.

4.5 Theories of Transport and Conductivity Mechanisms

There are two complementary approaches to the theoretical modelling of ionic host polymer systems; quasithermodynamic and microscopic. The quasithermodynamic theories are based on the ideas of free volume, and configurational entropy. Microscopic theories are based on percolation models[48]. The local environment of ions in ionic host polymer systems has liquid-like degrees of freedom in the amorphous phase, as a consequence of the polymer host motion, and these motions influence the ionic transport. The first studies of the temperature dependence of the conductivity in amorphous ionic host polymer systems[1] showed a Vogel-Tamman-Fulcher relationship;

$$\sigma = \sigma_0 \exp[-B/(T-T_0)] \qquad (4.5)$$

where T_0 is a reference temperature (the equilibrium glass transition temperature), and σ_0 contains a $T^{-\frac{1}{2}}$ term. The VTF equation was originally developed to model the viscosity properties of supercooled liquids. Conductivity data in ionic host polymer systems gives rise to one of five forms: (i) VTF behaviour throughout the temperature range, (ii) Arrhenius behaviour at low temperatures and VTF behaviour at higher temperatures, (iii) Arrhenius

behaviour in two sections, one with a high activation energy (close to the glass transition) and one with a lower activation energy (at higher temperatures) (iv) VTF behaviour for temperatures slightly greater than the glass transition, but Arrhenius behaviour at higher temperatures, and (v) behaviour unlike VTF or Arrhenius throughout. The VTF equation itself is empirical although it has origins based on the free volume theory. The basic idea of this is to consider a liquid of incompressible spheres and apply statistical mechanics to calculate the most probable distribution for various sizes of void volume. In this treatment diffusion is not activated, but is the result of the redistribution of free volume. For ionic host polymer systems, this implies that the rate of ionic diffusion is fixed by the polymer solvent, since only when a hole appears can the solute move. The application of this simple theory does produce limitations on the degree of understanding obtainable. In a real ionic host polymer system, phases are inhomogeneous and thermal responses contain information on phase melting and ionic transport between phases, as well as bulk ionic transport. The simple model also neglects ion pairing and describes the motions of the polymer, not the charged species.

The theories can be extended by defining solid like and liquid like cells and percolation like motion between them. These modified free volume theories, are very similar to models based on configurational entropy. These models too only deal with the motion of the polymer host in ionic host polymer systems. The theory does provide implications which can be compared with experiment: the conductivity should decrease with pressure; the Tg of a system should increase as more salt is added (this relationship is linear where no crystallization is present); and the conductivity of a system should increase at a fixed temperature above Tg, if Tg is lowered. Long range ion motion is promoted by shorter range polymer motion. Free volume and configurational entropy models do seem to describe the temperature dependence of several transport properties, in ionic host

polymer systems, including conductivity, with a reasonable amount of success over a broad range. However, these models are static and non microscopic. As such they do not deal well with frequency dependent spectroscopic measurements, and actual rates and mechanisms of transport are not easily determined.

Initial attempts to deduce a microscopic model of ionic host polymer system ionic mobility, including the alkali metal ion hopping down the oxygen lined centre of a PEO helix[49] and a similar double helix model[20], are now accepted to be oversimplified. It was first shown by x-ray studies[47] on a PEO/SCN 4:1 sample that the metal ion in ionic host polymer systems resides outside the helical cavity, and it is now well accepted that the elastomeric amorphous phase is responsible for the conductivity[50]. Microscopic transport theories are now based on cations moving by breaking one or two M-O bonds and subsequently bonding to another oxygen, while the anion moves freely into holes available in the structure. A saturated system can be developed where the coordination numbers of the cations are satisfied by polyether oxygen lone pairs and under this condition there will be little cationic transport coincident with the lack of vacant hopping sites for the cation. Above the glass transition temperature saturated structures present in the system may dissociate as described below, n being the cation coordination number

$$M(PEO)_{n+x} \rightleftharpoons M(PEO)_n + (PEO)_x$$

The entire system will be in equilibrium between the formation and dissociation of complexes. For a particular cation the value of n will be constant, with the variation of x limited by cation size. When coordinately unsaturated PEO enters the vicinity of an opening complex, the electrostatic attraction of the cation for the already coordinated lone pair becomes weak and there is an increased probability of bonding with the incoming lone pairs. The lone pairs provide a pathway for

cation movement, with the transport electrical (driven by potential difference) or diffusive (driven by free volume). The motion of the ions is due to the combination of the ions themselves hopping and the dynamical free movement of segments of the host polymer providing additional hopping sites (lone pairs). At high concentrations, greater than ~20:1 a similar hopping mechanism has been proposed for the cation between clusters, as shown below

$$M^+X^-M^+ + X^-M^+ \longrightarrow M^+X^- + M^+X^-M^+$$

Hopping mechanisms of transport can be modelled using percolation theories. The static percolation theory was originally developed by Hammersley. A set of sites at which the moving species can reside is defined and the motion of these moving species is defined by the master equation.

$$\dot{P}_i = \sum_j{}' \{P_j W_{ji} - P_i W_{ij}\} \tag{4.6}$$

where $P_i = P_i(t)$, the probability of finding the carrier at site i at time t, and the $W_{ji} = W_{j \longrightarrow i}$ is the rate at which the carrier hops from site j to site i. The hopping is limited to nearest neighbour sites, as indicated by the prime on the sum of equation (4.8). The setting of a particular link between sites as open or closed is chosen randomly, with probability f of being open.

$$W_{ij} = \begin{cases} 0 & \text{Probability} = 1\text{-}f \\ W & \text{Probability} = f \end{cases} \tag{4.7}$$

However, the model does have limitations in applications to ionic host polymer systems, as the hopping particles of the model are independent, the model host material is static, and the sites involved form a regular array. Partly crystalline materials can be treated by bond percolation theory by assigning $W_{ij} = 0$ for crystalline regions and $W_{ij} = w$ for amorphous ones.

A dynamic bond percolation theory (d.b.p.t) can be useful in situations where the static model is not. In this case, the links between localization sites for mobile ions are open and closed, with a characteristic rate λ, with complementary renewal time $\tau_r = 1/\lambda$. The simplest of the d.b.p.t parameters is w, the hopping rate between neighbouring sites. For cation motion, the hopping is basically the changing of the coordination shell by breaking and making bonds. For anion motion, the hopping rate is the inverse of the time taken for movement from one available void volume to another. For typical diffusivities characteristic of ionic host polymer systems, the hop time 1/w is of the order of 10^{-12} s. τ_r, the renewal rate, characterizes the segmental motion of the polymer host. A real sample contains a distribution of renewal times, with a characteristic average of about 10^{-10} s. The parameter f represents the fraction of hopping pathways available. The renewal time is dependent only on the polymer host dynamics, whereas 1/w and f are determined by the ions.

For real ionic polymer host systems the conductivity data cannot often be explained by a single model. The condutivity behaviour of the system PEO/MAg_4I_5 (M=Rb,Li,K)[51], is in good agreement with that calculated by percolation theory. The conductive behaviour of amorphous films of $PEO/Cu(ClO_4)_2$ systems is well modelled by VTF behaviour[14]. The conductivity in the $PEO/LiCF_3SO_3$ 8:1 system obeys an Arrhenius law above and below 328 K, with distinct activation energies of 0.65 ev (~62 kJ mol^{-1}) and 2.0 eV (~192 kJ mol^{-1}) respectively[50]; as shown in Figure 4.9.

In continuous amorphous systems (PPO based for example) the temperature dependence of the conductivity reflects the segment mobility. The crystalline regions can be assumed to affect the conductivity in a number of ways including blocking conduction and decreasing chain mobility by fixing ends of polymer chains which protrude into amorphous regions. There will also be a temperature dependent balance between the concentration of ions in amorphous and crystalline

regions, and the carrier number will not be constant. This is not considered in d.b.p.t. However, the theory has been applied to the discussion of; the pressure dependence of ionic conductivity, the dependence of conductivity on polymer chain length and type, the dependence on counter-ion and stoichiometry, and the effect of plasticization; in terms of the variation of the parameters w, f and λ. Frequency dependent behaviour in d.b.p.t suggests that estimation of the product fw should be possible from microwave or infrared spectroscopy at high temperatures[12]. Although there are no values for PEO/$LiCF_3SO_3$ systems, the general approach, and in particular an extended d.b.p.t where W_{ij} can take several values, is promising as a theoretical construct to discuss transport in these very complex systems. To obtain insights to enable rational design of solid polymer electrolytes with particularly desired properties, such as conductivity or particular frequency responses, the d.b.p.t approach needs to incorporate ion-pairing and effects due to interfacial regions.

It has also been suggested that ion transport may also take place by a convective type mechanism, where the ions, remaining attached to polymer segments, are carried by the medium.

4.6 Ideal Properties and Proposed Architectures

The most studied and practically most important aspects of ionic host polymer systems which are useful as solid polymer electrolytes, are the ionic conductivity and the mechanical stability. High conductivity can be achieved by selection of a suitable ion-coordinating macromolecule which will form an amorphous matrix with a low glass transition temperature, together with a suitable salt in an optimized concentration. The amorphous phase of the system salt complex is responsible for the conductivity behaviour. PEO has been used in the majority of ionic host polymer systems due to its ability to coordinate cations and form homogeneous solutions, although a major disadvantage is the crystalization

behaviour which results in acceptable ionic conductivities only above the melting temperatures. For the PEO/$LiCF_3SO_3$ system it is advantageous to create a system which remains in an amorphous state over the temperature range of interest. This can be achieved in many ways[12]:

(i) Modification of PEO by,

(a) Formation of crosslinked networks,

(b) Formation of block or comb branch copolymers,

(c) Plasticisation;

(ii) The use of structurally similar polymers such as PPO;

(iii) The use of other amorphous polymers, with low glass transition temperatures, capable of dissolving salts.

One interesting method of producing highly amorphous polymeric electrolytes is the preparation of polyethylene co-polymers[52]. PEO with PPO systems have also attracted attention[53], where the conductivity obtained for co-polymers has been shown to depend strongly on the molar fraction of ethylene oxide, and is decreased for high PPO concentrations. X-ray diffraction experiments are often used to confirm the amorphous character of prepared co-polymers. High molecular weight PEO-PPO co-polymers exhibit high ambient temperature conductivity, but the mechanical properties of these systems can be poor.

Another possibility as a method of producing polymer electrolyte systems with increased conductivity is the synthesis of polymer blends and grafted co-polymers. Investigations of polymer blends must consider that platicizers should be completely miscible with the amorphous phase of the main polymer, and have high stability against electrode materials. It has been suggested that the use of mixed salts has a plastifying effect[54] in ionic host polymer systems, which favours, at the expense of the crystalline phase, the formation of an amorphous

phase. This has been investigated in the systems PEO/$LiCF_3SO_3$/NaI, 4:0.5:0.5 and 8:0.5:0.5[55]. The conductivity in the mixed system was increased in both cases, above the single salt systems, as shown in Figure 4.10.

Recently, poly(N-vinylacetamide) (PVAA) has been examined as a water soluble polymer for use in a $LiCF_3SO_3$ polymer electrolyte[56]. $LiCF_3SO_3$ was employed as a strong electrolyte and PEG as a plasticizer, and the composite polymer electrolyte system PVAA/$LiCF_3SO_3$/PEG was characterized. Conductivity plots for the PVAA composites were found to be convex when plotted against inverse temperature, characteristic of an electrolyte in very amorphous state. Work was also carried out investigating conductivity behaviour as a function of PEG content. As the plasticizer content is increased, the polymer chains become more flexible, but the ion concentration is reduced. It is the balance between these two facets that determines the plasticizer content which coincides with the maximum conductivity.

The majority of systems investigated to date have ambient temperature conductivities of the order of $10^{-4} - 10^{-5}$ Scm^{-1}, which with the use of thin film configurations are acceptable for most applications. There is a large interest in designing systems which retain high conductivities while showing improved physical and mechanical properties. A number of approaches have been made, including adding α-alumina as an inert filler. Another area of research has attempted to improve dimensional stability by radiation crosslinking PEO chains[58]. In both these cases reduction in ionic conductivity was minimal, although problems do exist, including the settling out of filler with time, and changes in PEO molecular weight distribution caused by chain scission as a consequence of a competitive crosslinking process. Another approach to obtaining improved PEO mechanical stability has been to form a polymer matrix where PEO is the conducting part and a second polymer forms the support. Nafion, Flemiaon and polymethacrylic acid(PMAA) have all been used as

supports in this manner. Polystyrene has been used as a support polymer in the PEO/$LiCF_3SO_3$ system, particularly in the 10:1 system[12]. The effect of this on the conductivity is shown in Figure 4.11.

In most systems the addition of support polymers to improve the mechanical properties, leads to a slight decrease in conductivity. However in some cases it is possible that support polymers can increase the conductivity of a system by limiting the size of crystalites which can form and thus increasing disorder.

4.7 Applications

The potential use of polymer electrolytes in an all solid state battery, was predicted in 1978[1]. It was suggested that thin film configurations would yield high energy densities. A typical design is shown in Figure 4.12. The first reports of actual battery testing concerned Li batteries which used intercalation electrodes and PEO[59]. These prototypes used $LiCF_3SO_3$ and $LiClO_4$ in an 8:1 ratio. Li/PEO-$LiCF_3SO_3$/V_6O_{13} cells needed temperatures of about 393-413 K for operation with current densities between 0.5 and 1.5 mA cm^{-2}.

There have been large scale joint projects (SNEA and IREQ) conducted, with a main interest in developing a battery for use in an electric vehicle[59,60]. This work included studies of the first scale up cells which had a surface area of 70 cm^2, as opposed to the previously investigated 6.5 cm^2.

For successful development of practical high energy density batteries, an understanding of the Li-polymer electrolyte interface is required. Direct current methods have shown that at low values of polarization the electrode process can be modelled as a simple charge transfer reaction with an exchange current density of the order of 1mA cm^{-2} at 373 K[61]. This current was significantly increased with temperature and was highly dependent on good interfacial contact, although it was less dependent on the PEO to salt ratio. At higher polarization values the

electrode became subject to concentration polarization, which eventually limits the current[62]. This is shown in Figure 4.13 for a symmetric cell Li|PEO/$LiCF_3SO_3$|Li. The limiting current fraction is a function of salt concentration as shown in Figure 4.14.

The Li-polymer electrolyte interface also exhibits a time dependent impedance corresponding to the formation of a resistive layer. This can be detected by alternating current impedance spectroscopy[38]. Initial studies suggested that the formation of this layer was due to lithium reacting with water in the electrolyte and forming an oxide layer, but it has been shown to exist even in very dry conditions[63]. At low salt concentrations film formation processes involve Li reacting with trace impurities in the electrolyte. At higher salt concentrations in the PEO/$LiCF_3SO_3$ system, two mechanisms for film formation have been suggested[12], which results in the formation of LiF and LiS respectively. It is clear that the presence of a film, and its electrical characteristics, will influence the behaviour of electrochemical cells, irrespective of the exact nature of the film. It has also been suggested that the thermal history profile imposed on the electrolyte during polymeric solid state battery formation, needs to be considered with reference to morphological changes of the system. These changes can be explained by the spherulitic model[64], discussed in Section 4.4.

Power densities in excess of 100W dm^{-3} are attainable from thin film configurations. Present systems have charge-discharge efficiencies as high as 95%, with no cell performance deterioration observed after 120 cycles. The mechanical properties of polymer electrolytes, and in particular their ability to deform, gives the system an advantage in electrode-electrolyte interface contact, compared to all solid state cells based on crystalline or vitreous solid electrolytes. It has been suggested[12] that practical energy densities of at least 200 Wh kg^{-1} might be possible, while retaining high rate capabilities.

With the development of ambient temperature systems[65], utilizing plasticizer salts (most recently $(C_nX_{2n+1}Y)_2N^-M^+$, where n=1 to 4, X is a halogen and Y is a functional group, acyl or sulfonyl), and polymer blending, many other applications are being considered. These include large area electrochromic 'smart' windows, novel power sources for implantable biomedical devices, and electrochemical supercapacitors.

References

1 M B Armand, J M Chabagno and M Cuclot
Second International Conference on Solid Electrolytes
St. Andrews, 1978.

2 D E Fenton, J M Parker and P V Wright
Polymer 14, 589, 1973.

3 P V Wright and C C Lee
Polymer, 19, 234, 1978.

4 A Landrebe and F McLarnon
Fuel Cells
R E White and A J Appleby Eds., The Electrochemical Society Softbound Proceedings Series, Perrington NE, 1989.

5 VR H Hammerle, R A Gorse Jr and J W Schiller
Acid Rain
Ford Research Technology Assessment Series, 1989.

6 R H Hammerle, J W Schiller and M J Schwartz
Global Warming
Fuel Research Technology Assessment Series, 1989.

7 D M Bernardi and M W Verbrugge
J. Electrochem Soc., 139, 2477, 1992.

8 P Tebbutt
New Scientist, (June), 1, 1991.

9 S Trinivason, D S Manco, H Koch, M A Enayetellah and J A Appleby
J. Power Sources, 29, 367, 1990.

10 C A Vincent
Prog. Solid State Chem., 17, 145, 1987.

11 M B Armand
Ann. Rev. Mater. Sci., 16, 245, 1986.

12 Polymer Electrolyte Reviews 1,
J R MacCallum and C A Vincent Eds
Elsevier Applied Science Publishers, London, 1987.

13 P G Bruce and C A Vincent
J. Chem. Soc. Faraday Trans., 89, 3187, 1993.

14 A Magistris, G Chiodellio, K Singh and P Ferloni
Solid State Ion., 38, 235, 1990.

15 J Shi, P G Bruce, C A Vincent
Electrochima Acta, 37, 1707, 1992.

16 Y Takahashi and H Takadoro
Macromolecules, 6, 672, 1973.

17 A S Tomlin, J R MacCallum, D P Tunstall and C A Vincent
J. Phys. Condens. Matter 1, 7483, 1989.

18 C A Angell, C Lice and E Sanchez
Nature (March), 362, 1993.

19 C Berthier, W Gorecki, M Minver, M B Armand, J M Chabagno and P Rigawd
Solid State Ion., 11, 91, 1983.

20 J M Parker, P V Wright and C C Lee
Polymer, 22, 1305, 1981.

21 T Hibma
Solid State Ion., 9/10, 1101, 1983.

22 P Lightfoot, M A Mehta and P G Bruce
J. Mater. Chem,. 2, 379, 1992.

23 P Lightfoot, M A Mehta, and P G Bruce
Science, 262, 883, 1993.

24 C D Robitaille and D Fauteux
J. Electrochem. Soc., 133, 315, 1986.

25 S M Zahwak, M L Kaplan, E A Rietman, D W Murphy and R J Cava
Macromol., 21, 654, 1988.

26 BK Teo and D C Joy Eds
EXAFS Spectroscopy Techniques and Applications
Plenum Press, New York 1981.

27 X Q Yang, J M Chan and T A Sothein
Phys. Rev. B, 40, 7948, 1989.

28 R J Latham, R G Linford and W S Schlinduein
Faraday Discuss. Chem. Soc., 88, 103, 1098.

29 R J Latham, R G Linford, R A J Pynenburg and W S Schlinduein
J. Electrochem. Soc., 140, 1056, 1993.

30 B L Papke, M A Ratner and D F Shriver
J. Electrochem Soc., 129, 1434, 1982.

31 M Minier, C Berthier and W Garecki
J. Physique, 45, 739, 1984.

32 D P Tunstall, A S Tomlin, J R MacCallum and C A Vincent
J. Phys. C. Solid State Phys., 21, 1039, 1988.

33 F L Tanzella, W Bailey, D Frydrych and H S Story
Solid State Ion., 5, 681, 1981.

34 S Bhattacharja, S W Smoot and D H Whitmore
Solid State Ion., 18/19, 306, 1986.

35 M Mali, J. Roos and D Brinkmann
Proc XXII Congress Ampere
K A Muler, R Kind and J Roos Eds, Zurich 1984.

36 A V Chadwick, J H Strange, and M R Warboys
Solid State Ion., 9/10, 1155, 1983.

37 P R Sorensen and T Jacobsen
Solid State Ion., 9/10, 1147, 1983.

38 J R Upton, K A Mungesamoorthi, J R Owen, P Fulton and J D Benjamin
J. Electrochem Soc. Reviews and News, 134, 8, 1987.

39 M Leveque, J F Le Nest, A Gandini and H Chevadame
J. Power Sources, 14, 27, 1985.

40 J Moocanin and E F Cuddihy
J. Poly. Sci. C, 14, 313, 1966.

41 T Wong M Brodwin, J I McOmber and D F Shriver
Solid State Comm., 35, 591, 1980.

42 G N Arkhipovich, S A Debronski, K S Kazanskii, N V Ptitsma and A N Shupik
Europ. Polymer Journal 18, 569, 1982.

43 L D Pettit and S Bruckenstein
J. Amer. Chem. Soc., 88, 4783, 1966.

44 R Longworth
Developments in Ionic Polymers-1
A D Wilson and H J Prosser Eds.
Applied Science Publishers, London and New York, 1983.

45 C L Marx, D F Caulfield and S L Cooper
Macromol., 6, 344, 1973.

46 W J Macknight and T R Earnest
J. Polym. Sci, Macromol. Rev., 16, 41, 1981.

47 T Hibma
Solid State Ion., 9/10, 1101, 1983.

48 F M Gray, J R MacCallum and C A Vincent
Solid State Ion., 18, 19, 282, 1986.

49 M B Armand, J M Chabagno, M Duelog P Fachista, J N Mundy, E K Shenoy
Fast Ion Transport in Solids
New York.

50 C Berthier, W Gorecki, M Minier, A B Armand, J M Chabagno, P Rigaud
Solid State Ion., 11, 91, 1983.

51 J R Stevens and B E Mellander
Solid State Ion., 21, 1986.

52 E Linden and J R Owen
Solid State Ion., 28, 994, 1988.

53 P Passiniemi, S Takkumaki, J Kankare and M Syrjämä
Solid State Ion., 28, 10091, 1988.

54 A Moryussef, M Bonat, M Fouletier and P Hicker
6th RISO Int. Symp. Metallurgy and Materials Science
RISO National Laboratory, Roskilde.

55 D P Tunstall, A S Tomlin, F M Gray, J R MacCallum and C A Vincent
J. Phys. Condens. Matter 1, 4035, 1989.

56 S. Iwatsuki, M Kubo and M Ohtake
The Chem. Soc. of Japan Chem. Lett., 519, 1992.

57 J E Weston and B C H Steele
Solid State Ion., 7, 75, 1982.

58 J R MacCallum, M J Smith and C A Vincent
Solid State Ion., 11, 307, 1984.

59 M Gauthier, D Fauteux, G Vassort, A Belanger, M Duval et al.
J. Electrochem. Soc., 132, 1333, 1985.

60 M Gauthier, D Fauteux, G Vassort, A Belanger, M Duval et al.
Power Sources, 14, 23, 1985.

61 F Bonino B\Scrosati and A Selvaggi
Solid State Ion., 18/19, 1050, 1986.

62 P R Sorensen
Solid State Ion., 9/10, 1147, 1983.

63 D Fauteux
Solid State Ion., 17, 133, 1985.

64 R Neat, M Glasse, R Linford
Solid State Ion.,18/19, 1088, 1986.

65 PSS Prasad, M Z A Munshi, B B Owens and W H Smyrl
Solid State Ion., 40/41, 959, 1990.

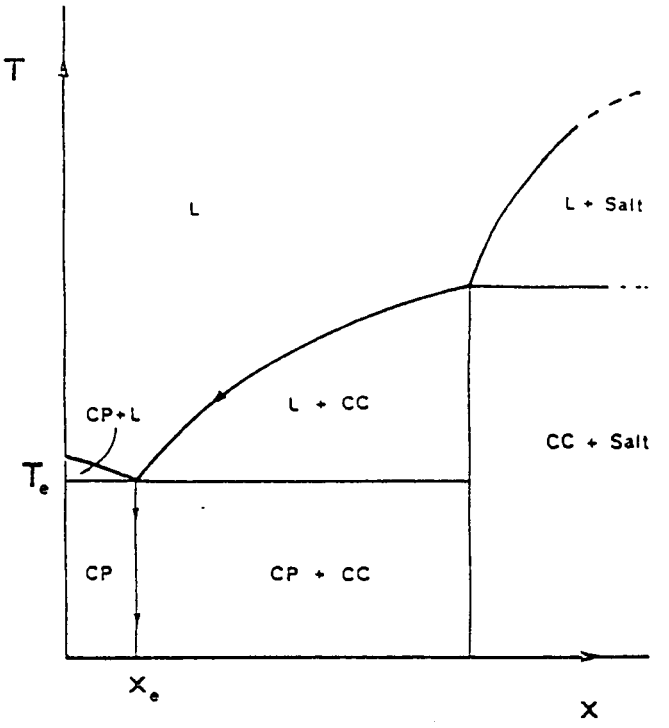

Figure 4.1 Schematic phase diagram. L:- liquid (ie amorphous phase); CC:-crystalline complex; CP: crystalline polymer; X_e: eutectic composition as mole fraction; T_e: eutectic temperature.

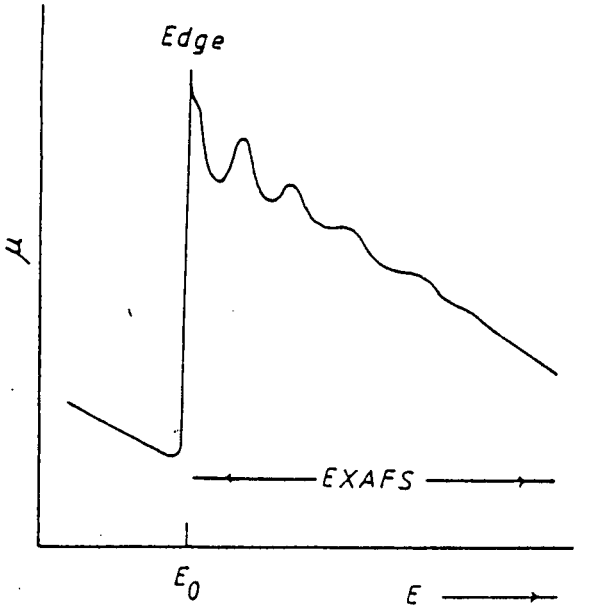

Figure 4.2 A schematic representation of an EXAFS spectrum; a plot of absorption coefficient, μ, versus x-ray energy, E.

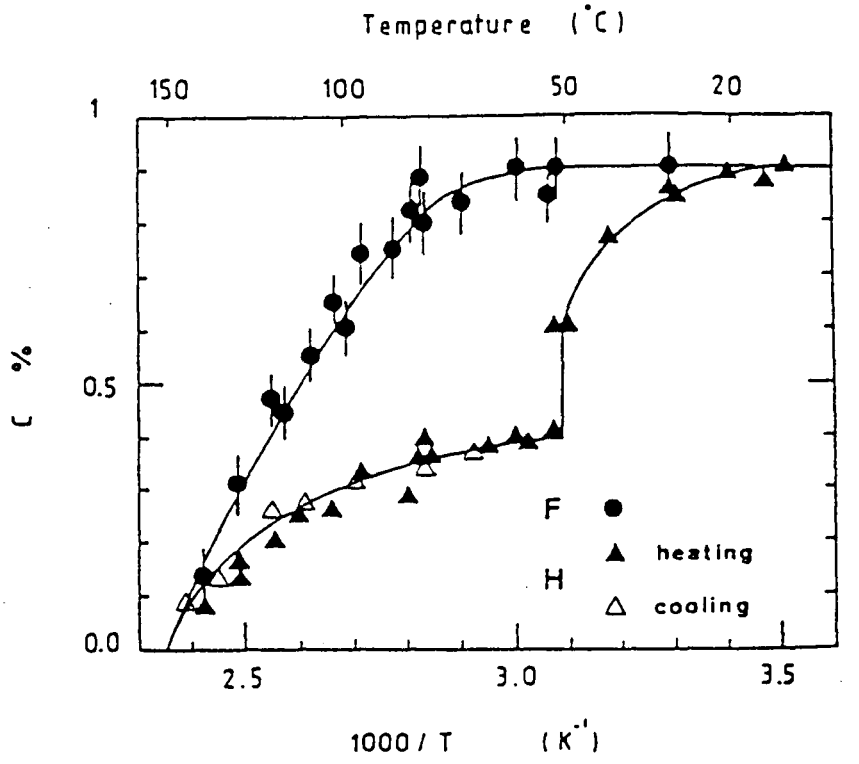

Figure 4.3 Fractions of ^{1}H and ^{19}F belonging to the crystalline phase in the 8:1 PEO/$LiCF_3SO_3$ system, determined from measurements of transverse nuclear magnetic relaxation time, T_2.

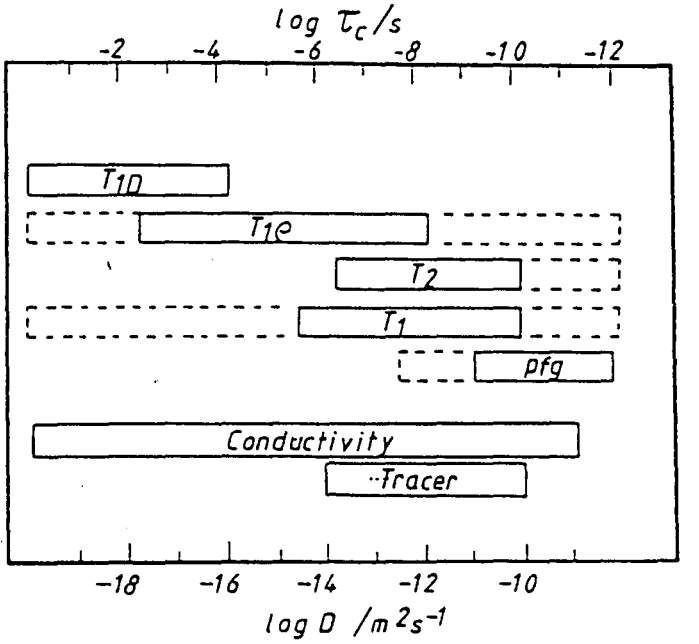

Figure 4.4 The range of diffusion coefficients that are accessible in n.m.r. experiments.

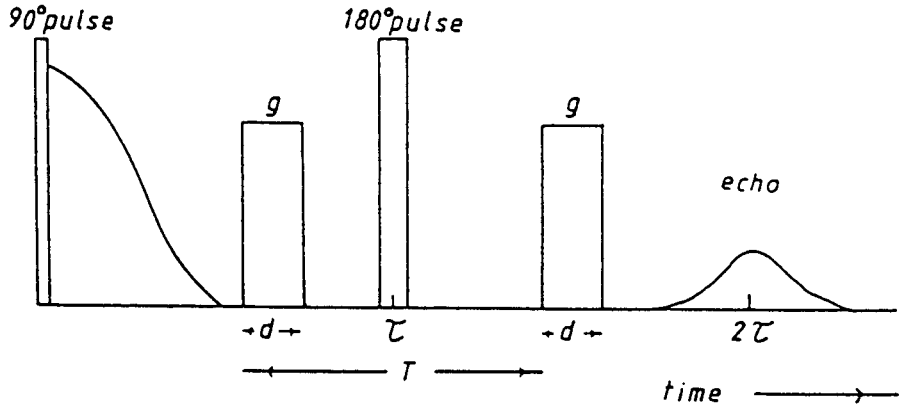

Figure 4.5 A schematic representation of the pulse sequence in a p.f.g n.m.r. experiment. The field gradient pulse is indicated by g.

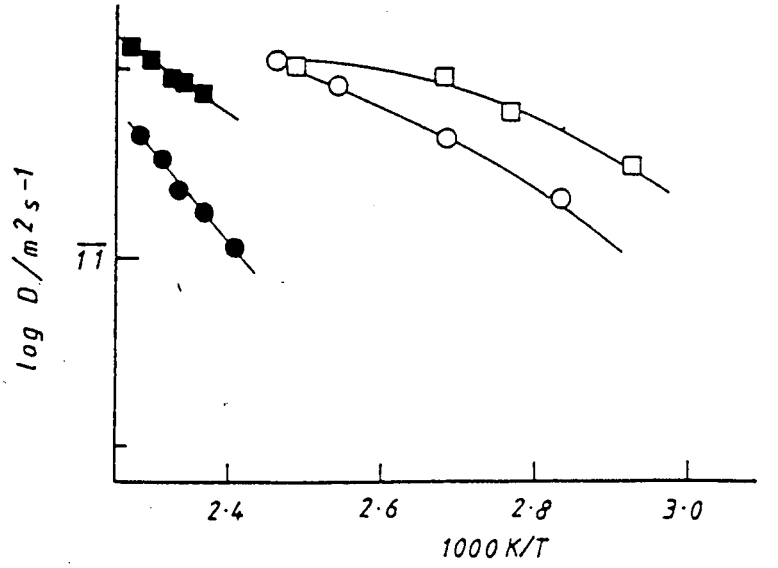

Figure 4.6 The p.f.g n.m.r. diffusion data for (●) ^{7}Li and (■) ^{19}F in the 8:1 PEO/$LiCF_3SO_3$ system, from reference 29: and for (O) ^{7}Li and (❑) ^{19}F from reference 54.

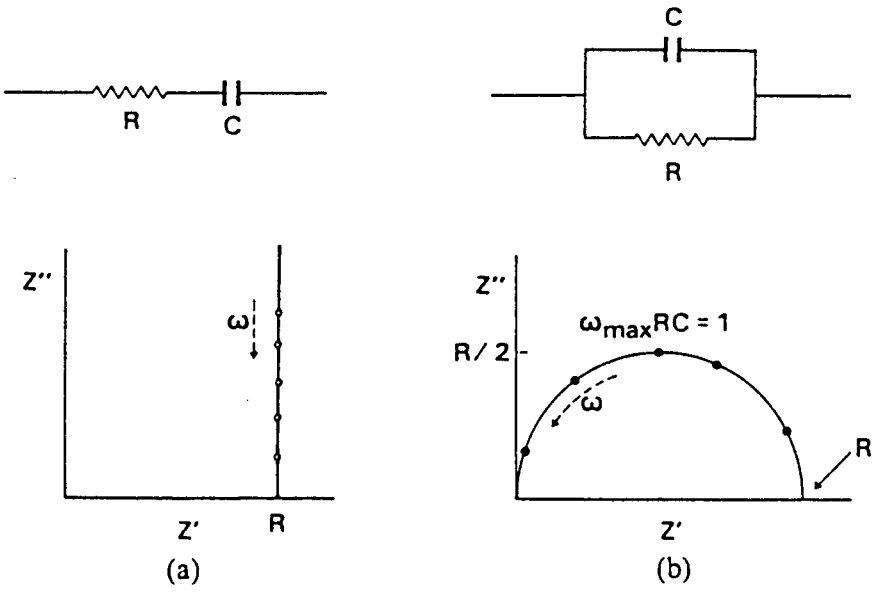

Figure 4.7 Complex impedance plots for combinations of a resistor, R, and capacitor, C, (a) in series and (b) in parallel.

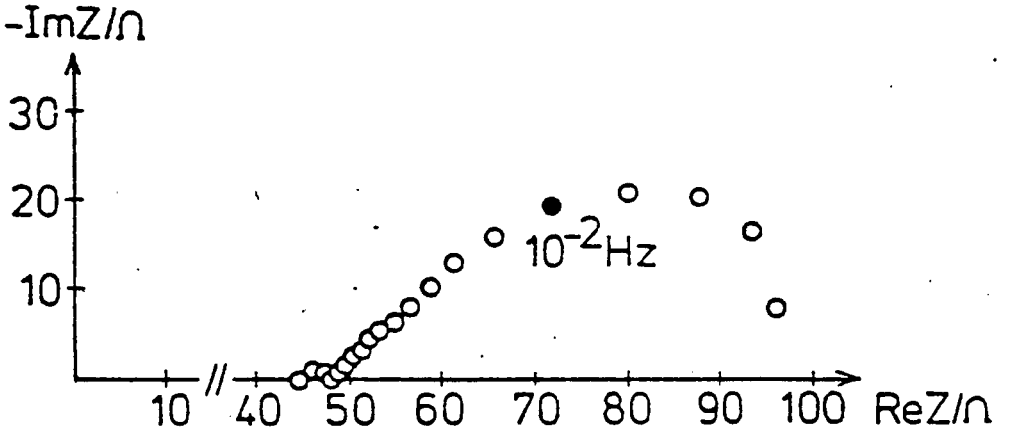

Figure 4.8 Complex impedance of a 40 μm thick 16:1 PEO/$LiCF_3SO_3$ film at 378 K. Filled circle is at 10^{-2} s^{-1}. There are five frequencies per decade.

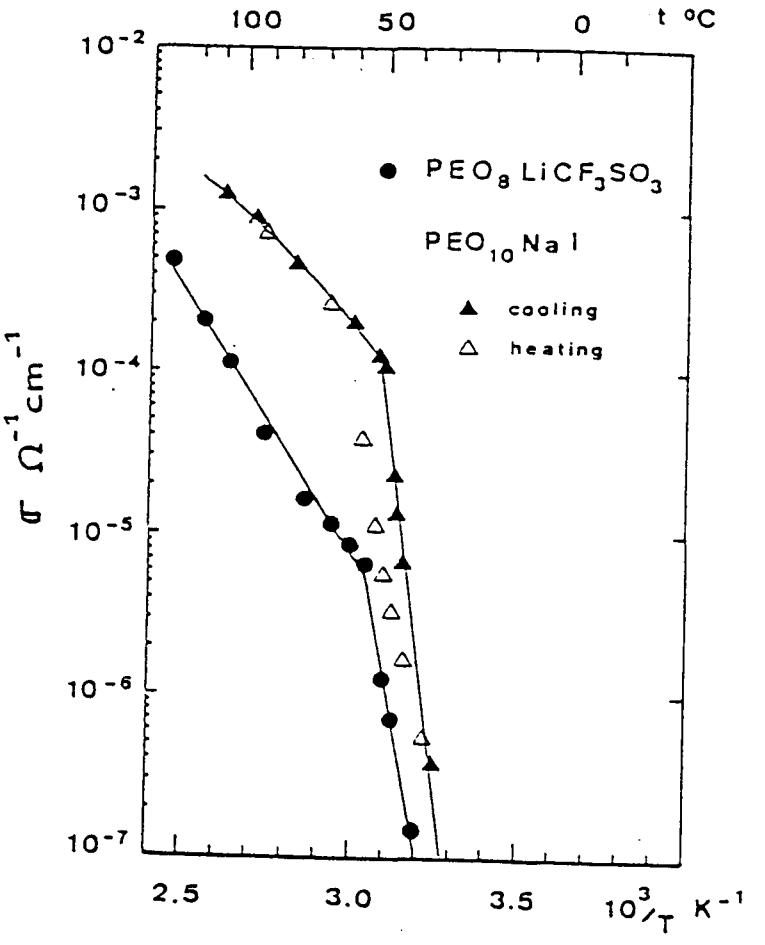

Figure 4.9 Log σ versus 1000/T for the 8:1 PEO/$LiCF_3SO_3$ system, compared to the 10:1 PEO/NaI system.

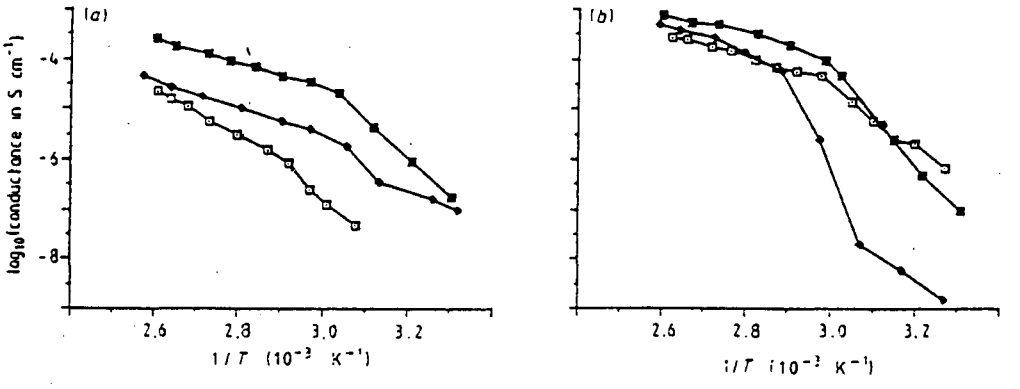

Figure 4.10 The logarithm of conductance against reciprocal temperature (a) for the 4:1 single and mixed-salt systems ■ mixed salt, ◆ NaI, ❑ $LiCF_3SO_3$, and (b) as (a) for an 8:1 system.

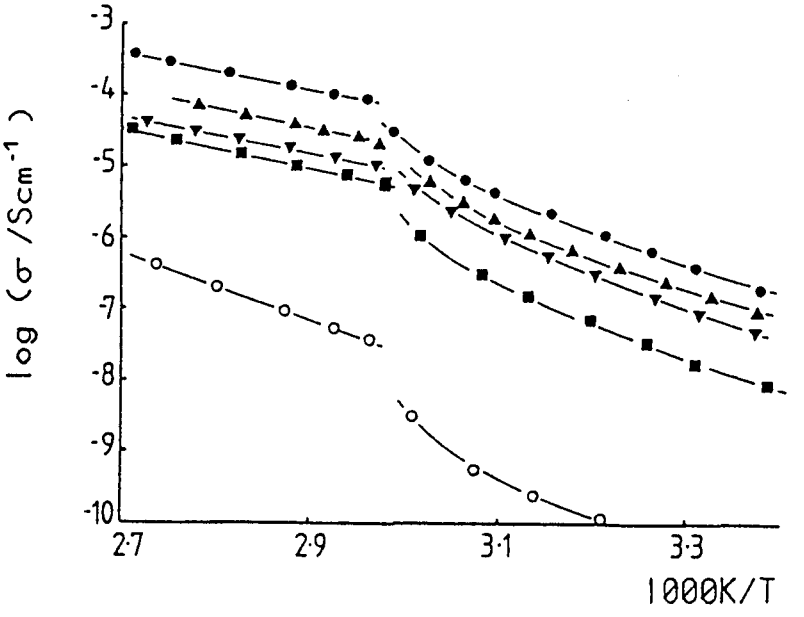

Figure 4.11 Conductivity variation with temperature for 10:1 PEO/$LiCF_3SO_3$ system films containing 0 vol% styrene (●), 20 vol% styrene (▲), 40 vol% styrene (▼), 60 vol% styrene (■) and 80 vol% styrene(O).

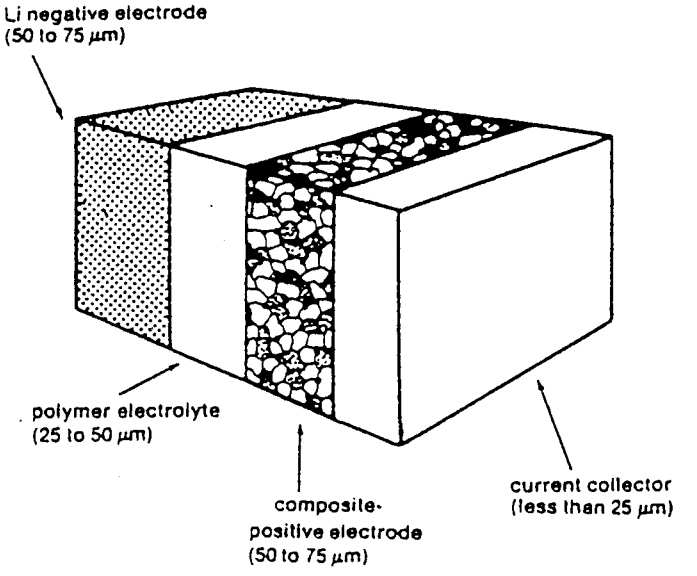

Figure 4.12 Schematic diagram of an all solid-state battery.

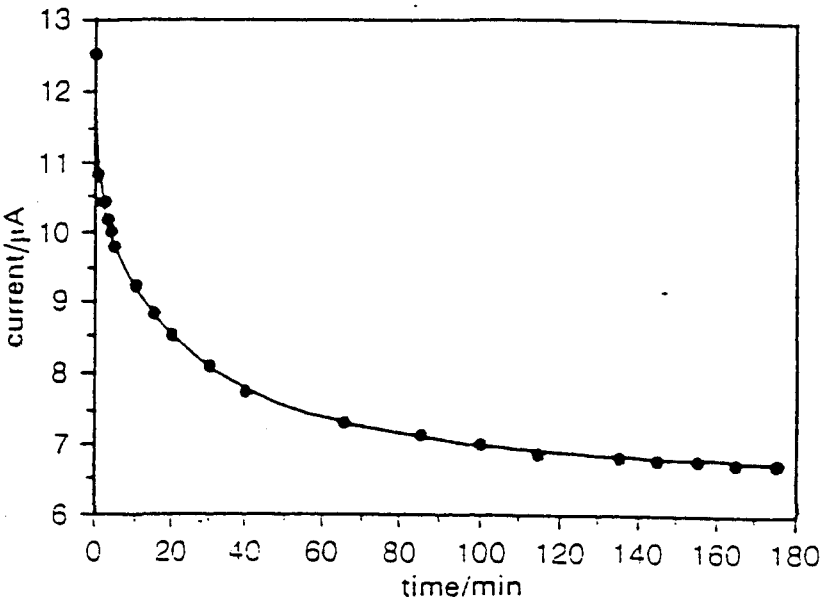

Figure 4.13 Variation of current with time from a value of I_0 = 12.5 μA at t = 0 to a steady state value of I_s = 6.75 μA for a symmetric cell Li(s) | PEO/$LiCF_3SO_3$ | Li(s) polarised by 10 mV at 381 K.

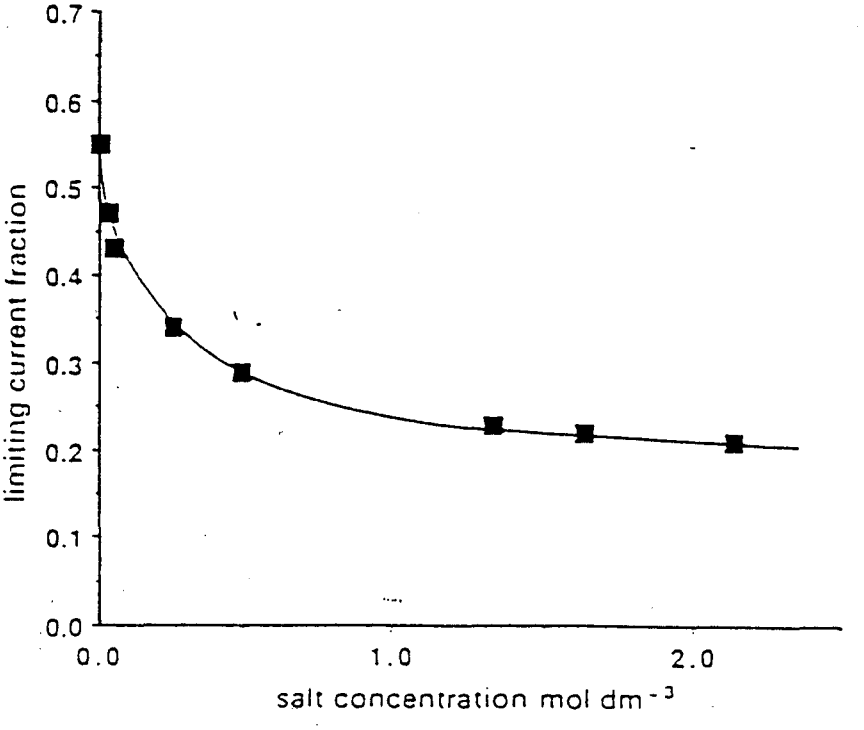

Figure 4.14 Limiting current fraction as a function of salt concentration for $LiCF_3SO_3$ in PEO at 393 K.

CHAPTER 5

^{19}F NUCLEAR MAGNETIC SPIN-LATTICE RELAXATION STUDIES IN POLYCRYSTALLINE $LiCF_3SO_3$

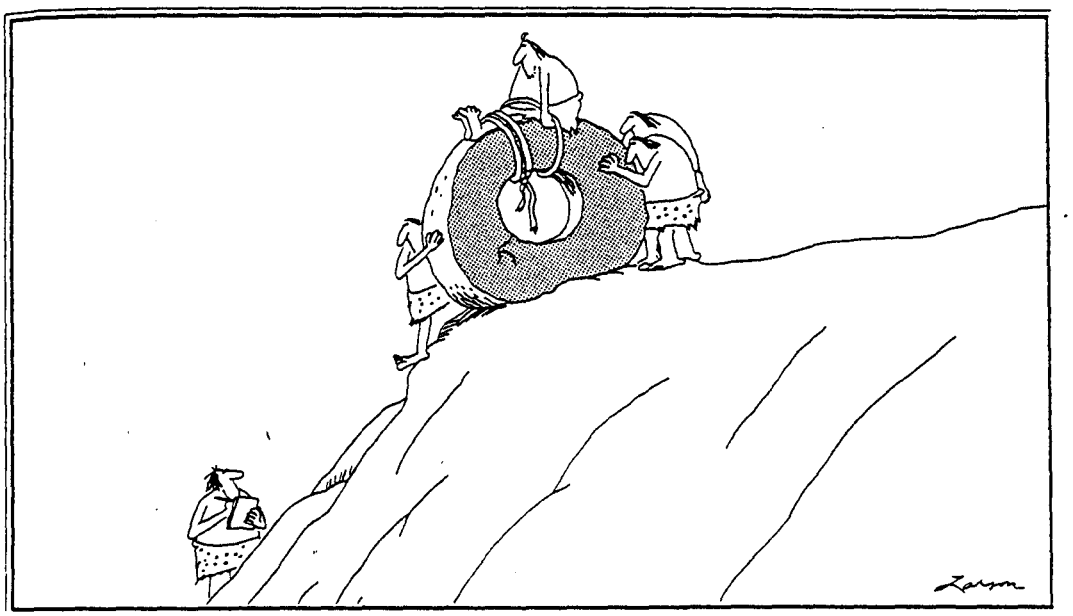

Early experiments in transportation

CONTENTS

5.1 Introduction

The study of molecular structure and dynamics in solids has always attracted interest, both from a fundamental perspective, and because of the need to understand macroscopic properties in terms of microscopic behaviour. Since the advent of the technique, n.m.r. spectroscopy has made important contributions to this general area of research. In particular, much effort has been devoted to predicting the functional form of nuclear magnetization recovery and nuclear spin relaxation behaviour for spin-bearing nuclei in molecular units undergoing thermally activated hindered reorientations[1-4]. This type of motion is characteristic of many solids and, for example, involves groups such as CH_3, NH_3,NH_4^+ and BF_4^-. The former offers an apparently simple system and has been widely studied. Although this chapter is primarily concerned with the behaviour of the trifluoromethyl group, CF_3, in polycrystalline $LiCF_3SO_3$, it is worthwhile briefly reviewing the results that have been obtained from ^1H spin-lattice relaxation investigations of the CH_3 group in solids.

A number of ^1H spin-lattice relaxation studies have been made in order to investigate the dynamics of the reorientation of the CH_3 group[5-15]. A considerable amount of work has been undertaken at temperatures where distinct minima in spin-lattice relaxation time versus temperature plots have been associated with quantum mechanical tunnelling behaviour[12,16-26]. The temperature below which quantum mechanical tunnelling becomes important in the ^1H spin-lattice relaxation behaviour of the reorientating CH_3 group is dependent on the height of the potential barrier separating the three potential wells that correspond to the equilibrium orientation. If the barrier to rotation is assumed to be time-independent then the potential function can be substituted into the Schrödinger equation, which can be solved to obtain the energy eigenvalues[16]. Eigenvalues less than the height of the barrier correspond to torsional oscillations of the CH_3 group and quantum mechanical tunnelling

between the three wells of the potential barrier is possible. This tunnelling through the barrier becomes simple rotation for those levels with eigenvalues greater than the barrier height. It is possible to calculate the 'tunnelling frequency', ν_t, as a function of temperature for different values of potential barrier, where, ν_t, is the frequency of reorientation. A plot of the logarithm of ν_t versus inverse temperature, taken from reference 15, is shown in Figure 5.1. These curves can be compared with the classical theory for activated processes, which predicts such a plot would be linear, with a slope indicating the activation energy and the intercept providing the infinite temperature limit of ν_t. For higher temperatures in Figure 5.1, the plots are consistent with the classical theory. However, at lower temperatures quantum mechanical behaviour dominates. The plots curve and, at very low temperatures ν_t decreases asymptotically toward the limit provided by the inherent tunnelling frequency of the ground torsional state.

Generally, spin-lattice relaxation time minima above ~125 K, have been associated with a classical hindered reorientation of the CH_3 group about its C_3 axis. The main feature of a hindered rotation is that the reorientating molecular group is considered to rotate discontinuously from one orientation to another, where the allowed orientations form a discrete set [27]. Given the assumption that probabilities of nuclear spin transitions depend only on the rotation of the isolated methyl group, a theoretical description of spin-lattice relaxation can be developed based on an invariant, continuous time walk on a finite group. According to BPP theory[28] spin-lattice relaxation can be described in terms of the reorientation of internuclear magnetic dipole-dipole vectors. This problem is complicated when the reorientational motion is hindered. A random time walk over possible orientations is now responsible for the modulation of the dipole-dipole interactions. In essence, an extra axis system is required to describe the nature of the hindered rotations. Isotropic motion would average out the need to consider this system. For a system of threefold symmetry undergoing hindered

molecular reorientation, the angle between the axis of reorientation and the principal direction of the relaxation interaction is fixed and the spin-lattice relaxation time is a function of this angle[3,4]. It is interesting to note that Gutowsky and Pake[29] first established in 1950 that the width of a dipolar spectral line depends on the angle between the rotation axis and the principal direction of the dipolar interaction. This phenomenon is analogous to that exploited in the reduction of spectral broadening by macroscopic reorientation of the sample at the so-called magic angle[30].

The classical high temperature 'hopping model' has been criticised in that it apparently ignores particle indistinguishability and nuclear spin symmetry. In a topological approach to methyl group rotation[31], Clough provides insight into the rotation of methyl groups in solids by comparisons with gauge theories of electromagnetism and particle physics. Sophisticated quantum mechanical approaches to methyl group rotation appear to contain certain fundamental contradictions. For instance, the torque exerted on a methyl group by the surrounding lattice requires a curved geometry, where as quantization rules impose an implicitly flat geometry. However, these quantization rules are based on quantum descriptions where spin symmetry and exclusion principles are retained at all temperatures. In actual fact symmetries are broken by a curved topology arising from the dynamical influence of the environment. The environment includes the lattice, and dipole-dipole interactions.

Measurements of ^1H spin-lattice relaxation rates for CH_3 groups in simple compounds have revealed significant deviations from predicted rates[32,33]. This has also been found to be the case for ^1H spin-lattice relaxation in NH_3 groups[34,35,36]. In general, nuclear spin-lattice relaxation is found to be less efficient than predicted by BPP models in which molecular reorientation occurs through jumps between fixed orientations. In some cases, predominantly in studies where the spin-lattice relaxation time minima occur at temperatures

between 50 K and 150 K, partial averaging of the magnetic dipolar Hamiltonian by torsional oscillations has been suggested as a cause of the anomaly[33]. This is discussed further in Section 5.6.

A review of the literature suggests that prior to the late 1960's CH_3 group ^1H spin-lattice relaxation was described by a single spin-lattice relaxation time and it was assumed that the nuclear magnetization recovery was single exponential. Subsequent studies established, however, that the ^1H spin-lattice relaxation of CH_3 group is inherently non-exponential to differing degrees, at all temperatures, even in systems containing no magnetically active nuclei other than the ^1H. The reason for this is briefly outlined below.

A common approximation is that macroscopic samples can be modelled by summing the pairwise contributions to nuclear spin-lattice relaxation[3]; that is

$$\frac{1}{T_1 SAMPLE} = \sum_{PAIRS} \frac{1}{T_1 PAIR} \qquad (5.1)$$

However, in solids, there is a local order and generally, individual pairs of spins are not isolated. This is clear for triads of nuclei at the corners of equilateral triangles, where each nucleus is involved in more than one 'relaxation pair'. It is clear that in such circumstances equation (5.1) no longer holds. Cross-correlations play an important role in such a system. It is these cross-correlations, which always act to retard spin-lattice relaxation[37], which are the source of non exponentiality in the nuclear magnetization recovery. However, it should also be remembered that, even in the absence of cross-correlations, a non-exponential decay of nuclear magnetization should in principle be observed in a polycrystalline sample. This is because the spin-lattice relaxation behaviour of each spin pair will be orientation dependent, so that the complete behaviour will be given by a sum over exponentials with different spin-lattice relaxation rates.

This will result in a non-exponential nuclear magnetization recovery[38]. It turns out that, as in the case described in this chapter, this effect is normally small.

For the work presented in this thesis it was essential to understand spin-lattice relaxation behaviour in the salt $LiCF_3SO_3$. The main ^{19}F spin-lattice relaxation mechanism is intuitively BPP, where the intramolecular ^{19}F magnetic dipole-dipole interactions are modulated by the hindered reorientation of the CF_3 group about its C_3 axis. The rotation of the $CF_3SO_3^-$ ion as a rigid unit seems unlikely; particularly as it has been shown in $CsCF_3SO_3$, [32] that considerable steric overlap of oxygen atoms would result for this rotation. No rotation of the $CF_3SO_3^-$ anion in $CsCF_3SO_3$ was found in inelastic neutron scattering studies[39]. The CF_3 group, like the CH_3 group, has been investigated by n.m.r. methods [32,38,40,41]. It is much less well endowed with rotational and torsional energy splittings than the methyl group because of its twenty six-fold increase in moment of inertia, and as a result it does not display striking quantum behaviour[6]. CF_3 groups have also been used as reporter groups on macromolecules[41]. As with CH_3 groups, and all triads of nuclei at the corners of equilateral triangles, cross-correlations play an important role in influencing the nuclear magnetization recovery.[2,37,38]

One aim of this chapter is to present experimental nuclear magnetization recoveries and explain how to define a 'cross-correlation free' spin-lattice relaxation time in systems with non-exponential nuclear magnetization recoveries. This then allows direct comparison of experimental spin-lattice relaxation times with those predicted by simple theories[3,4] in which cross-correlations are neglected and equation (5.1) is taken to hold. In this way a detailed dynamic model for the CF_3 group in polycrystalline $LiCF_3SO_3$ is derived.

5.2 The Effects of Cross-Correlation

In isolated systems of three dipolar coupled spin I = ½ nuclei fixed at the corners of an equilateral triangle, cross-correlations between relaxing spin pairs are expected to contribute significantly to the non-exponentiality of nuclear magnetization recovery. This model system has been studied in detail[2,4,37]. The results show that for single crystals non-exponentiality is predicted for all orientation angles with respect to the static magnetic field, and a sum of up to four exponentials is required to characterize the longitudinal nuclear magnetization recovery. For a polycrystalline powder numerical calculations give an average over all angles and predict significant non-exponentiality .

The random nature of the hindered motion walk over possible orientations gives autocorrelation functions for the molecular re-orientation (as described in Chapter 2), of the form $< F(t)F^*(t+\tau) >$; where F(t) is a random function of time corresponding to the orientation at time t, and F(t+τ) is the same function at time, t+τ. This inner product is for one pair of spins, assumed to be a relaxation unit, and the brackets indicate an average over all spin pairs. The specific form of the autocorrelation function is that of an exponential function with time constant τ_c, where τ_c is defined to be the correlation time. The larger the value of τ_c, the longer the correlation function takes to decay, the greater the phase memory, and the less efficient the relaxation.

Figure 5.2 shows a triad of spins a, b and c. Three internuclear vectors are introduced r_{ab}, r_{bc}, r_{ca}, and correspondingly there are three spin pairs. These individual pairs will exhibit correlated motion by virtue of their fixed arrangement with respect to one another. As well as the autocorrelation functions of the form $< F_{ab}(t)F_{ba}^*(t+\tau) >$, cross-correlations must be included of the form $<F_{ab}(t) F_{bc}^*(t+\tau) >$. In effect, the phase memory of the system is increased. Information about the orientation of the internuclear vector r_{ab} at time t is not only retained by

the autocorrelation function at $t+\tau$, but also by the cross-correlation function at $t+\tau$. The effective correlation time for the spin system has increased and the effectiveness of the reorientation of the internuclear vector in facilitating spin-lattice relaxation is reduced. The presence of cross-correlations between relaxing spin pairs retards the spin-lattice relaxation. The retardation is not in the form of a simple lengthening of spin-lattice relaxation time; the nuclear magnetization recoveries are slower decaying, non-exponential functions. In some systems the effects of cross-correlations may be masked. It has been shown that additional mechanisms of spin-lattice relaxation can counteract cross-correlation and so produce more exponential magnetization recoveries[8]. This is discussed in Section 5.3. As a general rule, systems which possess high motional symmetry and additional degrees of motional freedom are more likely to exhibit more exponential nuclear magnetization recoveries[42,43,44].

Mehring[38] suggests an interesting way of examining the origins of the non-exponential spin-lattice relaxation due to cross-correlation effects by considering the energy level diagram of a three spin $I = \frac{1}{2}$ system, shown in Figure 5.3. The energy levels consist of a quartet(A) and a doublet (E_a, E_b) where E_a and E_b are doubly degenerate. Consideration of only the intramolecular dipole interactions with the applied field parallel to the C_3 axis of the equilateral triangle of spins, together with the limitation of the dipolar Hamiltonian to its nonsecular part, that is

$$\mathcal{H}^D = \frac{\mu_0 \gamma_1 \gamma_2 \hbar^2}{4\pi r^3} [C+D+E+F]$$

restricts the possibilities of spin-lattice relaxation transitions associated with hindered reorientation about the C_3 axis to those represented by W in Figure 5.3. For the system originally in thermal equilibrium the levels will be populated according to the Boltzmann distribution. In the high temperature approximation, the population densities of the levels will be given by (Section 2.8.1)

$$\rho_0 = (mE/kT)/Tr\{1\} \tag{5.2}$$

where

$$E = \gamma\hbar B; \text{ and } Tr\{1\} = 8$$

The longitudinal magnetization established will be given by

$$M_z(0) = N\gamma\hbar\{\tfrac{3}{2}(\rho^{A}_{\frac{3}{2}} - \rho^{A}_{-\frac{3}{2}}) + \tfrac{1}{2}(\rho^{A}_{\frac{1}{2}} - \rho^{A}_{-\frac{1}{2}}) + \tfrac{1}{2}(\rho^{Ea}_{\frac{1}{2}} - \rho^{Ea}_{-\frac{1}{2}}) + \tfrac{1}{2}(\rho^{Eb}_{\frac{1}{2}} - \rho^{Eb}_{-\frac{1}{2}})\} \tag{5.3}$$

so that substitution from equation (5.2) gives

$$M_z(0) = \frac{N\gamma^2\hbar^2B}{8kT}\{\tfrac{3}{2}(8) + \tfrac{1}{2}(1) + \tfrac{1}{2}(1) + \tfrac{1}{2}(1)\}$$

which simplifies to

$$M_z(0) = \frac{6N\gamma^2\hbar^2B}{8kT} \tag{5.4}$$

If the magnetic field is now turned off, the system cannot reach an equal population of all levels, as required by the degeneracy of the levels in zero field, because the possibilities of spin-lattice relaxation are limited. In fact, a different equilibrium will be reached, with states linked by transitions denoted by the W . pathway reaching equal populations, and all other states keeping the same population densities; that is

$$(\rho^{A}_{-\frac{3}{2}}) = (\rho^{Ea}_{\frac{1}{2}}) = (\rho^{A}_{-\frac{3}{2}} + \rho^{Ea}_{\frac{1}{2}})/2$$

and

$$(\rho^{A}_{\frac{3}{2}}) = (\rho^{Eb}_{-\frac{1}{2}}) = (\rho^{A}_{\frac{3}{2}} + \rho^{Eb}_{-\frac{1}{2}})/2 \tag{5.5}$$

so that now the logitudinal nuclear magnetization established will be given by

$$M_z = N\gamma\hbar\{\tfrac{3}{4}[(\rho^{A}_{\frac{3}{2}} + \rho^{Eb}_{-\frac{1}{2}}) - (\rho^{A}_{-\frac{3}{2}} + \rho^{Ea}_{\frac{1}{2}})] + \tfrac{1}{2}(\rho^{A}_{\frac{1}{2}} - \rho^{A}_{-\frac{1}{2}}) + \tfrac{1}{4}[(\rho^{A}_{\frac{3}{2}} + \rho^{A}_{-\frac{1}{2}}) - 2\rho^{Ea}_{-\frac{1}{2}}]$$
$$+ \tfrac{1}{4}[(2\rho^{Eb}_{\frac{1}{2}} - (\rho^{A}_{\frac{3}{2}} + \rho^{Eb}_{-\frac{1}{2}})]\} \tag{5.6}$$

$$M_z = \frac{N\gamma^2\hbar^2B}{8kT}\{\tfrac{3}{4}(\tfrac{3}{2} - \tfrac{1}{2} + \tfrac{3}{2} - \tfrac{1}{2}) + \tfrac{1}{2}(1) + \tfrac{1}{4}(-\tfrac{3}{2} + \tfrac{1}{2} + 1) + \tfrac{1}{4}(1 - \tfrac{3}{2} + \tfrac{1}{2})\}$$

$$M_z = \frac{2N\gamma^2\hbar^2B}{8kT} \qquad (5.7)$$

Comparison with equation (5.4) demonstrates that even with the field off, magnetization equivalent to $M_z(0)/3$ is left in the system. This magnetization cannot relax by the intramolecular dipolar interaction alone, and the complete relaxation behaviour in this system will be non-exponential. This is an interesting example, but is restrictive in that only one orientation of the axes of moelcular reorientation to the applied field is considered. For a polycrystalline system of this nature, the form of nuclear magnetization recovery is discussed further in Section 5.3.

5.3 ^{19}F Nuclear Magnetization Recovery in Polycrystalline $LiCF_3SO_3$ and the Definition of Nuclear Spin-lattice Relaxation Time in Systems which Exhibit Non-Exponential Magnetization Recovery

Experimental

A study of ^{19}F nuclear magnetization recoveries was carried out on a polycrystalline sample of $LiCF_3SO_3$ over the temperature range 205 K to 340 K, at 24.05 MHz and 55.93 MHz. A $P_x(90)$-τ-$P_y(90)$ pulse sequence was used to produce a solid echo, with τ = 15 μs, as described in Chapter 3.

Results

The ^{19}F nuclear magnetization recoveries for polycrystalline $LiCF_3SO_3$ were found to be non-exponential to varying degrees, over the entire temperature range of the study. Figures 5.4 and 5.5 show the observed nuclear magnetization recoveries at 340 K and 215 K respectively.

In systems exhibiting straightforward exponential nuclear magnetization recoveries the definition and graphical acquisition of spin-lattice relaxation time is

reasonable straightforward. The longitudinal nuclear magnetization recovery is given by Bloch's equation (Section 2.11)

$$\frac{dM_z}{dt} = -\frac{(M_z - M_0)}{T_1}$$

where T_1 is the spin-lattice relaxation time for a system exhibiting exponential nuclear magnetization recovery. The solution to the above equation is given by

$$M_z = M_0(1-\exp(-t/T_1))$$

so that

$$\ln\left(\frac{M_0 - M_z}{M_0}\right) = -\frac{t}{T_1} \qquad (5.8)$$

Experimental values of M_0, and corresponding values of M_z at different times can be substituted into equation (5.8) to produce a linear plot of the logarithm of nuclear magnetization recovery versus time, with gradient $(-1/T_1)$. Some systems are well known to give non-exponential nuclear magnetization recoveries, which can be analysed as the sum of exponentials. This can arise where the resonant nuclei exists in more than one environment, each with a distinct spin-lattice relaxation time. At room temperature PEO contains ^1H nuclei in both amorphous and crystalline phases, and thus the ^1H nuclear magnetization recovery can be analysed as the sum of two exponential functions, with two distinct spin-lattice relaxation times. This particular system is discussed further in Chapter 8.

Non-exponential nuclear magnetization recoveries also result in polycrystalline samples due to the orientational dependence of the spin-lattice relaxation time, as described in Section 5.1. However, the ^{19}F magnetization recovery in $LiCF_3SO_3$ at 215 K is very close to being exponential, as shown in Figure 5.5, and any non-exponentiality due to this orientational dependence must therefore be negligible.

In systems where cross-correlations produce non-exponential magnetization recoveries, as discussed in Section 5.2, a graphical plot of $\ln((M_0-M_z)/M_0)$ versus time will not be linear. In such circumstances it is not straightforward to give an unequivocal definition of spin-lattice relaxation time.

The analysis of experimental magnetization recovery plots, such as those shown in Figures 5.4 and 5.5, is not straightforward. Over a restricted time range such non-exponential nuclear magnetization recoveries could appear linear. This would be especially true for measurements where the data is subject to experimental uncertainties. A number of selective experiments could produce a variety of spin-lattice relaxation times, corresponding to a variety of gradients, dependent on which section of the decay was analysed. This is demonstrated in Figure 5.6. If the magnetization recovery is assumed to be linear over all selective regions of the decay studied, a spread of spin-lattice relaxation times; 857 ms, 693 ms and 521 ms, are obtained. These values of spin-lattice relaxation time depend upon the region studied, and upon the distribution of data points within that region.

The degree of non-exponentiality due to cross-correlations varies with correlation time, and thus with temperature. This can be seen by a simple comparison of Figures 5.4 and 5.5. There would appear to be a larger spread of spin-lattice relaxation times experimentally obtainable at some temperatures than others. At temperatures around the spin-lattice relaxation time minimum and above, corresponding to $\omega\tau_c \leq 1$, the non-exponentiality is more marked. At lower temperatures, corresponding to $\omega\tau_c > 1$, there is little deviation from exponential behaviour. The effect of cross-correlation upon the form of the nuclear magnetization recovery is temperature dependent. In one region of a spin-lattice relaxation time versus temperature plot, cross-correlations may play an important role, and in another they may be negligible. If the spin-lattice relaxation time is measured non-critically, as described in Figure 5.6, then this feature could

wrongly be interpreted as non-Arrhenius behaviour. The situation is clearly unacceptable, and a clear definition of spin-lattice relaxation time in systems exhibiting non-exponential nuclear magnetization recoveries due to cross-correlation is required. The most useful spin-lattice relaxation time to obtain for such a system, would be the value which would have resulted if cross-correlations had been neglected from the spin-lattice relaxation mechanism. Such values of spin-lattice relaxation time could then be compared with simple models which neglect cross-correlations[3,4], thereby providing motional parameters.

The explicit theoretical functional form of the ^{19}F nuclear magnetization recovery in polycrystalline $LiCF_3SO_3$, can be deduced using the results of calculations performed by Hubbard and Hilt[2]. The model used in the calculation consists of an ensemble of spin systems, each system consiting of three identical spin $I = \frac{1}{2}$ nuclei, located at the vertices of an equilateral triangle. Each spin system is presumed to undergo hindered rotation about an axis perpendicular to the plane of the spins, and orientated at an angle β to the external field. It is assumed that the spin-lattice relaxation is due to magnetic dipole-dipole interactions between the nuclei within each group. The calculation is performed by use of the semiclassical form of the density operator theory of relaxation, described in Chapter 2.

If cross-correlations are neglected, Hubbard and Hilt[2] obtain

$$\langle I^0 \rangle - \langle I^0 \rangle^T = (\cos\theta - 1)\langle I_0 \rangle^T \exp(-t/T_1) \qquad (5.9)$$

where $\langle I^0 \rangle$ is the ensemble average of the expectation value of the spin operator, ($I^0 \equiv I_z$), and $\langle I^0 \rangle^T$ is the equilibrium value of this quantity. The quantity θ represents the pulse angle, and when $\theta = 90°$ equation (5.9) becomes equivalent to equation (5.8)) and T_1 is the spin-lattice relaxation time, given by

$$\frac{1}{T_1} = \frac{9}{16}\left(\frac{\mu_0}{4\pi}\right)\frac{\gamma^4\hbar^2}{r^6}\tau_c\left\{(1-\cos^4\beta)\left(\frac{1}{1+\omega_0^2\tau_c^2}\right) + (1 + 6\cos^2\beta + \cos^4\beta)\left(\frac{1}{1+4\omega_0^2\tau_c^2}\right)\right\}$$

(5.10)

If the axis of hindered rotation of the three spin systems are orientated isotropically, equation (5.10) can be averaged over all orientations so that,

$$\frac{1}{T_1} = \frac{1}{2}\int_0^{\pi} \frac{9}{16}\left(\frac{\mu_0}{4\pi}\right)\frac{\gamma^4\hbar^2}{r^6}\tau_c\left\{\left(\frac{1}{1+\omega_0^2\tau_c^2}\right)(1-\cos^4\beta)\sin\beta d\beta + \left(\frac{1}{(1+4\omega_0^2\tau_c^2)}\right)(1+6\cos^2\beta+\cos^4\beta)\sin\beta d\beta\right\} \quad (5.11)$$

which can be solved to give

$$\frac{1}{T_1} = \frac{9}{20}\left(\frac{\mu_0}{4\pi}\right)\frac{\gamma^4\hbar}{r^6}\left[\frac{\tau_c}{1+\omega_0^2\tau_c^2} + \frac{4\tau_c}{1+4\omega_0^2\tau_c^2}\right] \quad (5.12)$$

This is consistent with expressions calculated by Woessner[3] and Allen[4]. However, where cross-correlations are included, Hubbard and Hilt[2] obtain

$$\langle I^0\rangle - \langle I^0\rangle^T = (\cos\theta-1)\langle I^0\rangle^T \sum_{j=1}^{4} cj\ \exp[(9/8)T_0^{-1}p_jt] \quad (5.13)$$

where $T_0^{-1} \equiv \gamma\hbar^2\tau_c/r_0^6$. The quantities c_j and p_j are more complicated. They are related to the eigenvalues of a 4 × 4 matrix and its adjoint. The explicit calculation is detailed in reference 2, but is rather lengthy and involved. The result, in general, is the sum of four decaying exponentials. Computed values of c_j and p_j have been tabulated as a function of $\cos\beta$ and $\omega_0\tau_c$ by the authors. These are available upon application, and are not given in reference 2, although graphical results are presented for six values of $\cos\beta$ for $(\omega\tau_c)^2 << 1$. These are shown in Figure 5.7.

Of particular interest is $\cos\beta = 1$. It can be seen from Figure 5.7 that for $\beta=0$, the ensemble does not relax to its thermal equilibrium distribution via the intramolecular dipole-dipole mechanism. This is exactly the case considered by Mehring, discussed in Section 2.2.

If the axes of hindered rotation of the three spin systems are orientated isotopically, the longitudinal nuclear magnetization of the ensemble, denoted by $[\langle I^0\rangle - \langle I^0\rangle^T]_{AV}$, is the average over all orientations. This averaging process is identical to that performed on equation (5.10), so that

$$[\langle I^0\rangle - \langle I^0\rangle^T]_{AV} = \tfrac{1}{2}\int_0^{\pi} (\cos\theta - 1)\langle I^0\rangle^T \sum_{j=1}^{4} cj\ \exp[(9/8)T_0^{-1}p_j t]\sin\beta d\beta \qquad (5.14)$$

The integration of equation (5.14) must be performed by numerical methods. Hubbard and Hilt used Simpson's formula, and results are again tabulated, and available on application. Reference 2 does contain magnetization recovery plots for the average over orientation, for three values of $(\omega_0\tau_c)^2$, where cross-correlations have been included and neglected. These are shown in Figure 5.8. The theoretical calculations in Figure 5.8 show that the initial gradients of the magnetization recoveries are identical whether cross-correlations are included or neglected. This suggests that a detailed experimental study of the initial nuclear magnetization recovery would be useful, and indeed that an 'operational' spin-lattice relaxation time can be obtained from the gradient of the first 20% of non-exponential nuclear magnetization recoveries, which will be independent of cross-correlation. In this chapter these initial gradient values are denoted by $T_1(^{19}F)$ for convenience.

Although the calculation involved in evaluating equation (5.14) is rather lengthy and complicated, the theoretical nuclear magnetization recovery plots shown in Figure 5.8, can be directly compared with experimental plots of appropriate correlation time fulfilling $\omega\tau_c = 1$ and $\omega\tau_c = \sqrt{10}$. Results described in the discussion of Section 5.4, allow a calculation which gives, for 24.05 MHz, $\omega\tau_c \sim 1$ corresponds to 242 K, and $\omega\tau_c = \sqrt{10}$ corresponds to 220 K. Figure 5.9 shows the appropriate experimental ^{19}F nuclear magnetization recovery for polycrystalline

$LiCF_3SO_3$, compared with the theoretical nuclear magnetization recovery calculated for $\omega\tau_c \sim 1$ using the model of Hubbard and Hilt[2]. Similarly, Figure 5.10 shows the superposition of the first 25% of the experimental and theoretical ^{19}F nuclear magnetization recoveries for $\omega\tau_c = \sqrt{10}$.

There is good agreement between experiment and theory in the initial stages of magnetization recovery. This is important, as this region is precisely where a spin-lattice relaxation time independent of the effects of cross-correlation can be measured. There are deviations at longer times, which are clearly apparent in Figure 5.9. The enhanced rate of nuclear magnetization recovery at longer times, compared to theoretical prediction, is likely to be due to other sources of ^{19}F spin-lattice relaxation, such as intermolecular ^{19}F-^{19}F and ^{19}F-^{7}Li dipolar interactions, and chemical shielding anisotropy, not included in the theoretical model used for the calculation. The presence of other spin-lattice relaxation mechanisms producing more exponential nuclear magnetization recoveries than cross-correlated behaviour suggests, has been discussed in some detail by Baud and Hubbard[8]. The authors consider the gradient of a theoretical nuclear magnetization recovery plot of the type shown in Figure 5.8, which is negative and decreases in magnitude as time increases. Another spin-lattice relaxation mechanism which by itself would produce an exponential nuclear magnetization recovery, would contribute a term $(-1/T_1')$ to the gradient of the complete nuclear magnetization recovery, where T_1' is the time constant of the added mechanism. This $(-1/T_1')$ would have more effect for larger times, as the gradient of the theoretical cross-correlated nuclear magnetization recovery decreases. The authors also observed this effect experimentally in the ^{1}H nuclear magnetization recovery of the CH_3 group in solid CH_3CN.

5.4 A ^{19}F Spin-lattice Relaxation Study in Polycrystalline $LiCF_3SO_3$

Experimental

A ^{19}F nuclear spin-lattice relaxation study was carried out on a polycrystalline sample of $LiCF_3SO_3$ over the temperature range 205 K to 340 K, at 24.05 MHz and 55.93 MHz. A $P_x(90)$-t-$P_x(90)$-τ-$P_y(90)$ pulse sequence, with τ = 15 μs, was used as described in Chapter 3. $T_1(^{19}F)$ values were determined as a function of temperature by monitoring in detail the first 20% of nuclear magnetization recovery plots, as discussed in Section 5.3. Typically, in a given experiment, the order of 8-10 different delays were used in this region and signal averaging was employed to improve the signal-to-noise ratio. A linear least squares fitting procedure was used to calculate the gradient of a straight line through the logarithm of the initial data points. As a check on each measurement of $T_1(^{19}F)$, the value of the intercept of this line at zero time delay, returned by the procedure, was required to be within a few percent of the equilibrium nuclear magnetization value, M_0. M_0 was measured separately by monitoring the echo amplitude after the sample had been in the applied field for at least five minutes. In principle, the measurement of the initial gradient of a nuclear magnetization recovery plot is straightforward, but in practice it has to be recognised that very little magnetization will have recovered at short delay times so that the accurate measurement of small signal amplitudes is required.

It should be noted that it is important to keep within spectrometer detectability limits. M_z values of less than ~5% M_0 are unlikely to give reliable data points on a plot of nuclear magnetization recovery. For values of M_z measured at very short time delays, the signal is very small, and so is difficult to measure precisely. Even if M_0–M_z can be measured to within 1% of M_0, for values less than about 5%, the corresponding data point on the logarithmic scale of the nuclear

magnetization recovery plot can be misleading. For example, consider M_z values of 5% M_0 and 4% M_0. These give values presented in Table 5.1.

Table 5.1 Important parameters in the calculation of spin-lattice relaxation time for two small values of M_z, assuming normalized data.

M_z	M_0-M_z	$\ln(M_0-M_z)$
4% M_0	0.96	–0.0408
5% M_0	0.95	–0.0513

Table 5.1 shows that even though the values of (M_0-M_z) differ by about 1%, the values of $\ln(M_0-M_z)$ differ by about 20%.

For values of M_z measured at long time delays there will be a very small change in the amplitude of M_z for substantial changes in time. Table 5.2 shows M_z as a percentage of M_0, with corresponding times for a system exhibiting an exponential nuclear magnetization recovery.

Table 5.2 The nuclear magnetization recovery for a system obeying equation (5.8)

Time	M_z/M_0
3.0 T_1	95%
3.2 T_1	96%
3.5 T_1	97%
3.9 T_1	98%
4.6 T_1	99%

Even if the signal amplitudes can be measured to within 1% of M_0, at M_z values of the order of 95% M_0, separate measurements made at time intervals less than 0.2 T_1 apart could easily produce the same experimental value. For values of M_z of about 98% M_0, separate measurements made at time intervals less than 0.7 T_1 apart again may not be distinguishable. Obviously, two values of the same $\ln(M_0-M_z)$ for different delay times, is not consistent with an exponential plot and such data points would be misleading.

Results

Figure 5.11 shows the temperature dependence of the ^{19}F spin-latice relaxation behaviour in polycrystalline $LiCF_3SO_3$, measured at 24.05 MHz and 55.93 MHz, plotted in the form of a graph of $\ln(T_1(^{19}F))$ versus inverse temperature. A single spin-lattice relaxation time minimum was observed at both frequencies, as shown in Table 5.3. The solid lines were calculated as described in the discussion.

Table 5.3 ^{19}F Spin-lattice relaxation time minima for polycrystalline $LiCF_3SO_3$

Frequency/MHz	$T_{1\ MIN}$/ms	T_{MIN}/K
24.05	53	250
55.93	122	272

Discussion

The values of $T_1(^{19}F)$ that have been measured are independent of the effects of cross-correlation. The theoretical spin-lattice relaxation behaviour of ^{19}F in $LiCF_3SO_3$ can be calculated in a straightforward manner with the omission of the effects of cross-correlation. In a simple model spin-lattice relaxation can be attributed to intramolecular ^{19}F-^{19}F magnetic dipolar interactions modulated by hindered reorientational motion of the CF_3 groups around their three fold axes. Woessner[3] and Allen[4] have described the dipolar relaxation of a two-spin system undergoing anisotropic reorientation where

$$\frac{1}{T_1} = \frac{3}{10}\left(\frac{\mu_0}{4\pi}\right)\frac{\gamma^2\hbar^2}{r^6}\, I(I+1)\, f(\varepsilon)\{J(\omega_0) + 4J(2\omega_0)\} \qquad (5.15)$$

and

$$f(\varepsilon) = 4\cos^2\varepsilon\sin^2\varepsilon + \sin^4\varepsilon$$

with

$$J(\omega_0) = \tau_c/(1+(\omega_0\tau_c)^2)$$

The correlation time, τ_c, is assumed to have an Arrhenius dependence on temperature; that is

$$\tau_c = \tau_0 \exp(E_A/RT) \tag{5.16}$$

The angle ε is the angle between the axis of reorientation and the principal direction of the spin-lattice relaxation interaction; all other quantities have their usual meaning. For the CF_3 group, the angle between the principal direction of the dipole interaction and the C_3 axis, ε, is 90°, as shown in Figure 5.12, so that equation (5.15) becomes

$$\frac{1}{T_1(^{19}F)} = \frac{9}{40}\left(\frac{\mu_0}{4\pi}\right)\frac{\gamma_F^4\hbar^2}{r_{FF}^6}\{J(\omega_0) + 4J(2\omega_0)\} \tag{5.17}$$

In the CF_3 group each ^{19}F is being relaxed by two others. Neglecting cross-correlations and assuming equation (5.1) holds, the above expression must be multiplied by two, giving

$$\frac{1}{T_1(^{19}F)} = \frac{9}{20}\left(\frac{\mu_0}{4\pi}\right)\frac{\gamma_F^4\hbar^2}{r_{FF}^6}\left[\frac{\tau_c}{1+(\omega_0\tau_c)^2} + \frac{4\tau_c}{1+(2\omega_0\tau_c)^2}\right] \tag{5.18}$$

Taking the purely intramolecular ^{19}F-^{19}F dipolar interactions, only the internuclear distance r_{FF} in the CF_3 group is required to calculate the ^{19}F spin-lattice relaxation behaviour. At the time of this study there was no crystallographic data available for $LiCF_3SO_3$. Subsequently, at the end of 1992, a crystal structure was proposed using powder x-ray diffraction data and ab-initio methods[45]. It should be noted that this structure predicts a significant intermolecular contribution to ^{19}F spin-lattice relaxation, and this is discussed again in due course. However, the geometry of the $CF_3SO_3^-$ ion has been investigated previously by x-ray diffraction techniques in hydrogen bond studies of trifluoromethanesulphonic acid hydrates[46,47,48]. The CF_3 group was found to be very nearly tetrahedral. The structure of the ion was found to be nearly identical in different hydrates, and at different temperatures; 83, 85, 225 and

298 K. The average C-F bond length was 0.1318 nm with the average S-C-F angle 110.1°. Values of C-F bond lengths and F-C-F angles for the CF_3 groups in a number of molecules have also been determined from rigid lattice ^{19}F n.m.r. line shapes by Garg, Ripmeester and Davidson[49], and have been compared with gas-phase data obtained from electron diffraction[50,51] and microwave[52,53] studies. The C-F bond length in every case was 0.133 ± 0.001 nm, with F-C-F angles about 1° less than tetrahedral. There appears to be strong evidence that the geometry of the CF_3 group is insensitive to substituents in these molecules. The application of simple trigonometry with the use of average values of bond length and angles gives an average ^{19}F-^{19}F distance, r_{FF}, in the CF_3 group of 0.2144 nm and this value was used in equation (5.18) to simulate spin-lattice relaxation behaviour over a wide range of correlation times between 10^{-6} s and 10^{-11} s.

This simulation can be converted to a function of temperature rather than correlation time in the following manner. For $\omega\tau_c \gg 1$, corresponding to the high temperature limit equation, equation (5.18) reduces to

$$\frac{1}{T_1(^{19}F)} = 5K\tau_c \qquad (5.19)$$

where

$$K = \frac{9}{20}\left(\frac{\mu_0}{4\pi}\right)\frac{\gamma_F^2\hbar^2}{r_{FF}^6}$$

Substitution of equation (5.16) gives

$$T_1(^{19}F) = 1/(5K\tau_0\exp[E_A/RT])$$

so that

$$\ln(T_1(^{19}F)) = \ln(1/(5K\tau_0)) - (E_A/RT) \qquad (5.20)$$

Similarly for $\omega\tau_c \gg 1$, corresponding to the low temperature limit, equation (5.18) reduces to

$$\frac{1}{T_1(^{19}F)} = \frac{2K}{\omega_0^2\tau_c} \qquad (5.21)$$

and the substitution of equation (5.16) gives

$$T_1(^{19}F) = (1/2K)\ \omega_0^2\tau_0 \exp[E_A/RT]$$

so that

$$\ln(T_1(^{19}F)) = \ln(\omega_0^2\tau_0/(2K)) + (E_A/RT) \qquad (5.22)$$

It is clear from equations (5.20) and (5.22) that a plot of $\ln(T_1(^{19}F))$ versus reciprocal temperature will exhibit a linear nature on either side of the spin-lattice relaxation time minimum. The gradients of these linear sections are given by (E_A/R) and $-(E_A/R)$ for the low and high temperature sides respectively.

The value of the correlation time for which the spin-lattice relaxation time is a minimum is dependent on the external field and can be obtained from equation (5.18) for a particular value of that field. The corresponding value of temperature at which the spin-lattice relaxation time minimum occurs is obtained from experiment. The substitution of E_A, $\tau_{c\ MIN}$ and T_{MIN} into equation (5.16) allows the extraction of the motional parameter, τ_0, for the reorientating CF_3 group.

The solid lines in Figure 5.11 were calculated using equation (5.18) with r = 0.2144 nm and assuming an Arrhenius dependence of the correlation time, as described by equation (5.16). The activation energy was determined from the gradient returned by a linear least squares fit to the experimental data points taken at both frequencies, in the high temperature region. In this region the spin-lattice relaxation time is independent of frequency, as suggested by equation (5.19). In the low temperature region the spin-lattice relaxation time is proportional to ω_0^2, as suggested by equation (5.21). Low temperature data is more likely to be influenced by geometrical changes in the structure of the lattice and activation energies obtained from low temperature data are more likely to be unreliable.

Motional parameters extracted for the rotation of the CF_3 group are given in Tables 5.4 and 5.5.

Table 5.4 Activation energies obtained for CF_3 group reorientation in polycrystalline $LiCF_3SO_3$

Frequency/MHz	E_A/kJ mol^{-1} (High T)	E_A/kJ mol^{-1} (Low T)	E_A/kJ mol^{-1} (Av)
55.93	23.01 ± 0.64	23.93 ± 0.28	23.47 ± 0.92
24.05	25.46 ± 0.55	27.01 ± 1.46	26.24 ± 3.56
Both Data Sets	24.40 ± 0.69		

The similarity of the high and low temperature data activation energies, at each frequency, is good, as required by the symmetrical properties of equation (5.17) about its minimum.

Table 5.5 Pre-exponential factors obtained for CF_3 group reorientation in polycrystalline $LiCF_3SO_3$

Frequency/MHz	T_{MIN}/K	$\tau_{c\ MIN}$/s	τ_0/s
55.93	272	17.5×10^{-10}	3.59×10^{-14}
24.05	250	41.0×10^{-10}	3.25×10^{-14}
Average			3.42×10^{-14}

An explicit Arrhenius relationship containing motional parameters for the reorientating CF_3 group in polycrystalline $LiCF_3SO_3$ is given by

$$\tau_c = (3.42 \pm 0.17) \times 10^{-14}\ \text{s}\ \exp\{(24.40 \pm 0.69)\ \text{kJ mol}^{-1}/RT\} \qquad (5.23)$$

A good fit to the experimental data was obtained, particularly in the region of the spin-lattice relaxation time minima. The small but consistent difference, for both frequencies, between the experimental and theoretical $T_1(^{19}F)$ values exhibited at low temperatures may be due to an increase in the activation energy barrier for the rotation of the CF_3 group due to contraction of the lattice. No crystallographic studies have been carried out as a function of temperature, but studies conducted on $CsCF_3SO_3$[32] have reported a temperature dependent activation energy.

The theoretical fit to the results in Figure 5.11 confirms that the observed relaxation is predominantly due to an intramolecular magnetic dipolar spin-lattice relaxation mechanism. However, the proposed crystal structure of $LiCF_3SO_3$, as mentioned previously, predicts a significant intermolecular contribution to ^{19}F spin-lattice relaxation behaviour. This structure is shown in Figure 5.13. This study was the first reported determination of a previously unknown structure by the maximum entropy and likelihood method from powder diffraction data; a technique which has not, as yet, been tested extensively. The CF_3 group described in the $LiCF_3SO_3$ crystal structure is asymmetric and strictly speaking there is no C_3 axis: although it has to be recognized that the x-ray structure gives the time averaged positions for the ^{19}F atoms in the CF_3 group. This asymmetry is discussed further in Chapter 7. The reported r_{FF} distances in the CF_3 group are given in Table 5.6.

Table 5.6 Internuclear ^{19}F-^{19}F distances in the reported $LiCF_3SO_3$ structure[45]

Internuclear vectors	Distance/nm
$r_{FF}(1)$	0.2169
$r_{FF}(2)$	0.2165
$r_{FF}(3)$	0.2050
$r_{FF}(AV)$	0.2128

The average r_{FF} distance given by the crystal structure makes a negligible difference to the predicted intramolecular ^{19}F spin-lattice relaxation behaviour; that is $(r_{FF}\ (LiCF_3SO_3\ (structure))^6/(r_{FF}(CF_3SO_3^-\ ion\ studies))^6 \sim 96\%$.

The structure can also be used to evaluate intermolecular ^{19}F-^{19}F second moments. The rigid lattice values can be calculated using

$$(M_2^{FF})_{RL} = \frac{9}{20}\left(\frac{\mu_0}{4\pi}\right)^2 \gamma_F^4 \hbar^2 \sum_j \frac{1}{r_{jk}^6} \qquad (5.24)$$

where the lattice sum is evaluated for all intermolecular spins within a sphere of defined radius about the reference spin. Figure 5.14 shows the calculated

intermolecular ^{19}F-^{19}F rigid lattice second moments for radii of 0.7 nm to 1.5 nm. There is a 1% difference in values obtained using a radius of 1.0 nm and 1.5 nm, and calculated values approach the value obtained for a radius of 1.5 nm asymptotically. Figure 5.15 shows the ^{19}F intermolecular rigid lattice dipolar second moment calculated for all relevant spins within a sphere of radius 1.5 nm for the three crystollographically unique reference spins. The average value is 1.30×10^9 rad^2 s^{-2}. To evaluate the contribution of these intermolecular interactions to ^{19}F spin-lattice relaxation the reduced second moments can be calculated; that is the ^{19}F spin-lattice relaxation mechanism can be described in terms of the equation

$$\frac{1}{T_1} = \tfrac{2}{3}\Delta M_2^{FF}\left(\frac{\tau_c}{1+\omega_0^2\tau^2} + \frac{4\tau_c}{1+(2\omega_0\tau_c)^2}\right) \qquad (5.25)$$

where

$$\Delta M_2^{FF} = (M_2^{FF})_{RL} - (M_2^{FF})_{MO} \qquad (5.26)$$

in which RL denotes rigid lattice and MO denotes motionally averaged. This approach is discussed in detail in Chapter 6. Chapter 7 discusses the explicit calculation of the motionally averaged second moments, and also an approximation in which the value is obtained from the rigid lattice second moments between a reference spin and three ^{19}F nuclei placed at the centre of masses of the relevant CF_3 groups. Figure 5.16 shows the motionally averaged intermolecular ^{19}F second moments calculated using this approximation for all spins within a sphere of defined radius. As before the calculated values approach the value obtained for a radius of 1.5 nm asymptotically. This gives a ^{19}F-^{19}F intermolecular reduced second moment of 6.48×10^8 rad^2 s^{-1}, which can be seen by substitution in equation (5.25) and comparison with equation (5.18), to represent approximately 17% of the intramolecular ^{19}F-^{19}F contribution. This is a significant contribution but one for which there is no evidence in the spin-lattice

relaxation behaviour. A single crystal X-ray or neutron diffraction investigation of $LiCF_3SO_3$ would be useful in resolving this problem.

5.5 A Dynamic Model for ^{19}F Spin-lattice Relaxation Behaviour in Polycrystalline $LiCF_3SO_3$

It has been shown in Section 5.4 that despite the significant ^{19}F-^{19}F intermolecular magnetic dipolar contribution predicted from the proposed crystal structure of $LiCF_3SO_3$, a simple model for ^{19}F spin-lattice relaxation behaviour, in which intramolecular ^{19}F-^{19}F magnetic dipolar interactions dominate, and the CF_3 group undergoes thermally activated hindered rotations about its C_3 axis, provides a good fit to the spin-lattice relaxation results. Other ^{19}F spin-lattice relaxation mechanisms do exist and warrant investigation.

Heteronuclear ^{19}F-^{7}Li magnetic dipole interactions will also be modulated and so contribute to the ^{19}F spin-lattice relaxation. In general, this is a more complicated problem than the intermolecular ^{19}F-^{19}F contribution, as it is a heteronuclear system (considered in detail in Chapter 6). However, the dominant factor in determining if this process contributes significantly to ^{19}F spin-lattice relaxation is still the ratio of interaction strength compared with the ^{19}F-^{19}F intramolecular magnetic dipolar interaction. For one pair of spins this can be given approximately by $(\gamma_F^4/(r_{FF\ INTRA})^6):(\gamma_F^2\gamma_{Li}^2/(r_{F\ Li})^6)$. The crystal structure of $LiCF_3SO_3$, shown in Figure 5.13 gives two nearest ^{7}Li spins, at a distance $r_{F\ Li} \sim 0.4$ nm. This gives the relative interaction strengths as 0.5%, indicating that the contribution of ^{19}F-^{7}Li magnetic dipolar interactions to the ^{19}F spin-lattice relaxation behaviour in polycrystalline $LiCF_3SO_3$ can be neglected.

Chemical shielding anisotropy can also provide a spin-lattice relaxation pathway for ^{19}F in a CF_3 group undergoing hindered reorientation. The particular case of CF_3 groups attached to spherical moelcules undergoing rotational diffusion has been analysed by Matson[41]. The chemical shielding spin-lattice relaxation

mechanism for a system of threefold symmetry undergoing hindered molecular reorientation has been described in general terms by Allen[4].

In Chapter 2, the chemical shielding Hamiltonian was described using a second rank cartesian coupling tensor given by

$$\begin{pmatrix} \sigma_{xx} & \sigma_{xx} & \sigma_{xz} \\ \sigma_{yx} & \sigma_{yy} & \sigma_{yz} \\ \sigma_{zx} & \sigma_{zy} & \sigma_{zz} \end{pmatrix}_{LAB} \longrightarrow \begin{pmatrix} \sigma_{11} & 0 & 0 \\ 0 & \sigma_{22} & 0 \\ 0 & 0 & \sigma_{33} \end{pmatrix}_{PAS} = \bar{\sigma} \begin{pmatrix} 1 & 0 & 0 \\ 0 & 1 & 0 \\ 0 & 0 & 1 \end{pmatrix}$$

$$+\delta \begin{pmatrix} -\frac{1}{2}(1+\eta) & 0 & 0 \\ 0 & -\frac{1}{2}(1-\eta) & 0 \\ 0 & 0 & 1 \end{pmatrix} \qquad (5.27)$$

where
$\bar{\sigma} = \frac{1}{3}(\sigma_{xx} + \sigma_{yy} + \sigma_{zz}) = \frac{1}{3}(\sigma_{11} + \sigma_{22} + \sigma_{33})$,

and where the definitions $|\rho_{zz}| \geq |\rho_{xx}| \geq |\rho_{yy}|$, $\rho_{zz} = \delta$, and $\eta = (\rho_{yy} - \rho_{xx})/\rho_{zz}$, ensure that $0 \leq \eta \leq 1$.

For the ^{19}F spin-lattice relaxation due to the chemical shielding interaction in a CF_3 group undergoing hindered molecular reorientation Allen[4] gives

$$\frac{1}{T_1} = \frac{9}{40}\gamma_F^2 B_0^2 \delta_z^2 F(\varepsilon,\zeta,\eta)\,\frac{\tau_c}{1+\omega_0^2\tau_c^2} \qquad (5.28)$$

and

$$F(\varepsilon,\zeta,\eta) = \sin^2\varepsilon(1 + \tfrac{1}{3}\eta\cos 2\zeta)\{4 - 3\sin^2\varepsilon(1 + \tfrac{1}{3}\eta\cos 2\zeta)\} + \tfrac{4}{9}\eta^2 \qquad (5.29)$$

where ε is the angle between the C_3 axis and the C-F bond, and ζ is the angle between the plane containing ε and the y axis of the principal axis frame. This is shown in Figure 5.12. However, before proceding further it is important to realise that the symmetry parameter η, and principal value δ_z featured in equations (5.28) and (5.29) are not directly equivalent to the η and δ discussed above and in Chapter 2. Allen[4] defines,

$$\begin{pmatrix} \sigma_{11} & 0 & 0 \\ 0 & \sigma_{22} & 0 \\ 0 & 0 & \sigma_{33} \end{pmatrix}_{LAB} = \bar{\sigma} \begin{pmatrix} 1 & 0 & 0 \\ 0 & 1 & 0 \\ 0 & 0 & 1 \end{pmatrix} + \delta_z \begin{pmatrix} -\frac{1}{2}(1-\eta) & 0 & 0 \\ 0 & -\frac{1}{2}(1+\eta) & 0 \\ 0 & 0 & 1 \end{pmatrix} \qquad (5.30)$$

where $\delta_z \gg \delta_x \gg \delta_y$ and $\eta = (\delta_x - \delta_y)/\delta_z$

Using these definitions, η is positive, but is not restricted to values less than 1. Encountering different conventions and notation is not uncommon in the field of nuclear magnetic resonance shielding tensors. In July, 1992, a meeting of the NATO ARW was held at the University of Maryland to propose guidelines for reporting nuclear magnetic shielding tensors, declaring that '... the terms anisotropy (Δ) and asymetry (η) now have too many definitions. The group suggests that the principal axes be labelled according to $\sigma_{11} < \sigma_{22} < \sigma_{33}$; that the skew parameter, $\kappa = 3(\sigma_{ISO} - \sigma_{22})/(\sigma_{33} - \sigma_{11})$ be used instead of the asymmetry η; and that the span, $\Omega = \sigma_{33} - \sigma_{11}$, be used instead of the anisotropy Δ.

^{19}F shielding tensors in the principal axis system for molecules containing CF_3 groups bonded to carbon, namely CF_3CN, CF_3CCl_3, CF_3COOD, CF_3CD_2OD, $CF_3COO^-Ag^+$ and $(CF_3CO)_2O$), have been measured by the analysis of solid state n.m.r. lineshapes[49]. These are given in Table 5.67. It was found that the principal axis of largest shielding, σ_{33}, lies along the C–F bond. The x axis of shielding σ_{11} is perpendicular to the C–F bond within the C–F plane (which is represented by the shaded plane in Figure 5.12), and the y axis of shielding σ_{22} is perpendicular to this plane. It can be seen from Figure 5.12 that ζ =90° and ε = 69.9°[46-49]. σ_{av} can be subtracted from σ_{11}, σ_{22} and σ_{33} values given in Table 5.7, in accordance with equations (5.30) and (5.27), to give the components of the traceless symmetric second rank tensor. These are δ_x, δ_y and δ_z in the notation of Allen[4], and ρ_{xx}, ρ_{yy} and ρ_{zz} in notation consistent with Chapter 2. Which values of $\sigma_{11}-\sigma_{av}$, $\sigma_{22}-\sigma_{av}$, and $\sigma_{33}-\sigma_{av}$ correspond to which values of δ_x, δ_y, δ_z and ρ_{xx}, ρ_{yy}, ρ_{zz} is determined by the definitions $\delta_z > \delta_x > \delta_y$ and $|\rho_{zz}| > |\rho_{xx}| > |\rho_{yy}|$ respectively. Results are summarized in Table 5.7.

Table 5.7 ^{19}F shielding tensor components (in ppm) for molecules containing CF_3 groups in the solid state

Experimental (from reference 49)					Notation Consistent with Allen				Notation Consistent with Chapter 2			
Molecule	σ_{11}	σ_{22}	σ_{33}	σ_{av}	δ_x	δ_y	δ_z	η	ρ_{xx}	ρ_{yy}	ρ_{zz}	η
CF_3CCl_3	191	282	341	271	11	–80	70	1.30	70	11	–80	0.74
CF_3CN	197	287	341	275	12	–78	66	1.36	66	12	–78	0.69
CF_3COOD	180	280	335	265	15	–85	70	1.43	70	15	–85	0.65
CF_3CD_2OD	180	279	341	267	12	–87	74	1.34	74	12	–87	0.71
$CF_3COO^-Ag^+$	190	261	332	261	0	–71	71	1.00	71	0	–71	1.00
$(CF_3CO)_2O$	185	259	336	260	–1	–75	76	0.97	–75	–1	76	0.97
Average							71	1.23				0.79

The average values of δ_z and η can be substituted into equations (5.28) and (5.29), along with the values of ζ and ε. The spin-lattice relaxation time can be calculated explicitly for values of $\omega\tau_c = 1$, approximately corresponding to the ^{19}F-^{19}F intramolecular magnetic dipole interaction spin-lattice relaxation time minimum. The results are given in Table 5.8.

Table 5.8 Spin-lattice relaxation times calculated for the chemical shielding anisotropy mechanism

B_0/T	Frequency/MHz	τ_c/s ($\omega\tau_c$=1)	T_1/s	% Intramolecular ^{19}F-^{19}F
1.396	55.93	2.85×10^{-9}	115	0.10
0.600	24.05	6.62×10^{-9}	268	0.02

It can be seen from Table 5.8 that the ^{19}F chemical shielding anisotropy spin-lattice relaxation mechanism is of negligible importance compared to the intramolecular ^{19}F magnetic dipolar spin-lattice relaxation mechanism, in polycrystalline $LiCF_3SO_3$.

5.6 Discussion

The experimental spin-lattice relaxation time results presented in Figure 5.11 were extracted from the initial stages of magnetization recovery plots, as detailed

in Section 5.4. In the initial analysis of experimental results such stringent conditions were not adopted. This resulted in values of spin-lattice relaxation time being obtained that were consistently larger than those now reported, especially around the spin-lattice relaxation time minimum where the effects of cross-correlations are pronounced. In the initial analysis the 'usual' approach to the measurement of spin-lattice relaxation times from exponential magnetization recoveries, as described in Chapter 3, was used. In this approach only one or two readings were taken in the initial stages of magnetization recovery, leading to a spin-lattice relaxation time strongly influenced by readings taken at later stages of magnetization recovery. These later readings would have included the effects of cross-correlation, and the spin-lattice relaxation times extracted in this manner were longer than those predicted by the BPP model.

Initial analysis of the experimental ^{19}F spin-lattice relaxation time data produced spin-lattice relaxation time minima of 155 ms and 67 ms for experiments carried out at 55.93 MHz and 24.05 MHz respectively. In contrast the corresponding T_1 (^{19}F) minimum values extracted as described in Section 5.4 are 122ms and 53ms. This represents a discrepancy of 26% and 27% respectively in the spin-lattice relaxation time minima.

Ratcliffe and Dunnel[32] in their study of polycrystalline $CsCF_3SO_3$ found that the experimental value for the ^{19}F spin-lattice relaxation time minimum was significantly larger than that calculated using equation (5.18) with r = 0.2144 nm. Their original paper reports spin-lattice relaxation time measurements for different types of three-fold rotor system, NH_3 in NH_3SO_3, CF_3 in CF_3SO_3Cs and CH_3 in CH_3SO_3Cs. Their experimental description implies that in each compound the value of spin-lattice relaxation time was determined by taking an average of two values, each obtained from data measured by a different experimental technique. The first value was obtained from the initial gradient of the appropriate magnetization recovery plot, although there is no definition of

initial and no details are given on how the initial slope is measured. The second value was calculated from the 'null time' observed in an inversion recovery sequence by using the standard formula for a well behaved system in which the spin lattice relaxation time is defined,

$$T_1 = t_{null}/\ln 2 \qquad (5.31)$$

In a private communication one of the authors (C.I.R.) has indicated that the spin-lattice relaxation times for CF_3SO_3Cs were in fact measured solely by the first method. Cross-correlation effects, which always act to retard magnetization recovery, will influence 'null time' measurements, effectively increasing spin-lattice relaxation times obtained by this method, with respect to a non cross-correlated value. Ratcliffe and Dunnel[32] also noted that other workers had found similar discrepancies between experimental and calculated values of spin-lattice relaxation time minima. A number of these values are given for reorientating CH_3,CF_3 and NH_3 groups in solids, in Table 5.9.

Table 5.9 Some studies where discrepancies in the value of spin-lattice relaxation minima have been observed.

Compound	Hindered Rotor	Theoretical T_1 minimum/ms	Experimental T_1 minimum/ms	% Discrepancy	Reference
NH_3SO_3	NH_3	11	15	36	32
CF_3SO_3Cs	CF_3	66	92	39	32
CH_3SO_3Cs	CH_3	18	24	33	32
N_2H_5Cl	NH_3	13	22	69	34
N_2H_5Br	NH_3	13	21	61	34
$N_2H_6SO_4$	NH_3	10	14	40	35
$N_2H_6Cl_2$	NH_3	10	12	20	35
$N_2H_6Br_2$	NH_3	10	13	30	35
$N_2H_6Br_2.2H_2O$	NH_3	10	12	20	35

The influence of cross-correlation has been taken into account, in a ^1H spin-lattice relaxation study of CH_3PCl_2[12]. The authors observed significantly non-exponential spin-lattice relaxation near the spin-lattice relaxation time minimum

and on the high temperature side. At low temperatures, where $\omega\tau_c \gg 1$ the observed spin-lattice relaxation was predominantly exponential. In the case of exponential spin-lattice relaxation, a form of equation (5.17) was used to extract spin-lattice relaxation times. However, when this was applied at the spin-lattice relaxation time minima a predicted value of 18 ms resulted, which did not compare favourably with the experimentally observed value of 26 ms. Hence, when non-exponential spin-lattice relaxation was observed an expression developed from the work of Hubbard[2] and Runnels[37] was used. For the expectation value $\langle M_z \rangle$ of a nuclear magnetization recovery following a 180° pulse, using a hindered rotation model for the CH_3 group, including cross-correlations it can be shown that

$$M_0 - \langle M_z(t) \rangle = 2M_0 \sum_{j=1}^{4} A_{je}^{a_j t} \qquad (5.32)$$

where A_j and a_j are constants. This is equivalent to equation (5.13). It can be shown that this expression leads to a minimum value of $(2.19) \times (r^6\omega_0/\gamma^4\hbar^2)$ for a spin-lattice relaxation time defined as $t_{null}/\ln 2$[8], where t_{null} is measured in the conventional way by inversion recovery. This analysis predicted a spin-lattice relaxation time minimum of 25 ms, in good agreement with experimental observation.

The percentage discrepancies in the spin-lattice relaxation time minima presented in Table 5.9 are similar in many cases to those between initial ^{19}F spin-lattice relaxation minima obtained in $LiCF_3SO_3$, where the effects of cross-correlation were not taken into account, and those now reported, obtained as described in Section 5.4. In some cases, however, it is clearly unlikely that the discrepancy would have been a consequence purely of the effects of cross-correlations being neglected. Other factors can influence the magnitude of spin-lattice relaxation times, for example; the motion of a molecular group over an asymmetric potential

surface will lead to an increase in spin-lattice relaxation time as the asymmetry of the surface increases[54]. It has also been shown that a decrease in the efficiency of spin-lattice relaxation can result from the partial averaging of the magnetic dipolar Hamiltonian by torsional oscillations[33]. This has been calculated for ^1H spin-lattice relaxation in CH_3 groups. In the hindered molecular reorientation model the reorientating group spends most of its time in certain allowed orientations. The jumps between these orientations are fast compared with the time spent in a a particular orientation. It is suggested that oscillations of the group, between the reorientations through large angles, cause a reduction of the magnetic dipolar Hamiltonian by a factor R and a subsequent reduction in spin-lattice relaxation rate by the factor R^2. Taking a harmonic approximation the authors give torsional eigenvalues

$$E_n = 3\hbar(V/qI)^{\frac{1}{2}}(n+\tfrac{1}{2}) - (9/16)(\hbar^2/I)(n^2 + n + \tfrac{1}{2}) \qquad (5.33)$$

where V is the barrier height of the potential function hindering the reorientation of the group, and I is the moment of inertia of the group. For each torsional state the reduction factor is given by

$$R_n = \exp(-1/\alpha^2)\, L_n(2/\alpha^2) \qquad (5.34)$$

where $\alpha^2 = (9IV/2\hbar^2)^{\frac{1}{2}}$ and $L_n(2/\alpha^2)$ is a Laguerre polynomial. In general, the reduction factor is given by

$$R = \sum_{n=0}^{\infty} R_n \exp(-E_n/kT) \Big/ \sum_{n=0}^{\infty} \exp(-E_n/kT) \qquad (5.35)$$

For a barrier height of 16.7 kJ mol^{-1}, at 250 K, the reduction factor for ^1H spin-lattice relaxation time in the CH_3 group is calculated by the authors to be, R^2 = 0.88. This value can be obtained from equations (5.33), (5.34) and (5.35), using only the first two terms of equation (5.35); that is, only involving $L_0(2/\alpha^2) = 1$, and $L_1(2/\alpha^2) = 1-(2/\alpha^2)$.

A similar calculation can be performed to establish the reduction in the ^{19}F spin-lattice relaxation minimum in polycrystalline $LiCF_3SO_3$ by torsional averaging. The barrier height, V, is approximately the activation energy of the hindered reorientation, given by Section 5.4 to be ~24.40 kJ mol^{-1}. The temperatures corresponding to the spin-lattice relaxation time minima observed at the frequencies used in this study are given in Table 5.3 as 250 K and 272 K. The moment of inertia of the CF_3 group about its axis of hindered reorientation can be calculated, and is given by

$$I = 3my^2 \qquad (5.36)$$

where m is the mass of the ^{19}F atom, and y is the distance between the ^{19}F nuclei and the axis of reorientation. This can easily be calculated, taking the ^{19}F-^{19}F distance to be 0.2144 nm and assuming an equilateral triangle arrangement as 0.124 nm. Substitution into equation (5.32), gives $I = 1.45 \times 10^{-45}$ kgm^2. The results of the calculation of the reduction factor are given in Table 5.10.

Table 5.10. The reduction factor for the ^{19}F spin-lattice relaxation time minima observed in polycrystalline $LiCF_3SO_3$, due to partial averaging of the magnetic dipolar Hamiltonian.

Temperature/K	Barrier Height/kJ mol^{-1}	R^2
250	24.40	0.98
272	24.40	0.99

It can be seen from Table 5.9, that the torsional averaging effect is negligible in analysing the ^{19}F spin-lattice relaxation behaviour in polycrystalline $LiCF_3SO_3$.

The depth of a particular spin-lattice relaxation time minimum is not always easily interpreted and individual cases should be treated on their merits. However, it has been shown that the non-critical measurement of initial gradients of magnetization recovery plots can lead to larger than expected values of spin-

lattice relaxation time. One source of ambiguity, the effects due to cross-correlation, can be removed by the careful measurement of spin-lattice relaxation times from well defined initial gradients of detailed magnetization recovery plots, as described in Section 5.4.

The value of the pre-exponential factor of the Arrhenius relationship, τ_0, obtained for the CF_3 group in polycrystalline $LiCF_3SO_3$ in this study; $(3.42 \pm 0.17) \times 10^{-14}$ s; compares favourably with other values found in other spin-lattice relaxation studies of the CF_3 group, given in Table 5.11.

Table 5.11. Some values of τ_0 obtained for the reorientating CF_3 group

Compound	τ_0/s	Ref
$LiCF_3SO_3$	3.42×10^{-14} s	This work.
$C_6H_5CF_3$	2.3×10^{-14} s	55
$CF_3CONFCl_3$	3.3×10^{-13} s	40
$CF_3COO^-Ag^+$	2.0×20^{-15} s	38,56

τ_0 represents the infinite temperature limit of correlation time and is independent of the potential barrier classically hindering the reorientation. It is characteristic of a particular molecular group, and as such, values given in Table 5.11 would be expected to be similar.

A direct comparison with results obtained for polycrystalline CF_3SO_3Cs is not straightforward because the activation energy for the rotation of the CF_3 group in this compound was found to be markedly temperature dependent, except at temperatures below that of the observed spin-lattice relaxation time minimum. This non-Arrhenius type behaviour could result from the effects of cross-correlations, as described in Section 5.3. The cross-correlation contribution to spin-lattice relaxation time is temperature dependent and in this way could cause otherwise inherently linear portions of the $\ln(T_1(^{19}F))$ versus inverse temperature plot to appear curved. Selective low temperature data analysis for CF_3SO_3Cs (in the region where the cross-correlations have least influence)

gives $\tau_0 = (4.4 \pm 0.5) \times 10^{-13}$s, which compares favourably with the pre-exponential factors given in Table 5.10. The activation energy is (16.7 ± 0.2) kJ mol^{-1}. This activation energy is less than that calculated for the lithium salt, in this study. This suggests a dependence of activation energy on the nature of the metal cation. In simple metal salts this would not be unreasonable. For example, there have been a number of n.m.r. studies carried out in polycrystalline samples of ionic hydrogendifluorides, namely $NaHF_2$[57], KHF_2[58,59], NH_4HF_2[60] and $CsHF_2$[61,62] where there is evidence for the expansion of the lattice with increasing radii of metal cation. This would correspond to a reduction in activation energy of any molecular reorientational process.

5.8 Conclusion

The ^{19}F spin-lattice relaxation in polycrystalline $LiCF_3SO_3$ has been studied in some detail. The temperature dependence of the non-exponentiality of the nuclear magnetization recovery plots is very strong evidence for the influence of cross-correlation on the relaxation behaviour. In such circumstances motional parameters for the reorientation of CF_3 groups can be obtained by analysis of the temperature dependence of values of $T_1(^{19}F)$ which are measured from initial gradients, that is the first 20% of appropriate ^{19}F nuclear magnetization recovery plots as described in Section 5.3. This approach is markedly different to that normally employed in spin-lattice relaxation time studies of solids. The advantage is that spin-lattice relaxation time values are obtained which are independent of the influence of cross-correlation effects. These may be used to obtain motional parameters from relatively simple relaxation models, which do not consider the effects of cross-correlation. The approach is quite general and can be used in the spin-lattice relaxation study of any solid.

References

1 J C Pratt
J. Chem. Phys. 77, 118, 1982.

2 R L Hilt and P S Hubbard
Phys. Rev., 134, 392, 1964.

3 D E Woessner
J. Chem. Phys., 36, 1, 1962.

4 P S Allen
J. Phys. C. Solid State Phys., 6, 3174, 1973

5 W M M J Bové, J Vriend, J A Peters, J M A Baas and B Van de Groaf
Mol. Phys., 41, 933, 1980.

6 P S Allen and P Branson
J. Phys. C. Solid State Phys., 11, 121, 1978.

7 J D Cutnell and W Venable
J. Chem. Phys., 60, 3795, 1974.

8 M F Baud and P S Hubbard
Phys. Rev., 170 (2), 384, 1968.

9 R A Wind, S Emid, J F J M Pourquié and J Smidt
J. Chem. Phys., 67, 2436, 1977.

10 A M Albano, P A Beckmann, M E Carrington, E E Fisch, F A Fusco, A E O'Neill and M E Scott
Phys. Rev. B, 30, 2334, 1984.

11 H B Brom and S Enid
Physica, 113B, 121, 1982.

12 A Kumar and C S Johnson Jr
J. Chem. Phys., 60, 137, 1974.

13 T Hasebe and S Ottoni
J. Chem. Soc. Faraday Trans., 84, 187, 1988.

14 A Gryff Keller and L Poppe
J. Chem. Soc. Perkin Trans., 11, 603, 1985.

15 E T Olejinczak
J. Mag. Res., 81, 392, 1989.

16 E O Stejskal and H S Gutowsky
J. Chem. Phys., 28, 388, 1958.

17 S Watanabe, Y Abe and B Yoshizaki
J. Phys. Soc. Japan, 54, 41, 1985.

18 E O Stejskal, D E Woessner, T C Farrar and H S Gutowsky
J. Chem. Phys., 31, 55, 1959.

19 D E O'Reilly and T Tsong
Phys. Rev., 157, 417, 1967.

20 P S Allen and A Cowking
J. Chem. Phys., 49, 789, 1968.

21 D E O'Reilly, E M Peterson and S R Lammert
J. Chem. Phys., 52, 1700, 1970.

22 H M McIntyre and C S Johnson Jr
J. Chem. Phys., 55, 345, 1971.

23 S Albert, H S Gutowsky and J A Ripmeester
J. Chem. Phys., 56, 1332, 1972.

24 S Albert, H S Gutowsky and J A Ripmeester
J. Chem. Phys., 56, 3672, 1972.

25 P S Allen and S Clough
Phys. Rev. Lett., 22, 1351, 1969.

26 J E Carolan, S Clough, N D McMIllan and B Mulady
J. Phys. C., 5, 631, 1972.

27 Z Zimpel and W Medycki
J. Mag. Res., 92, 377, 1991.

28 N Bloembergen, E M Purcell and R V Pound
Phys. Rev., 73, 679, 1948.

29 H S Gutowsky and G E Pake
J. Chem. Phys. 18, 162, 1950.

30 E R Andrew
Progress in Nuclear Magnetic Resonance Spectroscopy Vol. 8
Pergamon, Oxford.

31 S Clough
Mol. Phys., 68, 1255, 1989.

32 C I Ratcliffe and B A Dunell
J. Chem. Soc. Faraday Trans. 2, 77, 2169, 1981.

33 C S Johnson Jr.
J. Mag. Res., 24, 63, 1976.

34 C I Ratcliffe, B A Dunell and T C Waddington
J. Chem. Soc. Faraday Trans. 2, 74, 1417, 1978.

35 C I Ratcliffe
J. Mag. Res., 38, 283, 1980.

36 E R Andrew, W S Hinshaw, M E Hutchins, R O I Sjoblom
Mol. Phys., 34, 1695, 1977.

37 L K Runnels
Phys. Rev., 134, A28, 1964.

38 M Mehring and H Raber
J. Chem. Phys., 59, 1116, 1973.

39 C I Ratcliffe, T C Waddington and J Howard
J. Chem. Soc. Faraday Trans 2, 78, 1881, 1982.

40 G E Kibrik, I A Kyuntsel, V A McKeeva, Yu I Rozenberg and G B Soifer
Sov. Phys. Solid State, 17, 598, 1975

41 G B Matson
J. Chem. Phys., 67, 5152, 1977.

42 P S Hubbard
J. Chem. Phys., 51, 1647, 1969.

43 P S Hubbard
J. Chem. Phys., 52, 536, 1970.

44 L G Werbelow and A G Marshall
J. Mag. Res., 21, 299, 1973.

45 M Tremayne, P Lightfoot, M A Mehta and P G Burce et al
J. Solid State Chem., 100, 191, 1992.

46 R G Delaplane, J O Lundgren and I Olovson
Acta Cryst., B31, 2202, 1975.

47 J B Spencer and J O Lundgren
Acta Cryst., B29, 1923, 1973.

48 R G Delaplane, J O Lundgren and I Olovsson
Acta Cryst., B31, 2208, 1975.

49 S K Garg, J A Ripmeester and D W Davidson
J. Chem. Phys., 79, 4101, 1983.

50 A A J Magdenberg
J. Mol. Struct., 41, 61, 1977.

51 R L Livingston and G Vaughn
J. Am. Chem. Soc., 78, 2711, 1956.

52 L F Thomas, J S Heers and J Sheridan
Z. Elektrochem., 61, 935, 1957.

53 R Holm, M Mitzlaff and H Hartmann
Z. Naturforsch, 23, 1040, 1968.

54 J E Anderson
J. Mag. Res., 11, 398, 1973.

55 J E Anderson and W P Slichter
J. Chem. Phys., 43, 433, 1965.

56 M Punkkinen, L P Ingman, D G Taylor and P S Allen
J. Phys. Chem., 8, 2159, 1975.

57 PhD. Thesis
N F Peirson
The Open University, Feb, 1992.

58 Y Furukawa and H Kinyama
Bull. Chem. Soc. Japan, 51, 3438, 1978.

59 Yu G Kriyer, N K Moroz and S P Gabuda
Sov. Phys. Solid State 18, 514, 1976.

60 E C Reynhardt, A Watton and H E Petch
J. Chem. Phys., 71, 4421, 1979.

61 Yu. G. Kriger, S P Ganuda and N K Moroz
Sov. Phys. Solid State, 17, 2239, 1976.

62 M Mortimer, E A Moore, D C Apperley and G Oates
J. Chem. Soc. Faraday Trans., 89, 693, 1993.

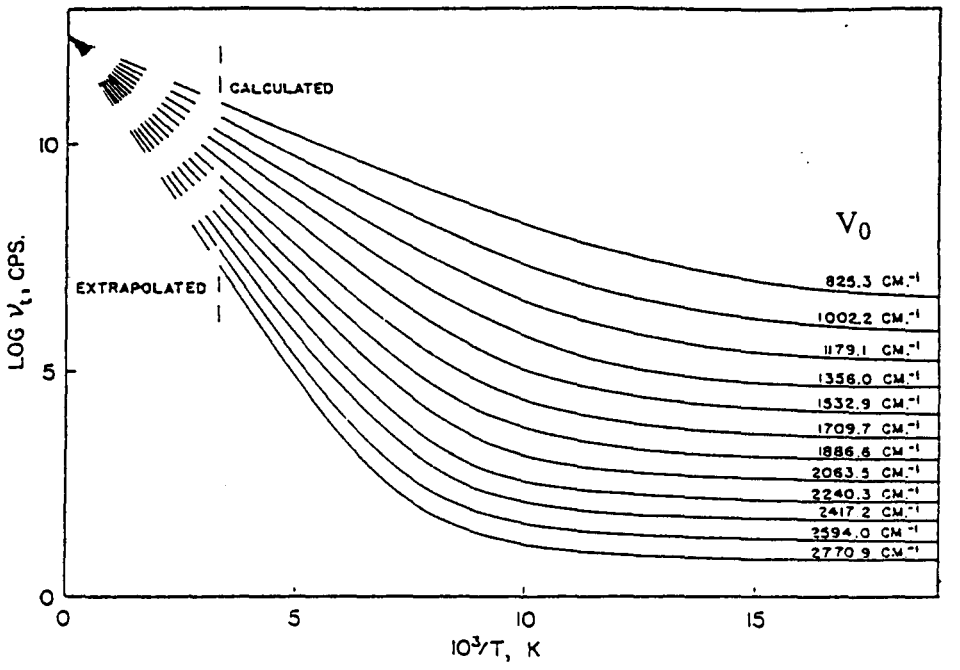

Figure 5.1 The average 'tunneling frequency', ν_t, as a function of temperature for various barrier heights V_0.

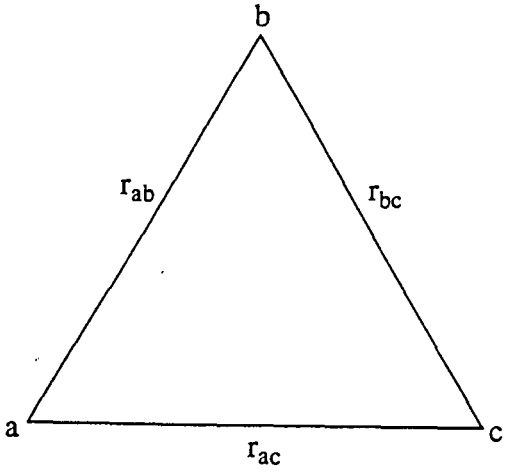

Figure 5.2 A triad of spin $I = \frac{1}{2}$ nuclei, a, b and c, and the three internuclear vectors r_{ab}, r_{bc} and r_{ca}.

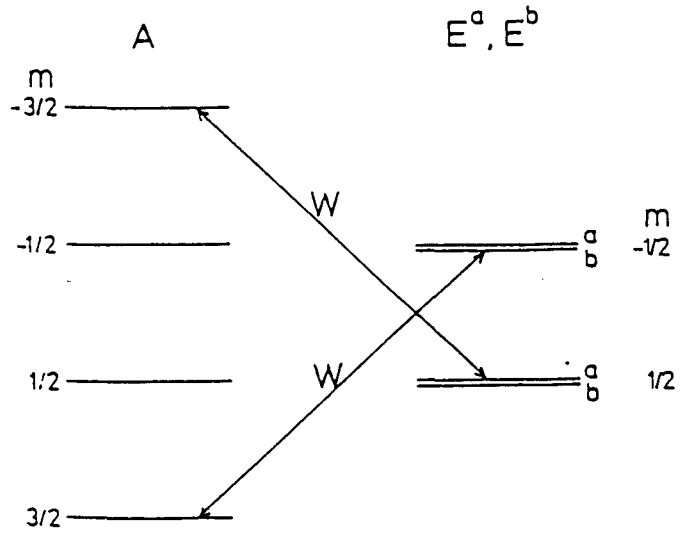

Figure 5.3 Energy level diagram for the three spin I = ½ system, consisting of a quartet (A) and a doublet (E^a, E^b). The states of the E representation are doubly degenerate. Secular dipolar interactions are neglected for simplicity. The relaxation transitions (W) are the only ones in effect, when intramolecular dipole interaction is considered, and the C_3 axis of the system is parallel to the applied field.

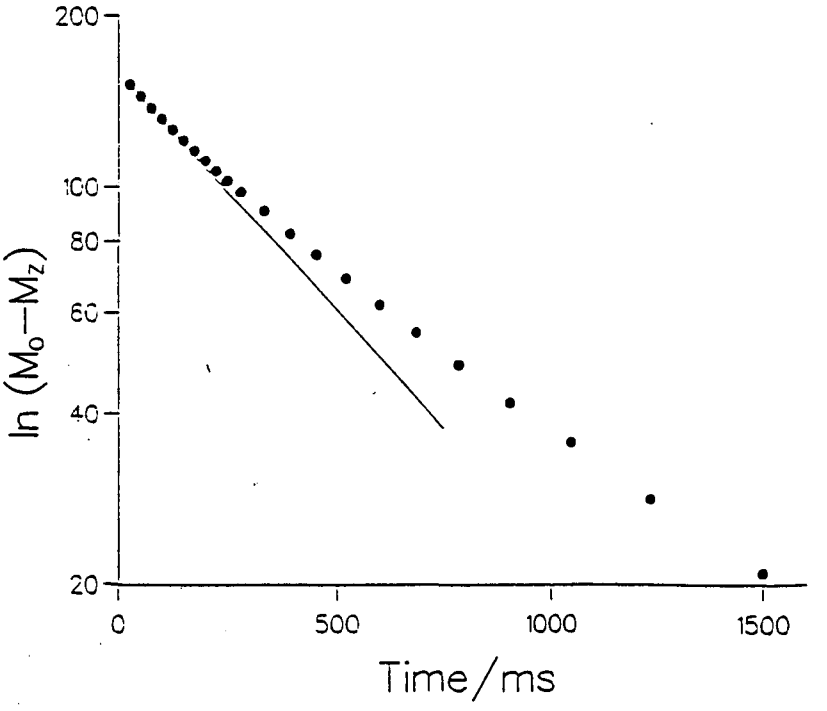

Figure 5.4 The ^{19}F nuclear magnetization recovery recorded at 24.05 MHz and 340 K from polycrystalline $LiCF_3SO_3$. The gradient of the solid line is calculated from the initial points.

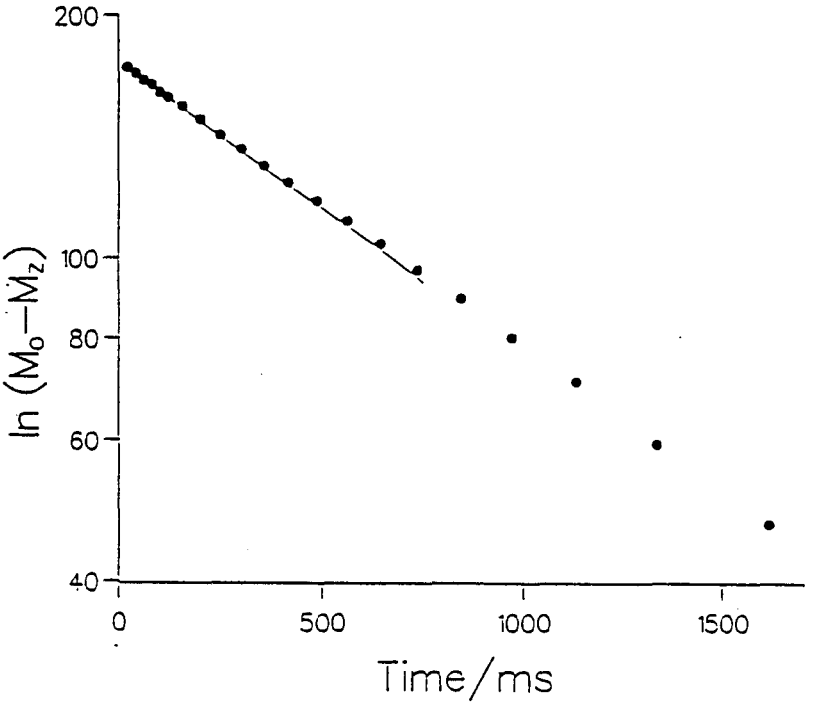

Figure 5.5 The ^{19}F nuclear magnetization recovery recorded at 24.05 MHz and 215 K from polycrystalline $LiCF_3SO_3$. The gradient of the solid line is calculated from the initial points.

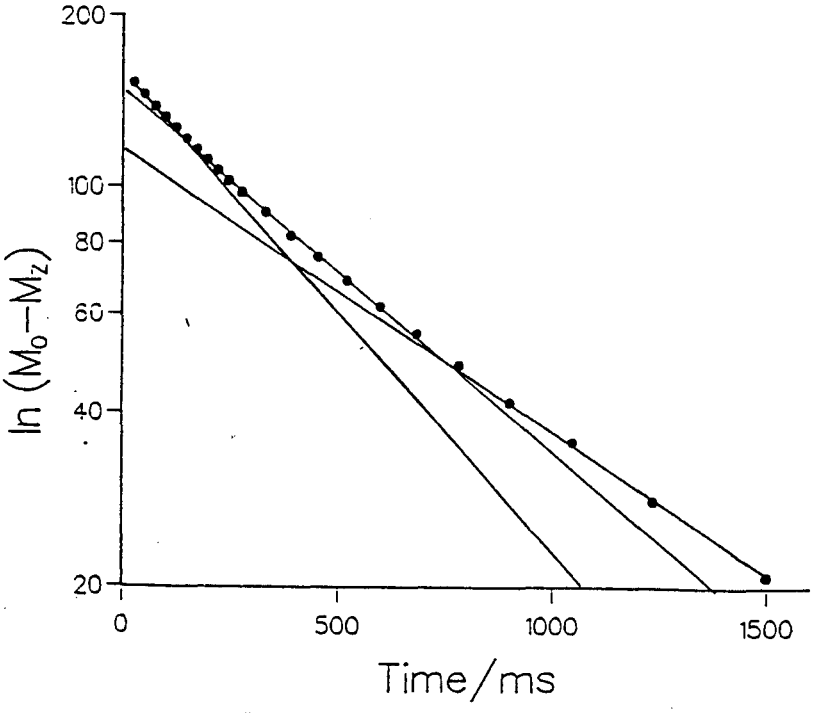

Figure 5.6 A selective analysis of Figure 5.4, with the three gradients producing three distinct spin-lattice relaxation times; 857 ms, 693 ms, and 521 ms.

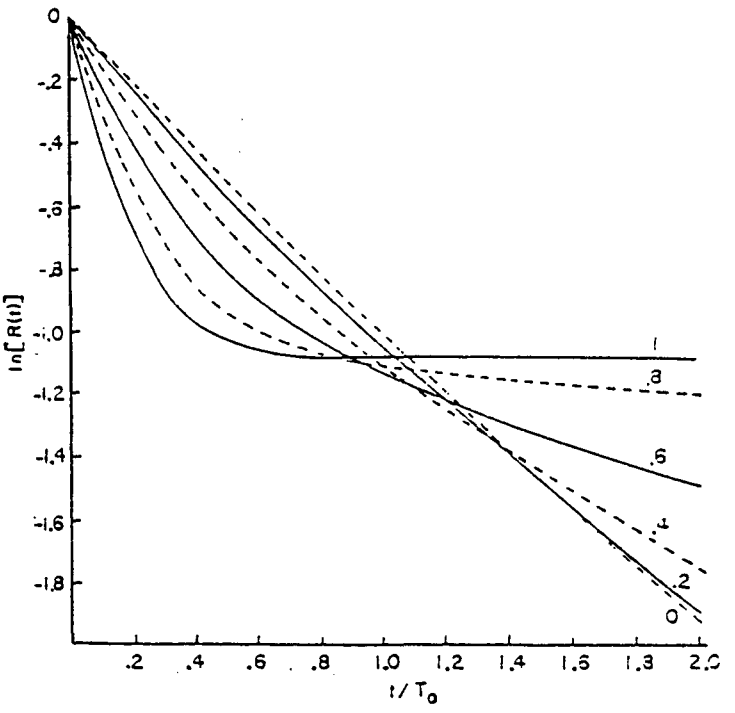

Figure 5.7 The time dependence of the logarithm of the relaxation plotted as a function of t/T_0 for $(\omega\tau_c)^2 << 1$ and six values of $\cos\beta$. $R(t) = [\langle I_0\rangle^T - \langle I_0\rangle]/2\langle I_0\rangle^T$ and $1/T_0 \equiv \gamma^2\hbar^2\tau_c/r_0^6$.

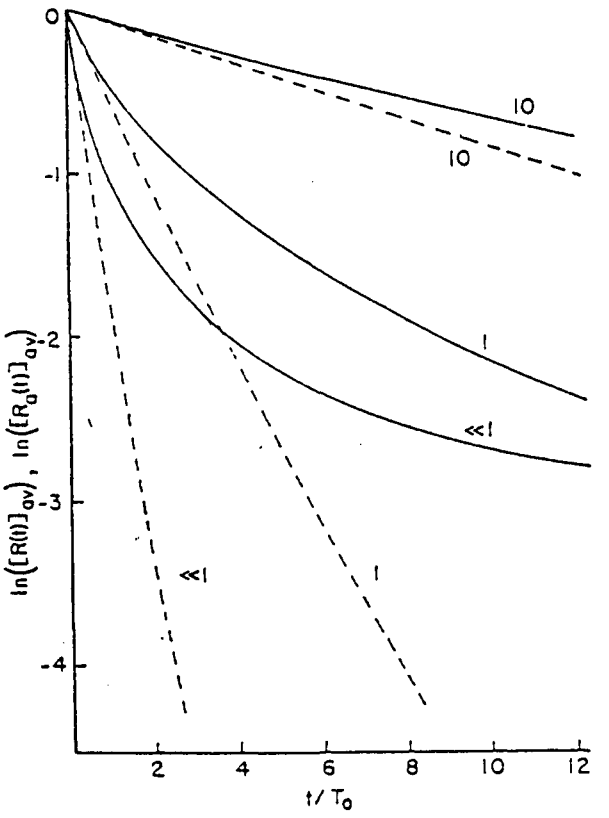

Figure 5.8 The time dependence of the logarithm of the average over orientation of the relaxation, plotted as a function of t/T_0, for three values of $(\omega_0\tau_c)^2$. R(t) and $R_a(t)$ are given by $\langle I_0\rangle^T - \langle I_0\rangle]/2\langle I_0\rangle^T$ and $1/T_0 = \gamma^2\hbar^2\tau_c/r_0^6$, where the two functions neglect and consider cross-correlations respectively.

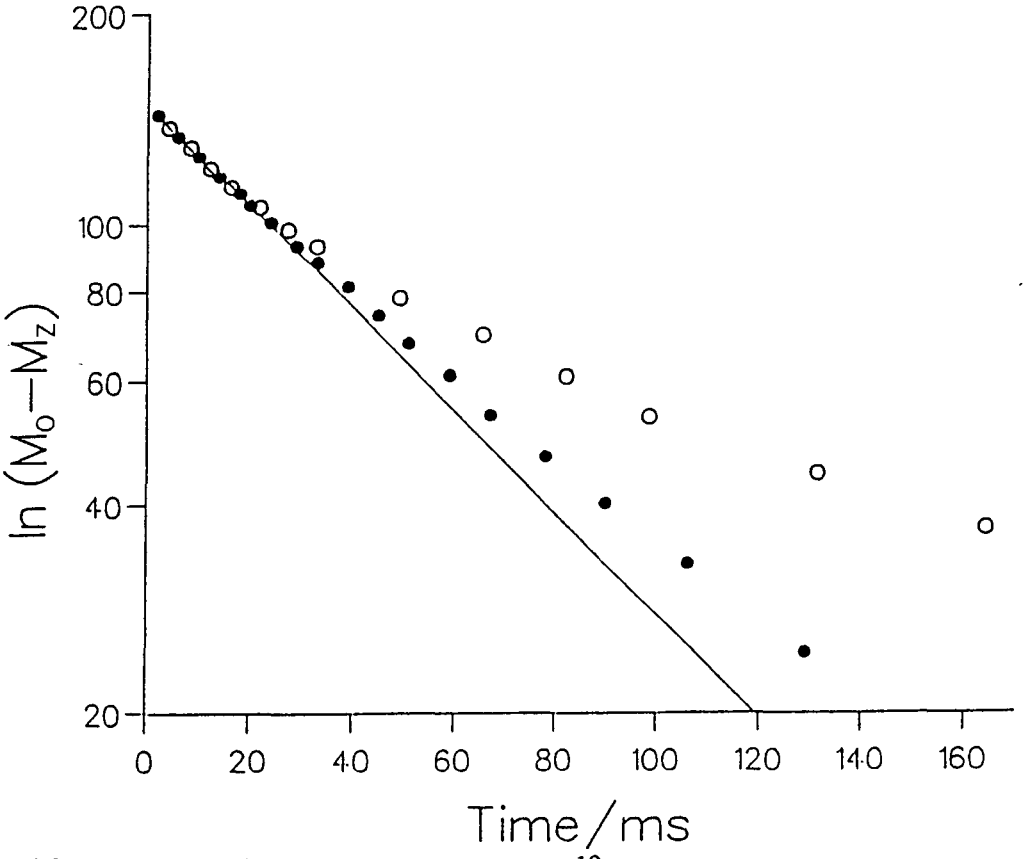

Figure 5.9 A comparison of the experimental ^{19}F nuclear magnetization recovery for polycrystalline $LiCF_3SO_3$, measured at 24.05 MHz and 242 K (●), and the corresponding theoretical recovery calculated using the model of Hubbard and Hilt, (O).

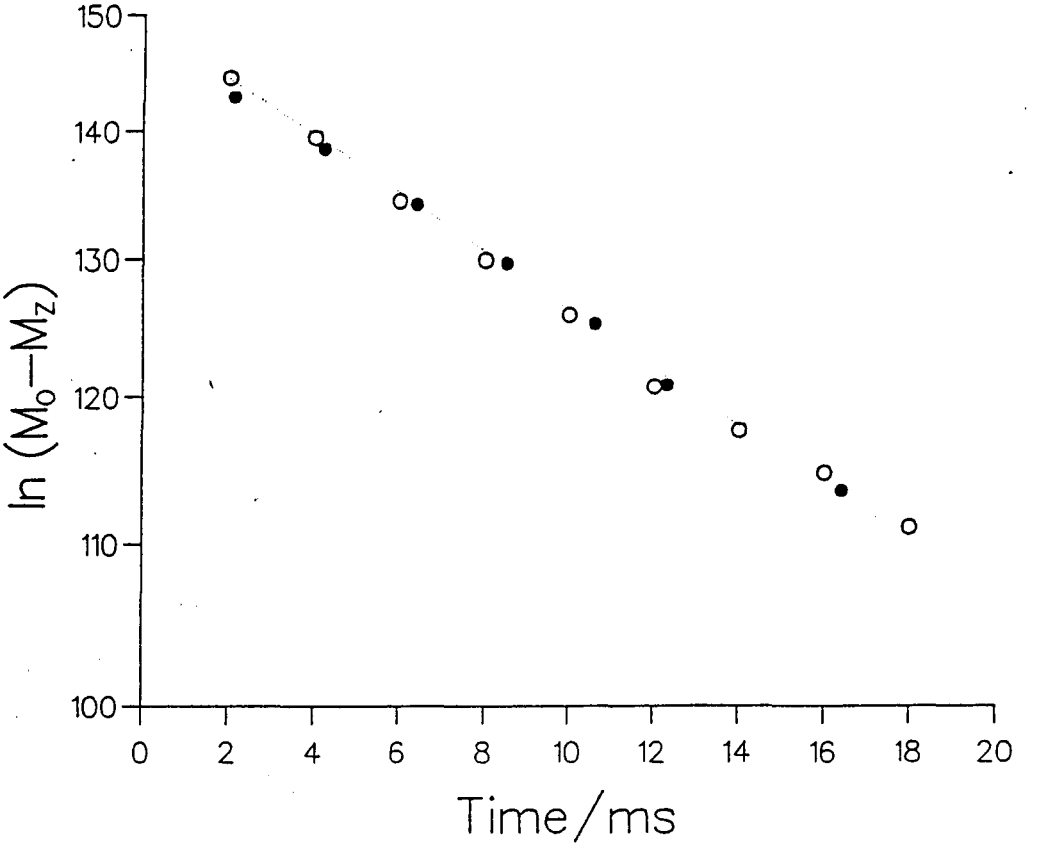

Figure 5.10 A comparison of the first 25% of the experimental ^{19}F nuclear magnetization recovery for polycrystalline $LiCF_3SO_3$, measured at 24.05 MHz and 220 K (●), and the corresponding theoretical recovery calculated using the model of Hubbard and Hilt, (O).

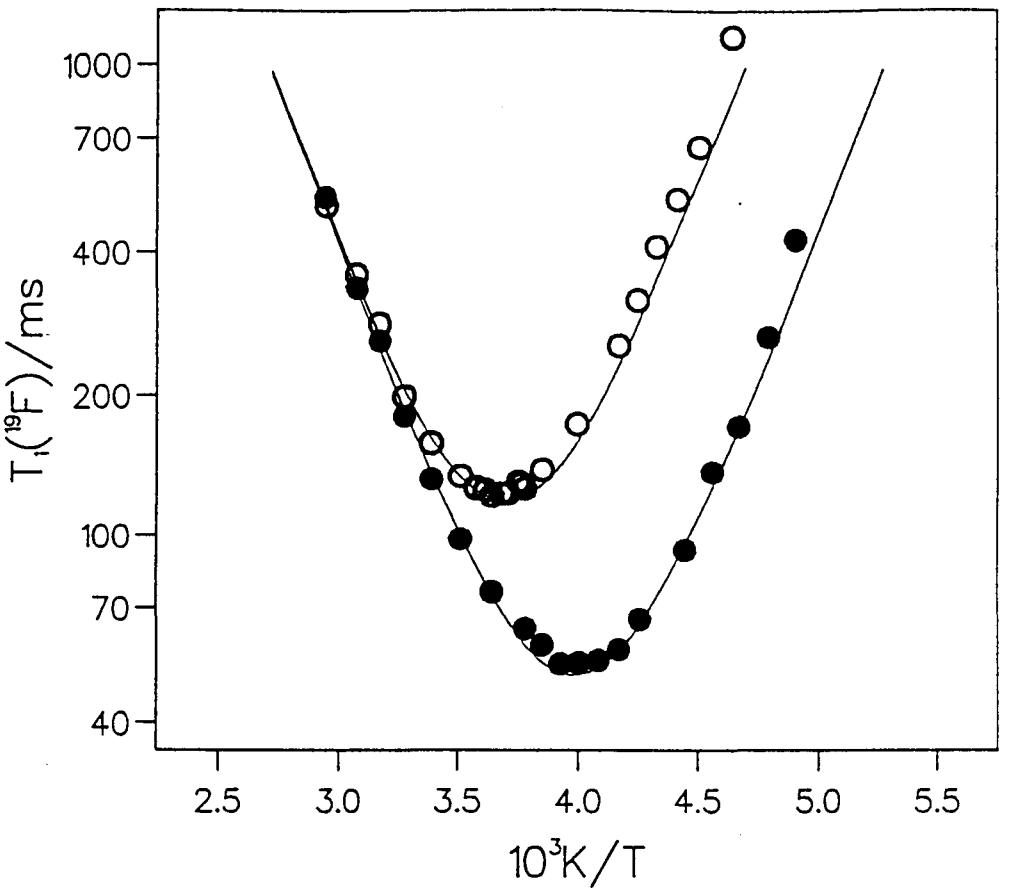

Figure 5.11 The temperature dependence of the ^{19}F spin-lattice relaxation behaviour in polycrystalline $LiCF_3SO_3$, measured at 24.05 MHz (●) and 55.93 MHz (O).

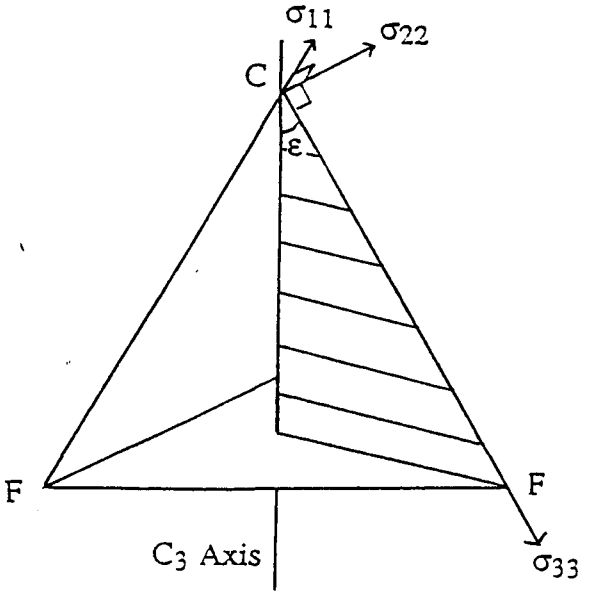

Figure 5.12 The geometry of the CF_3 group and of the ^{19}F chemical shielding tensor.

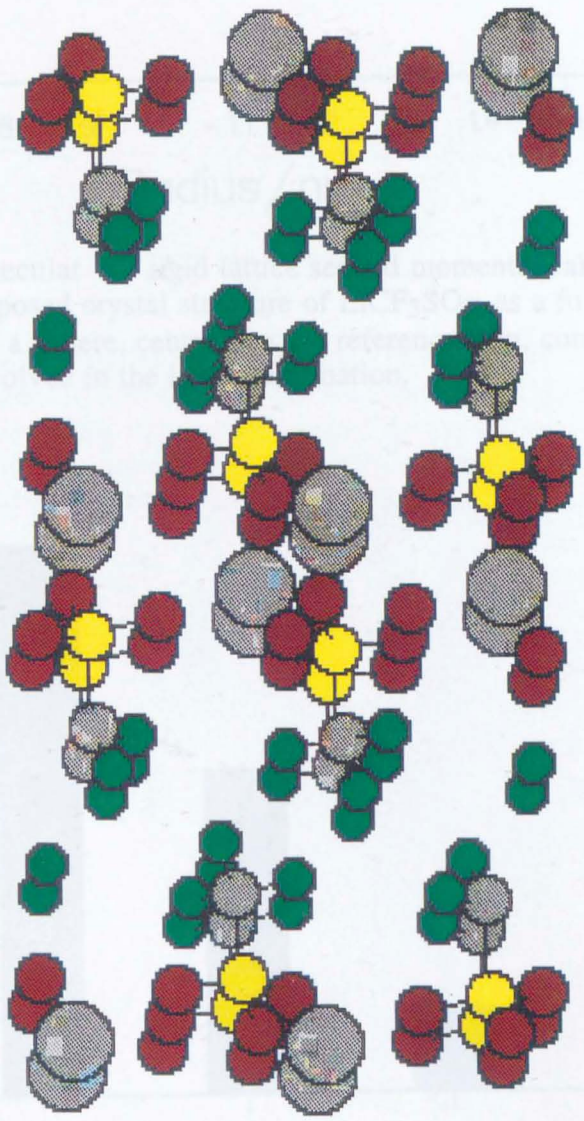

Figure 5.13 The proposed crystal structure of $LiCF_3SO_3$, from reference 45. ^{19}F atoms are represented as green, ^{16}O as red, ^{12}S as yellow, ^{12}C as grey, and ^{7}Li as the larger grey spheres.

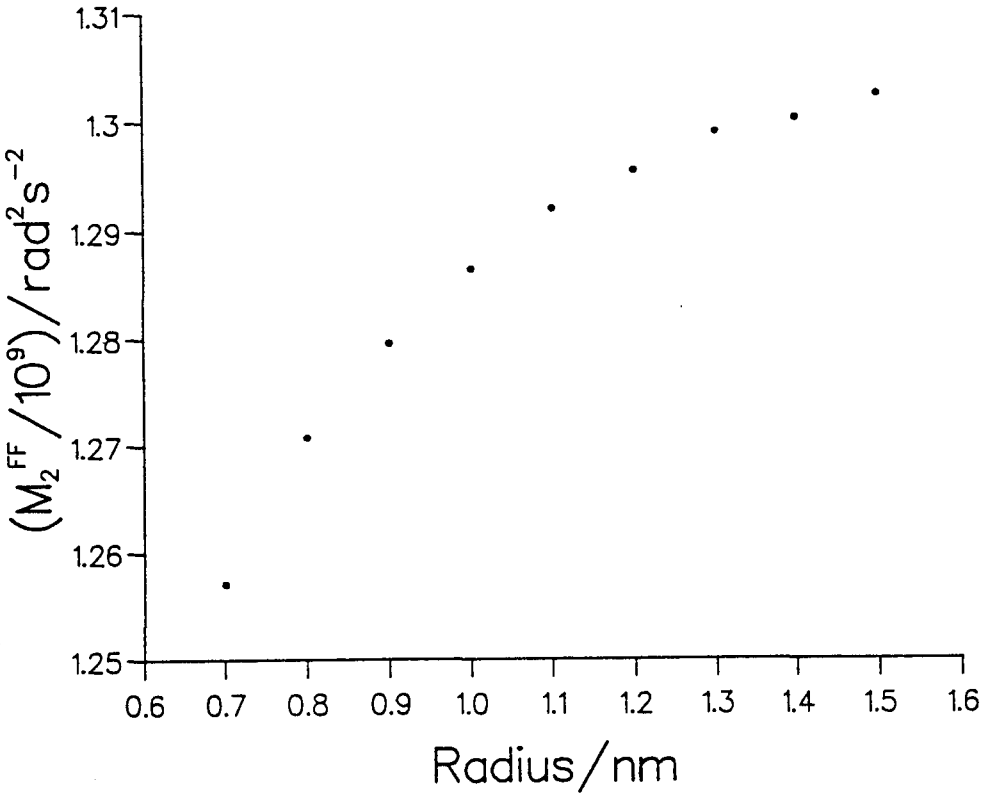

Figure 5.14 The intermolecular ^{19}F rigid lattice second moments, calculated from the proposed crystal structure of $LiCF_3SO_3$, as a function of the radius of a sphere, centred on the reference spin, containing all nuclei involved in the lattice summation.

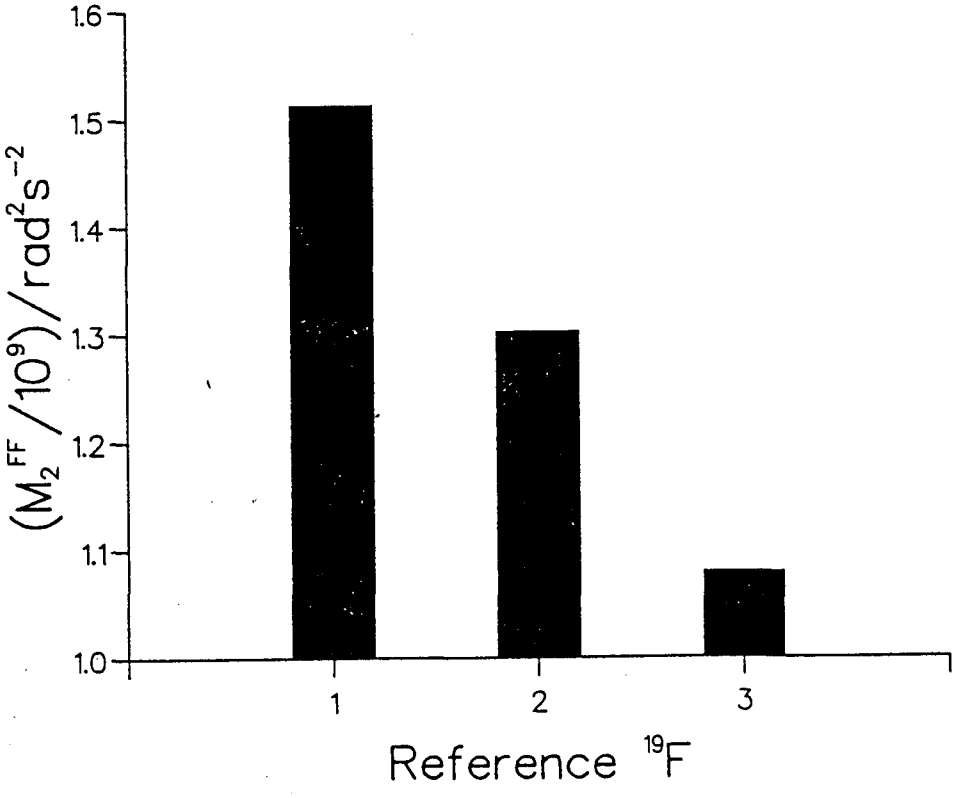

Figure 5.15 The intermolecular ^{19}F rigid lattice second moments, calculated from the proposed crystal structure of $LiCF_3SO_3$; for all unique crystallographic ^{19}F positions. The lattice summation involves all spins within 1.5 nm of the reference nuclei.

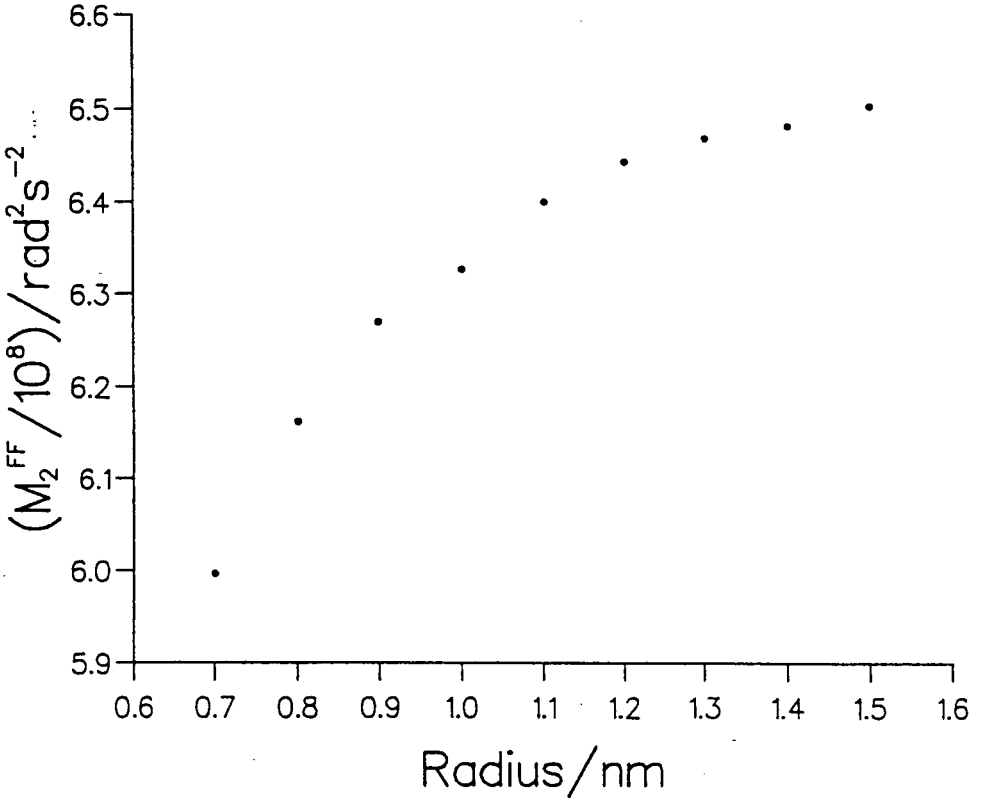

Figure 5.16 The motionally averaged intermolecular ^{19}F second moments, calculated from the proposed crystal structure of $LiCF_3SO_3$, as a function of the radius of a sphere centred on the reference spin containing all nuclei involved in the lattice summation. The motional averaging process used is described in the text.

CHAPTER 6

^{19}F NUCLEAR MAGNETIC SPIN-LATTICE RELAXATION STUDIES IN PEO/$LICF_3SO_3$ SYSTEMS

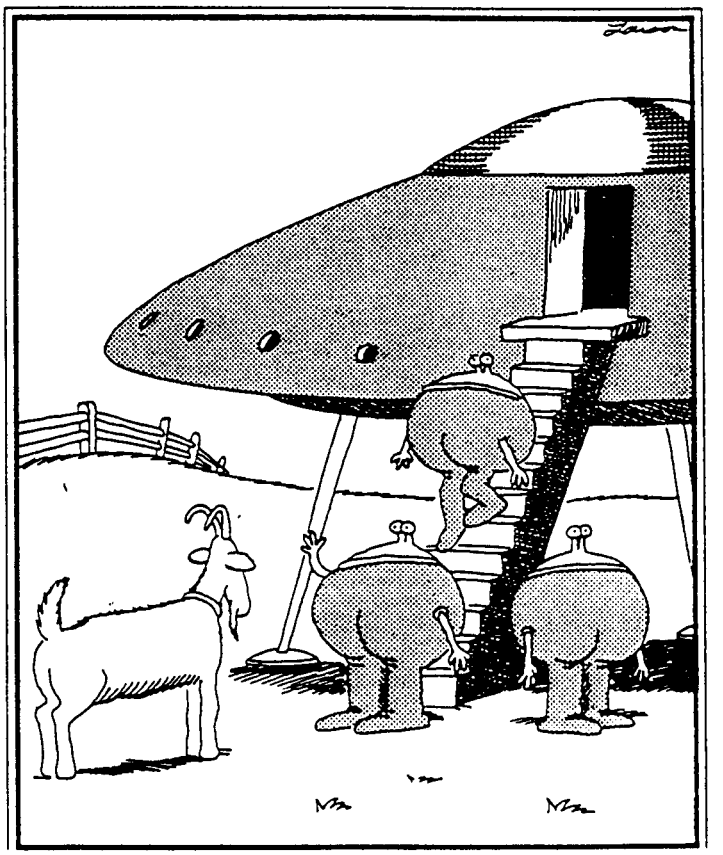

When worlds collide

CONTENTS

6.1 Introduction

The ^{19}F spin-lattice relaxation behaviour in polycrystalline $LiCF_3SO_3$ has been studied in detail in Chapter 5. The aim of this chapter is to present and discuss the results of a ^{19}F spin-lattice relaxation study carried out on the 3.5:1 and 9:1 $PEO/LiCF_3SO_3$ ionic host polymer systems. The comparison of the respective spin-lattice relaxation behaviours gives insight into the molecular dynamics of the CF_3 group in the ionic host polymer systems, and the local motional environment of the $CF_3SO_3^-$ anion.

The first part of the chapter is concerned with the ionic host polymer system samples themselves and their characterization. The results of the ^{19}F spin-lattice relaxation study are then presented and a dynamic model is proposed, involving a general treatment of the nuclear spin-lattice relaxation behaviour of two unlike, dipolar coupled, spin $I = \frac{1}{2}$ nuclei. This motional model is discussed with reference to a proposed crystal structure for the stoichiometric complex. Finally, the implications resulting from the interpretation of the spin-lattice relaxation behaviour, for the anion distribution within the ionic host polymer systems are discussed.

6.2 Sample Selection

The ratio of O:Li selected for the ionic host polymer systems studied was determined with reference to the literature. A number of thermal and conductivity studies carried out on the $PEO/LiCF_3SO_3$ system[1-4] have suggested that a single stoichiometric crystalline complex exists for the O:Li ratio 3.5:1. However, it is interesting to note that since the preparation of the samples studied, it has been suggested, in 1992, that the stoichiometric crystalline complex corresponds to a O:Li ratio of 3:1[10]. In November 1993, a crystal structure for a $PEO/LiCF_3SO_3$ complex was published [11], obtained by Rietveld analysis, and

the use of soft chemical constraints. This model required a stoichiometry of 3:1, and is shown in Figure 6.1. This is discussed further in Section 6.6.

The O:Li 8:1 system has received much attention[4-6], particularly with respect to polymer electrolyte battery research[7,8]. The phase equilibria in this system is complicated[4,5]. A phase diagram of the PEO/$LiCF_3SO_3$ system[1] is shown in Figure 6.2. For an 8:1 PEO/$LiCF_3SO_3$ system, at temperatures below about 330 K, pure crystalline PEO, a salt rich crystalline complex and an amorphous phase coexist. At about 330 K the pure crystalline PEO melts and from 330 K to the liquidus temperature of the complex (~429 K), the salt rich crystalline complex gradually dissolves in the amorphous phase.

The samples selected for study in this thesis were a system with O:Li ratio, 3.5:1; and a system with ratio 9:1. The latter exhibits phase equilibria similar to the 8:1 system, and has been studied previously, but not in detail, by n.m.r. methods[9].

6.3 Characterization of Samples

PEO/$LiCF_3SO_3$ systems were prepared by the evaporation method, as described in Chapter 3. The ratios of O:Li selected were 3.5:1 and 9:1, as discussed in Section 6.2. Previous studies have used XRD, FTIR, DSC, molecular weight measurement, and electron spectroscopy for chemical analysis (ESCA) for characterization of polymer electrolyte films[12]. In this work the techniques available were XRD and DSC.

X-ray diffraction data was obtained as described in Chapter 3. The main purpose of this study was as a qualitative characterization technique to ensure that the synthesised ionic host polymer systems were distinct. Figure 6.3 shows the XRD pattern for PEO, $LiCF_3SO_3$, a discrete mix of the polymer and salt, in the ratio 3.5:1, and the 3.5:1 and 9:1 ionic host polymer systems. The pattern produced by the mixture is a simple superposition of the individual diffraction

patterns. However, the 3.5:1 ionic host polymer system data is distinctive, and in particular shows none of the characteristic pure salt reflections, clearly present in the simple mixture (2θ ~ 31-34°). This provides evidence that a distinct complex has been formed. The 9:1 ionic host polymer system data again shows no characteristic pure salt reflections, and the pattern is consistent with a superposition of the diffraction patterns of the 3.5:1 system and the of the pure PEO data.

XRD data has previously been obtained for PEO/$LiCF_3SO_3$ systems of ratios between 1:1 and 16:1[2]. The results are in good agreement with the results presented here, although the authors suggest the existence of a second complex with stoichiometric ratio of 7:1, and argue this is reasonable for PEO. Systems with other salts were also studied by the authors, but PEO/$LiCF_3SO_3$ was found to be unique in this respect. Other workers did not find evidence for more than one crystalline complex in the PEO/$LiCF_3SO_3$ system[1,4]. This is discussed further in the context of the DSC results. It is worth noting that the current suggestion of a 3:1 stoichiometric crystalline complex in the PEO/$LiCF_3SO_3$ system, would probably be inconsistent with the formation of a second 7:1 complex.

DSC data was obtained as described in Chapter 3. Thermal analysis has been used quite extensively to investigate phase behaviour in PEO/$LiCF_3SO_3$ systems[2,4,10,12-15]. Figure 6.4 shows DSC traces for PEO, and the 3.5:1 and 9:1 PEO/$LiCF_3SO_3$ systems, over the temperature range 193 K to 473 K. (This work was carried out at the University of Nottingham with the collaboration of M Hey and S M Ilett.) The PEO trace shows a single endotherm at ~336 K, which corresponds to sample melting[15]. The 3.5:1 PEO/$LiCF_3SO_3$ system trace shows a single endotherm at ~408 K. This corresponds to the melting of a single crystalline stoichiometric complex. The 9:1 PEO/$LiCF_3SO_3$ system trace shows two endothermic events, at ~338 K and at ~408 K, corresponding to the presence

of a crystalline stoichiometric complex and excess crystalline PEO. These results are largely consistent with previous studies and suggests that the 9:1 PEO/$LiCF_3SO_3$ system consists of a stoichiometric crystalline complex of ratio ~3.5:1, with extra PEO present. A previous ^1H spin-spin relaxation time study[17] is consistent with this idea and suggests that 50% of the 9:1 PEO/$LiCF_3SO_3$ system is pure crystalline PEO with 12% the corresponding amorphous fraction. This leaves all of the $LiCF_3SO_3$ in 38% of the 9:1 system, corresponding to a ratio of ~3.5:1.

However, in one particular study[2] of systems in the O:Li range, 12:1 to 5:1[2] an endothermic shoulder was observed near to the PEO melting endotherm at ~334-335 K. When the samples were cooled and reheated this shoulder was found to sometimes repeat, but not consistently. The authors suggested that this endothermic shoulder may be additional evidence for the existence of a second crystalline stoichiometric phase, specifically of ratio 7:1, as suggested by XRD data in the same study.

Figure 6.5 shows DSC traces for PEO, the 3.5:1 and 9:1 PEO/$LiCF_3SO_3$ systems, and $LiCF_3SO_3$, over the reduced temperature range 293 K to 393 K. (This work was carried out at a later date at the Open University with the collaboration of G. Imlach.) The PEO and PEO/$LiCF_3SO_3$ traces are largely consistent with Figure 6.5, although it would appear a small amount of crystalline PEO may be present in the 3.5:1 ionic host polymer system. This may indicate that the ratio of the stoichiometric crystalline complex is indeed slightly less than 3.5:1. The detection of a small amount of PEO present in the 3.5:1 PEO/$LiCF_3SO_3$ system by one DSC study and not in the other may be due to system inhomogeneity. That is, the original cast sample as a whole may contain a small amount of PEO, but it is still possible to extract two samples from this, one containing a small amount of PEO and one not. It is interesting to note that the $LiCF_3SO_3$ trace shows an endothermic event at ~335 K. This DSC study was repeated using $LiCF_3SO_3$ of

different purities, produced by different companies (Aldrich 99%, Flurochem 97%), and using samples of different ages, including one directly from a freshly opened bottle. The endothermic behaviour was observed in all cases. The enthalpy change corresponding to the endotherm was found to be different in the different purity samples and it was suggested that an impurity may be responsible. The data sheets describing the production of the $LiCF_3SO_3$ samples (obtained from the appropriate companies) showed that the major impurity in all cases was lithium fluoride (LiF). A DSC trace of LiF between 293 K and 393 K was found to be featureless. This suggests that there may be some phase change behaviour in polycrystalline $LiCF_3SO_3$ itself although the proposed crystal structure[16] provides no evidence for this. This may be responsible for endotherms reported in studies of O:Li, 12:1 to 5:1 systems which the authors attributed to the presence of a 7:1 stoichiometric complex. This is an area for further work.

6.4 A ^{19}F Spin-lattice Relaxation Study of 3.5:1 and 9:1 PEO/$LiCF_3SO_3$ Systems

Experimental

A ^{19}F spin-lattice relaxation study of the 3.5:1 and 9:1 PEO/$LiCF_3SO_3$ systems was carried out over the temperature range 200 K to 340 K. The amount of ^{19}F in these samples was considerably less than that present in the study of the pure salt, and to maximize signal amplitudes the maximum ^{19}F frequency available (55.93 MHz) was used. A $P_x(90)$-t-$P_x(90)$–τ-$P_y(90)$-t´ pulse sequence was used, with τ = 15 μs, as described in Chapter 3. The spin-lattice relaxation time values were obtained from the initial 20% of nuclear magnetization recoveries to obtain results independent of the effects of cross-correlation, as described in Chapter 5.

Results

Figure 6.6 shows the temperature dependence of the ^{19}F spin-lattice relaxation behaviour presented in the form of a plot of $\ln(T_1(^{19}F))$ versus inverse temperature for both PEO/$LiCF_3SO_3$ samples. For comparison the results for polycrystalline $LiCF_3SO_3$ are also included in the plot. The character, depth and corresponding temperature of $T_1(^{19}F)$ minima are summarized in Table 6.1.

Table 6.1 The character, depth and corresponding temperature of experimentally determined $T_1(^{19}F)$ minima

Sample	Minima	$T_1(^{19}F)$/ms	T/K
$LiCF_3SO_3$	single	122	272
3.5:1	double	122,168	272,222
9:1	double	130,165	270,222

Qualitative Discussion

The ^{19}F spin-lattice relaxation behaviour of the 3.5:1 and 9:1 PEO/$LiCF_3SO_3$ systems is very similar. This is in good agreement with the XRD and DSC results described in Section 6.3, which suggest that the 9:1 sample is similar to the 3.5:1 sample, but with extra PEO present.

A previous ^{19}F spin-lattice relaxation study[9] found no evidence of a double minimum in the ^{19}F spin-lattice relaxation behaviour of the 3.5:1 or 9:1 PEO/$LiCF_3SO_3$ systems. However, in this work, the temperature increment between measurements of $T_1(^{19}F)$ was of the order of ~25 K. The temperature difference between the minima shown in Figure 6.6 is ~50 K. Thus, it could well be that the minimum behaviour may have been missed in this previous study, since only two data points were collected in the relevant temperature range. There is also the possibility that non-critical measurement of $T_1(^{19}F)$ in the presence of cross-correlations may have masked this feature. However, although a double minimum was not observed, the $\ln((T_1(^{19}F))$ versus inverse

temperature plot did span a temperature range some 40 K larger than that obtained for the polycrystalline $LiCF_3SO_3$ sample. This is consistent with the behaviour observed in the present work.

One possibility is that the observed double minimum behaviour is due to the presence of ^{19}F nuclei in two distinct motional environments. It would appear that, if this is the case, one environment is crystalline with similar potential barriers hindering the CF_3 group reorientation as in the polycrystalline $LiCF_3SO_3$. This is shown by the coincidence of the first minima in the 3.5:1 and 9:1 $PEO/LiCF_3SO_3$ systems and the pure salt minimum. To a good approximation then, the remaining environment will have a ^{19}F spin-lattice relaxation behaviour described by

$$\left(\frac{1}{T_1}\right)_{OTHER} = \left(\frac{1}{T_1}\right)_{PEO/LiCF_3SO_3} - \left(\frac{1}{T_1}\right)_{LiCF_3SO_3} \qquad (6.1)$$

The result of the separation of the two contributions is shown in Figure 6.7. A two environment model would seem to be unlikely as the realistic source of $T_1(^{19}F)$ double minimum behaviour in 3.5:1 and 9:1 $PEO/LiCF_3SO_3$ systems, as the activation energy for the motional process in the second environment would have to be roughly an order of magnitude greater than that found in polycrystalline $LiCF_3SO_3$.

A more realistic model is that the observed double minimum in the ^{19}F spin-lattice relaxation behaviour can be accounted for by ^{19}F-^1H cross-relaxation processes; that is, the ^{19}F spins in the CF_3 groups of the $CF_3SO_3^-$ anions interact with the ^1H spins of the PEO chain. This behaviour can give rise to non-exponential nuclear magnetization recoveries, although it should be remembered that to provide $T_1(^{19}F)$ values independent of the effects of cross-correlation they were measured using the initial gradient method described in Chapter 5. In this respect the analysis of both, (i) low temperature ^{19}F nuclear magnetization

recoveries, where the effects of cross-correlation are minimal, and (ii) ^{1}H nuclear magnetization recoveries; are important. Figure 6.8 shows that the ^{19}F nuclear magnetization recovery in the 3.5:1 PEO/$LiCF_3SO_3$ system measured at 190 K, is close to single exponential for about 80% of the recovery. The results of ^{1}H n.m.r. experiments are described in detail in Chapter 8, but typical ^{1}H magnetization recoveries in the 3.5:1 PEO/$LiCF_3SO_3$ system are shown in Figure 6.9. These ^{1}H magnetization recoveries are close to single exponential. ^{19}F-^{7}Li cross-relaxation can be neglected on the basis that it did not contribute significantly to the spin-lattice relaxation behaviour in polycrystalline $LiCF_3SO_3$.

In the next section a dynamic model for the ^{19}F spin-lattice relaxation behaviour in the 3.5:1 PEO/$LiCF_3SO_3$ system is considered in which ^{19}F-^{1}H cross-relaxation is important.

6.5 A Dynamic Model for the ^{19}F Spin-lattice Relaxation Behaviour in a 3.5:1 PEO/$LiCF_3SO_3$ system Including a General Treatment of Heteronuclear Spin-Lattice Relaxation

To develop a model of ^{19}F spin-lattice relaxation behaviour in PEO/$LiCF_3SO_3$ systems in which the modulation of ^{19}F-^{1}H dipolar interactions play an important role, it is necessary to understand the latter in some detail. In particular it is important to determine the characteristic features should be observed when such interactions make a contribution. As a first step a model two-spin system is considered. It should be noted that this discussion is also relevant to ^{7}Li-^{19}F interactions, encountered later in Chapter 7.

Nuclear Spin-lattice Relaxation in a Model System of Two Unlike, Dipolar-Coupled, Spin $I = \frac{1}{2}$ Nuclei

For two unlike dipolar coupled spin $I = \frac{1}{2}$ nuclei, denoted by (1) and (2), the time evolution of longitudinal nuclear magnetizations can be described by two coupled differential equations (Chapter 2).

$$\frac{d}{dt} < I_z^{(1)} > = -(w_0 + 2w_1 + w_2)\ (<I_z^{(1)} > - I_\infty^{(1)}) - (w_2 - w_0)(<I_z^{(2)} > - I_\infty^{(2)})$$

and

$$\frac{d}{dt} < I_z^{(2)} > = -(w_0 + 2w_1' + w_2)\ (< I_z^{(2)} > - I_\infty^{(2)}) - (w_2 - w_0)(< I_z^{(1)} > - I_\infty^{(1)})$$

More generally these equations can be written as

$$\frac{d}{dt} < I_z^{(1)} > = -\frac{1}{T_1^{(11)}}\ (< I_z^{(1)} > - I_\infty^{(1)}) - \frac{1}{T_1^{(12)}}\ (< I_z^{(2)} > - I_\infty^{(2)}) \qquad (6.2)$$

$$\frac{d}{dt} < I_z^{(2)} > = -\frac{1}{T_1^{(22)}}\ (< I_z^{(2)} > - I_\infty^{(2)}) - \frac{1}{T_1^{(21)}}\ (< I_z^{(1)} > - I_\infty^{(1)}) \qquad (6.3)$$

where $T_1^{(11)}$ is the spin-lattice relaxation time corresponding to the total contribution of all mechanisms returning longitudinal magnetization to spin (1), which are dependent upon the longitudinal magnetization of spin (1); and similarly for $T_1^{(22)}$. $T_1^{(12)}$ is the spin-lattice relaxation time corresponding to the total contribution of all mechanisms returning longitudinal magnetization to spin (1), which are dependent upon the longitudinal magnetization of spin (2), and similarly for $T_1^{(21)}$. Equations (6.2) and (6.3) can be rewritten as

$$(\mathcal{D} + a) < I_z^{(1)} > + b< I_z^{(2)} > = aI_\infty^{(1)} + bI_\infty^{(2)} \qquad (6.4)$$

$$(\mathcal{D} + c) < I_z^{(2)} > + d < I_z^{(1)} > = cI_\infty^{(2)} + d\ I_\infty^{(1)} \qquad (6.5)$$

where $\mathcal{D} = d/dt$, $a = 1/T_1^{(11)}$, $b = 1/T_1^{(12)}$, $c = 1/T_1^{(22)}$ and $d = 1/T_1^{(21)}$.

Equations (6.4) and (6.5) can be represented in matrix form by

$$\begin{pmatrix} \mathcal{D}+a & b \\ d & \mathcal{D}+c \end{pmatrix}\begin{pmatrix} < I_z^{(1)} > \\ < I_z^{(2)} > \end{pmatrix}=\begin{pmatrix} aI_\infty^{(1)} + bI_\infty^{(2)} \\ cI_\infty^{(2)} + dI_\infty^{(1)} \end{pmatrix} \tag{6.6}$$

and this equation can be solved by the method described in Appendix 1.

Thus

$$< I_z^{(1)} > = \begin{vmatrix} aI_\infty^{(1)} + bI_\infty^{(2)} & b \\ cI_\infty^{(2)} + dI_\infty^{(1)} & \mathcal{D}+c \end{vmatrix} \Big/ \begin{vmatrix} \mathcal{D}+a & b \\ d & \mathcal{D}+c \end{vmatrix} \tag{6.7}$$

$$< I_z^{(2)} > = \begin{vmatrix} \mathcal{D}+a & aI_\infty^{(1)} + bI_\infty^{(2)} \\ d & cI_\infty^{(2)} + dI_\infty^{(1)} \end{vmatrix} \Big/ \begin{vmatrix} \mathcal{D}+a & b \\ d & \mathcal{D}+c \end{vmatrix} \tag{6.8}$$

Multiplying out the determinants gives

$$\{\mathcal{D}^2 + (a+c)\mathcal{D} + (ac-bd)\} < I_z^{(1)} > = (aI_\infty^{(1)} + bI_\infty^{(2)})\,(\mathcal{D}+c) - b(cI_\infty^{(2)} + dI_\infty^{(1)}) \tag{6.9}$$

$$\{\mathcal{D}^2 + (a+c)\mathcal{D} + (ac-bd)\} < I_z^{(2)} > = (cI_\infty^{(2)} + dI_\infty^{(1)})\,(\mathcal{D}+a) - b(aI_\infty^{(1)} + bI_\infty^{(2)}) \tag{6.10}$$

Putting $\mathcal{D} = d/dt$, and noting $\mathcal{D}$ (const) = 0, gives two second order differential equations

$$\frac{d^2}{dt^2} < I_z^{(1)} > + (a+c)\frac{d}{dt} < I_z^{(1)} > + (ac-bd) < I_z^{(1)} > = (ac-bd)\, I_\infty^{(1)} \tag{6.11}$$

$$\frac{d^2}{dt^2} < I_z^{(2)} > + (a+c)\frac{d}{dt} < I_z^{(2)} > + (ac-bd) < I_z^{(2)} > = (ac-bd)\, I_\infty^{(2)} \tag{6.12}$$

Second order differential equations (6.11) and (6.12) are solved with the use of an auxillary equation and a trial solution. Hence, the solution of equation (6.11) is given by

$$< I_z^{(1)} > = A\exp(-\lambda_1 t) + B\exp(-\lambda_2 t) + C + I_\infty^{(1)} \qquad (6.13)$$

where

$$\lambda_{1,2} = 1/2\{-(a+c) \pm ((a+c)^2 - 4(ac-bd))^{\frac{1}{2}}\} \qquad (6.14)$$

For the condition $t = \infty$, then $< I_z^{(1)} > = I_\infty^{(1)}$. Substitution of this condition into equation (6.13) gives $C = 0$, and similarly for the solution of equation (6.12). In general then

$$< I_z^{(1)} > - I_\infty^{(1)} = A\exp(-\lambda_1 t) + B\exp(-\lambda_2 t) \qquad (6.15)$$

and

$$< I_z^{(2)} > - I_\infty^{(2)} = A'\exp(-\lambda_1 t) + B'\exp(-\lambda_2 t) \qquad (6.16)$$

The nuclear magnetization recoveries of both spins are double exponential, with characteristic decay constants λ_1 and λ_2, corresponding to the reciprocal values of the observable spin-lattice relaxation times. Substitution of the explicit values of a, b, c and d into equation (6.14), gives the decay constants as

$$\lambda_{1,2} = \frac{1}{2}\left\{\frac{1}{T_1^{(11)}} + \frac{1}{T_1^{(22)}} \pm \left[\left(\frac{1}{T_1^{(11)}} + \frac{1}{T_1^{(22)}}\right)^2 - 4\left(\frac{1}{T_1^{(11)}}\frac{1}{T_1^{(22)}} - \frac{1}{T_1^{(12)}}\frac{1}{T_1^{(21)}}\right)\right]^{\frac{1}{2}}\right\} \qquad (6.17)$$

where λ_1 takes the positive sign. These solutions are also the eigenvalues of the relaxation matrix:

$$\begin{pmatrix} (T_1^{(11)})^{-1} & (T_1^{(12)})^{-1} \\ (T_1^{(21)})^{-1} & (T_1^{(22)})^{-1} \end{pmatrix} \qquad (6.18)$$

found by solving the determinant equation

$$\begin{vmatrix} (T_1^{(11)})^{-1} - \lambda & (T_1^{(12)})^{-1} \\ (T_1^{(21)})^{-1} & (T_1^{(22)})^{-1} - \lambda \end{vmatrix} = 0 \qquad (6.19)$$

$$((T_1^{(11)-1} - \lambda)((T_1^{(22)})^{-1} - \lambda) - (T_1^{(12)})^{-1}(T_1^{(21)})^{-1} = 0 \qquad (6.20)$$

This two spin treatment can be extended to the more general case of a multi-spin system, assuming that pairwise interactions can be summed; that is, there are no cross-correlations.

The spin-lattice relaxation time $T_1^{(11)}$, defined previously, can be further reduced to two components. Firstly, there is a spin-lattice relaxation time corresponding to homonuclear interactions returning longitudinal magnetization to spin (1), which are dependent on the longitudinal magnetization of spin (1). These include homonuclear dipolar interactions which are denoted here by $T_1^{(111)}$. There is also a spin-lattice relaxation time corresponding to heteronuclear interactions returning longitudinal magnetization to spin (1), where the returning magnetization is again dependent upon the longitudinal magnetization of spin (1), but the process is mediated by spin (2). This is denoted here by $T_1^{(121)}$, and includes heteronuclear dipolar interactions. So,

$$\frac{1}{T_1^{(11)}} = \frac{1}{T_1^{(111)}} + \frac{1}{T_1^{(121)}} \tag{6.21}$$

and similarly

$$\frac{1}{T_1^{(22)}} = \frac{1}{T_1^{(222)}} + \frac{1}{T_1^{(212)}} \tag{6.22}$$

Equations (6.21) and (6.22) can be written in the form

$$\lambda_{11} = \lambda_{111} + \lambda_{121} \tag{6.23}$$

and

$$\lambda_{22} = \lambda_{222} + \lambda_{212} \tag{6.24}$$

The substitution of these expressions into equation (6.17) gives

$$\lambda_{1,2} = \tfrac{1}{2}\{(\lambda_{111} + \lambda_{121} + \lambda_{222} + \lambda_{212}) \pm [(\lambda_{111} + \lambda_{121} - \lambda_{222} - \lambda_{212})^2 + 4\lambda_{12}\,\lambda_{21}]^{\frac{1}{2}}\} \tag{6.25}$$

In general the notation described in equations (6.21) and (6.22) is not used in other reported studies[19-26]. However, care should be taken when studying the literature, as the notation used is not always consistent. Generally I and S are used to label two spins, as opposed to (1) and (2). $(T_1^{(II)})^{-1}$ is often used as an element of the relaxation matrix, corresponding to $(T_1^{(11)})^{-1}$ in this thesis. However, λ_{II} is also used, not to represent $(T_1^{II})^{-1}$, but to denote the quantity referred to in this thesis as $(T_1^{(121)})^{-1}$. In such cases λ_I is equivalent to $(T_1^{(111)})^{-1}$. The notation used in this thesis is designed to avoid any confusion between the inverse of the total spin-lattice relaxation time for the longitudinal magnetization recovery of a spin dependent on its own longitudinal magnetization, and its hetronuclear contribution.

The coefficients in equations (6.15) and (6.16) are dependent on the boundary conditions of the system, that is, the initial conditions imposed by the pulse sequence used. Substitution of equations (6.15) and (6.16) into equations (6.2) and (6.3) gives

$$-\lambda_1 A\exp(-\lambda_1 t) - \lambda_2 B\exp(-\lambda_2 t) = (-\lambda_{111} - \lambda_{121})(A\exp(-\lambda_1 t) + B\exp(-\lambda_2 t)) - \lambda_{12}(A'\exp(-\lambda_1 t) + B'\exp(-\lambda_2 t)) \quad (6.26)$$

and

$$-\lambda_1 A'\exp(-\lambda_1 t) - \lambda_2 B'\exp(-\lambda_2 t) = (-\lambda_{222} - \lambda_{212})(A'\exp(-\lambda_1 t) + B'\exp(-\lambda_2 t)) - \lambda_{21}(A\exp(-\lambda_1 t) + B\exp(-\lambda_2 t)) \quad (6.27)$$

These general equations can be compared with initial conditions by setting $t = 0$; giving

$$-\lambda_1 A - \lambda_2 B = (-\lambda_{111} - \lambda_{121})(A+B) - \lambda_{12}(A'+B') \quad (6.28)$$

$$-\lambda_1 A' - \lambda_2 B' = (-\lambda_{222} - \lambda_{212})(A'+B') - \lambda_{21}(A+B) \quad (6.29)$$

$$-\lambda_1 A' - \lambda_2 B' = (-\lambda_{222} - \lambda_{212})(A' + B') - \lambda_{21}(A+B) \qquad (6.29)$$

For a 90° pulse only resonant for the (1) spins, applied at t = 0, equations (6.15) and (6.16) give

$$< I_z^{(1)} > - I_\infty^{(1)} = A + B = 1 \qquad (6.30)$$

$$< I_z^{(2)} > - I_\infty^{(2)} = A' + B' = 0 \qquad (6.31)$$

Substitution of these conditions into equation (6.28) gives

$$-\lambda_1 A - \lambda_2(1-A) = -\lambda_{111} - \lambda_{121}$$

$$A(\lambda_2 - \lambda_1) = -\lambda_{111} - \lambda_{121} + \lambda_2$$

$$A = (\lambda_{111} + \lambda_{121} - \lambda_2)/(\lambda_1 - \lambda_2) \qquad (6.32)$$

so that substitution into equation (6.30) gives

$$B = 1-A = 1 - \frac{(\lambda_{111} + \lambda_{121} - \lambda_2)}{(\lambda_1 - \lambda_2)} = (\lambda_1 - \lambda_{111} - \lambda_{121})/(\lambda_1 - \lambda_2) \qquad (6.33)$$

The substitution of equations (6.30) and (6.31) into equation (6.29) gives

$$-\lambda_1 A' + \lambda_2 A' = -\lambda_{12}$$

$$A' = \lambda_{12}/(\lambda_1 - \lambda_2) \qquad (6.34)$$

$$B' = -\lambda_{12}/(\lambda_2 - \lambda_2) \qquad (6.35)$$

Similarly, for a 90° pulse only resonant for the (2) spins, applied at t = 0

$$A' = (\lambda_{222} + \lambda_{212} - \lambda_2)/(\lambda_1 - \lambda_2)$$
$$B' = (\lambda_1 - \lambda_{222} - \lambda_{212})/(\lambda_1 - \lambda_2) \qquad (6.36)$$
$$A = \lambda_{12}/(\lambda_1 - \lambda_2);\ B = -\lambda_{12}/(\lambda_1 - \lambda_2)$$

It can be seen from equation (6.25) that

and hence

$$\lambda_{222} + \lambda_{212} - \lambda_2 = \lambda_1 - \lambda_{111} - \lambda_{121} \qquad (6.38)$$

so that comparing equations (6.36) with (6.32) and (6.33), it can be seen that for a 90° pulse resonant only for spin (2), the coefficients of the two exponential functions which contribute to the nuclear magnetization recovery, interchange compared with those for a 90° pulse resonant only for spin (1).

The components λ_{111}, λ_{121}, λ_{12} and λ_{222}, λ_{212}, λ_{21} determine the observable spin-lattice relaxation times and the form of the longitudinal magnetization recoveries. These components can be written in a form involving the motionally 'averaged out' part of the dipolar second moment[23,27,28]. The general validity of these reduced second moment relaxation expressions has been investigated[29]. A set of conditions were derived based on motional probabilities that must be satisfied for the general form of a relaxation expression to simplify to one involving the reduced second moment. The required conditions are always satisfied for intramolecular contributions to spin-lattice relaxation due to a single motional process, and for the spin-lattice relaxaton of a stationary group of nuclei due to a single motional process of a nearby group of nuclei. Generally the conditions are not met by intermolecular contributions to spin-lattice relaxation and the degree to which the reduced second moment approach is an approximation depends on the relative sizes of the intra and intermolecular contributions to the total spin-lattice relaxation behaviour. In circumstances where intermolecular spin-lattice relaxation is not dominant, spin-lattice relaxation expressions based on reduced second moments can be expected to give a good approximation to spin-lattice relaxation behaviour.

For a system undergoing restricted reorientation

$$\lambda_{111} = \frac{2}{3}\Delta M_2^{11}\left(\frac{\tau_c}{1+\omega^2\tau_c^2} + \frac{4\tau_c}{1+4\omega^2\tau_c^2}\right) \qquad (6.39)$$

$$\lambda_{121} = \frac{1}{2}\Delta M_2{}^{12}\left(\frac{\tau_c}{1+(\omega_1-\omega_2)^2\tau_c{}^2} + \frac{3\tau_c}{1+\omega_1{}^2\tau_c{}^2} + \frac{6\tau_c}{1+(\omega_1+\omega_2)^2\,\tau_c{}^2}\right) \quad (6.40)$$

$$\lambda_{12} = \frac{1}{2}\Delta M_2{}^{12}\left(\frac{6\tau_c}{1+(\omega_1+\omega_2)^2\tau_c{}^2} - \frac{\tau_c}{1+(\omega_1-\omega_2)^2\tau_c{}^2}\right) \quad (6.41)$$

where ΔM_2 are reduced second moments. Similar expressions exist for λ_{222}, λ_{212} and λ_{21}. For a system undergoing restricted reorientation within a known set of fixed orientations, ΔM_2 can be calculated explicitly by

$$\Delta M_2 = (M_2)_{RL} - (M_2)_{MO} \quad (6.42)$$

where RL denotes rigid lattice, and MO denotes motionally averaged. $(M_2)_{RL}$ involves the sum of internuclear vectors over the lattice, and $(M_2)_{MO}$ involves the sum over the lattice of the time averaged internuclear vectors. This is discussed in some detail in Section 7.3.

Simulation of the ^{19}F Spin-Lattice Relaxation Behaviour in the 3.5:1 PEO/$LiCF_3SO_3$ System.

The specific calculation of reduced second moments for the 3.5:1 PEO/$LiCF_3SO_3$ system is complex since both ^{19}F and ^{1}H nuclei will be undergoing independent thermally activated motions; that is, the ^{19}F nuclei will be involved in the hindered rotation of the CF_3 group and the ^{1}H nuclei in the motion of the polymer backbone. There is no evidence that the $CF_3SO_3^-$ anion can freely tumble in the host polymer or undergo large amplitude librational motions. However, the spin-lattice relaxation behaviour can be simulated over a range of ratios of reduced second moments. In this way, insight into the ^{19}F spin-lattice relaxation behaviour in the 3.5:1 PEO/$LiCF_3SO_3$ system can be gained. This approach can be taken further since specific features can be recognized in the experimentally observed spin-lattice relaxation behaviour. These are described in Table 6.2, which also includes relevant information from the corresponding ^{1}H spin-lattice relaxation study, dealt with in detail in Chapter 8. $T_1(^{19}F)$ minima are referred to as MIN1(^{19}F) and

relevant information from the corresponding ^1H spin-lattice relaxation study, dealt with in detail in Chapter 8. $T_1(^{19}F)$ minima are referred to as MIN1(^{19}F) and MIN2(^{19}F) corresponding to those observed at high and low temperature respectively. The ^1H spin-lattice relaxation time minimum is referred to as MIN3(^1H).

Table 6.2 Features that a proposed spin-lattice relaxation mechanism would be required to simulate

Parameter	Experimentally Determined Feature
Exponentiality of ^{19}F and ^1H Nuclear Magnetization Recoveries	$\geq 80\%$
MIN1(^{19}F)/MIN2(^{19}F)	~ 0.7
MIN3(^1H)/MIN1(^{19}F)	≥ 6

Methodology for the Investigation of Equations Governing Spin-lattice Relaxation in a System Involving Cross-Relaxation

Equations (6.39) to (6.41) and the corresponding expressions for spin (2) show that λ_{111}, λ_{121}, λ_{12}, λ_{222}, λ_{212}, and λ_{21} only depend upon four reduced second moments $\Delta M_2{}^{11}$, $\Delta M_2{}^{12}$, $\Delta M_2{}^{22}$ and $\Delta M_2{}^{21}$. Consequently, the form of the spin-lattice relaxation behaviour only depends upon these four reduced second moments. By taking spin(1) to be ^{19}F and spin (2) to be ^1H, and initially fixing the reduced second moment, $\Delta M_2{}^{11}$, to the experimental value of 3.104×10^9 rad^2 s^{-2} determined for the CF_3 group in polycrystalline $LiCF_3SO_3$; the observable spin-lattice relaxation times and their respective contributions to the form of the nuclear magnetization recoveries can be simulated for the dipolar coupled ^{19}F-^1H system using equations (6.25), (6.32) and (6.33), for differing values of the three ratios $\Delta M_2{}^{11}/\Delta M_2{}^{12}$, $\Delta M_2{}^{11}/\Delta M_2{}^{22}$ and $\Delta M_2{}^{12}/\Delta M_2{}^{21}$. The choice of the value of $M_2{}^{11}$ determines the absolute values of the calculated ^{19}F spin-lattice relaxation times in the simulations, but it does not affect the general form of the simulated relaxation behaviour when specific ratios of reduced second moment are used.

dipolar interactions experienced by the ^{19}F nucleus. The validity of this assumption will be discussed again in due course. As an initial step ^{19}F spin-lattice relaxation behaviour was simulated for a broad range of reduced second moment ratios, as given in Table 6.3.

Table 6.3 Values of ratios used in combinations to produce initial simulations

Parameter	Ratio Available for Simulation				
$\Delta M_2^{11}/\Delta M_2^{22}$	0.2	0.5	1	5	10
$\Delta M_2^{12}/\Delta M_2^{21}$	0.2	0.5	1	5	10
$\Delta M_2^{11}/\Delta M_2^{12}$	0.2	0.5	1	5	10

The range of ratios in Table 6.3 is such that 125 spin-lattice relaxation simulations can be carried out. It was clear from examining selected files that the experimental features described in Table 6.2 occur only for a restricted set of reduced second moment ratios. Figures 6.10 to 6.13 illustrate this point. The solid and dotted curves represent observable spin-lattice relaxation times $(\lambda_1)^{-1}$ and $(\lambda_2)^{-1}$ respectively. The solid circles and empty circles represent the coefficients, A and B, from equations (6.15) and (6.16).

The relevance of these simulations can be explained with reference to the simulated spin-lattice relaxation behaviour of a dipolar coupled ^{19}F-^{1}H system following a 90° pulse only resonant for ^{19}F, for fixed ratios of reduced second moments. The ^{19}F nuclear magnetization recovery will be given, for a particular value of correlation time, by the constant A (given by the filled circles) multiplied by an exponential function with decay constant λ_1 (given by the inverse value of the solid curve), plus another exponential function with decay constant λ_2 (given by the inverse of the value of the dotted curve), multiplied by the constant B (given by the open circles). So that in principle both observable spin-lattice relaxation times can be extracted from the ^{19}F nuclear magnetization recovery. However, when A is close to one and B is close to zero the simulated ^{19}F nuclear magnetization recovery will be close to single exponential with decay constant λ_1.

As discussed in Table 6.2 this would be consistent with the experimentally observed ^{19}F spin-lattice relaxation behaviour. For a 90° pulse only resonant for ^{1}H, the coefficients A and B interchange, as shown by equations (6.36) and (6.38), such that the ^{1}H nuclear magnetization recovery would be given, for a particular correlation time, by the constant B (given by the open circles) multiplied by an exponential function with decay constant λ_1 (given by the inverse of the value of the solid curve) plus another exponential function with decay constant λ_2 (given by the inverse of the value of the dotted curve) multiplied by the constant A (given by the filled circles). Once again, in principle both observable spin-lattice relaxation times can be extracted from the ^{1}H nuclear magnetization recovery. However, when A is close to 1 and B is close to zero, the simulated ^{1}H nuclear magnetization recovery will be close to single exponential with decay constant λ_2. As discussed in Table 6.2, this would be consistent with the experimentally observed ^{1}H spin-lattice relaxation behaviour.

The three digit number in the bottom left hand corner of Figures 6.10 to 6.13 indicate the ratios of reduced second moments used. The first digit gives $\Delta M_2^{11}/\Delta M_2^{22}$; the second $\Delta M_2^{12}/\Delta M_2^{21}$; and the third $\Delta M_2^{11}/\Delta M_2^{12}$. Figure 6.10 shows simulations for $\Delta M_2^{11} = \Delta M_2^{22} = \Delta M_2^{12} = \Delta M_2^{21}$. Clearly the functional form of the observable spin-lattice relaxation time data is unlike that found experimentally for the ^{19}F spin-lattice relaxation behaviour in the 3.5:1 PEO/$LiCF_3SO_3$ system. The second minimum of the solid curve, corresponding to long correlation time, or low temperature, is lower than the first, and there is a large degree of non-exponentiality to the magnetization recoveries over a large range of correlation times. Figure 6.11 shows the change when the ratio $\Delta M_2^{11}/\Delta M_2^{12}$ is altered from one to ten. Now the second minimum of the solid curve is higher than the first, the ratio of the two observable spin-lattice relaxation times changes, as does the degree of non-exponentiality in the magnetization recoveries. Figure 6.12 shows the change when $\Delta M_2^{11}/\Delta M_2^{12}$ is

kept at ten, and $\Delta M_2^{11}/\Delta M_2^{22}$ is now changed to five. The ratio of the observable spin-lattice relaxation times is different, and non-exponential magnetization recoveries are only observed at long correlation times, or low temperatures. Figure 6.13 shows the change when $\Delta M_2^{12}/\Delta M_2^{21}$ is now set to five. The degree of non-exponentiality of the magnetization recoveries is very much reduced for these values of reduced second moment ratios.

The results show that the behaviour of both the observable spin-lattice relaxation times, and the coefficients of the exponential components of magnetization recovery, do depend significantly on ratios of reduced second moments. The dependence of specific features of the spin-lattice relaxation behaviour can now be investigated more thoroughly. Observable spin-lattice relaxation time minima are labelled in all further discussion as shown in Figure 6.13

Figure 6.14 is a typical plot of the ratio MIN1/MIN2 as a function of $\Delta M_2^{11}/\Delta M_2^{12}$ and $\Delta M_2^{12}/\Delta M_2^{21}$, for the fixed ratio $\Delta M_2^{11}/\Delta M_2^{22}$ in the range 1-9. The specific value is 6, but over this range the general behaviour on invarient to the choice of this value. Values of MIN1/MIN2 plotted at zero, correspond to an observable spin-lattice relaxation time function with only one minimum, where the second minimum (MIN2) has become a point of inflection. When $\Delta M_2^{11}/\Delta M_2^{22} < 1$ the characteristic shape of the plot is slightly different, as shown in Figure 6.15 for $\Delta M_2^{11}/\Delta M_2^{22} = 0.5$.

The ratio MIN3/MIN1 is shown in Figures 6.16 to 6.19 as a function of $\Delta M_2^{11}/\Delta M_2^{12}$ and $\Delta M_2^{12}/\Delta M_2^{21}$, for fixed ratios of $\Delta M_2^{11}/\Delta M_2^{22}$ given by 9, 6, 3, and 0.5, respectively. The shape of this plot is a function of $\Delta M_2^{11}/\Delta M_2^{22}$, and for $\Delta M_2^{11}/\Delta M_2^{22} \geq 1$ the magnitude of MIN3/MIN1 for a particular combination of the other reduced second moments reduces as $\Delta M_2^{11}/\Delta M_2^{22}$ is reduced. As the ratio becomes <1 the shape of the plot changes drastically and for lower values of $\Delta M_2^{11}/\Delta M_2^{22}$ the magnitude of MIN3/MIN1 increases.

Application to the ^{19}F Spin-lattice Relaxation in the 3.5:1 PEO/$LiCF_3SO_3$ System

The simulations described above and their characteristics can be used to determine the constraints on the reduced second moment ratios that give good agreement with experiment. Figure 6.14 and similar plots suggest that for MIN1/MIN2 ~0.7, then $\Delta M_2^{11}/\Delta M_2^{12}$ ~6. The data plotted in Figure 6.17 suggests that for this value of $\Delta M_2^{11}/\Delta M_2^{12}$, and MIN3/MIN1 ~6 then $\Delta M_2^{11}/\Delta M_2^{22}$ ~5-6. For fixed ratios of the other reduced second moments, as $\Delta M_2^{12}/\Delta M_2^{21}$ increases, MIN1/MIN2 slowly falls, and MIN3/MIN1 increases.

The observable spin-lattice relaxation times and coefficients of the corresponding exponentials contributing to the nuclear magnetization recovery can be examined as a function of $\Delta M_2^{12}/\Delta M_2^{21}$, for probable values of $\Delta M_2^{11}/\Delta M_2^{22}$ and $\Delta M_2^{11}/\Delta M_2^{12}$, as shown by Figures 6.20 and 6.21 respectively. The experimental ratios of system minima are close to experimental values for $\Delta M_2^{12}/\Delta M_2^{21} \leq 10$. Figure 6.21 shows that for $\Delta M_2^{12}/\Delta M_2^{21} \geq 6$, the degree of non-exponentiality of the observed magnetization recovery is less than 15%. Experimentally about 85% of nuclear magnetization recoveries are measured as discussed previously, and simulated recoveries of this form would in reality appear close to single exponential when measured.

A simulation of ^{19}F spin-lattice relaxation behaviour in the 3.5:1 PEO/$LiCF_3SO_3$ system can be carried out using this model with ratios of reduced second moments $\Delta M_2^{11}/\Delta M_2^{22} = 6$, $\Delta M_2^{12}/\Delta M_2^{21} = 6$, and $\Delta M_2^{11}/\Delta M_2^{12} = 6$. In the simulation a value of $M_2^{FF} = 2.388 \times 10^9$ rad^2 s^{-2} was taken, and this is discussed further in Section 6.6. This is shown in Figure 6.22.

The simulation, as already described, was based on a single correlation time. The spin-lattice relaxation time minima occur at $\tau_c = 1.9 \times 10^{-9}$ s and $\tau_c =$ $3{:}9 \times 10^{-8}$ s. Assuming an Arrhenius temperature dependence

$$\tau_c = \tau_0 \exp(E_A/RT) \qquad (6.43)$$

then it is straightforward to derive

$$E_A = (30.33 \pm 0.54) \text{ kJ mol}^{-1}$$

This gives a reasonable value of the pre-exponential factor,

$$\tau_0 = (2.83 \pm 0.61) \times 10^{-15} \text{ s}$$

6.6 Discussion and Conclusions

The functional form of the experimental ^{19}F spin-lattice relaxation times in the 3.5:1 PEO/$LiCF_3SO_3$ system can be modelled by a dipolar relaxation mechanism in which ^{19}F-^1H cross relaxation is important, as shown in Figure 6.22. It must be noted however, that the value of ΔM_2^{FF} used in the simulation was 2.388×10^9 rad^2 s^{-2}. This is different from the value of 3.104×10^9 rad^2 s^{-2}, which was experimentally determined for the CF_3 group in polycrystalline $LiCF_3SO_3$, by 30%. This value was shown to be compatible with purely intramolecular F-F interactions in the pure salt (Chapter 5), and assuming that intramolecular F-F interactions again dominate in the stoichiometric complex, there is a discrepancy.

The simplest explanation of this is that the geometry of the CF_3 group and hence the F-F internuclear distance is different in the PEO/$LiCF_3SO_3$ stoichiometric complex and polycrystalline $LiCF_3SO_3$. The reported CF_3 group geometries from the crystal structures, reported and discussed previously, give sufficiently different F-F distances to account for only about a 12% difference in the strength of interaction. It is difficult, in terms of a simple model, to see how to account for the remainder of the discrepancy.

In reality, the problem of correlation times in cross-relaxing systems will be more complicated where both interacting nuclei are moving independently, as is probably the case in the 3.5:1 PEO/$LiCF_3SO_3$ system. It is not known how the

$$\tau_c = \tau_0 \exp(E_A/RT) \qquad (6.43)$$

then it is straightforward to derive

$$E_A = (30.33 \pm 0.54) \text{ kJ mol}^{-1}$$

This gives a reasonable value of the pre-exponential factor,

$$\tau_0 = (2.83 \pm 0.61) \times 10^{-15} \text{ s}$$

6.6 Discussion and Conclusions

The functional form of the experimental ^{19}F spin-lattice relaxation times in the 3.5:1 PEO/$LiCF_3SO_3$ system can be modelled by a dipolar relaxation mechanism in which ^{19}F-^1H cross-relaxation is important, as shown in Figure 6.22. It must be noted however, that the value of ΔM_2^{FF} used in the simulation was 2.388×10^9 rad^2 s^{-2}. This is different from the value of 3.104×10^9 rad^2 s^{-2}, which was experimentally determined for the CF_3 group in polycrystalline $LiCF_3SO_3$, by 30%. This value was shown to be compatible with purely intramolecular F-F interactions in the pure salt (Chapter 5), and assuming that intramolecular F-F interactions again dominate in the stoichiometric complex, there is a discrepancy.

The simplest explanation of this is that the geometry of the CF_3 group and hence the F-F internuclear distance is different in the PEO/$LiCF_3SO_3$ stoichiometric complex and polycrystalline $LiCF_3SO_3$. The reported CF_3 group geometries from the crystal structures, reported and discussed previously, give sufficiently different F-F distances to account for only about a 12% difference in the strength of interaction. It is difficult, in terms of a simple model, to see how to account for the remainder of the discrepancy.

In reality, the problem of correlation times in cross-relaxing systems will be more complicated where both interacting nuclei are moving independently, as is probably the case in the 3.5:1 PEO/$LiCF_3SO_3$ system. It is not known how the

to probable errors of about 20% in ratios of second moments. To calculate motionally averaged values and hence reduced second moments is complex, as discussed. Nonetheless the rigid lattice values can give some idea of expected relative orders of magnitude of reduced second moments.

It was shown in Chapter 2 that, for a polycrystalline sample the homonuclear rigid lattice second moment of a nucleus of spin I is given, in frequency units, by

$$M_2^{II} = \frac{3}{5}\gamma_I^4\hbar^2 I(I+1)\sum_k \frac{1}{r_{jk}^6} \qquad (6.44)$$

For a heteronuclear interaction between two spins I and S, the rigid lattice second moment is given by

$$M_2^{IS} = \frac{4}{15}\gamma_I^2\gamma_S^2\hbar^2 S(S+1)\sum_k \frac{1}{r_{jk}^6} \qquad (6.45)$$

Using the crystal structure data of the suggested 3:1 PEO/$LiCF_3SO_3$ complex to evaluate the lattice sums in equations (6.44) and (6.45), M_2^{FF}, M_2^{HH}, M_2^{FH} and M_2^{HF} were calculated, summing over all relevant nuclei within a sphere of defined radius centred on the reference spin. This radius was varied from 0.7 to 1.5 nm with a 0.1 nm increment. Figures 6.23 to 6.26 show the results of these calculations for M_2^{FF}, M_2^{HH}, M_2^{FH} and M_2^{HF} respectively for particular ^{19}F and ^{1}H reference spins in the complex crystal structure. In all cases the second moments calculated by summing over a sphere of radius 1.0 nm were less the 1% different to those obtained by using a sphere of 1.5 nm radius and the values approached that obtained for 1.5 nm asymptotically. The calculation was repeated, over a 1.5 nm sphere, for the reference nuclei taking all unique positions in the reported crystal structure; this involved three distinct ^{19}F sites and twelve distinct ^{1}H sites. The results are shown in Figures 6.27 to 6.30. Taking the average values of the unique position rigid lattice second moments the following ratios were obtained:

M_2^{FF}/M_2^{HH} ~0.3, M_2^{FF}/M_2^{FH} ~4 and M_2^{FH}/M_2^{HF} ~4.

These ratios of rigid lattice second moments are not directly comparable with the predicted values of reduced second moment ratios, as the extent to which the respective ^{19}F and ^{1}H second moments are motionally averaged is unclear. However these rigid lattice ratios might be expected to give a broad indication of the probable ratios of reduced second moments. The ratios M_2^{FH}/M_2^{HF} and M_2^{FF}/M_2^{FH} compare reasonably well with those deduced from the analysis of the ^{19}F spin-lattice relaxation behaviour described in Section 6.5. However, the ratio $M_2^{FF}/M_2^{HH} = 0.3$ is very different from the suggested value of ~6. One explanation of this discrepancy may be the oversimplification of using one correlation time in the simulations of spin-lattice relaxation time behaviour as mentioned previously. Strictly the problem would require a different formulation of equations (6.39) to (6.41). This would be an interesting area for a further general study.

The explicit form of the Arrhenius temperature dependence used in the simulation is given by

$$\tau_c = ((2.83 \pm 0.61) \times 10^{-15}\ \text{s})\ \exp((30.33 \pm 0.54)\text{kJ mol}^{-1}/RT) \qquad (6.60)$$

Despite, the simplicity of the model used, the parameters given in this equation compare well with those derived for the CF_3 group in Chapter 5, and in other studies, as shown in Table 6.4.

Table 6.4 - Infinite temperature correlation times for the CF_3 group

Compound	τ_0/s	Ref
3.5:1 PEO/$LiCF_3SO_3$	2.83×10^{-15}	Chapter 6
$LiCF_3SO_3$	3.42×10^{-14}	Chapter 5
$C_6H_5CF_3$	2.30×10^{-14}	31
$CF_3COO^-Ag^+$	2.00×10^{-15}	32

The fact that the ^{19}F spin-lattice relaxation behaviour in the 9:1 PEO/$LiCF_3SO_3$ system also involves ^{19}F-^{1}H cross-relaxation, and the activation energy of

motional processes facilitating the relaxation is greater than the activation energy of CF_3 group reorientation in polycrystalline $LiCF_3SO_3$, suggests that over the temperature range of the study (200-340 K) the entire anion population resides in a stoichiometric crystalline complex (~3.5:1 PEO/$LiCF_3SO_3$). If the anion were present in the amorphous fraction of the system, the activation energy for CF_3 group reorientation, would be greatly reduced, as would the ^{19}F spin-lattice relaxation times, due to motions other than simple hindered reorientation.

A previous study of $LiCF_3SO_3$[9] also shows ^{19}F spin-lattice relaxation time data for 4:1 and 9:1 PEO/$LiCF_3SO_3$ systems with similar activation energy to that found in $LiCF_3SO_3$ (indicated by very similar high temperature gradients). However, this study did not calculate explicit motional parameters, and did not report double minima, as discussed in Section 6.4.

A previous study of the 5:1 PEO/$LiCF_3COO$ system[33] found difficulty in measuring ^{19}F spin-lattice relaxation behaviour and attributed this to long spin-lattice relaxation times. However, the authors reported no narrowing of the ^{19}F resonance line until sample melting, indicating that at temperatures below this, the anion population resides in a crystalline phase.

In studies of mixed salt systems PEO/$LiCF_3SO_3$/NaI[34,35] it has been suggested that the $CF_3SO_3^-$ ions are contained deep in crystalline regions of spherulites. Recrystalization measurements[35] indicated that all the $CF_3SO_3^-$ ions in these systems, of ratio 8:0.5:0.5, reside in a crystalline complex and there is evidence that, in general anion/cation pairs of a particular salt have distinct environments.

It is interesting to note that pulsed field gradient n.m.r. measurements on an 8:1 PEO/$LiCF_3SO_3$ system[36] over the temperature range 428-448 K, show both the anion and the cation to be exhibiting Arrhenius diffusion behaviour. This is shown in Chapter 4 in Figure 4.6. Surprisingly, the anion is found to be more mobile than the cation. The activation energy of the anion diffusion is quoted as 0.261 eV ~ 25

kJ mol^{-1}. This is very similar to the activation energy of CF_3 group reorientation, suggesting there may be a connection between this reorientation and the diffusive motion of the cation. The diffusion coefficients cannot be extrapolated to the temperature range of this study, due to system phase changes over the extrapolated range.

APPENDIX 1

Consider two simultaneous equations given in matrix form by

$$\begin{pmatrix} \alpha_{11} & \alpha_{12} \\ \alpha_{21} & \alpha_{22} \end{pmatrix} \begin{pmatrix} x \\ y \end{pmatrix} = \begin{pmatrix} b_1 \\ b_2 \end{pmatrix}$$

so that

$$(1) \qquad \alpha_{11}\, x + \alpha_{12}\, y = b_1$$

$$(2) \qquad \alpha_{21}\, x + \alpha_{22}\, y = b_2$$

These equations can be solved in the normal way by considering

$$\alpha_{22} \times (1) - \alpha_{12} \times (2)$$

which gives

$$\begin{array}{ll} + & \alpha_{11}\alpha_{22}x + \alpha_{12}\alpha_{22}\, y = b_1\alpha_{22} \\ & \underline{-\alpha_{12}\alpha_{21}\, x - \alpha_{12}\alpha_{22}\, y = -b_2\alpha_{12}} \\ & (\alpha_{11}\alpha_{22} - \alpha_{21}\alpha_{12})x = b_1\alpha_{22} - b_2\alpha_{12} \end{array}$$

which is equivalent to

$$x = \frac{b_1\alpha_{22}q\text{-}b_2\alpha_{12}}{\alpha_{11}\alpha_{22} - \alpha_{21}\alpha_{12}}$$

$$x = \begin{vmatrix} b_1 & \alpha_{12} \\ b_2 & \alpha_{22} \end{vmatrix} \Big/ \begin{vmatrix} \alpha_{11} & \alpha_{12} \\ \alpha_{21} & \alpha_{22} \end{vmatrix}$$

Similarly for y

$$y = \begin{vmatrix} \alpha_1 & b_{12} \\ \alpha_2 & b_{22} \end{vmatrix} \Big/ \begin{vmatrix} \alpha_{11} & \alpha_{12} \\ \alpha_{21} & \alpha_{22} \end{vmatrix}$$

REFERENCES

1 C D Robitaille and D Fauteux
J. Electrochem. Soc., 133, 315, 1986.

2 S M Zahurak, M L Kaplan, E A Rietman, D W Murphy and R J Cava
Macromol., 21, 654, 1988.

3 C A Vincent
Polymer Electrolytes
Prog. Solid St. Chem., 17, 145, 1987.

4 M Minier, C Berthier and W Gorecki
J. Physique, 45, 739, 1984.

5 C Berthier, W Gorecki, M Minier, M B Armand, J M Chabagno and P Rigaud
Solid State Ion., 11, 91, 1983.

6 M Armand
Solid State Ion., 9/10, 745, 1983.

7 M Gauthier, D Faubeux, G Vassort, A Belanger and M Duval
J. Electrochem .Soc. Electrochem. Sci. and Tech.,, (June), 1332, 1985.

8 PSS Prasad, MZA Munshi, B B Owens and W H Smyrl
Solid State Ion., 40/41, 959, 1990.

9 D P Tunstall, A S Tomlin, J R MacCallum and C A Vincent
J. Phys. C. Solid State Phys., 21, 1039, 1988.

10 A Vallee, S Besner, J Prud'homme
Electrochim Acta, 37, 1579, 1992.

11 P Lightfoot, M A Mehta, P G Bruce
Science, 262, 883, 1993.

12 Y Ito, K Miyanchi and T Kudo
J. Phys. Chem. Solids, 48, 161, 1987.

13 J E Weston and B C H Steele
Solid State Ion., 2, 347, 1981.

14 J E Weston and B C H Steele
Solid State Ion., 7, 81, 1982.

15 R C Weast (Ed)
Handbook of Chemistry and Physics
Chemical Rubber Co., 1971.

16 M Tremayne, P Lightfoot, M A Mehta and P G Bruce et al
J. Solid State Chem., 100, 191, 1992.

17 D P Tunstall, A S Tomlin, J R MacCallum and C A Vincent
J. Phys. C Solid State Phys., 21, 1039, 1988.

18 G Stephenson
Mathematical Methods for Science Students
Longman, London 1973.

19 J. Yamauchi and C A McDowell
J. Chem. Phys., 75, 577, 1981.

20 B R McGarvey and S Schlick
Macromol., 17, 2392, 1984.

21 J E Anderson and W P Slichter
J. Chem. Phys., 43, 433, 1965.

22 W E Hull and B D Sykes
J. Chem. Phys., 63, 867, 1975.

23 A Walton, J C Pratt, E C Reynhardt and H E Petch
J. Chem. Phys., 77, 2344, 1982.

24 D E O'Reilly, E M Peterson and T Tsang
Phys. Rev., 160, 333, 1967.

25 S Albert and J A Ripmeester
J. Chem. Phys., 70, 1352, 1979.

26 M Mortimer, E A Moore, D C Apperley and G Oates
J. Chem. Soc. Faraday Trans., 89, 693, 1993.

27 S Albert, H S Gutowsky and J A Ripmeester
J. Chem. Phys., 56, 2844, 1972.

28 G Soda and H Chihara
J. Phys. Soc. Japan, 36, 954, 1974.

29 E A Moore and M Mortimer
J. Mag. Res., 91, 392, 1991.

30 P Lightfoot
Private Communication.

31 J E Anderson and W P Slichter
J. Chem. Phys., 43, 433, 1965.

32 G E Kibrik, I A Kyunslel, V A McKeeva, Yu I Rozenberg and G B Soifer
Sov. Phys. Solid State, 17, 598, 1975.

33 F L Tanzella, W Bailey, D Frydrych and H S Story
Solid State Ion., 5, 681, 1981.

34 D P Tunstall, A S Tomlin, F M Gray, J R MacCallum and C A Vincent
J. Phys. Condens. Matt., 1, 4035, 1989.

35 A J Tomlin, J R MacCallum, D P Tunstall and C A Vincent
J. Phys. Condens. Matt., 1, 7483, 1989.

36 S Bhattacharja, S W Smoot and D H Whitmore
Solid State Ion., 18\19, 306, 1986.

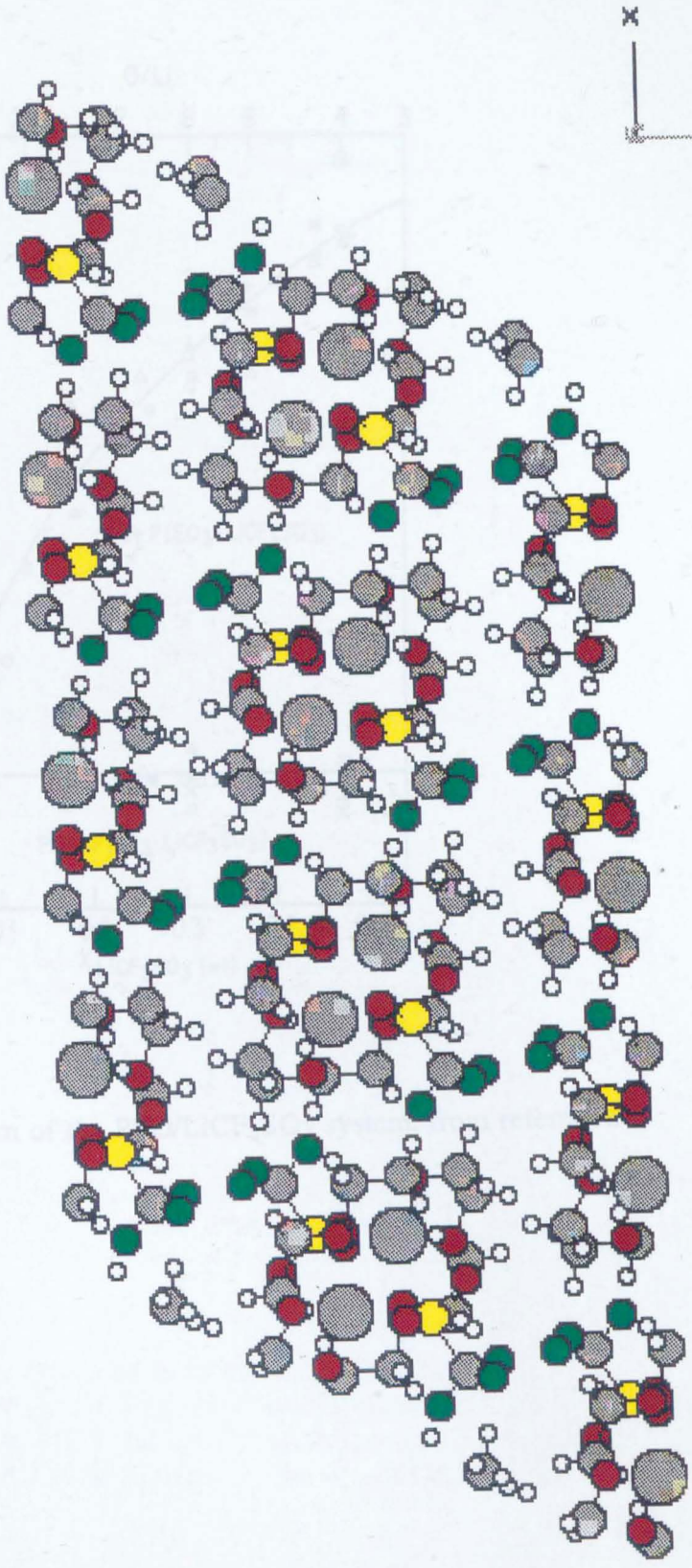

Figure 6.1 The proposed crystal structure of a 3:1 PEO/$LiCF_3SO_3$ stoichiometric complex, from reference 11. ^{19}F atoms are represented as green, ^{16}O as red, ^{12}S as yellow, ^{1}H as white, ^{12}C as grey and ^{7}Li as the larger grey spheres.

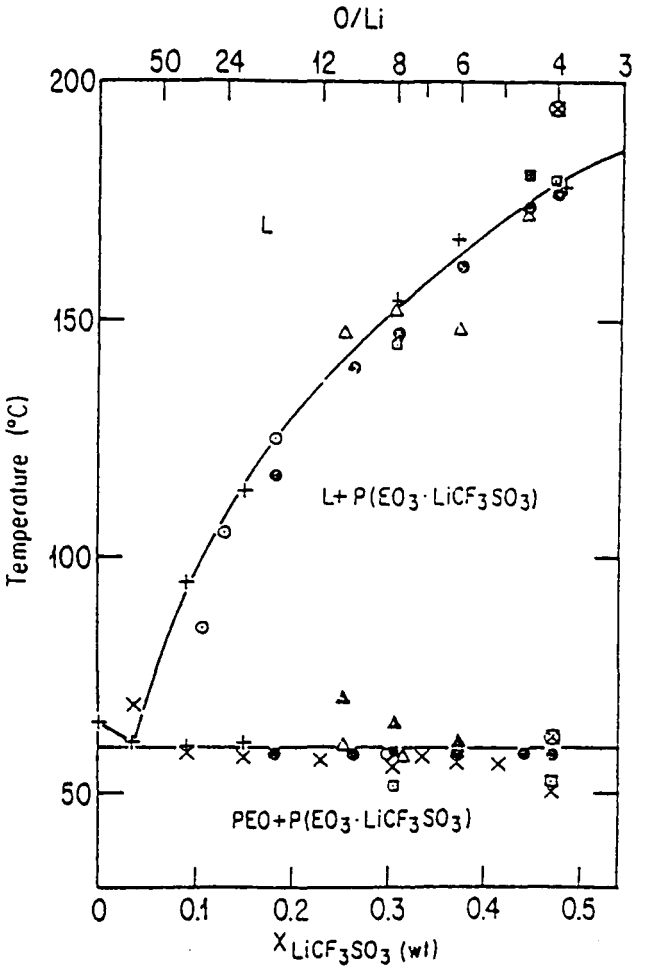

Figure 6.2 Phase diagram of the PEO/$LiCF_3SO_3$ system, from reference 1.

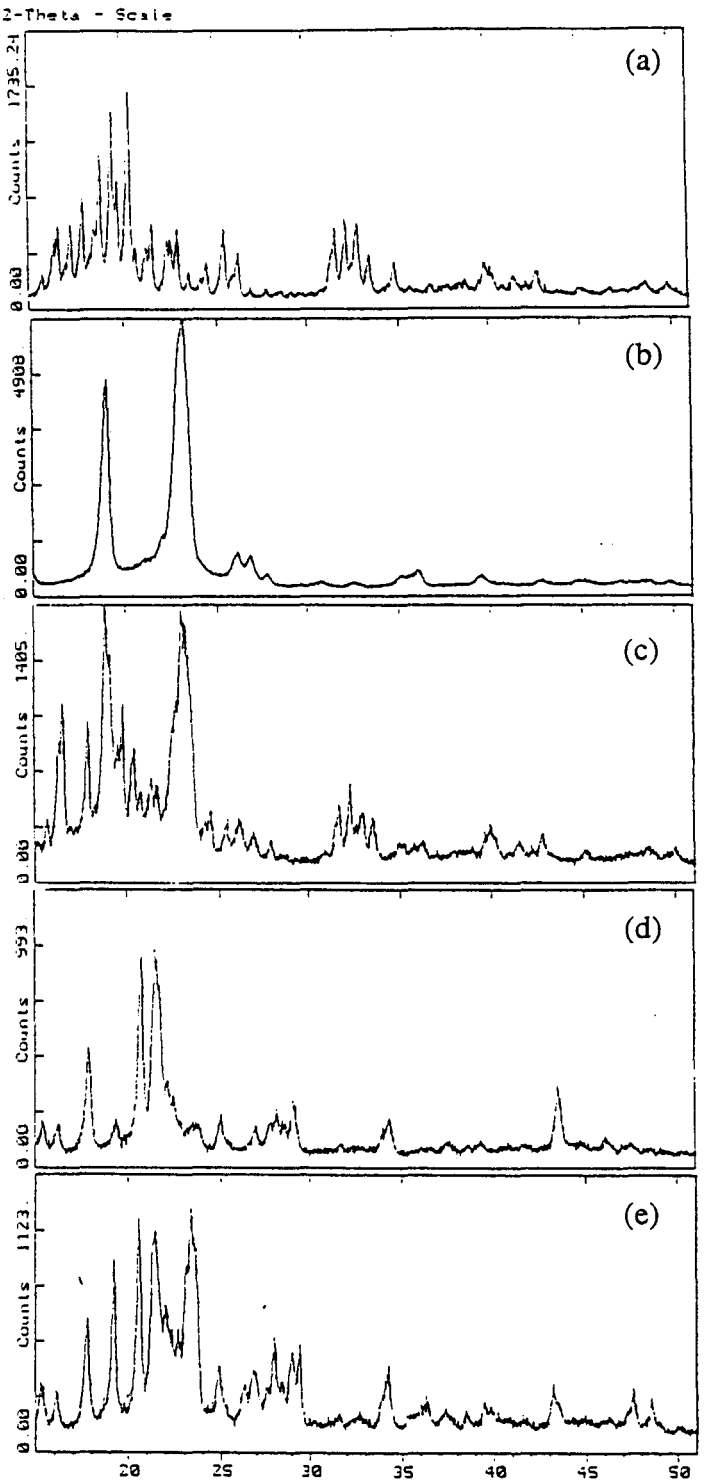

Figure 6.3 XRD spectra, measured at room temperature, of (a) polycrystalline $LiCF_3SO_3$, (b) polycrystalline PEO, (c) a discrete mix of PEO and $LiCF_3SO_3$ in the ratio 3.5:1, (d) the 3.5:1 PEO/$LiCF_3SO_3$ system, (e) the 9:1 PEO/$LiCF_3SO_3$ system.

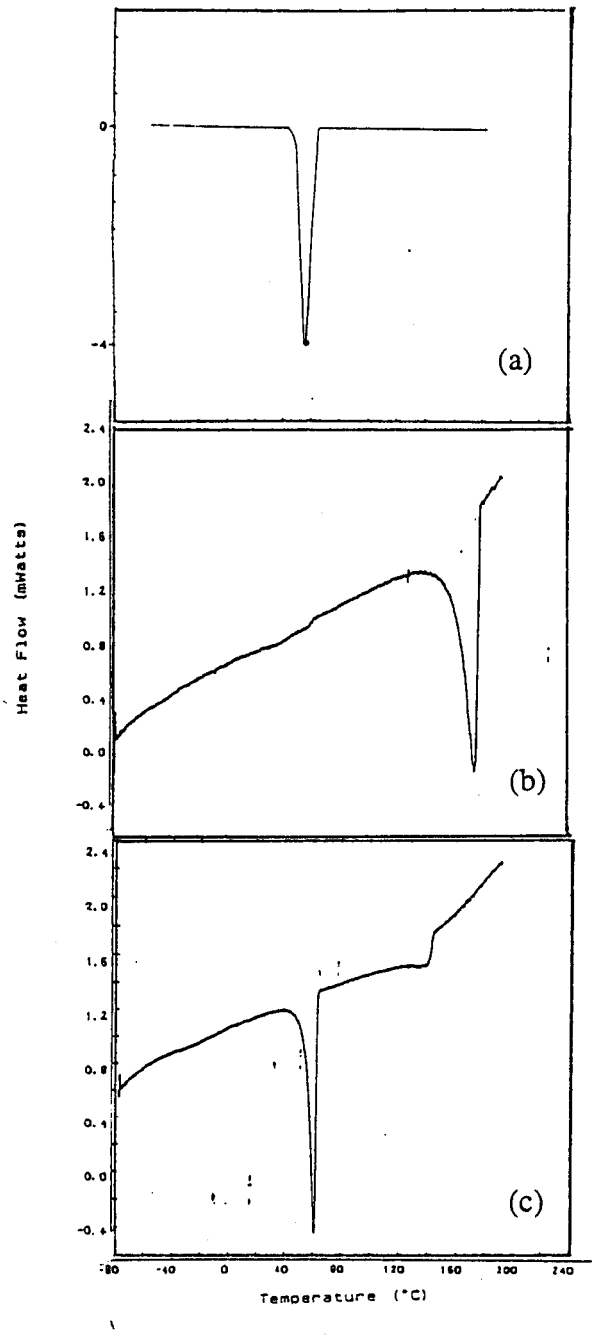

Figure 6.4 DSC traces of (a) polycrystalline PEO, and (b) and (c), the 3.5:1 and 9:1 PEO/$LiCF_3SO_3$ systems, over the temperature range 193 K to 473 K.

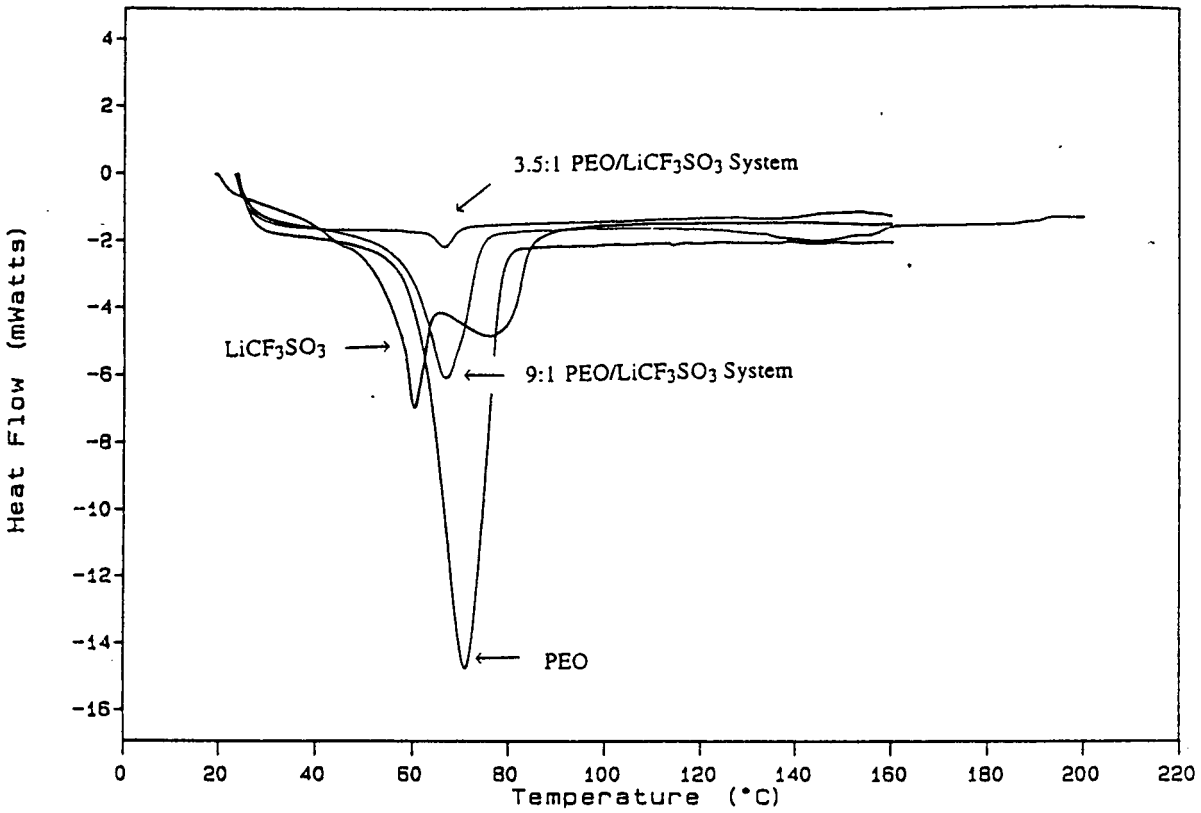

Figure 6.5 DSC traces of polycrystalline PEO, the 3.5:1 and 9:1 PEO/$LiCF_3SO_3$ systems, and polycrystalline $LiCF_3SO_3$, over the temperatue range 293 K to 393 K.

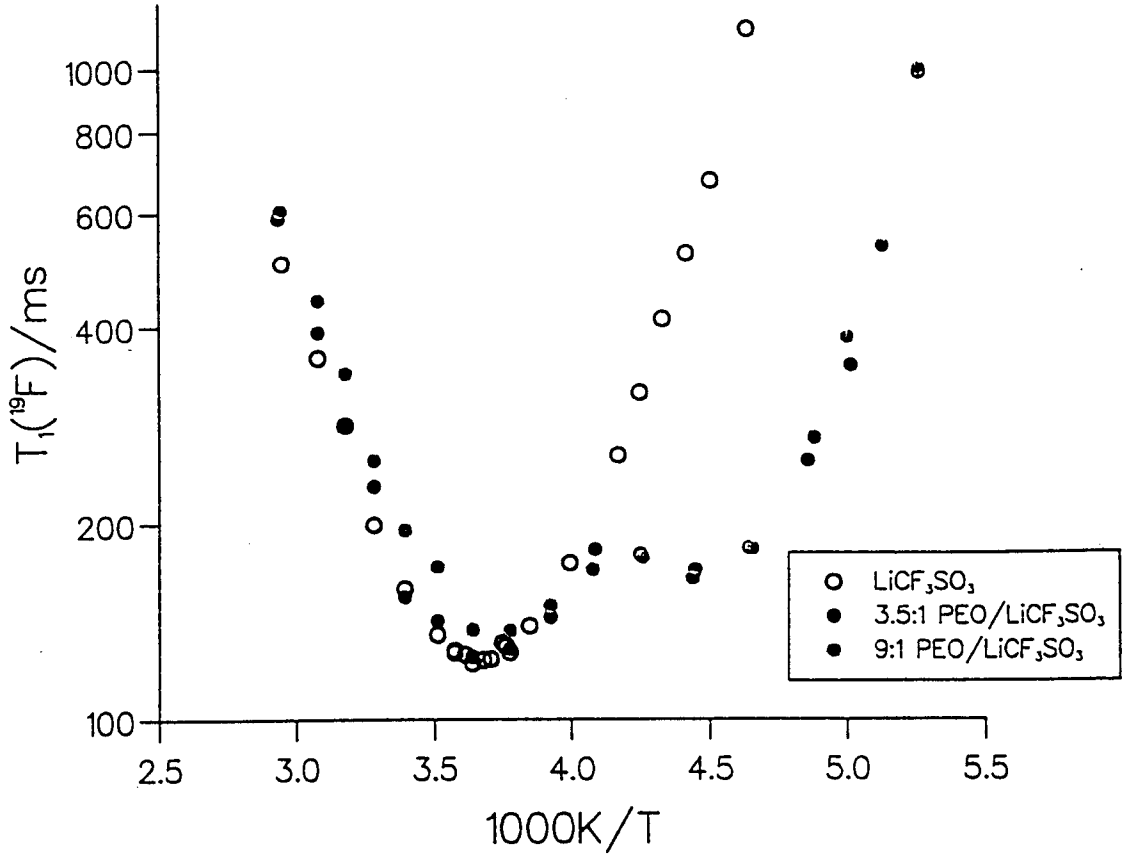

Figure 6.6 The temperature dependence of the ^{19}F spin-lattice relaxation behaviour, measured at 55.93 MHz, for the 3.5:1 and 9:1 $PEO/LiCF_3SO_3$ systems. For comparison the results for polycrystalline $LiCF_3SO_3$ are also included.

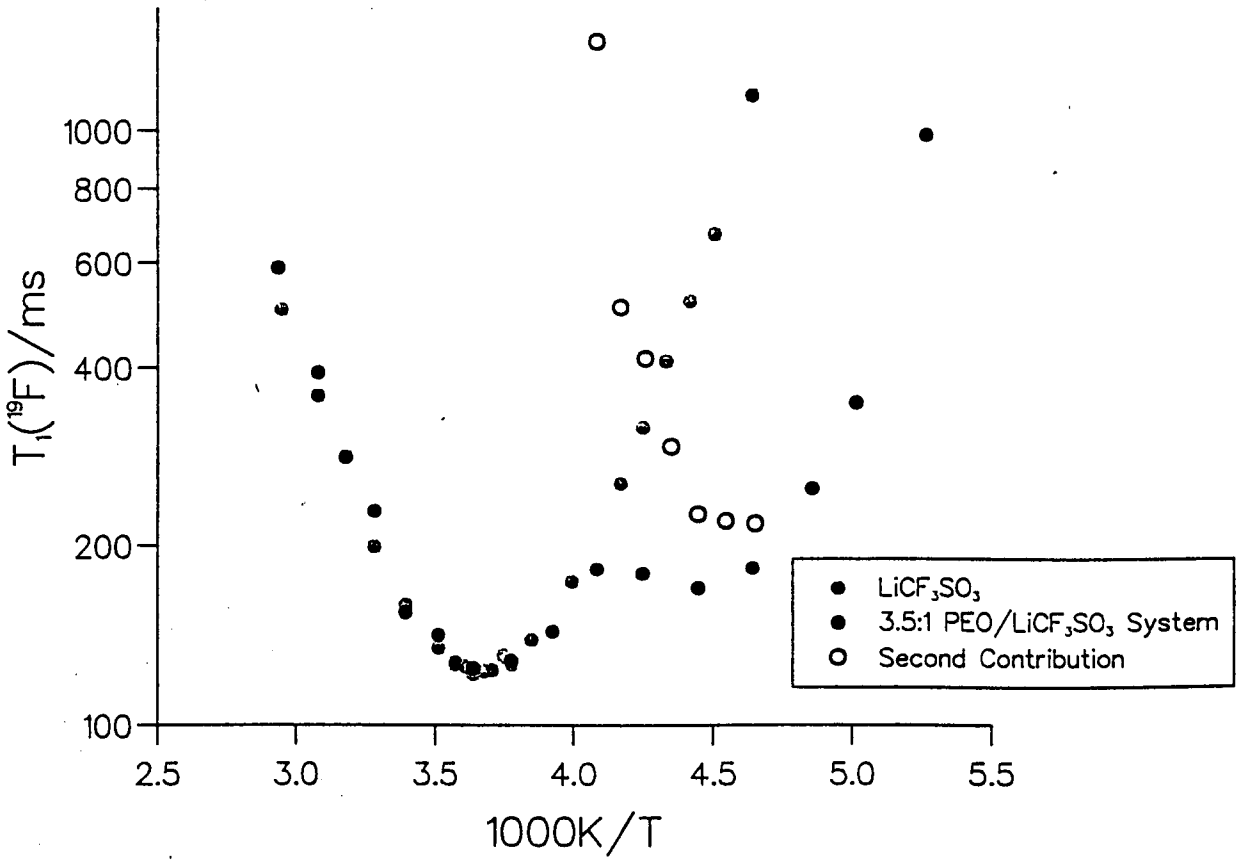

Figure 6.7 The temperature dependence of the ^{19}F spin-lattice relaxation behaviour, measured at 55.93 MHz, in the 3.5:1 $PEO/LiCF_3SO_3$ system, split into two contributions according to equation (6.1).

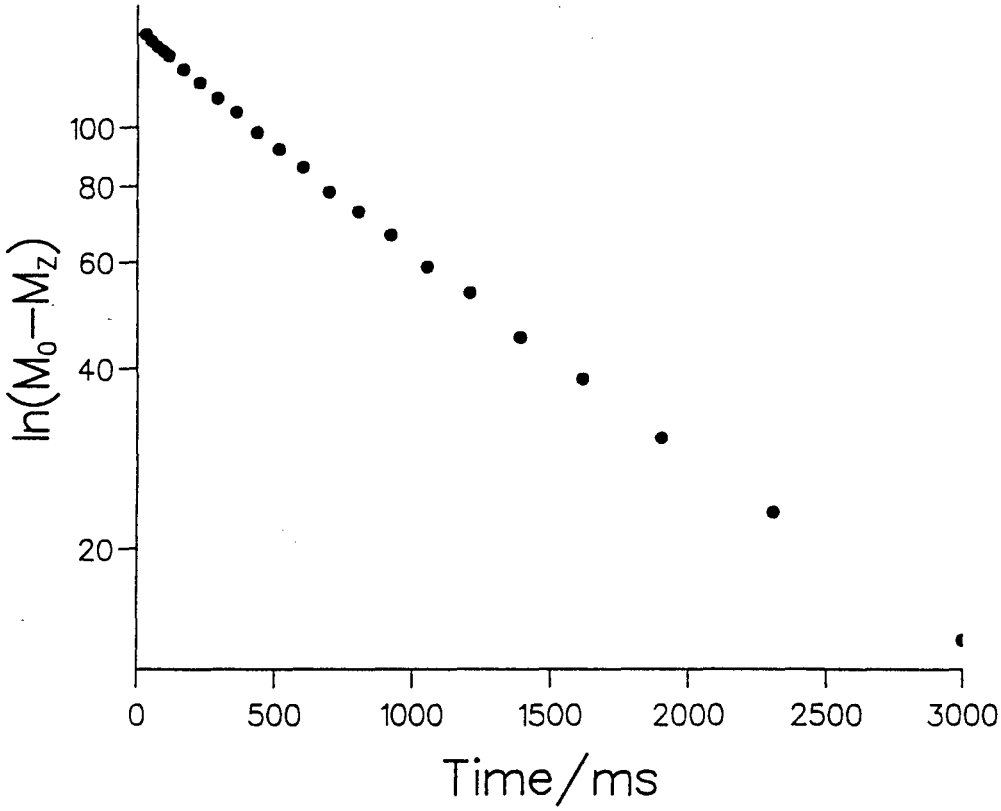

Figure 6.8 The ^{19}F nuclear magnetization recovery measured at 55.93 MHz and 190 K, for the 3.5:1 PEO/$LiCF_3SO_3$ system.

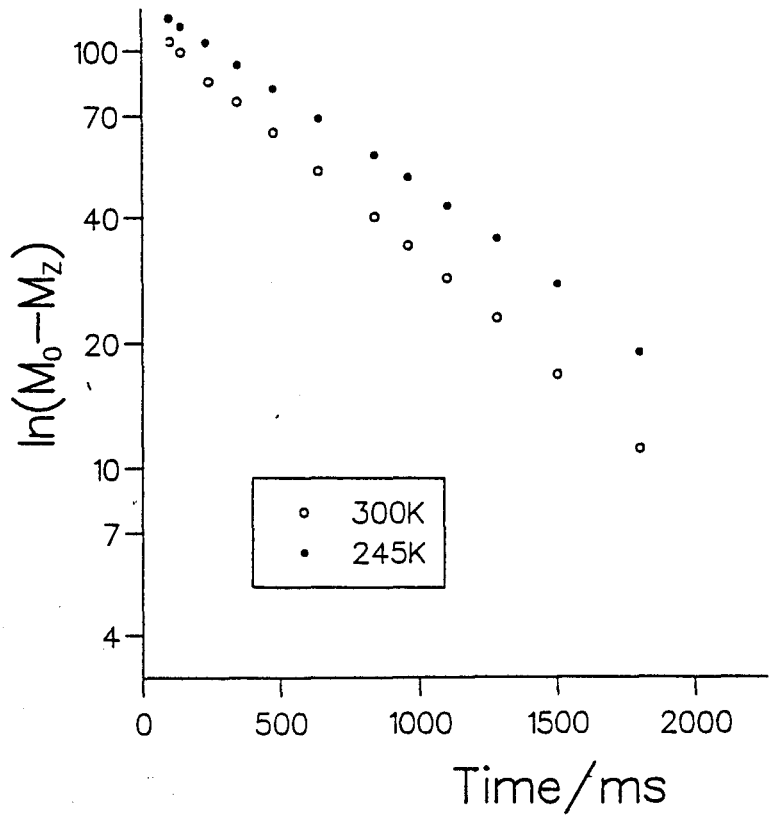

Figure 6.9 Typical ^1H nuclear magnetization recoveries in the 3.5:1 PEO/$LiCF_3SO_3$ system as measured at 59.45 MHz at 300 K and 245 K.

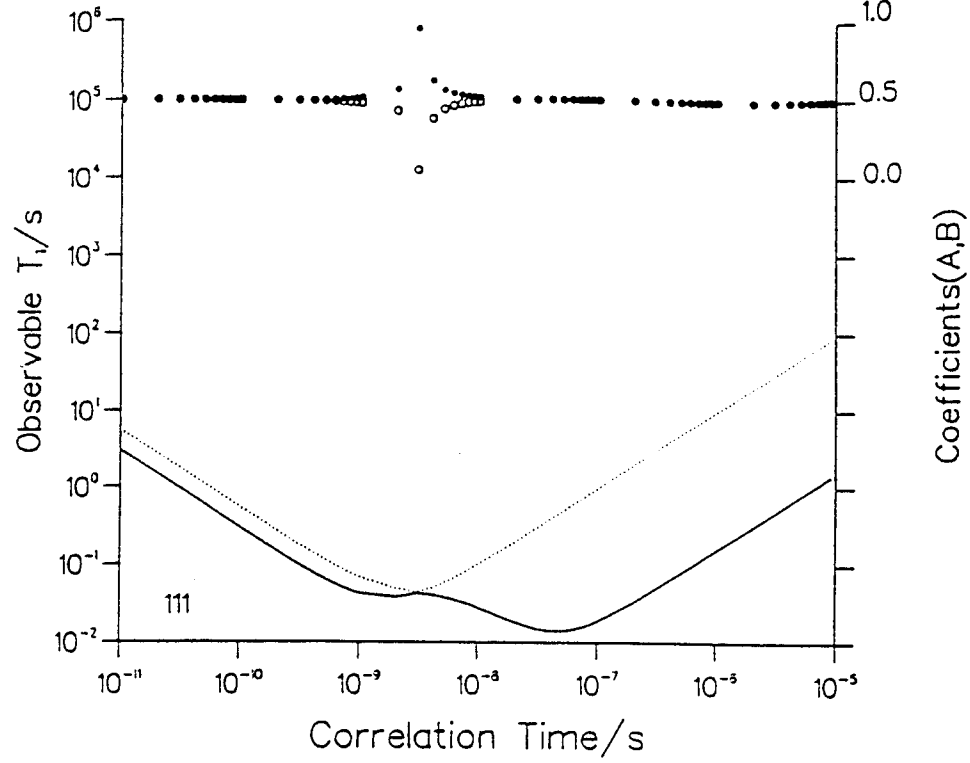

Figure 6.10 A simulation of the observable spin-lattice relaxation time behaviour, and the behaviour of the coefficients determining the contributions to nuclear magnetization recovery, as a function of correlation time; for $\Delta M_2^{11} = \Delta M_2^{22} = \Delta M_2^{12} = \Delta M_2^{21}$; for a model system of dipolar coupled unlike spin $I = \frac{1}{2}$ nuclei interacting in a pairwise manner. The double minimum arises because of the functional form of equation (6.40), where the term in $(\omega_1 - \omega_2)^{-2}$ is responsible for the lower temperature minimum.

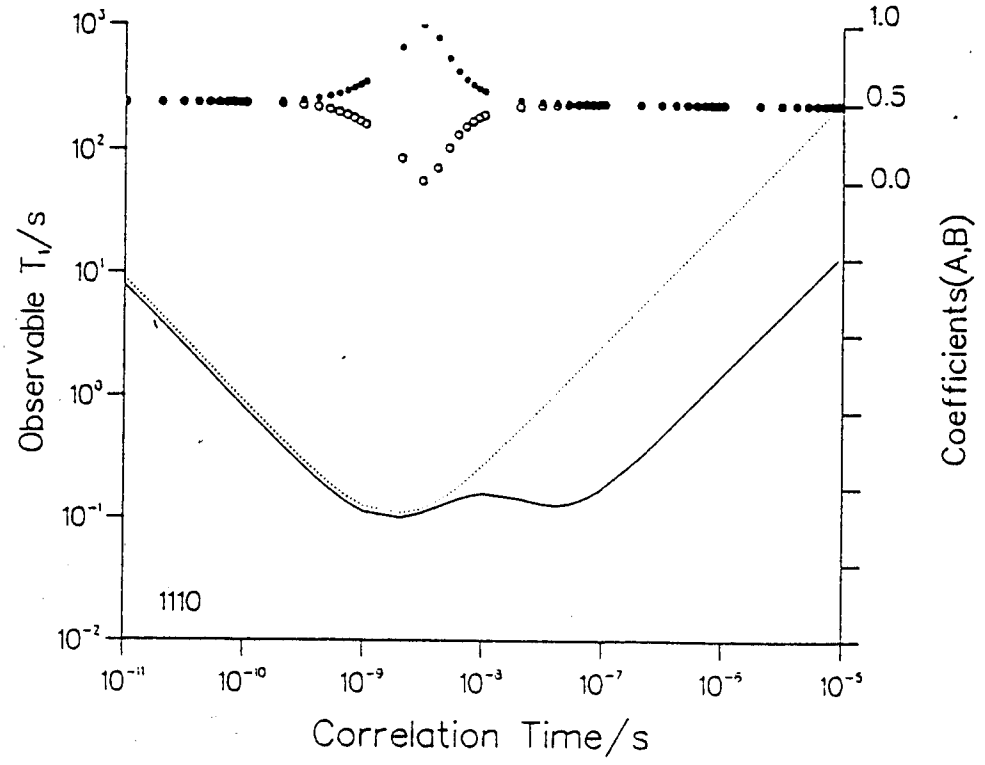

Figure 6.11 An identical simulation to Figure 6.10; for ratios $\Delta M_2^{11}/\Delta M_2^{22} = 1$ and $\Delta M_2^{12}/\Delta M_2^{21} = 1$ and $\Delta M_2^{11}/\Delta M_2^{22} = 10$.

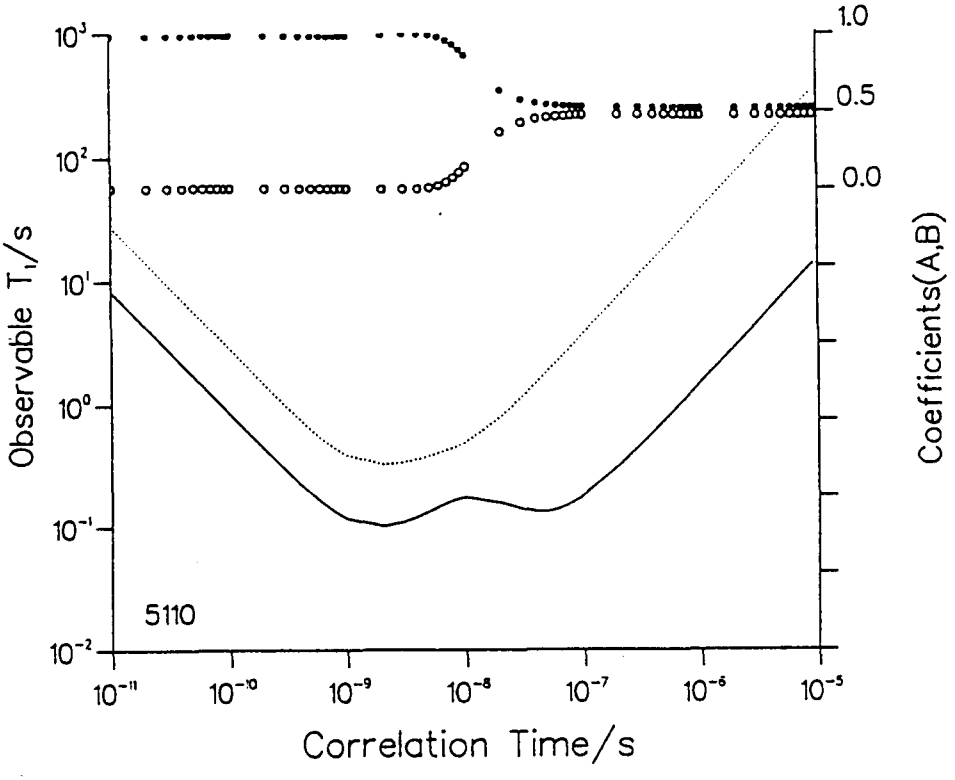

Figure 6.12 An identical simulation to Figure 6.10; for ratios $\Delta M_2^{11}/\Delta M_2^{12} = 5$, $\Delta M_2^{11}/\Delta M_2^{12} = 10$ and $\Delta M_2^{12}/\Delta M_2^{21} = 1$.

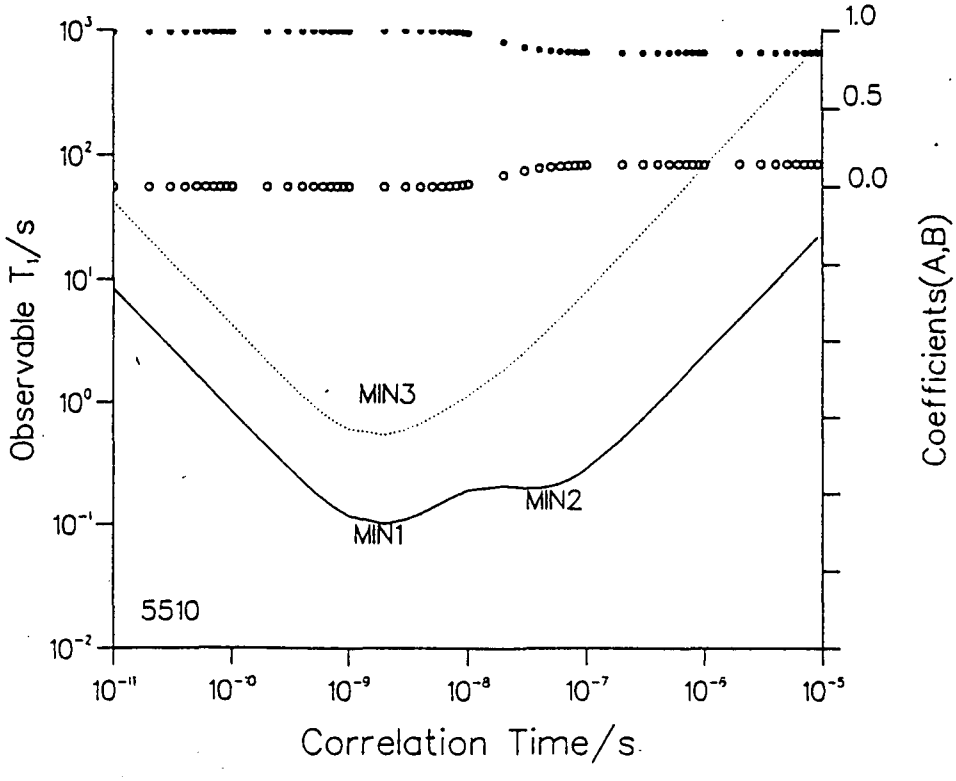

Figure 6.13 An identical simulation to Figure 6.10; for ratios $\Delta M_2^{11}/\Delta M_2^{22} = 5$, $\Delta M_2^{11}/\Delta M_2^{12} = 10$ and $\Delta M_2^{12}/\Delta M_2^{21} = 5$.

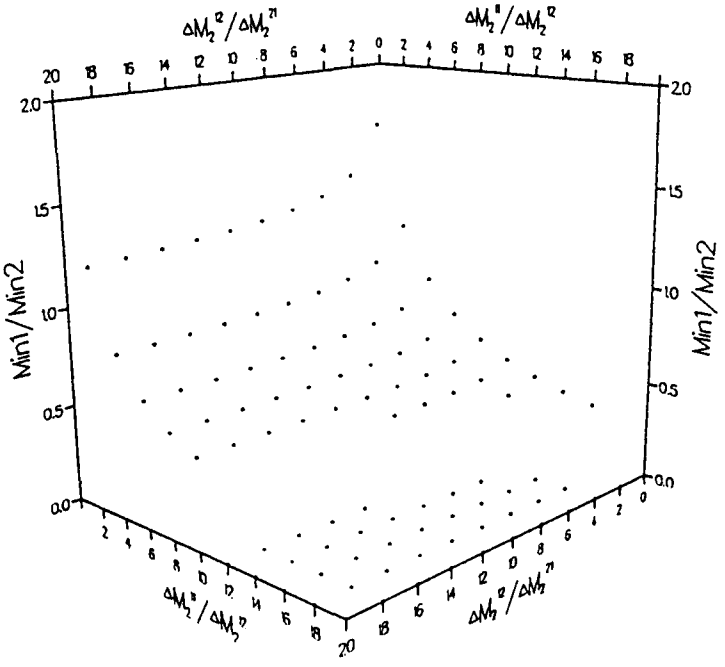

Figure 6.14 A typical plot of the ratio MIN1/MIN2; where these minima are defined in Figure 6.13; as a function of the ratios $\Delta M_2^{11}/\Delta M_2^{12}$ and $\Delta M_2^{12}/\Delta M_2^{21}$, for the fixed ratio $\Delta M_2^{11}/\Delta M_2^{22}$ in the range 1-9. Values of MIN1/MIN2 plotted at zero correspond to only one observable spin-lattice relaxation time minimum, where the second has become a point of inflection.

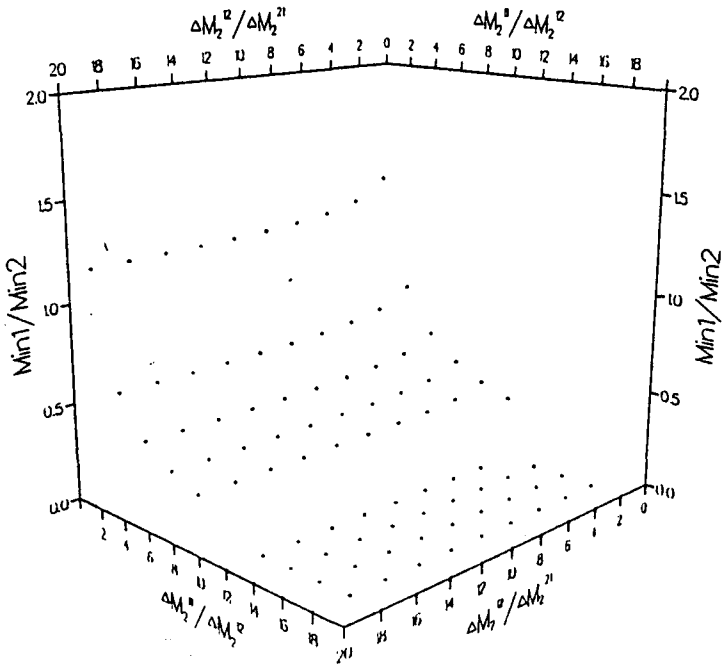

Figure 6.15 An identical plot to Figure 6.14, with the fixed ratio $\Delta M_2^{11}/\Delta M_2^{22} = 0.5$.

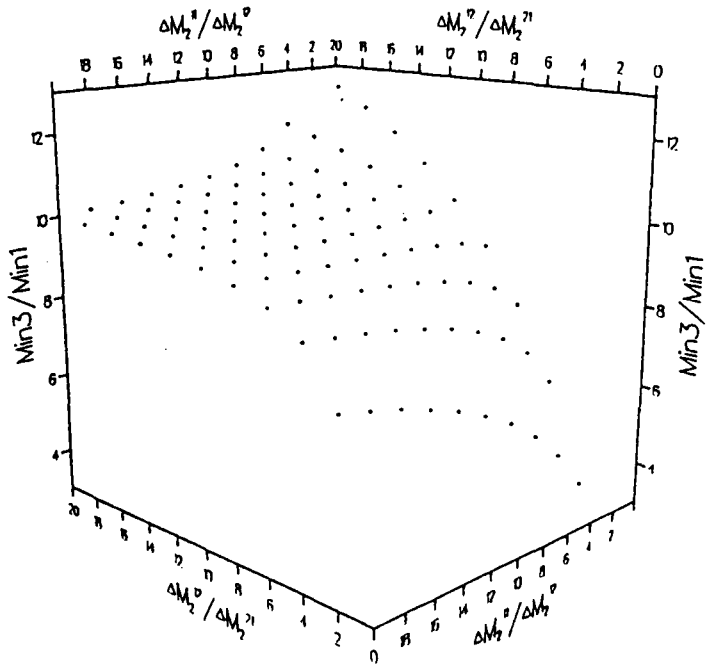

Figure 6.16 The ratio of MIN3/MIN1; where these minima are defined in Figure 6.13; as a function of the ratios $\Delta M_2{}^{11}/\Delta M_2{}^{12}$ and $\Delta M_2{}^{12}/\Delta M_2{}^{21}$ for the fixed ratio $\Delta M_2{}^{11}/\Delta M_2{}^{22} = 9$.

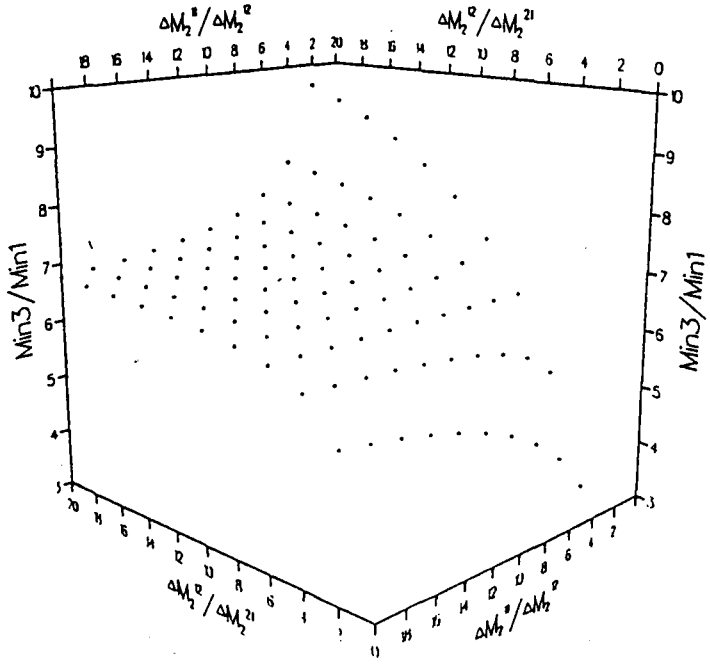

Figure 6.17 The ratio of MIN3/MIN1; where these minima are defined in Figure 6.13; as a function of the ratios $\Delta M_2{}^{11}/\Delta M_2{}^{12}$ and $\Delta M_2{}^{12}/\Delta M_2{}^{21}$ for the fixed ratio $\Delta M_2{}^{11}/\Delta M_2{}^{22} = 6$.

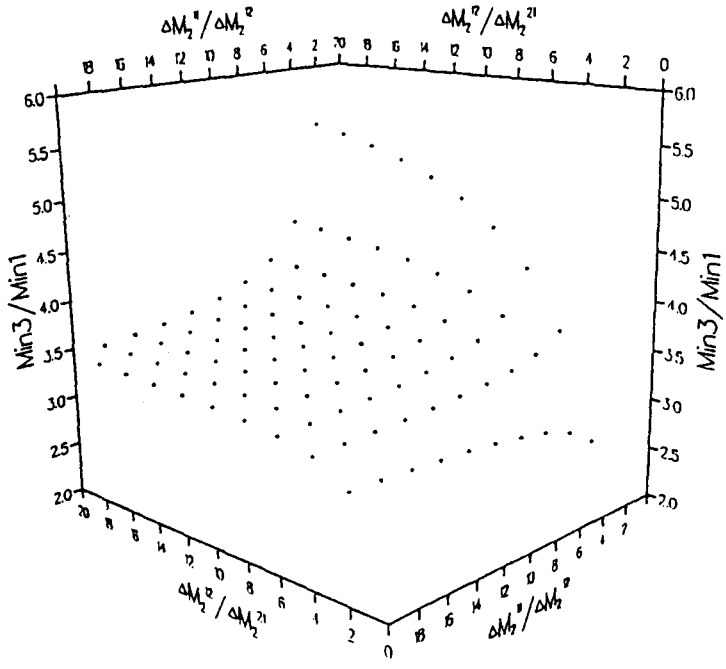

Figure 6.18 The ratio of MIN3/MIN1; where these minima are defined in Figure 6.13; as a function of the ratios $\Delta M_2{}^{11}/\Delta M_2{}^{12}$ and $\Delta M_2{}^{12}/\Delta M_2{}^{21}$ for the fixed ratio $\Delta M_2{}^{11}/\Delta M_2{}^{22} = 3$.

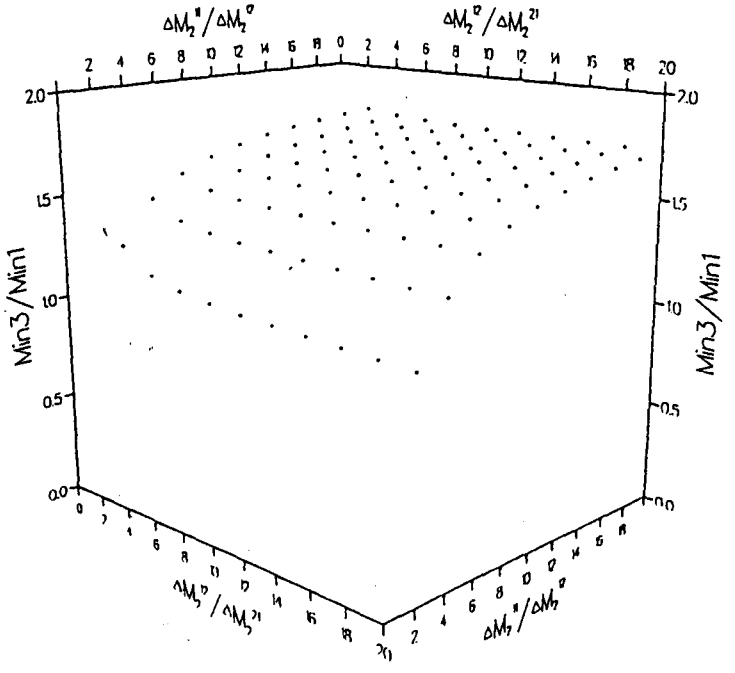

Figure 6.19 The ratio of MIN3/MIN1; where these minima are defined in Figure 6.13; as a function of the ratios $\Delta M_2{}^{11}/\Delta M_2{}^{12}$ and $\Delta M_2{}^{12}/\Delta M_2{}^{21}$ for the fixed ratio $\Delta M_2{}^{11}/\Delta M_2{}^{22} = 0.5$.

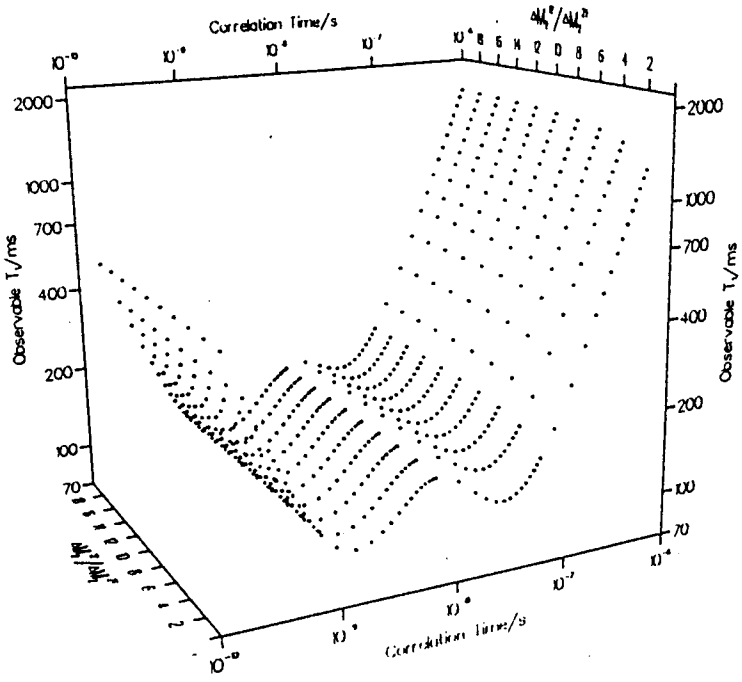

Figure 6.20 The simulated observable spin-lattice relaxation time exhibiting a double minimum as a function of correlation time, and of $\Delta M_2{}^{12}/\Delta M_2{}^{21}$ for $\Delta M_2{}^{11}/\Delta M_2{}^{22} = 6$ and $\Delta M_2{}^{11}/\Delta M_2{}^{12} = 6$, using a model system consisting of heteronuclear dipolar coupled nuclei interacting in a pairwise manner.

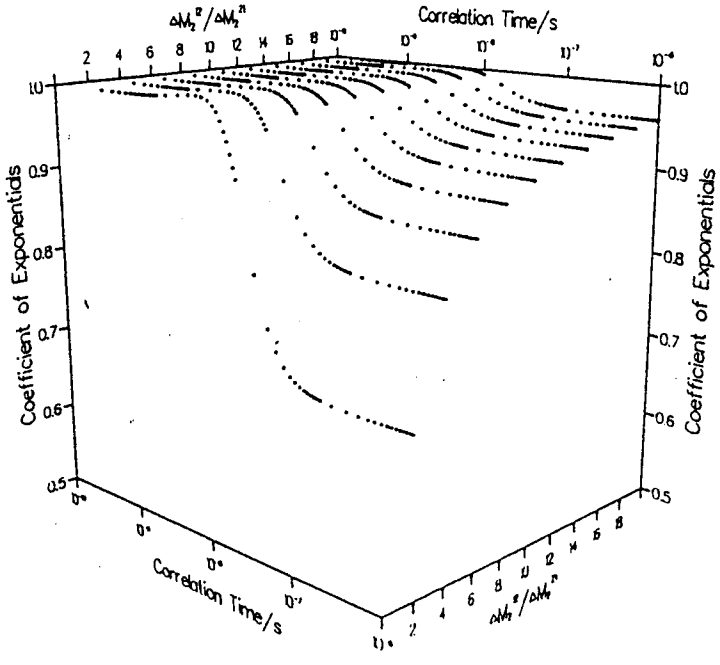

Figure 6.21 The simulated behaviour of the coefficient with which the decay constant corresponding to the observable spin-lattice relaxation times shown in Figure 6.20, would contribute to the nuclear magnetization recovery, in the model system described for those fixed ratios of reduced second moments.

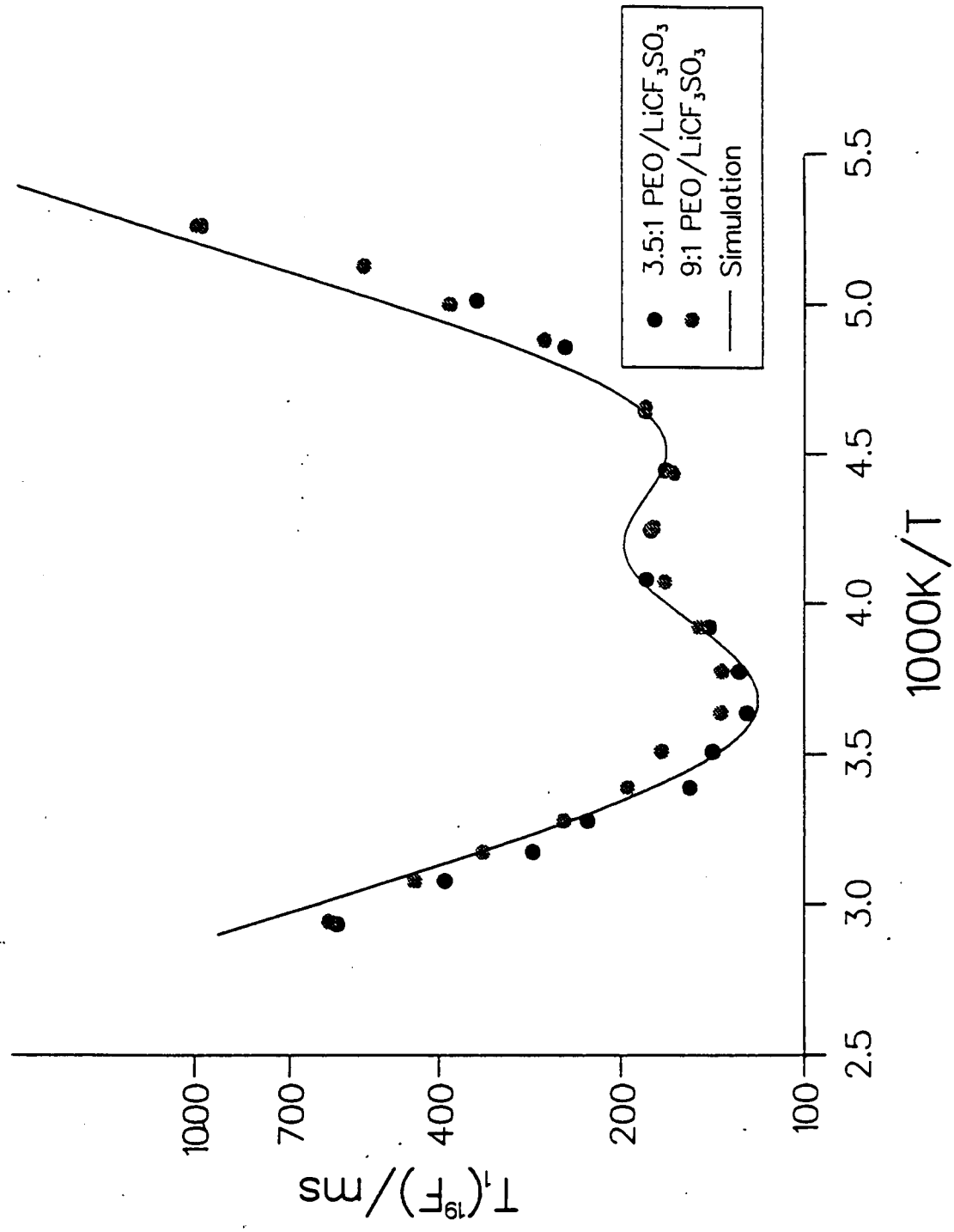

Figure 6.22 A simulation of the ^{19}F spin-lattice relaxation behaviour in the 3.5:1 PEO/$LiCF_3SO_3$ system, using a model system consisting of heteronuclear dipolar coupled nuclei interacting in a pairwise manner, with ratios of reduced second moments given by $\Delta M_2^{11}/\Delta M_2^{22} = 6$, $\Delta M_2^{12}/\Delta M_2^{21} = 6$ and $\Delta M_2^{11}/\Delta M_2^{12} = 6$. The motional parameters attributed to the dynamical process mediating the spin-lattice relaxation were $E_A = 30.33$ kJ mol^{-1} and $\tau_0 = 2.83 \times 10^{-15}$ s. ΔM_2^{FF} was taken to be 2.388×10^9 rad^{2}s^{-2}.

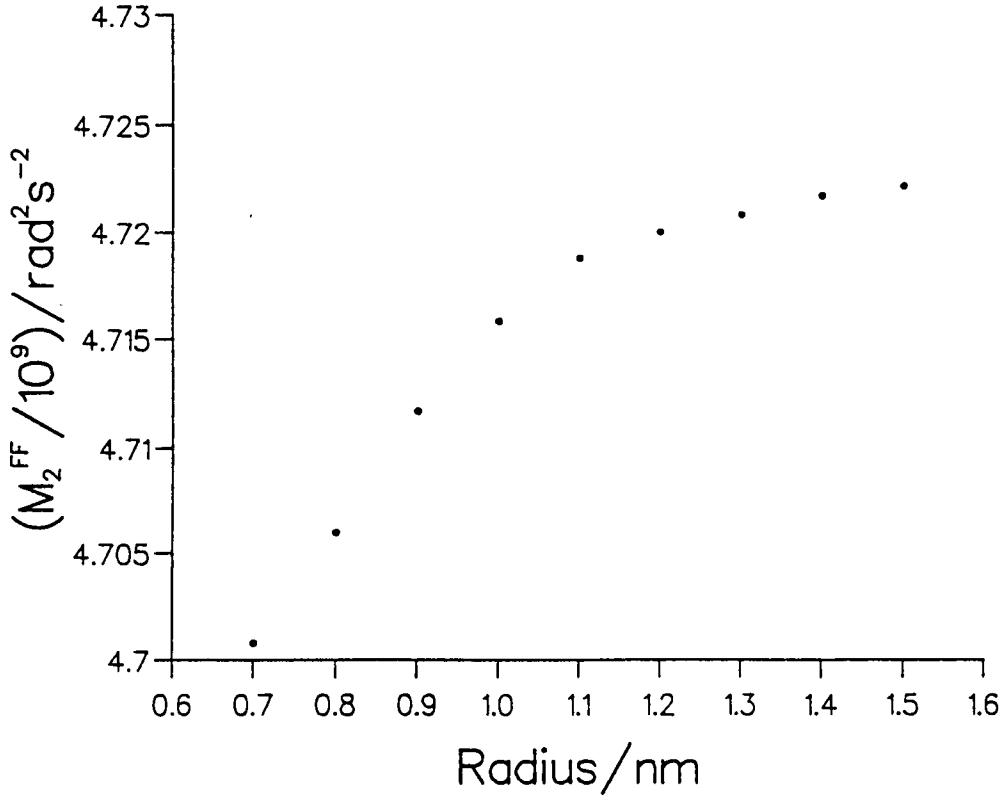

Figure 6.23 The homonuclear ^{19}F rigid lattice second moment calculated from the proposed crystal structure of the 3:1 PEO/$LiCF_3SO_3$ stoichiometric complex, as a function of the radius of a sphere, centred on the reference spin, containing all nuclei included in the lattice sum.

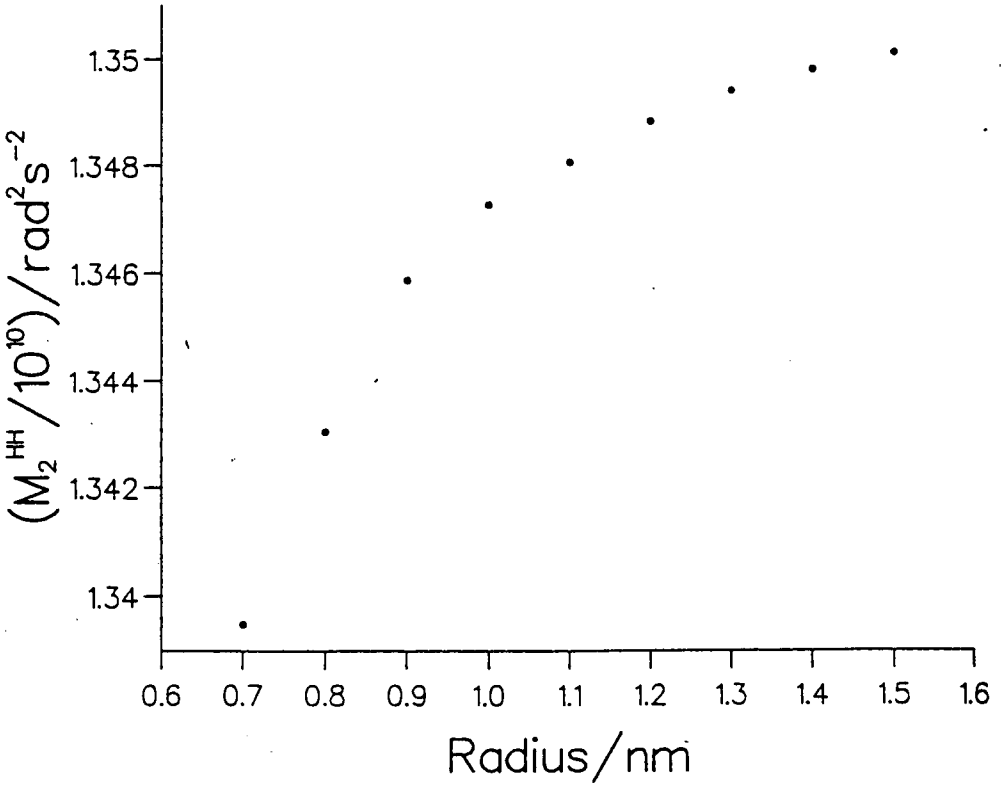

Figure 6.24 The homonuclear ^1H rigid lattice second moment calculated from the proposed crystal structure of the 3:1 PEO/$LiCF_3SO_3$ stoichiometric complex, as a function of the radius of a sphere, centred on the reference spin, containing all nuclei included in the lattice sum.

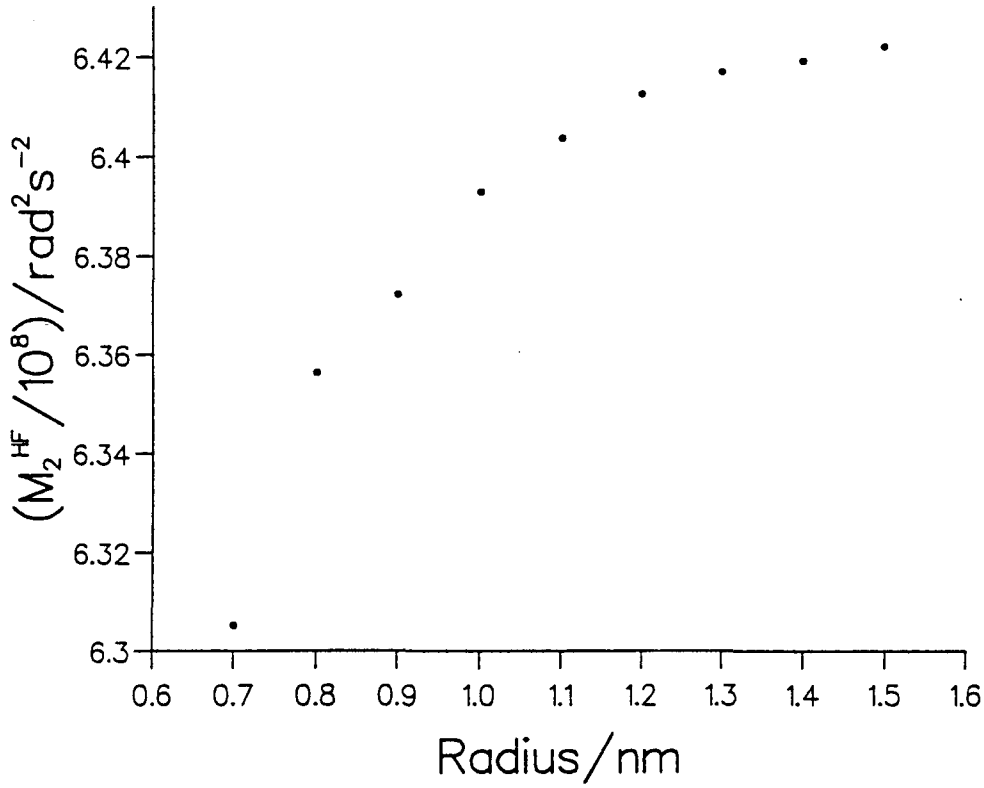

Figure 6.25 The heteronuclear ^1H-^{19}F rigid lattice second moment calculated from the proposed crystal structure of the 3:1 PEO/$LiCF_3SO_3$ stoichiometric complex, as a function of the radius of a sphere centred on the reference spin, containing all nuclei included in the lattice sum.

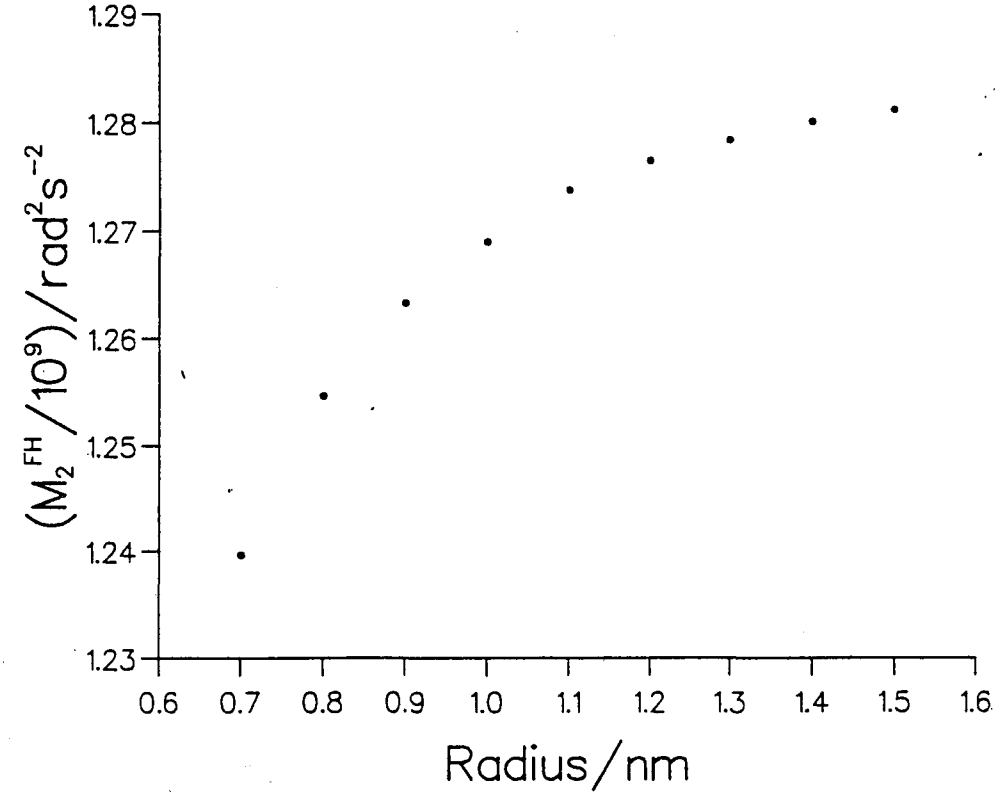

Figure 6.26 The heteronuclear ^{19}F-^1H rigid lattice second moment calculated from the proposed crystal structure of the 3:1 PEO/$LiCF_3SO_3$ stoichiometric complex, as a function of the radius of a sphere centred on the reference spin, containing all nuclei included in the lattice sum.

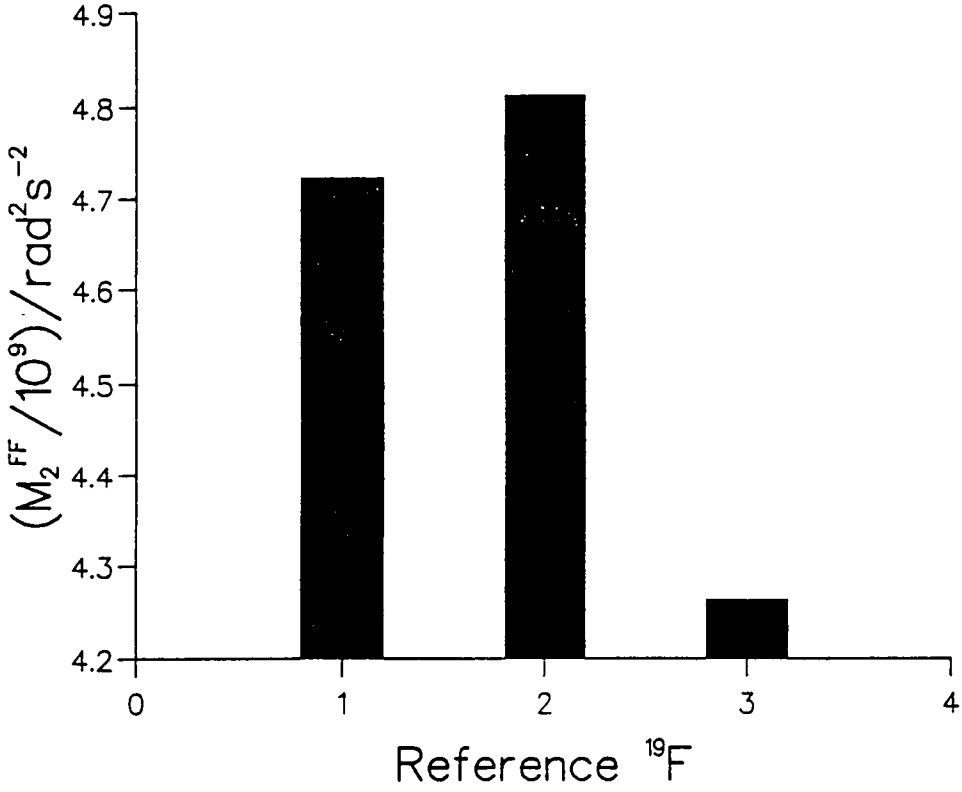

Figure 6.27 The homonuclear ^{19}F rigid lattice second moment calculated from the proposed crystal structure of the 3:1 PEO/$LiCF_3SO_3$ stoichiometric complex, for all unique crystallographic positions of the reference nuclei using all relevant nuclei within a 1.5 nm distance to evaluate the lattice sum.

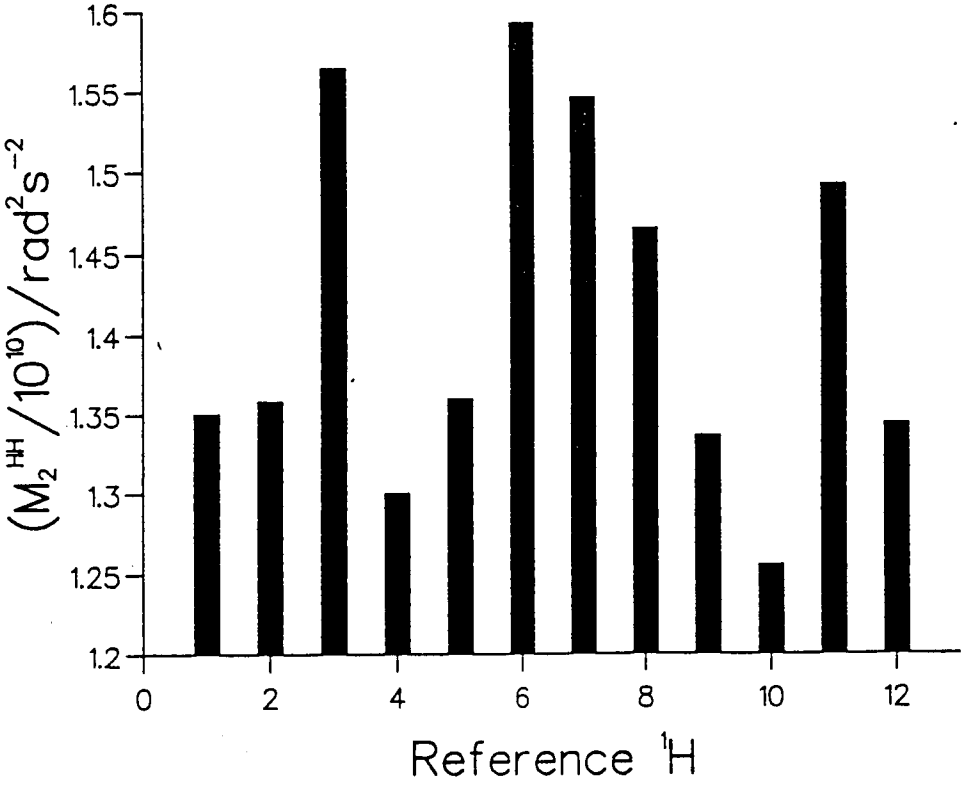

Figure 6.28 The homonuclear ^{1}H rigid lattice second moment calculated from the proposed crystal structure of the 3:1 PEO/$LiCF_3SO_3$ stoichiometric complex, for all unique crystallographic positions of the reference nuclei, using all relevant spins within a 1.5 nm distance to evaluate the lattice sum.

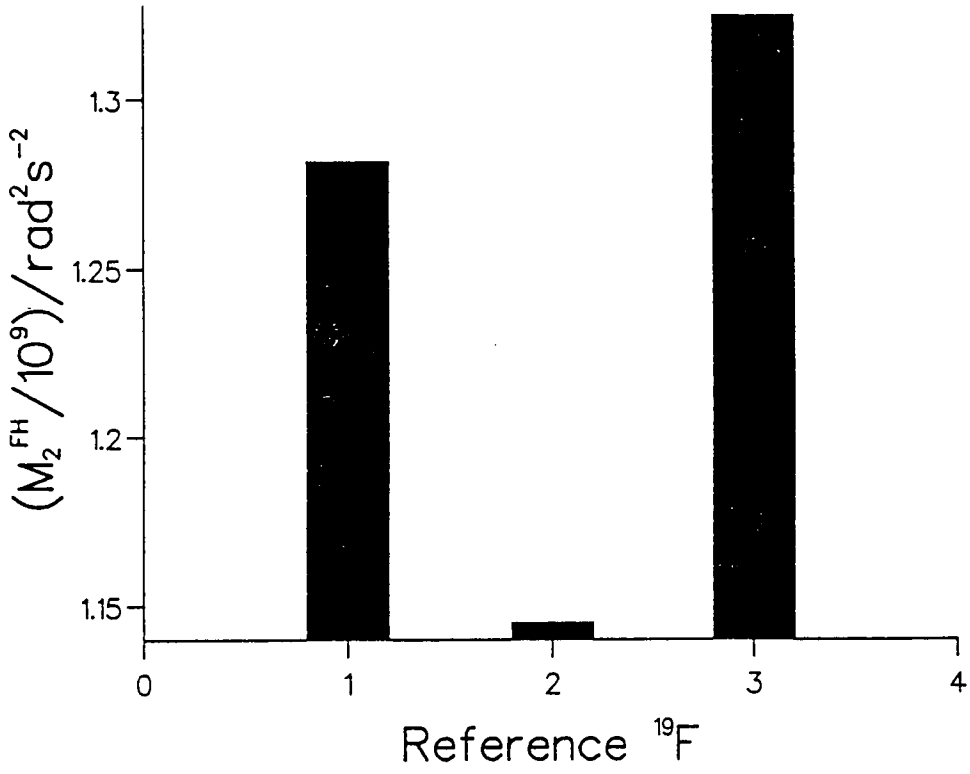

Figure 6.29 The heteronuclear ^{19}F-^{1}H rigid lattice second moment calculated from the proposed crystal structure of the 3:1 PEO/$LiCF_3SO_3$ stoichiometric complex, for all unique crystallographic positions of the reference nuclei, using all relevant spin within a 1.5 nm distance to evaluate the lattice sum.

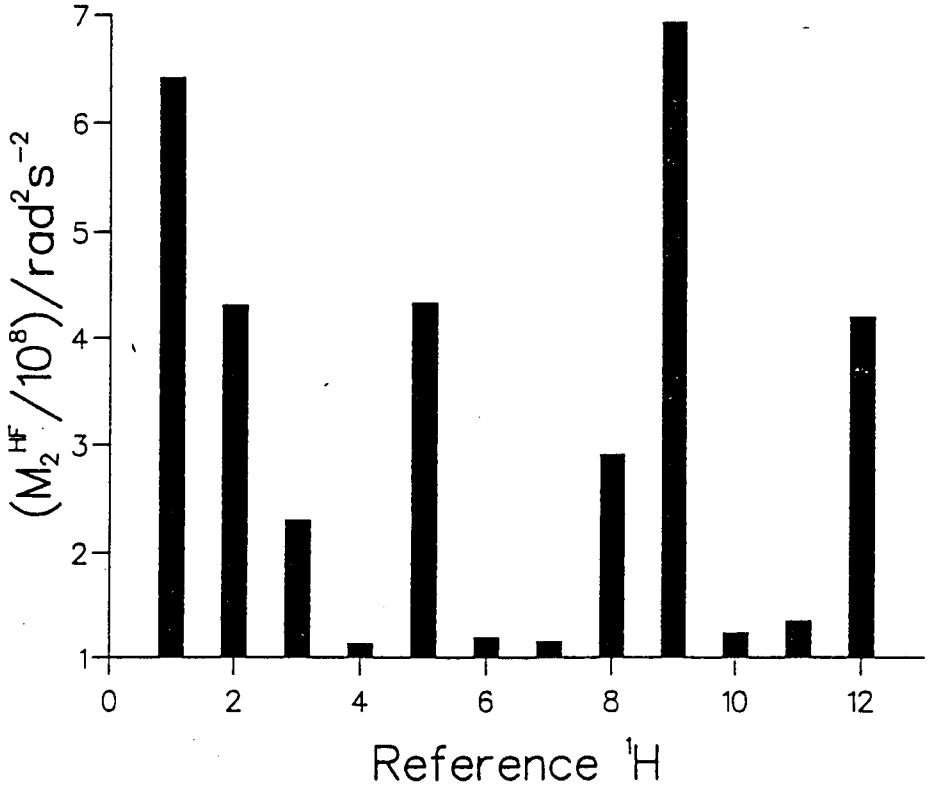

Figure 6.30 The heteronuclear ^{1}H-^{19}F rigid lattice second moment calculated from the proposed crystal structure of the 3:1 PEO/$LiCF_3SO_3$ stoichiometric complex, for all unique crystallographic positions of the reference nuclei, using all relevant spins within a 1.5 nm distance to evaluate the lattice sum.

CHAPTER 7

^{7}Li NUCLEAR MAGNETIC SPIN-LATTICE RELAXATION STUDIES IN $LiCF_3SO_3$ AND PEO/$LiCF_3SO_3$ SYSTEMS

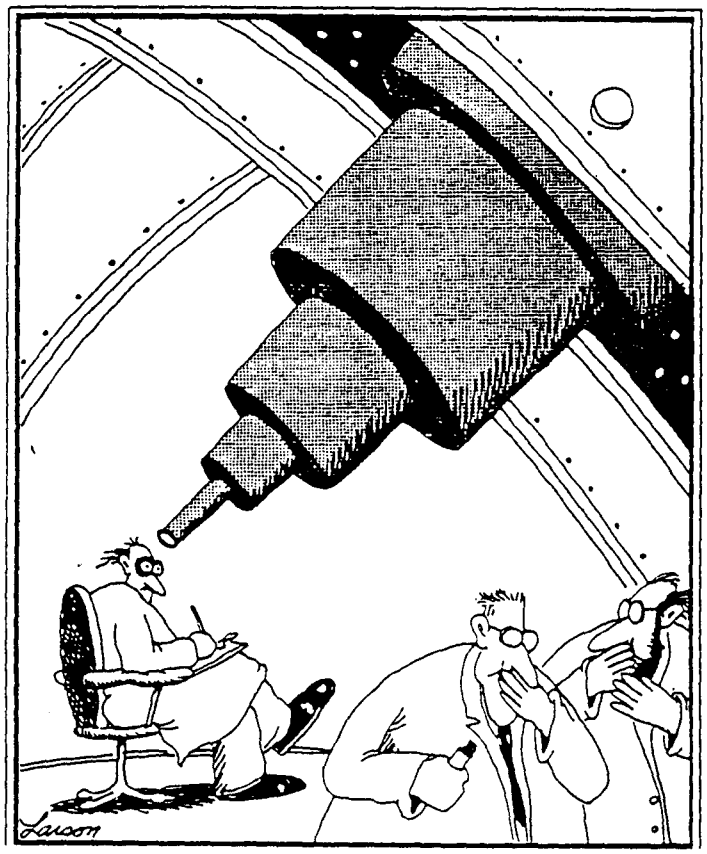

CONTENTS

7.1 Introduction

Chapters 5 and 6 have concentrated on ^{19}F spin-lattice relaxation studies in both polycrystalline $LiCF_3SO_3$ and the 3.5:1 and 9:1 $PEO/LiCF_3SO_3$ systems respectively, where the hindered rotation of the CF_3 group about its threefold axis played an important role. It is the aim of this chapter to investigate the dynamics of the lithium environment through ^7Li spin-lattice relaxation studies.

^7Li has a natural abundance of 92.58% and a spin I = 3/2. It does therefore possess a quadrupole moment. A key aim of this chapter is to investigate the magnetic dipolar and electric quadrupolar contributions to ^7Li spin-lattice relaxation. This can be done in detail for the pure salt, since a proposed crystal structure is available. The spin-lattice relaxation behaviour in the 3.5:1 and 9:1 $PEO/LiCF_3SO_3$ systems may be complicated by a type of ^7Li exchange process, and this is discussed with reference to ^7Li lineshape studies.

It should be noted that the spin-lattice relaxation expressions used in this Chapter are specific forms of general expressions described in the previous Chapter.

7.2 Experimental

A ^7Li spin-lattice relaxation study of polycrystalline $LiCF_3SO_3$ and the 3.5:1 $PEO/LiCF_3SO_3$ system was carried out at a frequency of 23.10 MHz, and over the temperature range 200 K to 340 K. A brass probe head was used for all measurements since this was found to reduce the problem of magnetoacoustic ringing, as discussed previously. ^7Li spin-lattice relaxation times were measured using a $P_x(90)$-t-$P_x(90)$-τ-$P_y(90)$-t´ pulse sequence with τ = 15 μs, as outlined in Chapter 3. These values are denoted in this Chapter by $T_1(^7Li)$, although this does not imply the measurement of spin-lattice relaxation times from only the initial gradient of nuclear magnetization recovery plots, as was the case in

Chapter 5 for $T_1(^{19}F)$, where the exclusion of cross-correlation effects was important.

The amplitude of the ^7Li signal in the 3.5:1 and 9:1 PEO/$LiCF_3SO_3$ systems was substantially lower than that obtained for polycrystalline $LiCF_3SO_3$, due to the reduction of the percentage of ^7Li nuclei in the sample. An initial investigation of the 9:1 PEO/$LiCF_3SO_3$ system found the ^7Li signal too small to give consistent amplitude values.

A JEOL 400 MHz high resolution n.m.r. spectrometer was also used to examine ^7Li lineshapes in polycrystalline PEO and the 3.5:1 and 9:1 PEO/$LiCF_3SO_3$ systems, at 293 K and 343 K, as described in Chapter 3.

7.3 A ^7Li Spin-lattice Relaxation Study of Polycrystalline $LiCF_3SO_3$

Results

Figure 7.1 shows a typical experimental ^7Li nuclear magnetization recovery in polycrystalline $LiCF_3SO_3$ as measured at 254 K. This and all other magnetization recoveries measured between 200 K and 340 K could be fitted, within experimental uncertainties, to a single exponential function. The estimated error in $T_1(^7Li)$ is of the order of 5%.

Figure 7.2 shows the behaviour of $T_1(^7Li)$ with temperature plotted in the form of a graph of ln $(T_1(^7Li))$ versus reciprocal temperature. There is a single spin-lattice relaxation time minimum ($T_1(^7Li)$ = 7.4s) at 250 K.

Qualitative Discussion

^7Li is quadrupolar nucleus with spin I = 3/2. It is possible, therefore, that spin-lattice relaxation behaviour involves both magnetic dipolar and electric quadrupolar mechanisms. Quadrupolar spin-lattice relaxation behaviour cannot, in general, be described by a single exponential nuclear magnetization recovery[1].

For the case of a nucleus with spin I = 3/2 an analytical expression has been derived for the relaxation rate[1-4], given by

$$< I_z > - < I_z >^T = < I_z >^T (\cos\theta - 1) \left[\frac{4}{5} \exp(-a_1 t) + \frac{1}{5} \exp(-a_2 t) \right] \qquad (7.1)$$

where

$$a_1 = 2(eQ/\hbar)^2 J_{-22}(2\omega_0) \qquad (7.2)$$

and

$$a_2 = -2(eQ/\hbar)^2 J_{-11}(\omega_0) \qquad (7.3)$$

θ is the angle of the applied pulse, and $J_{lk}(\omega)$ are the spectral densities of the appropriate correlation functions.

More generally the nuclear magnetization recoveries for quadrupolar nuclei are a weighted sum of exponentials. For nuclei with half integral spin, where I > 3/2, numerical diagonalization of the relaxation matrix[5,6] is required. Although pronounced deviations from simple exponential magnetization recoveries have been observed for ^{23}Na[7-12], deviations for ^{7}Li have been found difficult to detect[13-15]. In general, for half integral spins, the $m = \frac{1}{2} \rightarrow -\frac{1}{2}$ transition is the strongest and can dominate the nuclear magnetization recovery. It was shown in Chapter 2 that in a large magnetic field the energy levels of a quadrupolar nuclei are the Zeeman levels, perturbed by quadrupolar effects. Equation (2.101) gives, in first order

$$\Delta\nu = \nu_0 - \frac{3}{8} \chi \frac{(2m-1)}{I(2I-1)} (3\cos^2\theta - 1) \qquad (7.4)$$

where $\chi = e^2 Q q_{zz}/\hbar$ and θ is the angle between the applied field and q_{zz}. In the chase when $I = \frac{3}{2}$ equation (7.4) becomes

$$\Delta\nu = \nu_0 - (1/8) \chi (2m-1) (3\cos^2\theta - 1) \qquad (7.5)$$

It is now straightforward to see, from equation (7.5), that transitions other than m $= \frac{1}{2} \rightarrow -\frac{1}{2}$ will be angular dependent and consequently will give rise to broad lines for a polycrystalline sample. Experimentally, therefore, it is possible that these satellite transitions may not contribute significantly to spin-lattice relaxation and a single exponential nuclear magnetization recovery may result. This type of behaviour is taken to be the case for the ^{7}Li results presented in this Chapter. The observation of single exponential nuclear magnetization recoveries does not in itself indicate whether quadrupolar or dipolar processes are predominant spin-lattice relaxation mechanisms.

In general for a spin-lattice relaxation mechanism where the spectral density function $F(\tau_c)$, is the sum of terms, each of which is of the form

$$f_i(\tau_c) = \frac{a_i\tau_c}{1 + b_i\omega_0^2\tau_c^2} \tag{7.6}$$

where a and b are constants; then in the limit $\omega_0\tau_c << 1$

$$F(\tau_c) = \sum_i f_i(\tau_c) = \sum_i a_i\tau_c \tag{7.7}$$

If, in addition, the correlation time is given by

$$\tau_c = \tau_0 \exp(E_A/RT) \tag{7.8}$$

then the gradient of the high temperature side ($\omega\tau_c << 1$) of a $\ln(T_1)$ versus inverse temperature plot is equal to $-E_A/R$. In general therefore, where the motional processes can be described by a single correlation time, this gradient provides a means of measuring the activation energy for the motional process mediating the spin-lattice relaxation behaviour. This has been demonstrated in Chapter 5 for the specific case of ^{19}F spin-lattice relaxation in polycrystalline $LiCF_3SO_3$.

Figure 7.3 shows a combined plot of the ^{7}Li and ^{19}F spin-lattice relaxation behaviour in polycrystalline $LiCF_3SO_3$ as a graph of $\ln(T_1(^{7}Li))$ and $\ln(T_1(^{19}F))$ versus inverse temperature. It is clear from the respective high temperature gradients that the activation energies for the ^{7}Li and ^{19}F spin-lattice relaxation mechanisms are very similar. The ^{19}F spin-lattice relaxation behaviour in polycrystalline $LiCF_3SO_3$ is dominated by a magnetic dipolar relaxation mechanism associated with the hindered rotation of the CF_3 groups, as discussed in detail in Chapter 5. It seems reasonable then, that this motion may also be responsible for the observed ^{7}Li spin-lattice relaxation behaviour. One contribution will be due to the modulation of the ^{7}Li-^{19}F magnetic dipolar interactions. There is no evidence that the lithium atoms undergo any motional processes in the crystal lattice, on the scale of the n.m.r. experiment, over the temperature range of this study. It is also possible that there will be a quadrupolar contribution to be the spin-lattice relaxation. The relative contributions of these two mechanisms can be investigated by comparing experimental results with explicit calculations for the magnetic dipolar mechanism based on the suggested crystal structure of the salt. Such calculations will depend, however, quite critically on the accuracy of the crystal structure.

7.4 A Dynamic Model for the ^{7}Li Spin-lattice Relaxation Behaviour in Polycrystalline $LiCF_3SO_3$

In Chapter 6 equations were given which describe the spin-lattice relaxation behaviour in a model system of unlike, dipolar coupled, spin $I = \frac{1}{2}$ nuclei, interacting in a pairwise manner. Although in the case of the ^{7}Li-^{19}F system considered here ^{7}Li has a spin $I = \frac{3}{2}$, it seems reasonable to suggest that these equations can be applied, as the experimental ^{7}Li nuclear magnetization recoveries indicate that only the $m = \frac{1}{2} \longrightarrow -\frac{1}{2}$ transition contributes significantly to spin-lattice relaxation. Equation (6.25) gives the inverse observable spin-lattice relaxation times for a magnetic dipolar relaxation mechanism in the form

$$\lambda_{1,2} = \tfrac{1}{2}\{(\lambda_{LiLiLi} + \lambda_{LiFLi} + \lambda_{FFF} + \lambda_{FLiF}) \pm [(\lambda_{LiLiLi} + \lambda_{LiFLi} - \lambda_{FFF} - \lambda_{FLiF})^2 + 4\lambda_{LiF}\lambda_{FLi}]^{\frac{1}{2}}\} \quad (7.9)$$

The notation used in this equation is recapped briefly below.

λ_1 and λ_2: These are the two decay constants corresponding to two exponential functions which contribute to both ^{7}Li and ^{19}F nuclear magnetization recoveries. For a particular correlation time the relative contributions are determined by constants A and B given in equations (6.32) and (6.33). If A and B are such that double exponential behaviour is clearly observed then λ_1 and λ_2 may be in principle be extracted from the nuclear magnetization recoveries of either ^{7}Li and ^{19}F. The reciprocal values of these decay constants are known as the observable spin-lattice relaxation times.

Terms of the form λ_{LiLiLi}: These are decay constants that are the inverse of spin-lattice relaxation times associated with a particular mechanism. The first and last labels in the three label subscript respectively, denote the spin population to which nuclear magnetization is returning, and the spin population whose magnitude determines the rate of this return. The middle label denotes the spin mediating the interaction.

Terms of the form λ_{LiF}: These are decay constants that are the inverse of spin-lattice relaxation times associated with cross-relaxation. The first label in the subscript denotes the spin population to which nuclear magnetization is returning, and the second, the spin population whose magnitude determines the rate of this return.

For these equations to be used to calculate the ^{7}Li spin-lattice relaxation behaviour in polycrystalline $LiCF_3SO_3$, it is necessary for the model to be consistent with the ^{19}F spin-lattice relaxation behaviour. This is dominated by a magnetic dipolar relaxation mechanism associated with the hindered rotation of

the CF_3 groups. For the purpose of calculation it is reasonable to assume that this dominant ^{19}F spin-lattice relaxation mechanism is intramolecular. In this case the ^{7}Li-^{19}F cross relaxation is effectively decoupled, that is:

$$\lambda_1 = \lambda_{LiLiLi} + \lambda_{LiFLi} \tag{7.10}$$

and

$$\lambda_2 = \lambda_{FFF} \tag{7.11}$$

so that the nuclear magnetization recovery of the ^{7}Li and ^{19}F spin populations depends only on their respective spin populations. The quantity λ_{LiLiLi} is a ^{7}Li-^{7}Li dipolar contribution, which is zero as the lithium atoms are stationary, giving equation (7.10) as

$$\lambda_1 = \lambda_{LiFLi} \tag{7.12}$$

Equations (6.32) and (6.33) in Chapter 6 give the form of the coefficients with which the observable spin-lattice relaxation times contribute to the magnetization recovery. In the present study, and following a 90° pulse resonant for ^{7}Li, the coefficients are given by

$$A = (\lambda_{LiLiLi} + \lambda_{LiFLi} - \lambda_2)/(\lambda_1 - \lambda_2)$$

and

$$B = (\lambda_1 - \lambda_{LiLiLi} - \lambda_{LiFLi})/(\lambda_1 - \lambda_2)$$

Putting $\lambda_1 = \lambda_{LiFLi}$, $\lambda_2 = \lambda_{FFF}$ and $\lambda_{LiLiLi} = 0$ gives A = 1 and B = 0. The ^{7}Li nuclear magnetization recovery is predicted by the model system to be exponential, in agreement with experimental observation.

The magnetic dipolar spin-lattice relaxation expression given by equation (7.12) can be rewritten based on reduced second moments using equation (6.40), so that;

$$\lambda_1 = \frac{1}{2}\Delta M_2^{LiF}\left(\frac{\tau_c}{1+(\omega_{Li}-\omega_F)^2\tau_c^2}+\frac{3\tau_c}{1+\omega_{Li}^2\tau_c^2}+\frac{6\tau_c}{1+(\omega_{Li}+\omega_F)^2\tau_c^2}\right) \quad (7.13)$$

The problem of simulating the ^7Li spin-lattice relaxation behaviour in polycrystalline $LiCF_3SO_3$ now becomes one of calculating the reduced dipolar second moment ΔM_2^{LiF}.

The Calculation of Reduced Second Moments

The reduced second moment is the part of the dipolar interaction that provides a relaxation process. It can be written according to equation (6.42) by

$$\Delta M_2 = (M_2)_{RL} - (M_2)_{MO} \quad (7.14)$$

where RL denotes rigid lattice and MO denotes motionally averaged. The heteronuclear second moment of a nuclei of spin I, in frequency units, is given by

$$M_2^{IS} = \frac{1}{3}\left(\frac{\mu_0}{4\pi}\right)^2\gamma_I^2\gamma_S^2\hbar^2\, S(S+I)\sum_j \frac{(3\cos^2\theta_{ij}-1)^2}{r_{ij}^6} \quad (7.15)$$

For a polycrystalline sample equation (7.15) is averaged over all orientations. As described in Chapter 2, the result is a rigid lattice second moment given by

$$M_2^{IS} = \frac{4}{15}\left(\frac{\mu_0}{4\pi}\right)^2\gamma_I^2\gamma_S^2\hbar^2\, S(S+I)\sum_j \frac{1}{r_{ij}^6} \quad (7.16)$$

In the case of a motionally averaged polycrystalline second moment the $(3\cos^2\theta_{ij}-1)/r_{ij}^3$ term involved in the summation in equation (7.15) must first be time averaged over the motional processes before a powder average is taken. This calculation involves evaluation of

$$f = \langle\langle(3\cos^2\theta_{ij}-1)/r_{ij}^3 \gtrless^2 \rangle_p \quad (7.17)$$

where $\langle\ \rangle_c$ is the average over molecular motion, and $\langle\ \rangle_p$ is the polycrystalline average. It is convenient to express the pre-averaged function in terms of spherical harmonic functions giving

$$(3\cos^2\theta_{ij} - 1)/r_{ij}^3 = 2P_2(\cos\theta_{ij})/r_{ij}^3 \qquad (7.18)$$

where $P_2(\cos\theta_{ij})$ is a Legendre polynomial. By taking Racah's normalization of the spherical harmonics[18], denoted by $C_{kq}(\theta,\varphi)$, the addition theorem and orthogonality relationships can be used, which state respectively that

$$\sum_q (-1)^q C_{k-q}(\theta_1\varphi_1)\, C_{kq}(\theta_2\varphi_2) = P_k(\cos\omega) \qquad (7.19)$$

where ω is the angle between the two directions $(\theta_1\varphi_1)$ and $(\theta_2\varphi_2)$; and

$$\int_0^{2\pi}\int_0^{\pi} (-1)^q C_{k-q}(\theta\varphi)^* C_{KQ}(\theta\varphi)\sin\theta d\theta d\varphi = \delta_{kK}\delta_{qQ}4\pi/(2k+1) \qquad (7.21)$$

Using equation (7.19), equation (7.18) can be rewritten as

$$(3\cos^2\theta_{ij} - 1)/r_{ij}^3 = (2/r_{ij}^3)[\sum_q (-1)^q C_{2-q}(\theta_1\varphi_1)_{ij} C_{2q}(\theta_2\varphi_2)] \qquad (7.21)$$

The first step in the evaluation of equation (7.17) is to average equation (7.21) over all motional sites of the two dipolar coupled nuclei under consideration,

$$\begin{aligned}\langle(3\cos^2\theta_{ij} - 1)/r_{ij}^3\rangle_c = \langle(2/r_{ij}^3)[&C_{22}(\theta_1\varphi_1)_{ij}C_{2-2}(\theta_2\varphi_2)\\ &- C_{21}(\theta_1\varphi_1)_{ij}C_{2-1}(\theta_2\varphi_2)\\ &+ C_{20}(\theta_1\varphi_1)_{ij}C_{20}(\theta_2\varphi_2) - C_{2-1}(\theta_1\varphi_1)_{ij}C_{21}(\theta_2\varphi_2)\\ &+ C_{2-2}(\theta_1\varphi_1)_{ij}C_{22}(\theta_2\varphi_2)]\rangle_c\end{aligned} \qquad (7.22)$$

The terms on the right hand side of equation (7.22) are only subject to addition and subtraction operations, and as such the time averaging of individual terms gives the same results, that is, equation (7.22) can be rewritten as

$$\begin{aligned}\langle(3\cos^2\theta_{ij} - 1)/r_{ij}^3\rangle_c = [&\langle(2/r_{ij}^3)[C_{22}(\theta_1\varphi_1)_{ij}C_{2-2}(\theta_2\varphi_2)\rangle_c\\ &- \langle(2/r_{ij}^3)C_{21}(\theta_1\varphi_1)_{ij}C_{2-1}(\theta_2\varphi_2)\rangle_c\end{aligned}$$

$$+ \langle(2/r_{ij}^3)C_{20}(\theta_1\varphi_1)_{ij}C_{20}(\theta_2\varphi_2)\rangle_c$$
$$- \langle(2/r_{ij}^3)C_{2-1}(\theta_1\varphi_1)_{ij}C_{21}(\theta_2\varphi_2)\rangle_c$$
$$+ \langle(2/r_{ij}^3)C_{2-2}(\theta_1\varphi_1)_{ij}C_{22}(\theta_2\varphi_2)\rangle_c] \qquad (7.23)$$

The spherical harmonics constructed from θ_2 and φ_2 are only functions of the reference spin coordinates and are independent of time averaging. Using this fact, the square of equation (7.23) can be written as

$$\langle(3\cos^2\theta_{ij} - 1)/r_{ij}^3 \gtrless_c^2 = [\langle(2/r_{ij}^3)C_{22}(\theta_1\varphi_1)_{ij}\rangle_c C_{2-2}(\theta_2\varphi_2)$$
$$- \langle(2/r_{ij}^3)C_{21}(\theta_1\varphi_1)_{ij}\rangle_c C_{2-1}(\theta_2\varphi_2)$$
$$+ \langle(2/r_{ij}^3)C_{20}(\theta_1\varphi_1)_{ij}\rangle_c C_{20}(\theta_2\varphi_2)$$
$$- \langle(2/r_{ij}^3)C_{2-1}(\theta_1\varphi_1)_{ij}\rangle_c C_{21}(\theta_2\varphi_2)$$
$$+ \langle(2/r_{ij}^3)C_{2-2}(\theta_1\varphi_1)_{ij}\rangle_c C_{22}(\theta_2\varphi_2)]^2 \qquad (7.24)$$

The polycrystalline averaging takes the form of a sum over all possible reference spin positions, equivalent to a sum over all possible orientations of internuclear vector to the applied field. This is evaluated by a normalized integral of the form

$$f = (1/4\pi) \int_0^{2\pi} \int_0^{\pi} \langle(3\cos^2\theta_{ij} - 1)/r_{ij}^3 \gtrless_c^2 \sin\theta_2 d\theta_2 d\varphi_2 \qquad (7.25)$$

The substitution of equation (7.24) into equation (7.25) in a form in which the explicit integration can be carried out involves multiplying out the square bracket in equation (7.24), resulting in 25 terms. However, it is straightforward to see from the orthonormality relationship given in equation (7.20) that any terms containing the factor $C_{2-q}(\theta_2\varphi_2)C_{2Q}(\theta_2\varphi_2)$, where $q \neq Q$ will not contribute to the integral. This simplifies the required expression to

$$4\pi f = \langle(2/r_{ij}^3)C_{20}(\theta_1\varphi_1)_{ij} \gtrless_c^2 \int_0^{2\pi} \int_0^{\pi} C_{20}(\theta_2\varphi_2)C_{20}(\theta_2\varphi_2)\sin\theta_2 d\theta_2 d\varphi_2$$

$$+ \langle(2/r_{ij}^3)C_{22}(\theta_1\varphi_1)_{ij}\rangle_c \langle(2/r_{ij}^3)C_{2\text{-}2}(\theta_1\varphi_1)_{ij}\rangle_c \int_0^{2\pi}\int_0^{\pi} C_{2\text{-}2}(\theta_2\varphi_2)C_{22}(\theta_2\varphi_2)\sin\theta_2 d\theta_2 d\varphi_2$$

$$- \langle(2/r_{ij}^3)C_{21}(\theta_1\varphi_1)_{ij}\rangle_c \langle(2/r_{ij}^3)C_{2\text{-}1}(\theta_1\varphi_1)_{ij}\rangle_c \int_0^{2\pi}\int_0^{\pi} C_{2\text{-}1}(\theta_2\varphi_2)C_{21}(\theta_2\varphi_2)\sin\theta_2 d\theta_2 d\varphi_2$$

(7.26)

The solutions to the integrals in equation (7.26) are found with reference to equation (7.20), giving

$$4\pi f = \frac{16\pi}{5}\left[\langle(1/r_{ij}^3)C_{20}(\theta_1\varphi_1)_{ij}\rangle^2 + 2\langle(1/r_{ij}^3)C_{22}(\theta_1\varphi_1)_{ij}\rangle\langle(1/r_{ij}^3)C_{2\text{-}2}(\theta_1\varphi_1)_{ij}\rangle\right.$$

$$\left.-2\langle(1/r_{ij}^3)C_{21}(\theta_1\varphi_1)_{ij}\rangle\langle(1/r_{ij}^3)C_{2\text{-}1}(\theta_1\varphi_1)_{ij}\rangle\right] \qquad (7.27)$$

The modified spherical harmonics $C_{2q}(\theta_1\varphi_1)$ can be generated explicitly by the formula

$$C_{2q}(\theta_1\varphi_1) = (-1)^q\left[\frac{(2-q)!}{(2+q)!}\right]P_2^q(\cos\theta_1)\exp(iq\varphi_1) \qquad (7.28)$$

and subsequent substitution into equation (7.27) gives

$$\langle\langle(3\cos^2\theta_{ij}-1)/r_{ij}^3\rangle_c^2\rangle_p = (4/5)\{(1/4)\langle(3\cos^2\theta_{1ij}-1)/r_{ij}^3\rangle_c^2$$

$$+(3/4)\langle(\sin^2\theta_{1ij}\cos2\varphi_{1ij})/r_{ij}^3\rangle_c^2 + (3/4)\langle\sin\theta_{1ij}\sin2\varphi_{1ij}/r_{ij}^3\rangle_c^2$$

$$+3\langle(\cos\theta_{1ij}\sin\theta_{1ij}\cos\varphi_{1ij})/r_{ij}^3\rangle_c^2 + 3\langle(\cos\theta_{1ij}\sin\theta_{1ij}\sin\varphi_{1ij})/r_{ij}^3\rangle_c^2\} \qquad (7.29)$$

Dropping the subscripts for convenience, equation (7.29) gives

$$f = (12/5)[\langle\sin\theta\cos\theta\cos\varphi/r^3\rangle^2 + \langle\sin\theta\cos\theta\sin\varphi/r^3\rangle^2]$$

$$+ (3/5)[\langle\sin^2\theta\cos2\varphi/r^3\rangle^2 + \langle\sin^2\theta\sin2\varphi/r^3\rangle^2]$$

$$+ (1/5)[\langle(3\cos^2\theta-1)/r^3\rangle^2]$$

$$= 12/5[\langle\sin\theta\cos\theta\cos\varphi/r^3\rangle^2 + \langle\sin\theta\cos\theta\sin\varphi/r^3\rangle^2 + \langle\sin^2\theta\sin\varphi\cos\varphi/r^2\rangle^2]$$

$$+ \{(3/5)\langle\sin^2\theta\cos2\varphi/r^3\rangle^2 + (1/5) < (3\cos^2\theta - 1)/r^3\rangle^2\} \qquad (7.30)$$

The last two terms in equation (7.30) can be rewritten using trigonometric identities as

$$(3/5)\ \langle\sin^2\theta(2\cos^2\varphi-1)/r^3\rangle^2 + (1/5) < (3(1-\sin^2\theta) -1)/r^3\rangle^2$$

$$= (4/5)\langle1/r^3\rangle^2 + (12/5)\ (-\langle\sin^2\theta/r^3\rangle\langle\cos^2\theta/r^3\rangle$$

$$- \langle\sin^2\theta\cos^2\varphi/r^3\rangle\langle\sin^2\theta\sin^2\varphi/r^3\rangle\ ) \qquad (7.31)$$

In this form the terms can be substituted back into equation (7.30) to give

$$f = (4/5)\langle1/r^3\rangle^2 + (12/5)[\langle\sin\theta\cos\theta\cos\varphi/r^3\rangle^2 + \langle\sin\theta\cos\theta\sin\varphi/r^3\rangle^2 +$$

$$\langle\sin^2\theta\sin\varphi\cos\varphi/r^3\rangle^2 - \langle\sin^2\theta/r^3\rangle\langle\cos^2\theta/r^3\rangle$$

$$- \langle\sin^2\theta\cos\varphi/r^3\rangle\langle\sin^2\theta\sin^2\varphi/r^3\rangle] \qquad (7.32)$$

It is now straightforward to convert equation (7.32) into a cartesian form, where x, y and z are coordinates relative to the reference spin,

$$\langle\langle(3\cos^2\theta_{ij} - 1)/r_{ij}^3\rangle^2\rangle_p = (4/5)\{\langle1/r^3\rangle^2 - 3[\langle x^2/r^5\rangle\langle y^2/r^5\rangle + \langle x^2/r^5\rangle\langle z^2/r^5\rangle$$

$$+ \langle y^2/r^5\rangle\langle z^2/r^5\rangle - \langle xy/r^5\rangle^2 - \langle xz/r^5\rangle^2 - \langle yz/r^5\rangle^2]\} \qquad (7.33)$$

Using equations (7.15) and (7.33), the expression for the motionally averaged heteronuclear second moment in a polycrystalline sample is given by

$$M_2^{IS}{}_{MO} = \frac{4}{15}\left(\frac{\mu_0}{4\pi}\right)^2\gamma_I^2\gamma_S^2\hbar^2S(S+1)\ \sum_k U_{ik} \qquad (7.34)$$

where

$$U_{ik} = (\langle1/r_{ik}^3\rangle^2 - 3[\langle x_{ik}^2/r_{ik}^5\rangle\langle y_{ik}^2/r_{ik}^5\rangle + \langle x_{ik}^2/r_{ik}^5\rangle\langle z_{ik}^2/r_{ik}^5\rangle$$

$$+ \langle y_{ik}^2/r_{ik}^5\rangle\langle z_{ik}^2/r_{ik}^5\rangle - \langle x_{ik}y_{ik}/r_{ik}^5\rangle^2 - \langle x_{ik}z_{ik}/r_{ik}^5\rangle^2$$

$$- \langle y_{ik}z_{ik}/r_{ik}^5\rangle^2]) \qquad (7.35)$$

This result is the same as that previously derived[19]

Application to Polycrystalline $LiCF_3SO_3$

The proposed crystal structure of $LiCF_3SO_3$[20], described previously in Chapter 5, can be used to evaluate the appropriate lattice sums involved in equations (7.16), (7.34) and (7.35), and calculate the ^7Li-^{19}F second moments, given by

$$(M_2^{LiF})_{RL} = \frac{1}{5}\left(\frac{\mu_0}{4\pi}\right)^2 \gamma_F^2 \gamma_{Li}^2 \hbar^2 \sum_j \frac{1}{r_{ij}^6} \qquad (7.36)$$

$$(M_2^{LiF})_{MO} = \frac{1}{5}\left(\frac{\mu_0}{4\pi}\right)^2 \gamma_F^2 \gamma_{Li}^2 \hbar^2 \sum_k U_{ik} \qquad (7.37)$$

where U_{ik} is given in equation (7.35). For a sphere of defined radius about a reference ^7Li nucleus the cartesian x, y and z coordinates of all ^{19}F nuclei within the sphere were calculated. To simplify the motional averaging calculation, only ^{19}F nuclei belonging to CF_3 groups in which all three ^{19}F nuclei were within the defined radius were used in the second moment calculations. For a radius of 1.5 nm, the rigid lattice second moment was reduced by 0.2% due to this simplification. Figure 7.4 shows a reference ^7Li nucleus at the centre of a sphere surrounded by all ^{19}F nuclei within a 1.5 nm radius. Values of r_{ij} were calculated from the cartesian coordinates using Pythagorass' theorem in three dimensions, and equation (7.36) was evaluated for spheres of radius between 0.7 nm and 1.5 nm centred on a reference spin. The computed rigid lattice ^7Li-^{19}F second moment is shown as a function of radius in Figure 7.5. It is clear that an asymptotic value is reached at a radius of 1.5 nm.

In evaluating the time averaged lattice sum for a symmetric CF_3 group that is undergoing hindered reorientation about its C_3 axis, two distinct approaches can be used. Firstly, the calculation could be performed explicitly using equation (7.35). An alternative approach is also available. It has been shown[21,22] that

for a spherically symmetric rotation of a molecular group, the motionally averaged intermolecular second moment is equivalent to the rigid lattice second moment when all the nuclei in the groups are placed at the motional centres. Given this behaviour, it seems reasonable to suggest that the ^{7}Li-^{19}F rigid lattice second moment, calculated between a reference ^{7}Li nucleus and groups of three ^{19}F nuclei placed at the centre of masses of relevant CF_3 groups, would also give the motionally averaged ^{7}Li-^{19}F second moment.

However, the CF_3 group described in the $LiCF_3SO_3$ crystal structure is not symmetric, as discussed previously. There is no C_3 axis; although it has to be recognized that the x-ray structure gives time averaged positions for the ^{19}F atoms in the CF_3 group. Examining the structure shown in Figure 5.15, it seems reasonable to suggest that the asymmetry of the CF_3 group is a consequence of O-Li coordination. Lithium bonds do, in general, possess a degree of covalency, and even LiF only exhibits 92% ionic character[23]. The Li-O bond lengths in $LiCF_3SO_3$ are typical of Li in a tetrahedral oxygen-coordinated environment. This coordination is satisfied by two oxygens from one CF_3SO_3 anion and one each from two others, introducing asymmetry into the SO_3 group. The CF_3 groups adopt a staggered conformation with the SO_3 groups and, as such, it may be that the asymmetry of the SO_3 group induces asymmetry into the CF_3 group.

The asymmetry of the CF_3 group is imposed by the potential profile of the lattice and is not an inherent property of the CF_3SO_3 anion. Thus as the CF_3 groups jump between allowed crystallographic sites, specific bond lengths and angles will be changed slightly so that the new coordinate position of a specific ^{19}F nucleus will be identical to the old coordinate position of the ^{19}F nucleus it has replaced. Strictly speaking then, the calculation of the ^{7}Li-^{19}F motionally averaged dipolar second moment should be carried out explicitly. By placing three ^{19}F nuclei at the centre of mass of the CF_3 group, rigid rotation is inherently assumed and this is clearly unjustified as it assumes, for an asymmetric group, that the new

coordinate position of a specific ^{19}F nucleus after a jump between crystallographic sites is different to the old coordinate position of the replaced ^{19}F nucleus.

Figure 7.6 shows the explicitly calculated motionally averaged ^{7}Li-^{19}F second moment. It is interesting to carry out the calculation in the alternative way described, bearing in mind that this method is an approximation. The motionally averaged ^{7}Li-^{19}F second moment calculated in this way is shown in Figure 7.7. For comparison the figure also includes the explicitly calculated motionally averaged values. It is found that there is a significant discrepancy of approximately 10% between the two methods of calculation.

Figure 7.8 shows the ^{7}Li-^{19}F reduced second moment calculated by equation (7.14), using the explicitly time averaged values of the motionally averaged second moment. The values obtained for a calculation radius of 1.5 nm are given in Table 7.1.

Table 7.1 ^{7}Li-^{19}F second moment values in polycrystalline $LiCF_3SO_3$

Second Moment	Value Calculated/rad^2 s^{-2}
$(M_2^{LiF})_{RL}$	4.33×10^7
$(M_2^{LiF})_{MO}$	3.23×10^7
ΔM_2^{LiF}	1.09×10^7

A simulation of the ^{7}Li spin-lattice relaxation behaviour using equation (7.13),

$$\frac{1}{T_1(^7Li)} = \frac{1}{2}\Delta M_2^{LiF}\left(\frac{\tau_c}{1 + (\omega_{Li} - \omega_F)^2\tau_c^2} + \frac{3\tau_c}{1 + \omega_{Li}^2\tau_c^2} + \frac{6\tau_c}{1 + (\omega_{Li} + \omega_F)^2\tau_c^2}\right)$$

for values of τ_c between 10^{-8} s and 10^{-11} s, gives a single spin-lattice relaxation time minimum at $\tau_c = 4.9 \times 10^{-9}$ s. The experimental $T_1(^7Li)$ plot shown in Figure 7.2 has a single minimum at 250 K, and a linear least squares fit to the linear high temperature data gives

$$E_A = 24.28 \pm 0.71 \text{ kJ mol}^{-1}.$$

The simultaneous substitution of these parameters into the Arrhenius relationship given by equation (7.8) gives

$$\tau_0 = (4.12 \pm 0.25) \times 10^{-14} \text{ s}$$

The motional parameters for the CF_3 group reorientation obtained from the ^7Li spin-lattice relaxation results, compare well with those obtained in Chapter 5 from a ^{19}F spin-lattice relaxation time study. The results are shown in Table 7.2.

Table 7.2 CF_3 group motional parameters obtained from ^{19}F and ^7Li spin-lattice relaxation studies in polycrystalline $LiCF_3SO_3$.

Spin-lattice Relaxation Study	E_A/kJ mol^{-1}	τ_0/s
^{19}F	24.40 ± 0.69	$(3.42 \pm 0.17) \times 10^{-14}$
^7Li	24.28 ± 0.71	$(4.12 \pm 0.25) \times 10^{-14}$

The motional parameters extracted from the ^7Li spin-lattice relaxation results can be used in conjunction with equation (7.13) and the value of the ^7Li-^{19}F reduced second moment given in Table 7.1 to simulate the $\ln(T_1(^7Li))$ versus inverse temperature plot. This is shown in Figure 7.9.

A dipolar coupled ^7Li-^{19}F spin-lattice relaxation mechanism accounts for ~75% of the experimentally observed values of $T_1(^7Li)$. Any errors in the crystal structure will effect the calculated spin-lattice relaxation behaviour, and although both x-ray and neutron diffraction data were used in the structure determination[19] (due to the relatively poor scattering of x-rays by lithium), this study was the first reported determination of a previously unknown structure by the maximum entropy and likelihood method from powder diffraction data; a technique that has not, as yet, been tested extensively. At present it is not possible to say whether the errors in the crystal structure could be solely responsible for the discrepancy observed in Figure 7.9.

It is feasible that there are other contributions to the spin-lattice relaxation behaviour. It has been suggested that when a hindered rotation does not change the spatial distribution but merely permutes the locations of nuclear magnetic moments, the resulting spin-lattice relaxation of a nearby fixed nucleus is likely to be dipolar, even if the nucleus has a quadrupole moment[17]. However, there is the added complication in polycrystalline $LiCF_3SO_3$ that the CF_3 groups are asymmetric, and a quadrupolar spin-lattice relaxation mechanism should not be discounted. This mechanism would be described by[34.35]

$$\frac{1}{T_{1,Q}} = \frac{1}{16} e^2Q^2\hbar^2\left[A\frac{\tau_c}{1+\omega_{Li}{}^2\tau_c{}^2} + B\frac{\tau_c}{1+4\omega_{Li}{}^2\tau_c{}^2}\right] \qquad (7.39)$$

where

$$A = \langle\langle|\delta V_{xz}(t) + i\delta V_{yz}(t)|^2\rangle_c\rangle_p \qquad (7.40)$$

and

$$B = \langle\langle|\delta V_{xx}(t) - \delta V_{yy}(t) + 2i\delta V_{xy}(t)|^2\rangle_c\rangle_p \qquad (7.41)$$

and $V_{xz} = d^2V/dxdz$, $V_{yz} = d^2V/dydz$ etc, and δV_{xz} indicates the fluctuating part. These equations would be difficult to evaluate and would require ab-initio calculations.

7.5 A ^{7}Li Spin-lattice Relaxation Study of PEO/$LiCF_3SO_3$ Systems

Results

Figure 7.10 shows a typical ^{7}Li nuclear magnetization recovery in the 3.5:1 PEO/$LiCF_3SO_3$ system, as measured at 254 K. As in polycrystalline $LiCF_3SO_3$ the magnetization recoveries over the entire temperature range could be fitted within experimental uncertainties to a single exponential function. The estimated error in $T_1(^7Li)$ is of the order of 5%.

Figure 7.11 shows the behaviour of $T_1(^7Li)$ with temperature, plotted in the form of a graph of $\ln(T_1(^7Li))$ versus inverse temperature for polycrystalline $LiCF_3SO_3$ and the 3.5:1 PEO/$LiCF_3SO_3$ system. There is a single ^7Li spin-lattice relaxation time minimum ($T_1(^7Li)$ = 4.8 s) in the 3.5:1 PEO/$LiCF_3SO_3$ system at 250 K. This compares with a minimum ($T_1(^7Li)$ = 7.4 s) at 250 K for polycrystalline $LiCF_3SO_3$.

Discussion

It is clear from Figure 7.11 that the ^7Li spin-lattice relaxation behaviour in the 3.5:1 PEO/$LiCF_3SO_3$ system is different in character to that in polycrystalline $LiCF_3SO_3$. The gradient of the linear section of the high temperature side of the $\ln(T_1(^7Li))$ versus inverse temperature plot indicates that the activation energy of the motional process responsible for the ^7Li spin-lattice relaxation is considerably reduced compared to that in polycrystalline $LiCF_3SO_3$. A linear least squares fit to the data gives the ratio $E_A(LiCF_3SO_3)/E_A$(3.5:1 PEO/$LiCF_3SO_3$) ~ 6. Values of important parameters are shown comparatively in Table 7.3.

Table 7.3 The value and temperature of ^7Li spin-lattice relaxation minima, and calculated activation energies in $LiCF_3SO_3$ compared to 3.5:1 PEO/$LiCF_3SO_3$.

System	T_{1MIN}/s	T_{MIN}/K	E_A/kJmol^{-1}
$LiCF_3SO_3$	7.4	250	24.28 ± 0.69
3.5:1 PEO/$LiCF_3SO_3$	4.8	250	3.42 ± 0.15

The ratio of activation energies is in good agreement with previous work [13]. The authors did not calculate E_A explicitly but did plot values of $T_1(^7Li)$ versus temperature for polycrystalline $LiCF_3SO_3$ and for a 4:1 PEO/$LiCF_3SO_3$ system. Over the same temperature range as in this work the ratio of activation energies can be estimated as approximately 6. The authors did not comment on this

difference and suggested simply that the hindered rotation of the CF_3 group was responsible for ^7Li spin-lattice relaxation in both cases.

Two possible explanations for the difference in activation energies are as follows. Firstly, an amorphous fraction within the 3.5:1 PEO/$LiCF_3SO_3$ system may give rise to a ^7Li exchange mechanism and, secondly there may be some new motional process in the stoichiometric complex itself. These ideas are now dicussed further.

NMR studies of polymer electrolyte systems in a largely amorphous state have suggested that a process of bound to mobile conversion of species occurs, where the bound state represents ion aggregates[23-28]. It has been suggested that this process is crucial to fast ion transport. In amorphous systems, it has been shown that the spin-lattice relaxation behaviour of the cation is governed by a quadrupolar mechanism between the cation and the polymer lattice; this is true even when the anion involved has a reorientating molecular group, such as with CF_3SO_3[14]. In the 3.5:1 PEO/$LiCF_3SO_3$ system the DSC results discussed in Chapter 6 suggest there may be a small amount of excess PEO present which will contain an amorphous fraction. Futhermore, current research[30,31] suggests that a single stoichiometric crystalline complex exists with an O:Li ratio of 3:1 and not 3.5:1 as previously thought. This is an area for further work, but if correct, and the present work supports the suggestion to some extent, then it does not seem unreasonable to suggest a similar cation exchange process between crystalline and amorphous regions in the 3.5:1 PEO/$LiCF_3SO_3$ system. This would contribute to ^7Li spin-lattice relaxation.

There is a great deal of discussion in more amorphous systems on whether there are different cation environments due to the presence of ion aggregates and whether there is more than one population of cations each with different mobilities. A number of studies report finding no evidence for the existence of

more than one cation environment[14,29,30]. It has been suggested[14,29] that motional narrowing of the quadrupolar interaction, for quadrupolar nuclei in the amorphous systems, may provide an alternative explanation for experimental results interpreted in terms of the cation having distinct amorphous sites.

To investigate the possibility of ^7Li mobility between crystalline and amorphous fractions, and in the amorphous fraction itself, a study of ^7Li lineshapes was carried out.

Figure 7.12 shows ^7Li lineshapes for polycrystalline $LiCF_3SO_3$ and, for 3.5:1 and 9:1 PEO/$LiCF_3SO_3$ systems at 293 K. Figure 7.13 shows ^7Li lineshapes for polycrystalline $LiCF_3SO_3$ and for 3.5:1 and 9:1 PEO/$LiCF_3SO_3$ systems at 343 K. Table 7.4 summarizes the main features.

Table 7.4 Main characteristics of ^7Li lineshapes observed

T/K	293 K		T/343 K	
	% Sample	~ Linewidth/kHz	% Sample	~ Linewidth/kHz
Polycrystalline $LiCF_3SO_3$	100	8	90 10	8 1
3.5:1 PEO/$LiCF_3SO_3$	90 10	8 1	80 20	8 1
9:1 PEO/$LiCF_3SO_3$	60 40	8 1	30 70	8 1

The ^7Li lineshape measured in polycrystalline $LiCF_3SO_3$ at 293 K is broad and featureless. However, at the same temperature the ^7Li lineshape in the 3.5:1 PEO/$LiCF_3SO_3$ system shows the emergence of a narrower component, which narrows further and becomes a larger percentage of the signal in the 9:1 PEO/$LiCF_3SO_3$ system. This narrower component could provide evidence for more mobile ^7Li in an amorphous fraction of the systems, as suggested by the observed spin-lattice relaxation behaviour. This would explain the increase in the narrower component in the 9:1 PEO/$LiCF_3SO_3$ system, as an increased fraction of ^7Li is able to reside in an amorphous phase. At 343 K the amorphous fraction of

the 3.5:1 and 9:1 PEO/$LiCF_3SO_3$ increases and correspondingly the lineshapes observed show a larger percentage of the sample contributing to the narrower line.

It must be noted, that in polycrystalline $LiCF_3SO_3$ itself, the ^7Li lineshape at 343 K shows a narrowed component. This would be consistent with a phase change in polycrystalline $LiCF_3SO_3$, suggested by the DSC study discussed in Chapter 6. The higher temperature phase may contain sites in which a certain percentage of the ^7Li ions become more mobile. Whatever the origin of this behaviour, it seems reasonable to suggest that care should be taken over interpreting temperature dependent ^7Li lineshapes simply in terms of the distribution of ions throughout phases of the ionic host polymer system.

7.7 Conclusion

The ^7Li spin-lattice relaxation in polycrystalline $LiCF_3SO_3$ is dominated by a dipolar mechanism associated with the hindered reorientation of the CF_3 group.

In the 3.5:1 PEO/$LiCF_3SO_3$ system there is a small fraction (10%) of ^7Li nuclei that are more mobile than the rest. This fraction increases with amount of excess PEO in the system, and with temperature. The ^7Li spin-lattice relaxation behaviour in the 3.5:1 PEO/$LiCF_3SO_3$ system is more efficient than in polycrystalline $LiCF_3SO_3$ at a given temperature and may be influenced by an exchange mechanism between the stoichiometric complex and the amorphous phase. In the latter ^7Li quadrupolar relaxation could occur.

REFERENCES

1 F Lurcat
CRH Acad. Sci., 240, 2517, 1955.

2 P S Hubbard
J. Chem. Phys., 33, 985, 1970.

3 E R Andrew and D P Tunstall
Proc. Phys. Soc., 78, 1, 1961.

4 A Abragam
The Principles of Nuclear Magnetism
Clarendon, Oxford, 1961.

5 A Hudson and G R Luckhurst
Mol. Phys., 16, 395, 1969.

6 A Hudson and J W E Lewis
Faraday Soc., 66, 1297, 1970.

7 H J C Berendsen and H T Edzes
Ann. NY Acad. Sci., 204, 459, 1973.

8 J Andrasko
J. Mag. Res., 16, 502, 1974.

9 H Gustavsson, B Lindman and T Bull
J. Amer. Chem. Soc., 100, 4655, 1978.

10 J E Norne, H Gustavsson, S Forson,
Eur. J. Biochem., 98, 591, 1979.

11 A Delville, C Detellier and P Laselo
J. Mag. Res., 34, 301, 1979.

12 A Delville, J Grandjean, P Laszlo
Eur. J. Biochem., 105, 289, 1980.

13 D P Tunstall, A S Tomlin, J R MacCallum and C A Vincent
J. Phys. Chem., 21, 1039, 1988.

14 S H Chung, K R Jeffrey and J R Stevens
J. Chem. Phys., 94, 1803, 1991.

15 C P Slichter
Principles of Magnetic Resonance
Harper and Row, New York, 1963.

16 H W Spiess
NMR Basic Principles and Progress
Springer-Verlag, New York, 1978.

17 R S Parker and V H Schmidt
J. Mag. Res., 6, 501, 1972.

18 D M Brink and G R Satchler
Angular Momentum
Oxford University Press, Oxford, 1971.

19 G R Miller and H S Gutowsky
J. Chem. Phys., 39, 1983, 1963.

20 M Tremayne, P Lightfoot, M A Mehta, P G Bruce et al
J. Sol. State Chem., 100, 191, 1992.

21 G R Miller and H S Gutowsky
J. Chem. Phys., 39, 1983, 1963.

22 D W McCall and D C Douglas
J. Chem. Phys., 33, 777, 1960.

23 S G Greenbaum, K J Adamic, Y S Pak, M C Wintergill and J J Fontanella
Solid State Ion., 28, 1042, 1988.

24 K J Adamic, S G Greenbaum, M C Wintersgill and J J Fontanella
J. Appl. Phys., 60, 1342, 1986.

25 S Schantz, M Kakihana and M Sandberg
Solid State Ion., 40, 41, 645, 1990.

26 M C Wintersgill, J J Fontanella, M K Smith, S G Greenbaum, K J Adamic and C G Andeen
Polymer, 28, 633, 1987.

27 S G Greenbaum, Y S Pak, M C Wintersgill and J J Fontanella
Solid State Ion., 31, 241, 1988.

28 S G Greenbaum, Y S Pak, M C Wintersgill, J J Fontanella, J W Schultz and C G Andeen
J. Electrochem Soc., 135, 235, 1988.

29 R Spindler and D F Shriver
J. Am. Chem. Soc., 110, 3036, 1988.

30 J P Manning, C B Frech, B M Fung and R E Frech
Polymer, 32, 2939, 1991.

31 A Vallee, S Besner, J. Prud'homme
Electrochim Acta, 37, 1579, 1992.

32 R Kimmich and Kh Schmauder
Polymer, 18, 239, 1977.

33 P H Kasai and R J Myers
J. Chem. Phys., 30, 1096, 1968.

34 H T Stokes, D C Ailion and T A Case
Phys. Rev. B, 30, 4925, 1984.

35 D E O'Reilly
J. Chem. Phys., 58, 3023, 1973.

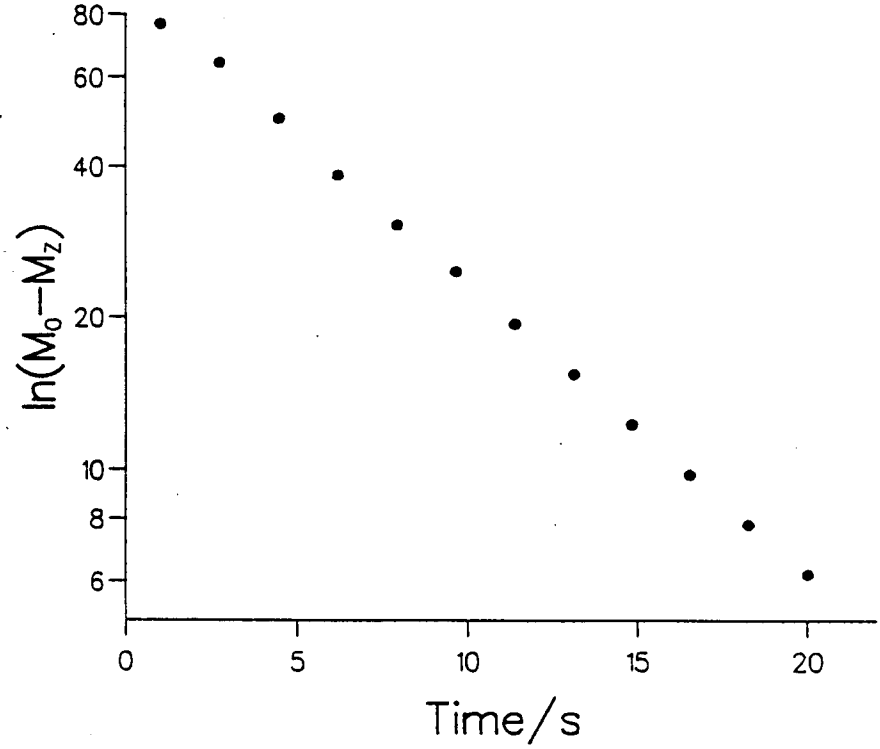

Figure 7.1 The ^7Li nuclear magnetization recovery measured at 23.10 MH_z and 254 K, in polycrystalline $LiCF_3SO_3$.

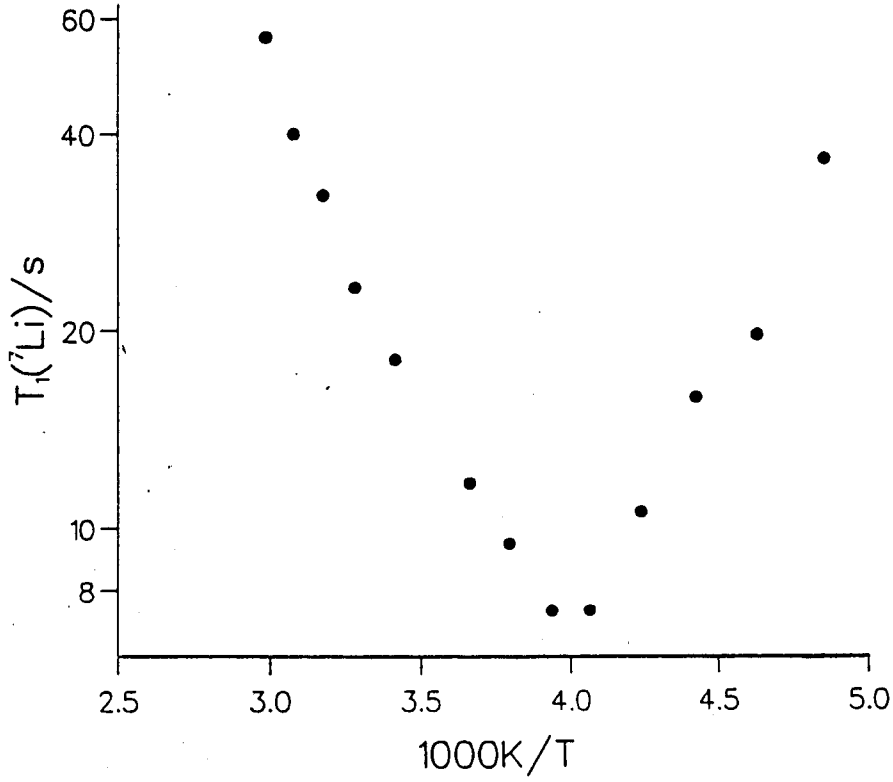

Figure 7.2 The temperature dependence of the ^7Li spin-lattice relaxation time, measured at 23.10 MHz in polycrystalline $LiCF_3SO_3$.

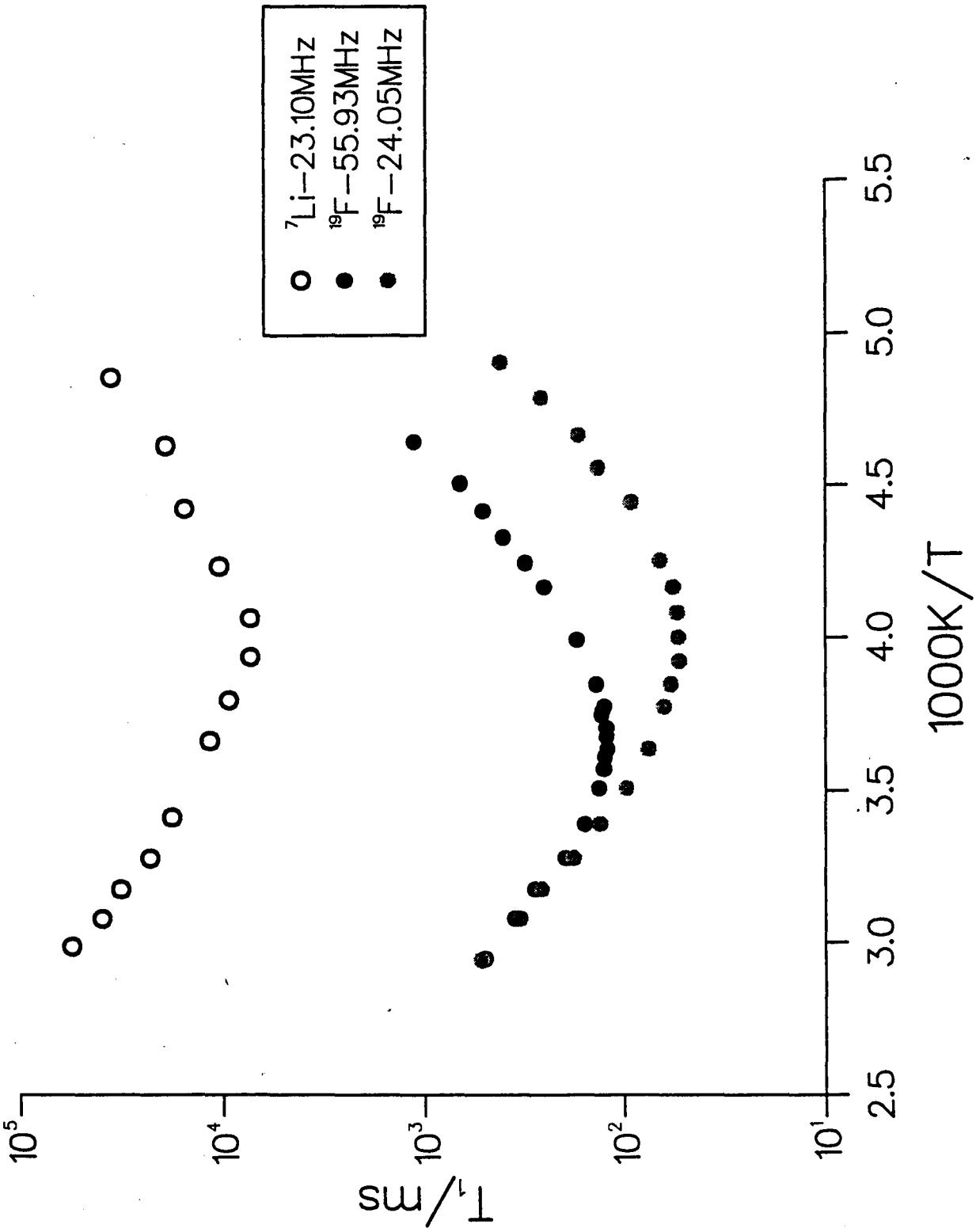

Figure 7.3 The temperature dependence of the ^{7}Li spin-lattice relaxation time, measured at 23.10 MHz in polycrystalline $LiCF_3SO_3$. For comparison, the corresponding ^{19}F spin-lattice relaxation behaviour is shown, measured at 24.05 MHz and 55.93 MHz.

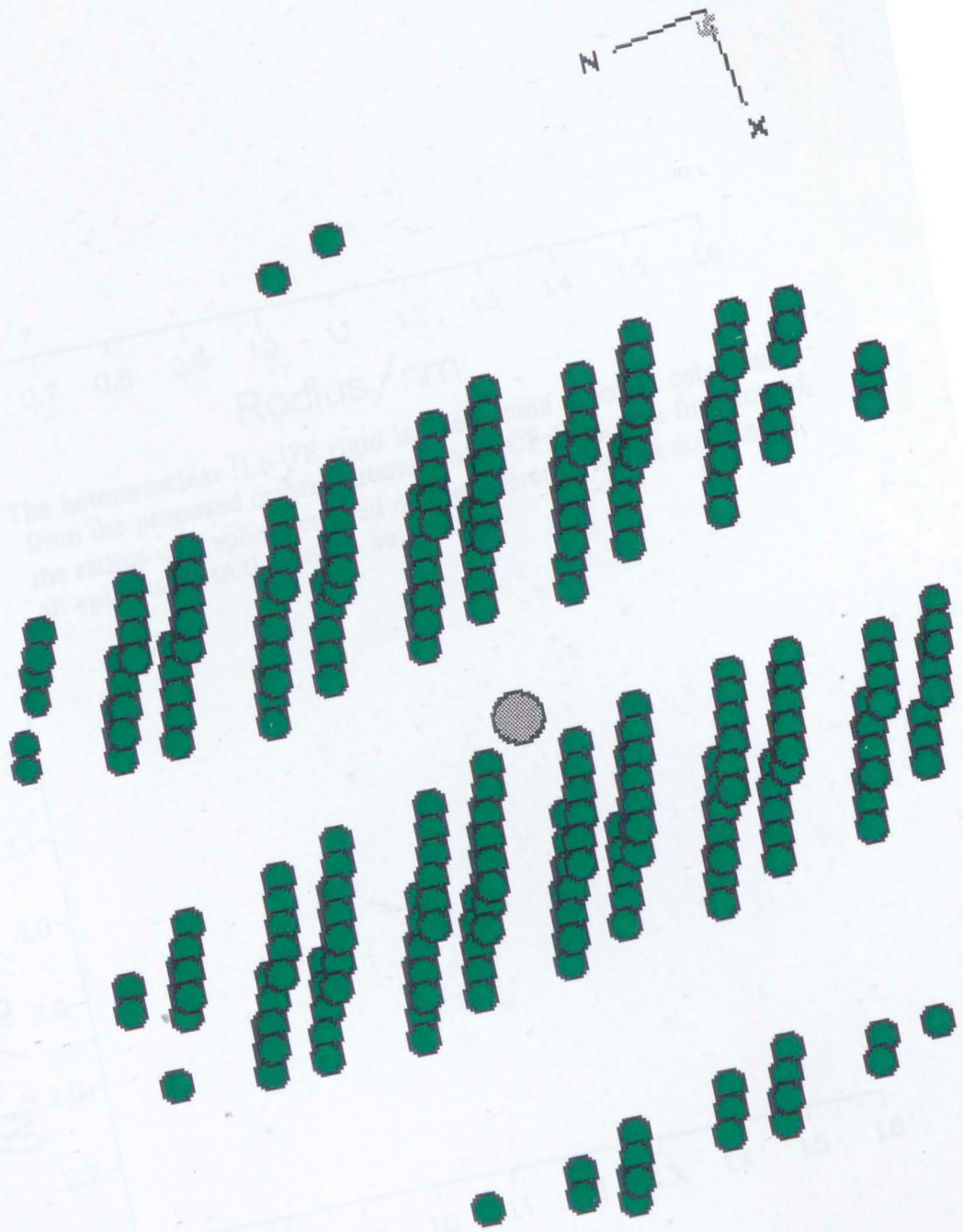

Figure 7.4 All ^{19}F nuclei within 1.5 nm of a reference ^{7}Li nucleus; calcu
from the proposed crystal structure of $LiCF_3SO_3$.

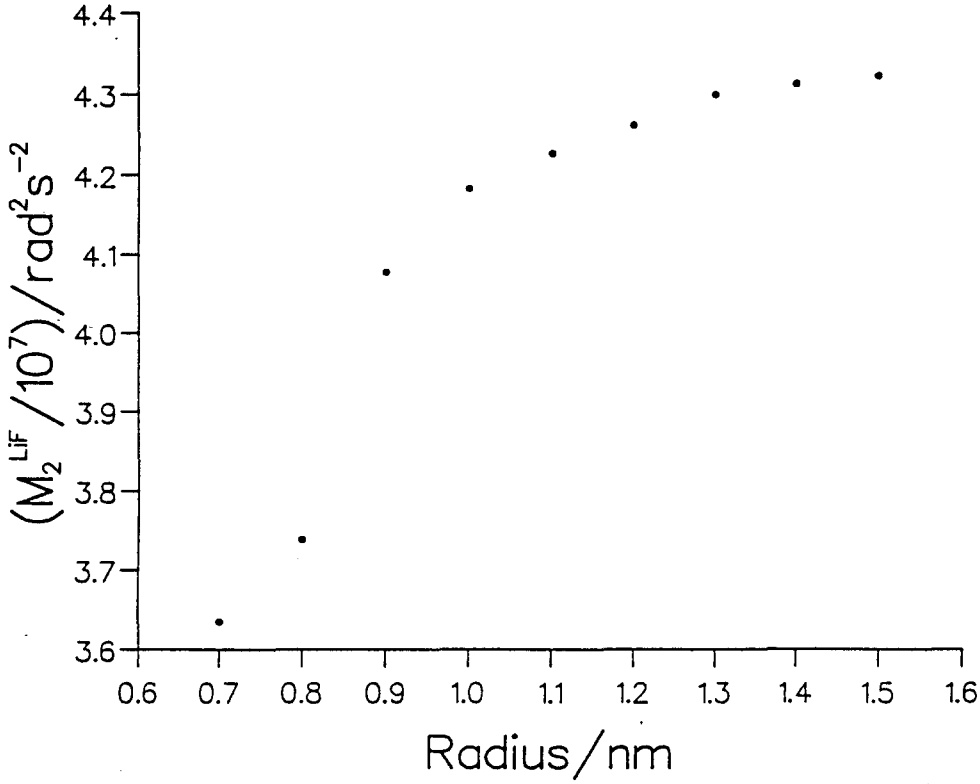

Figure 7.5 The heteronuclear ^7Li-^{19}F rigid lattice second moment calculated from the proposed crystal structure of $LiCF_3SO_3$, as a function of the radius of a sphere centred on the reference nuclei containing all spins used in the lattice summation.

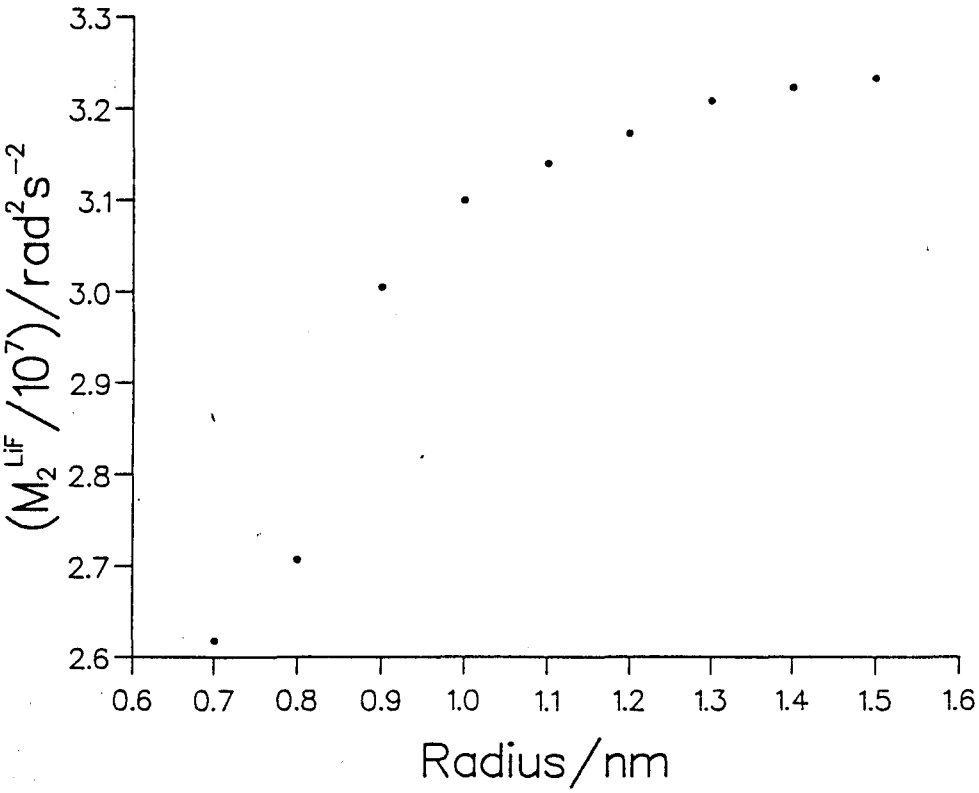

Figure 7.6 The explicitly motionally averaged heteronuclear second moment calculated from the proposed crystal structure of $LiCF_3SO_3$, as a function of the radius of a sphere, centred on the reference nuclei, containing all spins used in the lattice summation.

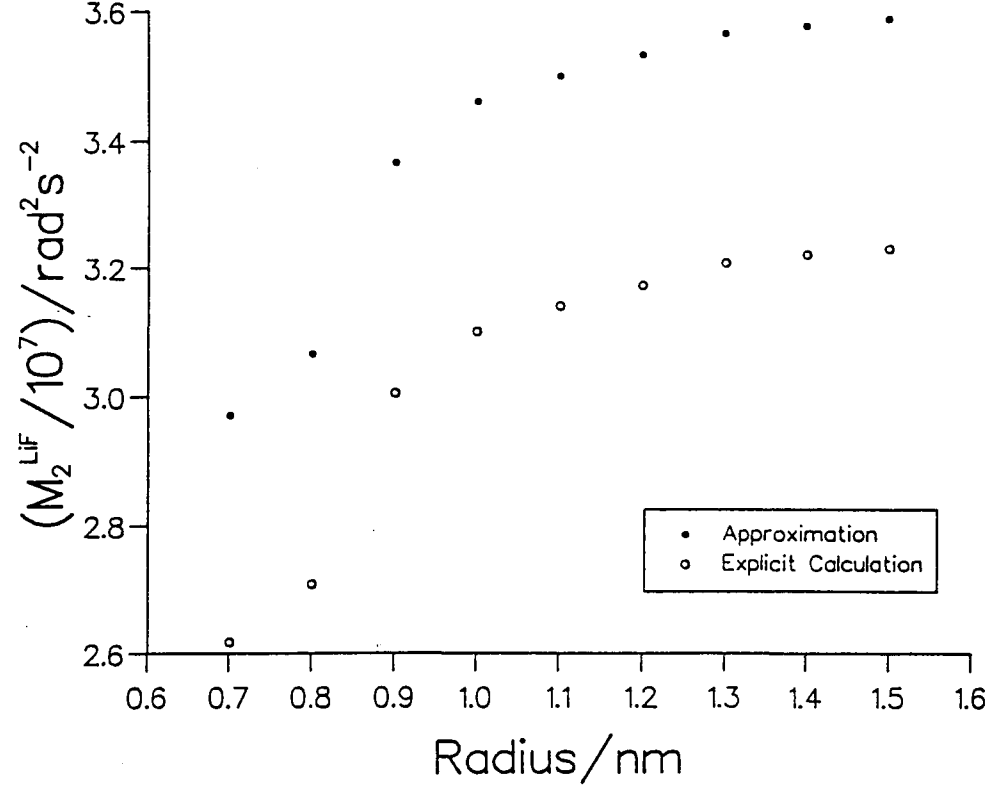

Figure 7.7 The heteronuclear ^{7}Li-^{19}F second moment motionally averaged using an approximate method of placing three ^{19}F nuclei at the centre of mass of the CF_3 group, as a function of the radius of a sphere, centred on the reference nuclei, containing all spins used in the lattice summation. The explicitly motionally averaged values are shown for comparison.

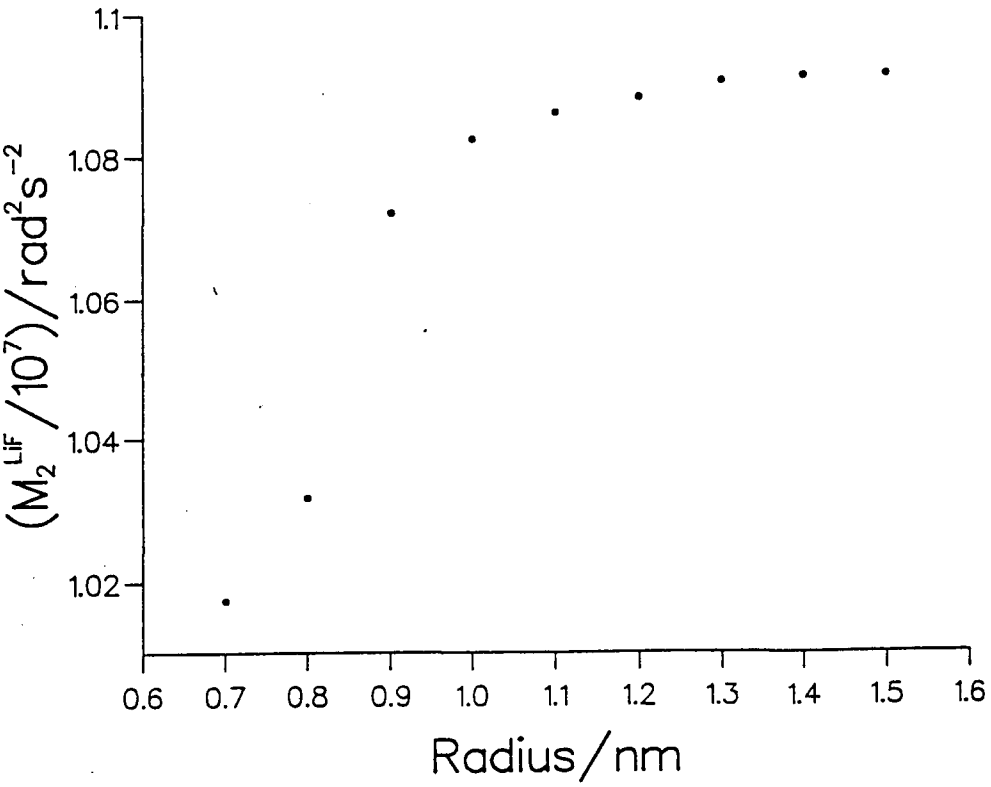

Figure 7.8 The heteronuclear ^{19}F-^{7}Li reduced second moment, for the proposed crystal structure of $LiCF_3SO_3$, as a function of the radius of a sphere, centred on the reference nuclei, containing all spins used in the lattice summation, calculated from a combination of Figures 7.6 and 7.7.

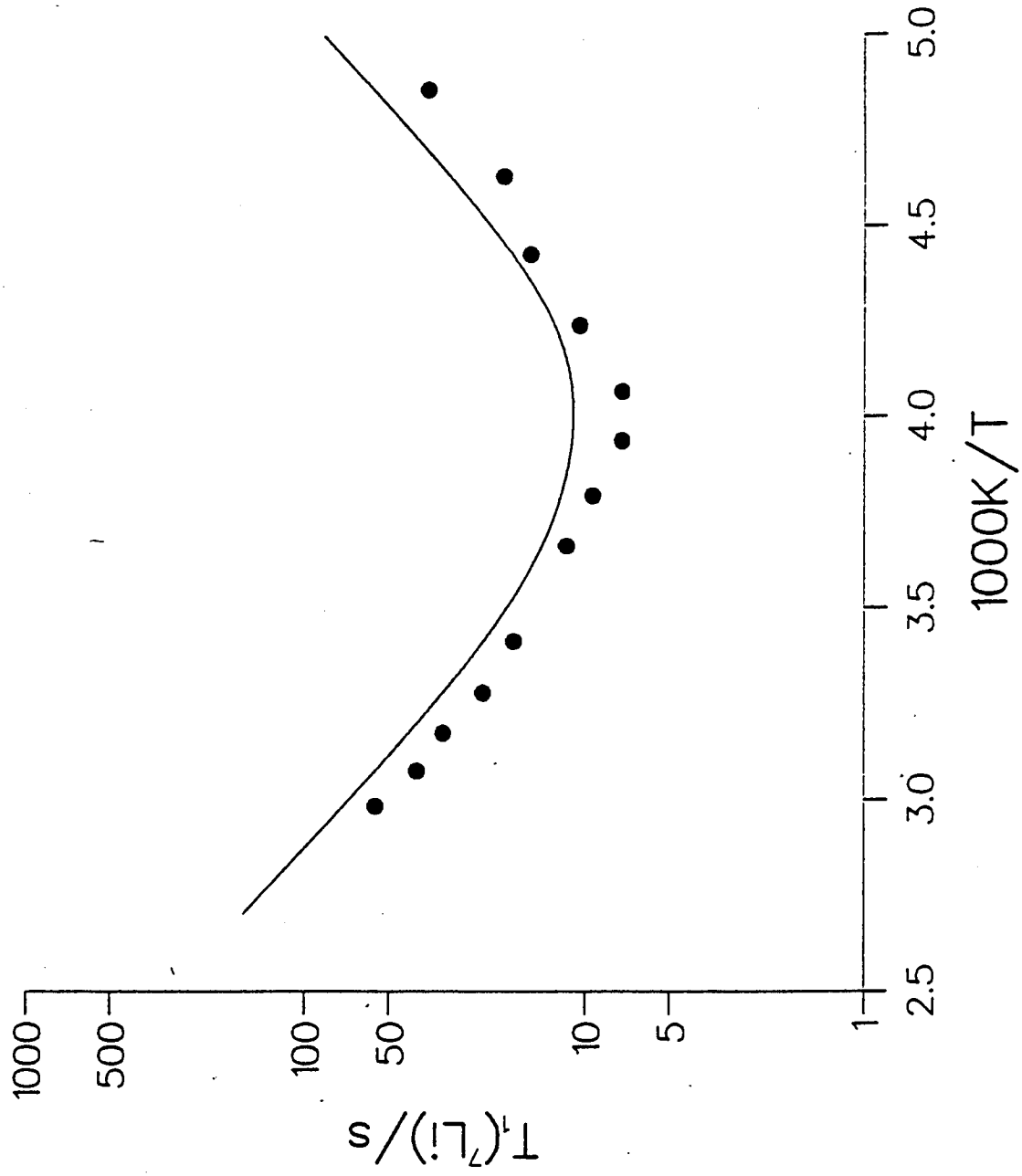

Figure 7.9 A simulation of the ^{7}Li spin-lattice relaxation behaviour, using a model system of ^{19}F-^{7}Li dipolar coupled nuclei interacting in a pairwise manner. The motional parameters relating to the dynamical processes mediating the spin-lattice relaxation are $E_A = 24.28$ kJ mol^{-1} and $\tau_0 = 4.12 \times 10^{-14}$s. The corresponding experimental results are shown for comparison.

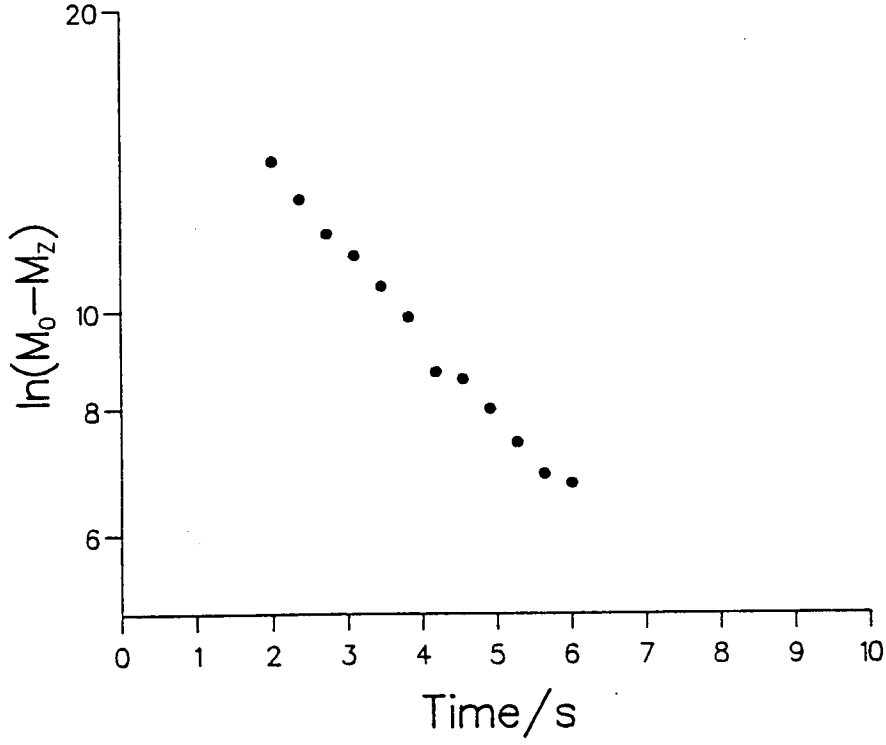

Figure 7.10 The ^7Li nuclear magnetization recovery measured at 23.10 MHz and 254 K, in the 3.5:1 PEO/$LiCF_3SO_3$ system.

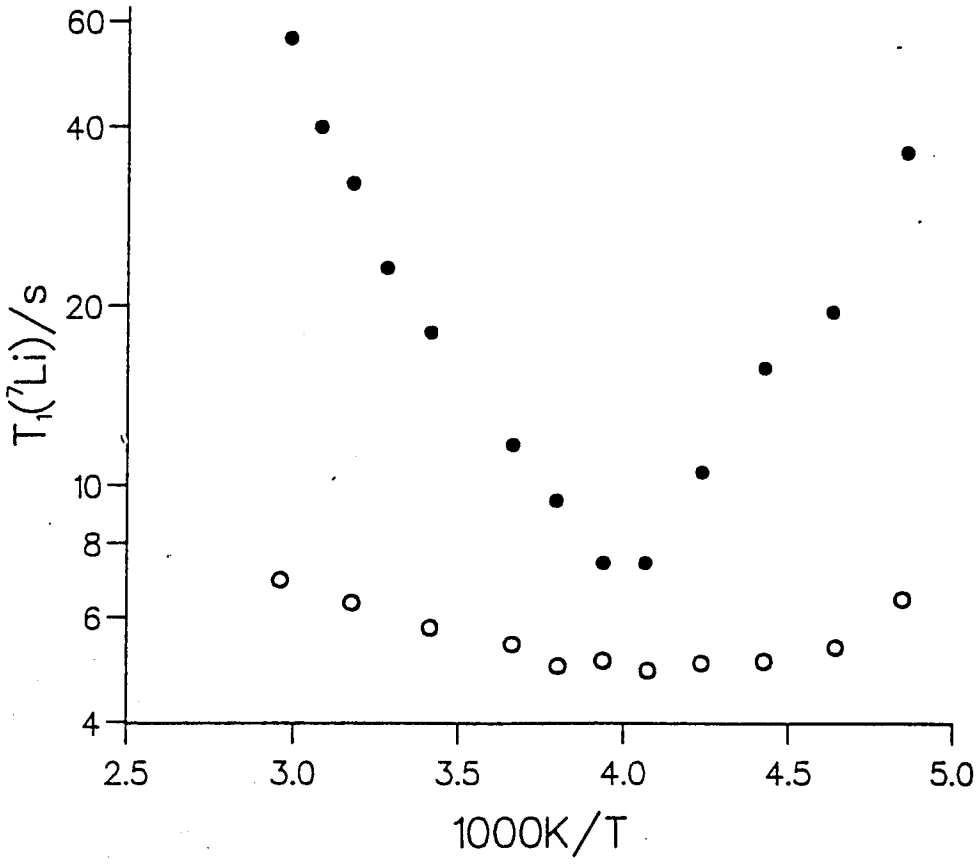

Figure 7.11 The temperature dependence of the ^7Li spin-lattice relaxation time measured at 23.10 MHz in the 3.5:1 PEO/$LiCF_3SO_3$ system (O). For comparison the corresponding results from polycrystalline $LiCF_3SO_3$ are also shown (●).

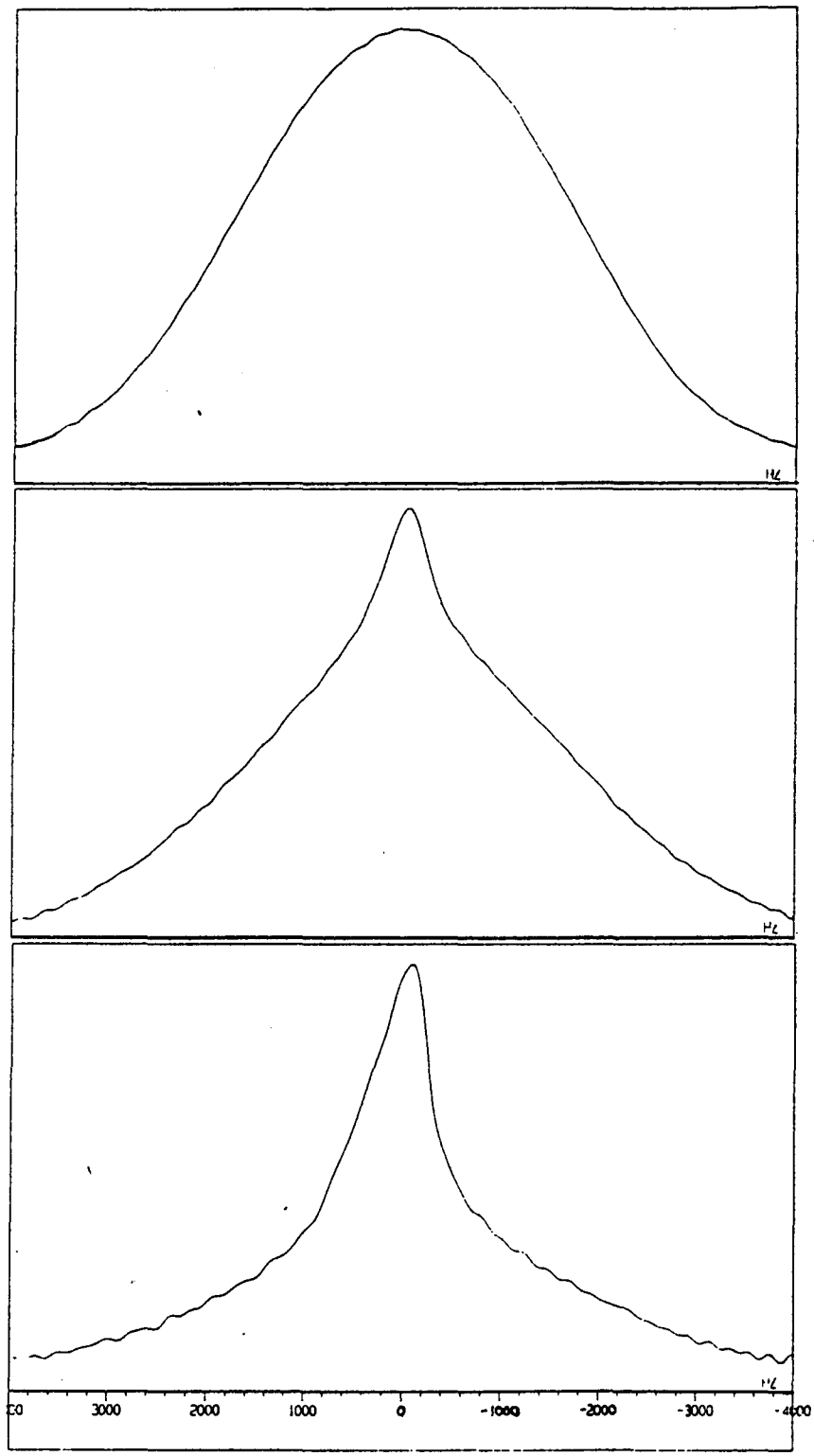

Figure 7.12 The ^{7}Li lineshapes measured at 400 MHz and 293 K in (a) polycrystalline $LiCF_3SO_3$ (b) the 3.5:1 PEO/$LiCF_3SO_3$ system and (c) the 9:1 PEO/$LiCF_3SO_3$ system.

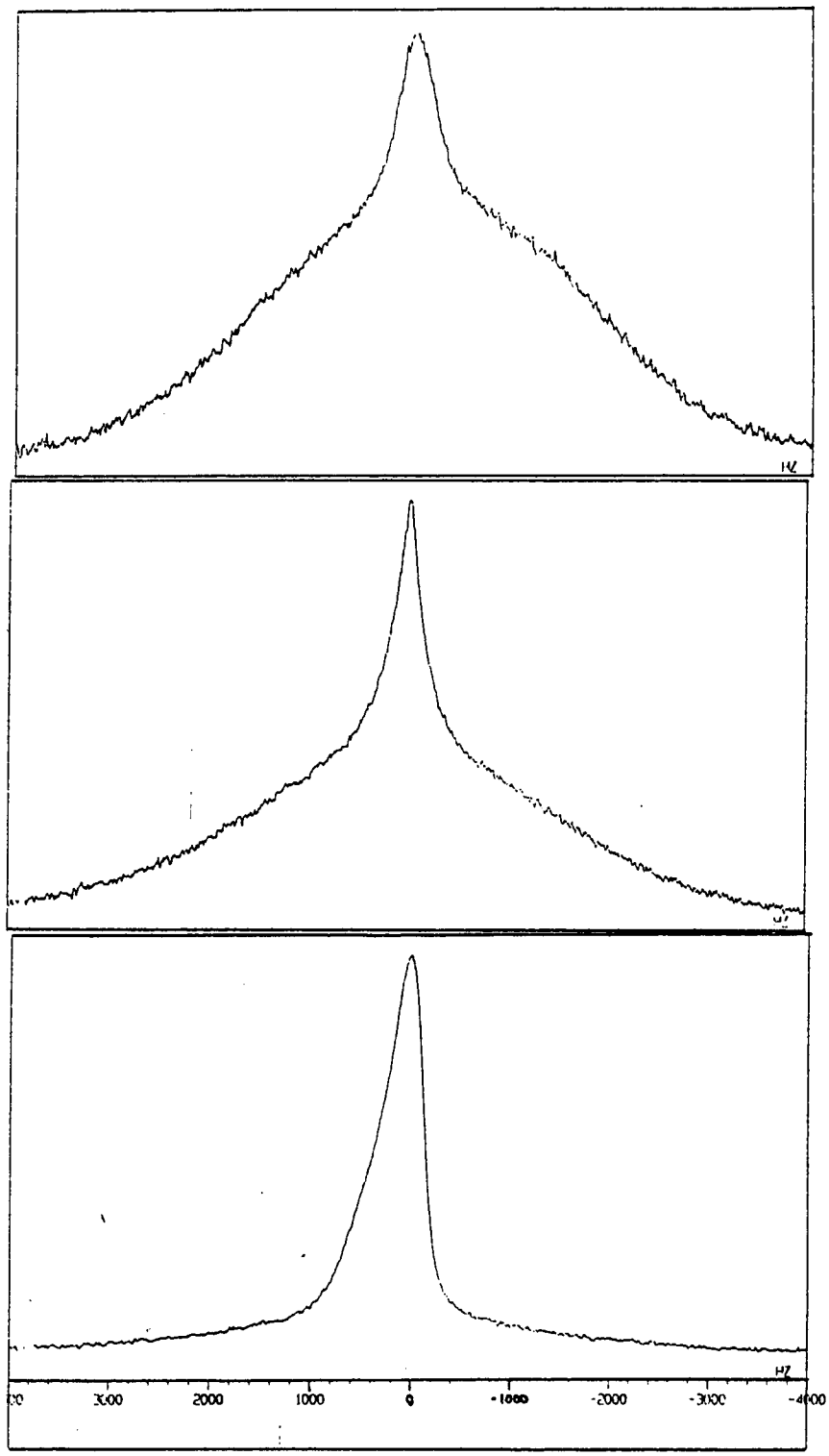

Figure 7.13 The ^{7}Li lineshapes measured at 400 MHz and 343 K in (a) polycrystalline $LiCF_3SO_3$, (b) the 3.5:1 PEO/$LiCF_3SO_3$ system, and (c) the 9:1 PEO/$LiCF_3SO_3$ system.

CHAPTER 8

^{1}H NUCLEAR MAGNETIC SPIN-LATTICE RELAXATION AND LINESHAPE STUDIES IN POLYCRYSTALLINE PEO AND PEO/$LiCF_3SO_3$ SYSTEMS

"This is not the end of the road.

It goes on, for maybe, miles and miles...."

Kings X, Gretchen goes to Nebraska.

CONTENTS

8.1 Introduction

Chapters 6 and 7 have concentrated in the main on ^{19}F and ^{7}Li nuclear spin-lattice relaxation studies in the 3.5:1 and 9:1 PEO/$LiCF_3SO_3$ systems. These nuclei were the most suitable 'n.m.r. labels' on the anion and cation of the 'guest' ionic salt. The respective nuclear spin-lattice relaxation investigations have given valuable information concerning structure and dynamics in the ionic host polymer systems at the molecular level. It is the aim of this chapter to present the results of ^{1}H n.m.r. studies of the host polymer, both as pure PEO, and as the ion coordinating macromolecule involved in the 3.5:1 and 9:1 PEO/$LiCF_3SO_3$ systems. It should be stated at the outset that the discussion is less quantative than that in previous chapters. This is because the ^{1}H nucleus does not act as a distinctive label but rather reflects the complexity, both in structural and motional terms, of the behaviour of the PEO molecule.

Initially the ^{1}H n.m.r. lineshapes derived from solid echoes are discussed as a function of temperature, both in polycrystalline PEO and the 3.5:1 and 9:1 PEO/$LiCF_3SO_3$ systems. An estimate of the experimental low temperature PEO second moment is compared with a rigid lattice value calculated from the proposed crystal structure. Simulations of the experimental ^{1}H f.i.ds are also discussed.

To finish the chapter the ^{1}H spin-lattice relaxation behaviour is investigated in both polycrystalline PEO and the 3.5:1 and 9:1 PEO/$LiCF_3SO_3$ systems. Observed double exponential nuclear magnetization recoveries are interpreted in terms of the presence of crytalline and amorphous polymer phases. It is recognized however, that the interpretation of these results in terms of just a 'two phase model' may be oversimplified and that this is an area for further work.

8.2 The Form of the ^1H FID

The simplest model system to choose to simulate the ^1H n.m.r. signal of polycrystalline PEO is that of a pair of dipolar-coupled ^1H nuclei, as found in a CH_2 group. It is, of course to be recognized that in reality the PEO polymer consists of linked (OCH_2CH_2) units, possibly undergoing complex motions. Not withstanding this point, however, it is useful to consider a two spin model and this is outlined in this section. The viability of such a model is discussed in due course.

It was shown in Chapter 2 that the normalized n.m.r. signal following a 90° pulse is given by

$$< I_x(t) > = \frac{\cos\Delta\omega t}{Tr\{I_x^2\}} \; Tr\{\exp(-i\mathcal{H}^D t) I_x \exp(i\mathcal{H}^D t) I_x\} \qquad (8.1)$$

This equation can be evaluated for isolated systems of spins, although the explicit calculation soon becomes complicated; for n spins the energy matrix has the dimension $n^2 \times n^2$. For two like spins the secular dipolar Hamiltonian is given, from equation (2.69), by

$$\mathcal{H}^D = \frac{\mu_0 \gamma_I^2 \hbar}{4\pi r^3} (1-3\cos^2\theta)[I_z^{(1)} I_z^{(2)} - \tfrac{1}{4}(I_+^{(1)} I_-^{(2)} + I_-^{(1)} I_+^{(2)})] \qquad (8.2)$$

The derivation of equation (8.1) relies on the commutability of $\mathcal{H}^D$ and $\mathcal{H}^{OFF}$, which only holds in this case if the two spins are both chemically and crystallographically equivalent[1]. If this condition holds then equation (8.2) can be used to evaluate the matrix elements of $\mathcal{H}^D$, for example

$$<\alpha\alpha|\mathcal{H}^D|\alpha\alpha> = <\alpha\alpha|a I_z^{(1)} I_z^{(2)}|\alpha\alpha > = \tfrac{1}{4}\, a \qquad (8.3)$$

and

$$< \alpha\beta \,|\mathcal{H}^D| \, \beta\alpha > = <\alpha\beta|-\tfrac{1}{4}\, a I_-^{(1)} I_+^{(2)}|\beta\alpha> = -\tfrac{1}{4}a \qquad (8.4)$$

where $a = \frac{\mu_0 \gamma_1^2 \hbar}{4\pi r^3} (1-3\cos^2\theta)$, so that the specific form of the matrix $\mathcal{H}^D$ is given by

$\mathcal{H}^D$	$\|\alpha\alpha\rangle$	$\|\alpha\beta\rangle$	$\|\beta\alpha\rangle$	$\|\beta\beta\rangle$	
$\langle\alpha\alpha\|$	$\frac{1}{4}a$	0	0	0	
$\langle\alpha\beta\|$	0	$-\frac{1}{4}a$	$-\frac{1}{4}a$	0	(8.5)
$\langle\beta\alpha\|$	0	$-\frac{1}{4}a$	$-\frac{1}{4}a$	0	
$\langle\beta\beta\|$	0	0	0	$+\frac{1}{4}a$	

This matrix is not diagonal, showing that the simple direct product basis states are not the eigenfunctions of this $\mathcal{H}^D$. To proceed in the evaluation of equation (8.1), $\mathcal{H}^D$ must be diagonalized. It is clear from the position of the non-zero off diagonal elements that $|\alpha\alpha\rangle$ and $|\beta\beta\rangle$ are eigenfunctions of $\mathcal{H}^D$. The other two eigenfunctions will be linear combinations of $|\alpha\beta\rangle$ and $|\beta\alpha\rangle$. These can be denoted by

$$|A\rangle = C_1|\alpha\beta\rangle + C_2|\beta\alpha\rangle$$

and (8.6)

$$|B\rangle = C_3|\alpha\beta\rangle + C_4|\beta\alpha\rangle$$

where

$$\mathcal{H}^D|A\rangle = E|A\rangle$$

and

$$\mathcal{H}^D|B\rangle = E|B\rangle \tag{8.7}$$

The orthonormality of the basis states $|\alpha\beta\rangle$ and $|\beta\alpha\rangle$ means that

$$C_1^2 + C_2^2 = C_3^2 + C_4^2 = 1$$

and

$$C_1C_3 + C_2C_4 = 0 \tag{8.8}$$

The matrix elements $\langle\alpha\beta|\mathcal{H}^D|A\rangle$ and $\langle\beta\alpha|\mathcal{H}^D|B\rangle$ can be written according to equations (8.6) and (8.7) by

$$\begin{aligned} \langle\alpha\beta|\mathcal{H}^D|A\rangle &= C_1\langle\alpha\beta|\mathcal{H}^D|\alpha\beta\rangle + C_2\langle\alpha\beta|\mathcal{H}^D|\beta\alpha\rangle \\ &= E(C_1\langle\alpha\beta|\alpha\beta\rangle + C_2\langle\alpha\beta|\beta\alpha\rangle) \\ &= E\,C_1 \end{aligned} \tag{8.9}$$

and

$$\begin{aligned} \langle\beta\alpha|\mathcal{H}^D|B\rangle &= C_3\langle\beta\alpha|\mathcal{H}^D|\alpha\beta\rangle + C_4\langle\beta\alpha|\mathcal{H}^D|\beta\alpha\rangle \\ &= E(C_3\langle\beta\alpha|\alpha\beta\rangle + C_4\langle\beta\alpha|\beta\alpha\rangle) \\ &= E\,C_4 \end{aligned} \tag{8.10}$$

For equations (8.9) and (8.10) to have non-trivial energy solutions then

$$\begin{vmatrix} \langle\alpha\beta|\mathcal{H}^D|\alpha\beta\rangle - E & \langle\alpha\beta|\mathcal{H}^D|\beta\alpha\rangle \\ \langle\beta\alpha|\mathcal{H}^D|\alpha\beta\rangle & \langle\beta\alpha|\mathcal{H}^D|\beta\alpha\rangle - E \end{vmatrix} = 0 \tag{8.11}$$

Multiplying out the determinant and replacing the matrix elements by their explicit values obtained from the matrix (8.5), gives a solvable quadratic equation in E; with solutions E = 0 and E = $-\frac{1}{2}$a. The substitution of these solutions into equations (8.9) and (8.10); ensuring appropriate solutions of C_1, C_2, C_3 and C_4 are necessarily consistent with the orthonormality relationships given in equation (8.8), gives the basis state eigenfunctions of this $\mathcal{H}^D$ as $|\alpha\alpha\rangle$, $|\beta\beta\rangle$ and $1/\sqrt{2}$ $(|\alpha\beta\rangle + |\beta\alpha\rangle)$, $1\sqrt{2}$ $(|\alpha\beta\rangle - |\beta\alpha\rangle)$. The diagonalized matrix $\mathcal{H}^D$ is now given by

$\mathcal{H}^D$	$\|\alpha\alpha\rangle$	$1/\sqrt{2}$ $(\|\alpha\beta\rangle + \|\beta\alpha\rangle)$	$1/\sqrt{2}$ $(\|\alpha\beta\rangle - \|\beta\alpha\rangle)$	$\|\beta\beta\rangle$
$\langle\alpha\alpha\|$	$\frac{1}{4}$ a	0	0	0
$1/\sqrt{2}$ $(\langle\alpha\beta\| + \langle\beta\alpha\|)$	0	$-\frac{1}{2}$ a	0	0
$1/\sqrt{2}$ $(\langle\alpha\beta\| - \langle\beta\alpha\|)$	0	0	0	0
$\langle\beta\beta\|$	0	0	0	$-\frac{1}{4}$ a

(8.12)

and correspondingly the exponential operator involved in the time evolution of the quantum mechanical system is given by the matrix:

$\exp(\pm i\mathcal{H}^D t)$	$\lvert\alpha\alpha\rangle$	$1/\sqrt{2}\,(\lvert\alpha\beta\rangle + \lvert\beta\alpha\rangle)$	$1/\sqrt{2}\,(\lvert\alpha\beta\rangle - \lvert\beta\alpha\rangle)$	$\lvert\beta\beta\rangle$	
$\langle\alpha\alpha\rvert$	$\exp(\pm\frac{i}{4}at)$	0	0	0	
$1/\sqrt{2}\,(\langle\alpha\beta\rvert + \langle\beta\alpha\rvert)$	0	$\exp(\pm\frac{i}{2}at)$	0	0	(8.13)
$1/\sqrt{2}\,(\langle\alpha\beta\rvert - \langle\beta\alpha\rvert)$	0	0	0	0	
$\langle\beta\beta\rvert$	0	0	0	$\exp(\pm\frac{i}{4}at)$	

The matrix elements of the operator I_x can be found using the raising and lowering operators according to equations (2.43) and (2.44);

I_x	$\lvert\alpha\alpha\rangle$	$1/\sqrt{2}\,(\lvert\alpha\beta\rangle + \lvert\beta\alpha\rangle)$	$1/\sqrt{2}\,(\lvert\alpha\beta\rangle - \lvert\beta\alpha\rangle)$	$\lvert\beta\beta\rangle$	
$\langle\alpha\alpha\rvert$	0	$\sqrt{2}$	0	0	
$1/\sqrt{2}\,(\langle\alpha\beta\rvert + \langle\beta\alpha\rvert)$	0	0	0	$\sqrt{2}$	(8.14)
$1/\sqrt{2}\,(\langle\alpha\beta\rvert - \langle\beta\alpha\rvert)$	$\sqrt{2}$	0	0	$\sqrt{2}$	
$\langle\beta\beta\rvert$	0	$\sqrt{2}$	0	0	

and the substitution of the matrices (8.13) and (8.14) into equation (8.1), noting that $\mathrm{Tr}\{I_x^2\} = 8$, gives

$$\langle I_x(t)\rangle = \cos\Delta\omega t[4\exp(-\tfrac{i}{4}at)\exp(-\tfrac{i}{2}at) + 4\exp(\tfrac{i}{4}at)\exp(\tfrac{i}{2}at)]/8 \quad (8.15)$$

which can be rewritten using trigonometric functions as

$$\langle I_x(t)\rangle = \cos\Delta\omega t\{4[\cos\tfrac{1}{4}at + i\sin(-\tfrac{1}{4}at)][\cos\tfrac{1}{2}at + i\sin(-\tfrac{1}{2}at)]$$

$$+ 4[\cos\tfrac{1}{4}at + i\sin\tfrac{1}{4}at][\tfrac{1}{4}\cos at + i\sin\tfrac{1}{2}at]\}/8$$

$$= \cos\Delta\omega t[\cos\tfrac{1}{4}at\cos\tfrac{1}{2}at - \sin(\tfrac{1}{4}at)\sin(\tfrac{1}{2}at)]$$

$$= \cos\Delta\omega t\cos\tfrac{3}{4}at \quad (8.16)$$

The term $\cos\Delta\omega t$ is a non-zero offset, with $\Delta\omega$ given by

$$\Delta\omega = \omega_R - \omega_0(1 + \sigma_{zz}) \tag{8.17}$$

so that it is always possible in principle to select ω_R to give $\Delta\omega = 0$. This chapter is concerned with ^1H nuclei, and in most cases the chemical shift range is less than 30 ppm. Furthermore the relative strength of chemical shielding interactions can be safely assumed to be considerably less than that of the magnetic dipolar intractions between ^1H nuclei, so that the chemical shielding interaction is unlikely to play any part in determining the offset, and an initial approximation in which $\Delta\omega = 0$ is reasonable. Equation (8.16) can now be rewritten as

$$\langle I_x(t)\rangle = \cos\left(\left\{\frac{3\mu_0\gamma^2\hbar}{16\pi r^3}\right\}(1-3\cos^2\theta)t\right) \tag{8.18}$$

For a polycrystalline sample, equation (8.18) must be averaged over all orientations. The result is a signal of the form

$$\langle I_x(t)\rangle = \frac{1}{2}\int_0^{\pi} \cos\left\{\frac{3\mu_0\gamma^2\hbar(1-3\cos^2\theta)t}{16\pi r^3}\right\}\sin\theta\, d\theta \tag{8.19}$$

which can be written as

$$\langle I_x(t)\rangle = \left(\frac{\pi}{6Kt}\right)^{\frac{1}{2}}\left[\cos(Kt)\int_0^{(6Kt/\pi)^{\frac{1}{2}}}\cos\frac{\pi}{2}x^2dx + \sin(Kt)\int_0^{(6Kt/\pi)^{\frac{1}{2}}}\sin\frac{\pi}{2}x^2dx\right] \tag{8.20}$$

where $K = 3\mu_0\gamma^2\hbar/16\pi r^3$ and $x = (6Kt/\pi)^{\frac{1}{2}}\cos\theta$. The integrals involved in the evaluation of equation (8.20) are the standard Fresnel Integrals, usually denoted by $C[6Kt/\pi]^{\frac{1}{2}}$ and $S[6Kt/\pi]^{\frac{1}{2}}$; and given in standard tables[2]. Finally, the ^1H f.i.d for an isotropic orientational distribution of an isolated homonuclear two spin system is given by

$$\langle I_x(t)\rangle = \left(\frac{\pi}{6Kt}\right)^{\frac{1}{2}}\left\{\cos(Kt)C\left[\frac{6Kt}{\pi}\right]^{\frac{1}{2}} + \sin(Kt)S\left[\frac{6Kt}{\pi}\right]^{\frac{1}{2}}\right\} \tag{8.21}$$

The functional form of equation (8.21) is shown in Figure 8.1. The most striking feature is its oscillatory nature which is not cyclic in time. Experimentally determined f.i.ds do not extend in time indefinitely. In reality, the many pairwise interactions in a real solid will give rise to a large number of oscillatory terms that will eventually destructively interfere and cause the signal to decay. As already indicated, to devise explicit functions that describe the form of the ^1H f.i.d for systems with many spins (in reality more than 5 or 6) is intractable. There is always uncertainty in the energy levels of an isolated system due to the spins not involved in the calculation. An alternative is to introduce an empirical decay function.

It is useful in considering a basis for this function to consider the moment expansion of an f.i.d.(Section 2.10). The moment expansion can include any number of spins, and can be approximated as

$$\langle I_x(t)\rangle = \exp(-\tfrac{1}{2}M_2t^2) \tag{8.22}$$

The Gaussian decay described by equation (8.22) can be used as an approximation to make theoretical expressions calculated for isolated systems comparable with experiment, by writing

$$\langle I_x(t)\rangle = \left[\tfrac{1}{2}\int_0^{\pi}\langle I_x(t)\rangle_{ISO}\sin\theta d\theta\right]\exp(-\tfrac{1}{2}M_2't^2) \tag{8.23}$$

or

$$\langle I_x(t)\rangle = \tfrac{1}{2}\int_0^{\pi}\left[\langle I_x(t)\rangle_{ISO}\exp(-\tfrac{1}{2}M_2't^2)\right]\sin\theta d\theta \tag{8.24}$$

where M_2' is the inter-system contribution to the second moment and includes all of the inter-system interactions not considered in an exact calculation for

isolated systems; and ISO denotes the result for a single isolated system given by equation (8.18).

8.3 Experimental

^1H spin-echoes following a $P_x(90)$-τ-$P_y(90)$ pulse sequence with τ=15μs were recorded at a frequency of 59.45 MHz over the temperature range of 335 K to 230 K, for samples of polycrystalline PEO, and the 3.5:1 and 9:1 PEO/$LiCF_3SO_3$ systems. The signal was recorded and Fourier transformed as described in Chapter 3.

A ^1H nuclear spin-lattice relaxation time study was carried out at this frequency, on all systems, using a $P_x(90)$-t-$P_x(90)$-τ-$P_y(90)$ pulse sequence where τ was again 15 μs. In the light of the lineshape studies carried out, and with due consideration of other studies of polymers with two phases, described in the literature[9,10], markedly double exponential ^1H nuclear magnetization recoveries were expected for PEO and the 9:1 PEO/$LiCF_3SO_3$ system between the PEO glass transition and melting temperatures, that is ~230 K < T < ~ 336 K.

Accordingly, the spin-lattice relaxation times were extracted from the data by fitting to a double exponential function. The two spin-lattice relaxation times were sufficiently different to obtain good initial approximations of their values from the limits of the logarithmic plots of experimental nuclear magnetization recoveries. In this case, where the initial "guesses" were good, it was found that the subtraction of an exponential function and the replotting of the data, again on a logarithmic scale gave a method of extraction more efficient than an unconstrained four parameters non-linear least squares fit.

8.4 A Study of ^1H FIDs and Lineshapes in Polycrystalline PEO

Results

Figures 8.2 to 8.4 show the 'half-echo signals' as a function of temperature; and Figure 8.5 shows the corresponding frequency domain lineshapes.

Discussion

At 336 K the ^1H n.m.r. signal is predominantly of an exponential type and the decay time (~4ms) is largely determined by the magnetic field inhomogeneity. This would be consistent with the existence of considerable degrees of motional freedom in PEO. This is in agreement with the phase behaviour of PEO, which shows that the sample has a melting transition at a temperature of ~336 K[3]. Correspondingly, the frequency spectrum is a narrow line. As the temperature is reduced the time domain signal clearly exhibits a solid like functional form at short times with a certain percentage of the sample contributing to an exponential type decay at longer times, although again it is expected that the magnetic field inhomogeneity will contribute to the detailed shape of the signal. The simple interpretation of this behaviour is that there are regions of crystalline PEO where the chain mobility is limited, and in contrast, amorphous regions where the chain is highly mobile. At ~285 K the solid signal began to show indications of some modulation. In general solid n.m.r. signals are modulated, as a given spin interacts 'strongly' with its immediate surroundings; that is, it experiences local order. The calculated FID of a locally ordered region will contain geometric information about this ordering. Even after powder averaging the signal would contain terms of an oscillatory nature, manifest in the modulation of the FID. In PEO it seems reasonable to suggest that the modulation may be due to an increasing 'isolation' of the CH_2 groups; so that these groups 'see' more local order as the motional processes in which they are involved become more restricted as the temperature is reduced.

The percentage of the sample contributing to the exponential type decay at longer times reduces as the temperature is reduced. Table 8.1 shows the approximate percentage of ^1H nuclei contributing to the exponential type signal as a function of temperature. The results were obtained by estimating the fractional area of the total signal accounted for by this region. For comparison, results obtained from two previous studies are also included in the table.

Table 8.1 Approximate percentage of ^1H nuclei contributing to the long time signal in the ^1H FID at different temperatures.

	Percentage 'Mobile Fraction' ^1H Nuclei		
Temp/K	This Work	Reference [4]	Reference [5]
335	85	–	78
320	30	28	35
293	25	21	26
287	25	20	23
281	22	19	20
275	20	19	17
269	18	18	14
250	15	13	10
230	0	2	2

The results summarized in the table show good agreement.

As the temperature is reduced the frequency domain lineshapes consist of a superposition of broad and narrow components, corresponding to the crystalline and amorphous regions respectively. It has also been suggested in previous studies that the only reasonable source of the narrow component is regions of high chain mobility; that is amorphous PEO[4-6]. Although there are indications of modulation in the time domain signal below ~285 K, the frequency spectra show no indications of a Pake-type spectrum, which would result from a system of spin pairs weakly coupled amongst themselves. At 230 K the frequency domain lineshape appears to be close to that of a single broad line, where the narrow component has broadened dramatically. This is close to the glass transition temperature where chain mobility is expected to slow down considerably, and is

consistent with a previous study[6] which showed that the spectrum can no longer be resolved into two components, on the basis of lineshape differences, below 230 K.

Figure 8.6 shows the time behaviour of the echo amplitude measured at 230 K, in the form of a graph of ln(Echo Amplitude) versus time squared. It was shown in Chapter 2, that to second order in time the form of the f.i.d can be written as,

$$\langle I_x(t) \rangle = \exp(-\tfrac{1}{2}M_2 t^2) \qquad (8.25)$$

so that the second moment can be extracted from the initial gradient of Figure 8.6. A linear least squares fit to the region $0 < t < 250\ \mu s^2$, yields

$$M_2 = (22 \pm 3.0) \times 10^{-8}\ T^2$$

The second moment is written as 22×10^{-8}, rather than 2.2×10^{-7} as might be expected in scientific notation. This is so that the 'front number' represents the second moment in $Gauss^2$. This unit is often found in the literature.

The crystal structure of PEO is well known[7] and is shown in Figure 8.7. The ^1H homonuclear rigid lattice second moment can be calculated, as before, using

$$M_2 = \frac{3}{5}\gamma^2\hbar^2 I(I+1) \sum_k \frac{1}{r_{jk}^6} \qquad (8.26)$$

Figure 8.8 shows the ^1H rigid lattice second moment as a function of the radius of a sphere centred on the reference spin, containing all ^1H nuclei used in the lattice summation. The difference between the results obtained using 1.5 nm and 0.8 nm was less than 1%, and the value approaches that obtained for 1.5 nm asympotically. Figure 8.9 shows the rigid lattice second moment calculated using a lattice sum including all ^1H nuclei within 1.5 nm, for 10 unique reference nuclei in the PEO chain. The average of these values gives

$$M_2^{HH} = 23.8 \times 10^{-8}\ T^2$$

This compares well with the value obtained experimentally at 230 K, and would seem to suggest that there is little line narrowing below 230 K. Previous studies have reported second moments determined experimentally at 77 K in samples of PEO of average molecular weight 5000[8] and 4×10^6[4]. In the former a value of 23×10^{-8} T^2 is reported, and indeed there is only 6% difference in the values determined at 230 K and 77 K. The latter is a study of oriented PEO. In data presented, corresponding to all selected angles between the applied field and draw direction, there is again only a 7% difference in second moments determined at 230 K and 77 K. The second moment of an isotropic PEO sample measured at 77 K was found to be 23.6×10^{-8} T^2, in good agreement with the present calculation.

The calculation of the ^1H rigid lattice second moment can be split into separate contributions, to give a more informative picture of the significant interactions affecting a reference spin. The results of such an approach are shown in Table 8.2, using all relevant spins within a distance of 1.5 nm from the reference spin.

Table 8.2: The contributions to M_2^{HH} in polycrystalline PEO

System	$M_2 \times 10^8/T^2$
Partner Spin in CH_2 Group	11.4
Intra-chain	5.2
Inter-chain	7.2
Total	23.8

The second moment of a reference spin due to all other spins with the exception of the 'partner' spin in the CH_2 group accounts for approximately 50% of the total second moment. This second moment that can be used to approximate the decay function used in equations (8.23) and (8.24) to simulate the experimental signal.

The integral involved in equation (8.23) has been considered previously, and the expression reduces to

$$\langle I_x(t)\rangle = \left(\frac{\pi}{6Kt}\right)^{\frac{1}{2}}\left\{\cos(kt)C\left[\frac{6Kt}{\pi}\right]^{\frac{1}{2}} + \sin(Kt)S\left[\frac{6Kt}{\pi}\right]^{\frac{1}{2}}\right\})\exp(-\tfrac{1}{2}M_2^{HH'}t^2) \quad (8.27)$$

where $K = 3\mu_0\gamma_H^2\hbar/16\pi r_{HH}^3$. Figure 8.10 shows the simulation described by equation (8.27) with $M_2^{HH'} = 12.4 \times 10^{-8}\ T^2$, compared with the normalized experimental signal. The simulation models the first part of the f.i.d ($t \leq 17\ \mu s$) very well. However, it is unable to describe any modulation of the signal. However, it is not surprising that this simulation is not a good overall model for the experimental f.i.d. A system in which 50% of the total second moment is due to spins not involved in the explicit calculation; that is, not in the CH_2 group, is unlikely to behave as predicted by a model based on pairs of spins loosely coupled amongst themselves. To represent the PEO chain by a 4 spin system would probably be more realistic, but the reward from such a complex calculation may not justify the effort, as inter chain interactions still account for ~30% of the total second moment, as shown in Table 8.2.

8.5 A Study of ^1H FIDs and Lineshapes in the 3.5:1 and 9:1 PEO/$LiCF_3SO_3$ Systems

Results

Figures 8.11 and 8.12 show the ^1H n.m.r. signals for the 3.5:1 system, at different temperatures in the range 335 K to 230 K, and Figure 8.13 shows the corresponding frequency domain lineshapes.

Similarly Figures 8.14 and 8.15 show the ^1H n.m.r. signals for the 9:1 system at different temperatures, and Figure 8.16 shows the corresponding Fourier transformed frequency domain lineshapes.

Discussion

3.5:1 PEO/$LiCF_3SO_3$ System

At 335 K the ^1H signal is already distinctly modulated and is some five times shorter than the corresponding ^1H signal in PEO, although it has to be remembered that the latter was determined by magnetic field inhomogeneities. This behaviour can be interpreted as indicating a reduction in polymer chain mobility at this temperature compared with pure PEO. Similar behaviour has also been found in the predominantly amorphous systems 16:1 PEO/$Zn(CF_3SO_3)_2$ and PEO/$Pb(CF_3SO_3)_2$[6]. The authors concluded that the activation energy for chain motion in stoichiometric complexes was substantially larger than for pure, amorphous PEO.

However, there remains evidence that there is a fraction of ^1H nuclei in a more mobile amorphous phase, as seen by the two component nature of the decay. This fraction is estimated to be a maximum of 15%, and reduces as the temperature is reduced, although it does not disappear completely until between 250 K and 230 K (as with the amorphous fraction in pure PEO). It is interesting that this provides additional evidence that the 3.5:1 PEO/$LiCF_3SO_3$ system does contain a small amount of excess PEO, as suggested in Section 6.3, and that a stoichiometric complex is formed for a smaller ratio as discussed previously.

As with PEO, the behaviour of the signal over the temperature range of the study gives two component lineshapes in the frequency domain, becoming increasingly broader in nature as the temperature is reduced. This is the same type of behaviour as found in pure polycrystalline PEO. The ^1H lineshape at 230 K has the appearance of a single broad line. Figure 8.17 shows the experimental ^1H half echo signals for polycrystalline PEO compared with the 3.5:1 PEO/$LiCF_3SO_3$ system, measured at 230 K. These are very similar; it is possible that the slight offset (of the order of ~ 1.5 μs) could be a consequence of the manipulation of the

echo data. This suggests that the total ^1H second moment is similar in both systems.

Rigid lattice second moments in the proposed 3:1 PEO/$LiCF_3SO_3$ stoichiometric complex crystal structure were calculated in detail in Chapter 6. These calculated values can be separated into various contributions, in the same manner as in the pure polymer. The results of such an approach are shown in Table 8.3.

Table 8.3: The contributions to M_2^H in the proposed 3:1 PEO/$LiCF_3SO_3$ complex

System	$M_2 \times 10^8/T^2$
CH_2 Group	12.3
Intra-chain H-H	5.5
Inter-chain H-H	2.0
H-F Interactions	0.4
Total	20.2

The total ^1H rigid lattice second moments are indeed similar. It is interesting to note that the intermolecular second moment is much smaller in the 3:1 PEO/$LiCF_3SO_3$ system than in pure polycrystalline PEO, accounting for only ~10% of the total, as opposed to ~30% in the latter. A simplistic interpretation of this is that the presence of the $LiCF_3SO_3$ acts as a 'spacer', holding individual PEO chains apart.

9:1 PEO/$LiCF_3SO_3$ System

At 335 K the ^1H n.m.r. signal is very similar to PEO; it is long (~4ms) and of an exponential type, being largely determined by magnetic field inhomogeneities. However, as the temperature is reduced, the signal starts to become modulated at ~300 K, some 15 K before this feature occurs in PEO. The decay at short times, corresponding to crystalline regions of reduced chain mobility, becomes dominant as the temperature is reduced and broadly speaking the behaviour is well modelled by a combination of that observed in PEO and the 3.5:1 PEO/$LiCF_3SO_3$ system. It is interesting to note that again the ^1H frequency

domain lineshape at 230 K appears to be well described by one broad line. Figure 8.18 shows the experimental ^1H half-echo signals for the 3.5:1 and the 9:1 $PEO/LiCF_3SO_3$ systems, at 230 K. Again, these are found to be very similar, as expected from a system consisting of a stoichiometric crystalline complex (~the 3.5:1 system) and pure crystalline PEO; where both these constituent systems possess very similar total ^1H second moments and exhibit similar spin echo behaviour.

It would be interesting to carry out a more rigorous extraction of experimental second moments, and to attempt a separation of the spin echo-into the two components, corresponding to the two distinct ^1H environments.

8.6 ^1H Nuclear Spin-lattice Relaxation Studies in PEO and the 3.5:1 and 9:1 $PEO/LiCF_3SO_3$ Systems

Results

Figures 8.19 to 8.21 show typical experimental ^1H nuclear magnetization recoveries for PEO and the 3.5:1 and 9:1 $PEO/LiCF_3SO_3$ ionic host polymer systems respectively, as measured at a temperature of 290 K. It is worth noting again that double exponential ^1H nuclear magnetization recoveries were expected for PEO and the 9:1 $PEO/LiCF_3SO_3$ system between the PEO glass transition and melting temperatures; that is ~230 K < T < ~336 K.

Figure 8.22 shows the temperature behaviour of the longer spin-lattice relaxation times (obtained from double exponential fitting described in Section 8.3), plotted in the form of a graph of $T_1(^1H)$ versus inverse temperature, for PEO, and Figure 8.23 shows the corresponding data for the 3.5:1 and 9:1 $PEO/LiCF_3SO_3$ systems. These ^1H nuclear spin-lattice relaxation times are referred to as $T_1(^1H)$, although this notation does not imply measurement from the initial gradient of

magnetization recoveries, as was discussed for $T_1(^{19}F)$ in Chapter 5. The main $T_1(^1H)$ minima exhibited in these systems are summarized in Table 8.4.

Table 8.4 The depth and temperature of $T_1(^1H)$ minima for polycrystalline PEO and the 3.5:1 and 9:1 PEO/$LiCF_3SO_3$ systems

Sample	T_{MIN}/K	$T_1(^1H)$/ms
PEO	285	510
3.5:1 PEO/$LiCF_3SO_3$	290	738
9:1 PEO/$LiCF_3SO_3$	295	576

The ^1H nuclear magnetization recoveries for PEO and the 9:1 PEO/$LiCF_3SO_3$ system were observed to be double exponential as expected, and the varying relative contributions of the two components was temperature dependent. The solid lines in Figures 8.19 to 8.21 are simple double exponential functions of the form.

$$M_0-M_z = AexpCt + BexpDt \qquad (8.28)$$

where A, B, C and D are obtained as described previously; and C and D are the inverse of the system ^1H spin-lattice relaxation times. The ^1H nuclear magnetization recovery in the 3.5:1 PEO/$LiCF_3SO_3$ system was found, within experimental uncertainties, to be exponential at all temperatures and the spin-lattice relaxation time was extracted as described in Chapter 3. Estimated errors in $T_1(^1H)$ were of the order of 5%.

Discussion

The main difficulty in the interpretation of the spin-lattice relaxation time data and in particular the minima, in these systems, is to determine a distinction between true motional minima and manifestations of phase changes in the system. A number of attempts have been made to construct nuclear spin-lattice relaxation theories specifically for polymeric systems but these concentrate on solutions.

The $T_1(^1H)$ values for PEO, shown in Figure 8.22 are consistent with other studies[5,11]. $T_1(^1H)$ values of the order of 100 ms were attributed to the amorphous PEO phase with the other value of the order of 1s being attributed to the crystalline region. Only the longer values of $T_1(^1H)$ are examined here, as the constant of the shorter spin-lattice relaxation time function was comparatively small (~10%). It is interesting to note that a previous n.m.r. study of PEO of various molecular weights, while attributing observed non-exponential magnetization recoveries to the existence of separate phases, does include a comment on the effects of cross-correlations of the ^1H dipole-dipole interaction in CH_3 groups in this respect.

It has been found that the observed $T_1(^1H)$ double minimum type behaviour in polycrystalline PEO is dependent on molecular weight. There are only indications of this type of behaviour for PEO of average molecular weight, for example 5000[8] and 6000[11], but it is far more distinct for higher molecular weights (2.8×10^6[11] and in this study); that is, this study is consistent with previous work in this respect. The $T_1(^1H)$ values in the 9:1 system shown in Figure 8.23 are consistent with a previous study[5].

In Chapter 6 the results of a ^{19}F spin-lattice relaxation study in the 3.5:1 PEO/$LiCF_3SO_3$ system were presented, and a ^{19}F-^1H dipolar coupled cross-relaxation mechanism was discussed in detail; so that, the simulation of the ^{19}F spin-lattice relaxation behaviour, presented in Figure 6.22 necessarily also predicts the complimentary ^1H spin-lattice relaxation behaviour in the 3.5:1 PEO/$LiCF_3SO_3$ system. Figure 8.24 shows this behaviour compared to the experimental values of $T_1(^1H)$. There is good agreement in the depth of the $T_1(^1H)$ minima, but a striking difference in the high temperature behaviour. This may be due to the fact that the ^{19}F-^1H dipolar coupled cross-relaxation model calculations are based on a single correlation time describing all motional processes and, as discussed in Chapter 6, this is obviously an oversimplification.

Initial attempts to base a simulation on two distinct correlation times did produce $T_1(^1H)$ curves in which the activation energy of the spin-lattice relaxation mechanism was much reduced at high temperatures. However, as discussed in Chapter 6, a rigorous calculation incorporating this feature would require a different approach to that of using reduced second moments.

In polycrystalline PEO and the 9:1 PEO/$LiCF_3SO_3$ system the spin-lattice relaxation time minima are lower than that observed in the 3.5:1 PEO/$LiCF_3SO_3$ system. It is possible that in polycrystalline PEO the backbone is undergoing some kind of thermally activated motion in the crystalline phase that is responsible for mediating ^1H spin-lattice relaxation. This would also be the case with the excess PEO in the 9:1 PEO/$LiCF_3SO_3$ system, although in this case the ^1H nuclear magnetization recovery may be expected, even in a simple model, to have at least three sources; that is crystalline PEO, amorphous PEO and the stoichiometric complex.

It has been suggested that spin diffusion may be of importance in semicrystalline systems[11,12]. Spin diffusion[13] leads to communication among spins at various sites in a solid. In disordered solids containing amorphous fractions it is common to observe multicomponent nuclear magnetization recoveries, usually interpreted as corresponding to different spatial or interfacial phases. These phases may communicate via spin diffusion, and in the PEO systems considered in this thesis it is feasible that the amorphous fractions could act as spin-lattice relaxation sinks, as these regions have very short spin-lattice relaxation times. Simulations of the effects of spin diffusion on spin-lattice relaxation in semicrystalline polymers[14] have shown that a simple two region model can give rise to up to four exponential components in its spin-lattice relaxation behaviour. Directly relating these parameters to physical regions is difficult as models may not be unique.

Domain structures in solid polymers are often investigated using the Goldman-Shen pulse sequence[15,16] and significant spin diffusion between crystalline and interfacial regions in oriented polyethylene has been reported[17], by authors using a combination of this sequence and a cross-polarization technique using ^{13}C. It is possible that similar techniques could be used to study spin diffusion in the systems examined in this thesis, to provide information on the spatial inhomogeneities within the system.

References

1 N Boden and P K Kahol
J. Mag. Res., 54, 491, 1983.

2 M Abramowitz and I A Stegun
Handbook of Mathematical Functions
Dover Publication Inc. New York, 1965.

3 R C Weast (Ed)
Handbook of Chemistry and Physics
Chemical Rubber Co., 1970.

4 H G Olf and A Peterlin
Die Makromolekulare Chemie, 104, 135, 1967.

5 D P Tunstall, A S Tomlin, J R MacCallum and C A Vincent
J. Phys. C. Solid State Phys., 21, 1039, 1988.

6 A Johansson, A Wendsjo and J Tegenfeldt
Electrochimica Acta, 37, 1487, 1992.

7 Y Takahashi and H Tadokoro
Macromol., 5, 675, 1973.

8 S Glowinkowski, K Jurga and Z Pajak
Polym. Bull., 5, 271, 1981.

9 M Wobst
J. Polym. Sci. Polym. Phys., Vol. 26, 527, 1988.

10 J J Dechter
J. Polym Sci. Polym Lett., 23, 261, 1985.

11 T M Connor and A Hartland
J. Polym. Sci., 27, 1005, 1969.

12 K J Liu and R Ullman
J. Chem. Phys., 48, 1158, 1968.

13 T T P Cheung
Phys. Rev. B, 23, 1404, 1981.

14 A M Kenwright, K J Packer and B J Jay
J. Mag. Res., 6, 426, 1986.

15 M Goldman and L Shen
Phys. Rev., 144, 321, 1966.

16 T T P Chewrg
J. Chem. Phys., 76, 1248, 1982.

17 T Kimura, K Neki and N Tamura
Polymer, 33, 493, 1992.

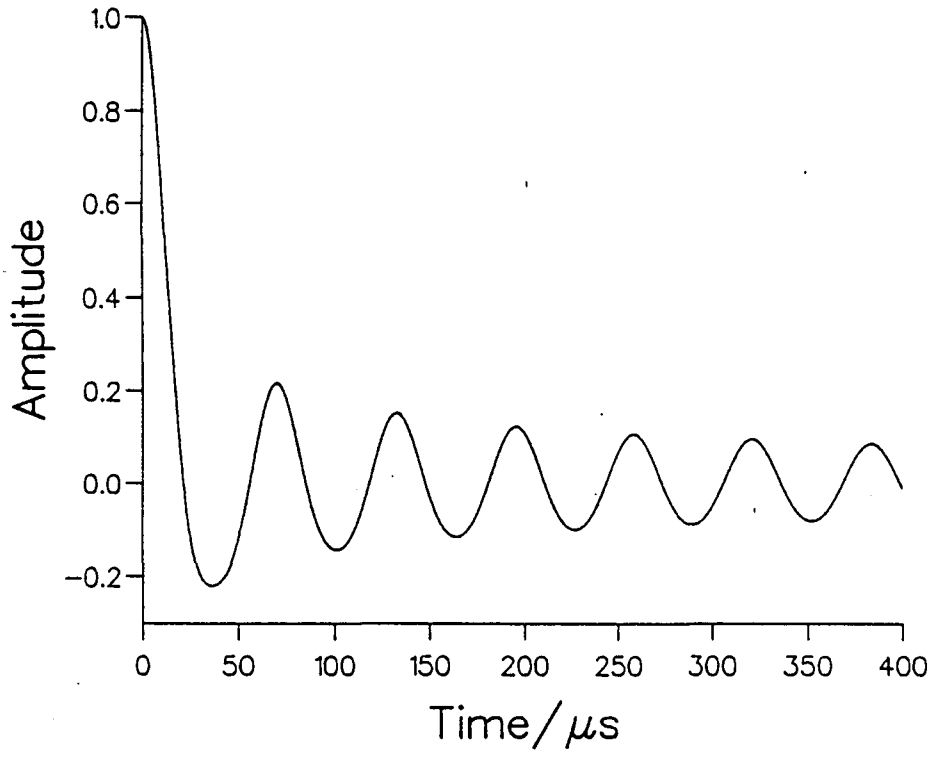

Figure 8.1 A ^{1}H f.i.d, calculated for a model system of an isotropic orientational distribution of isolated homonuclear spin pairs, with $r_{HH} = 0.178$ nm.

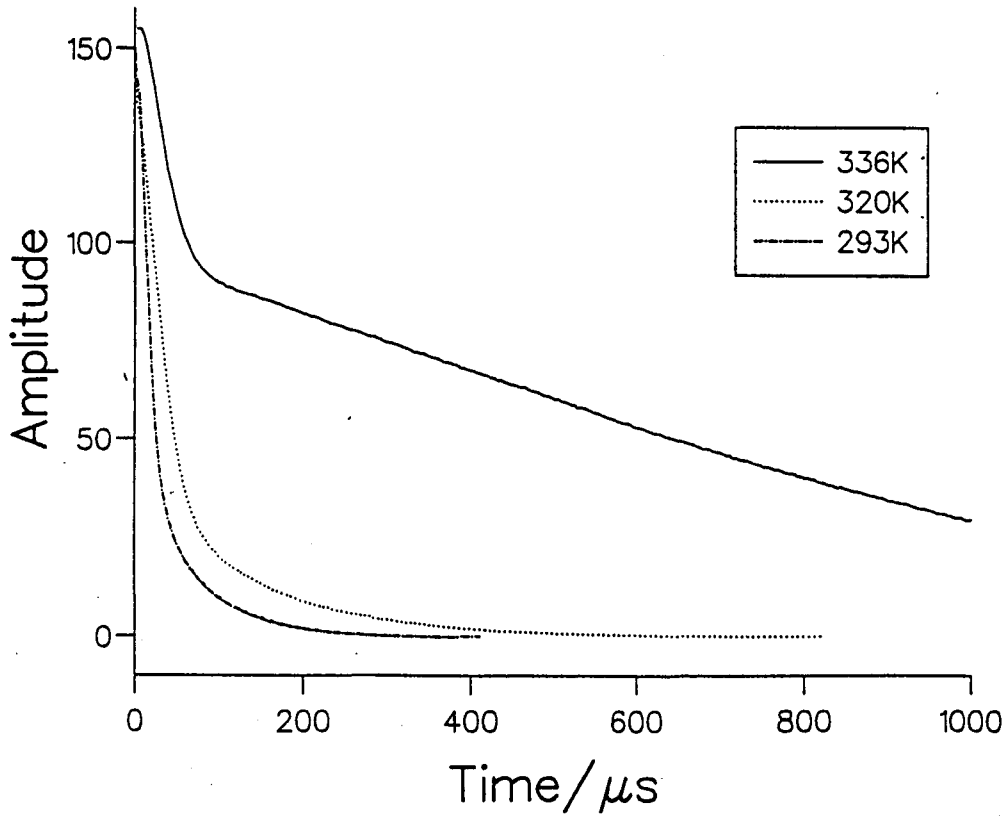

Figure 8.2 Experimental ^{1}H spin echoes measured as a function of temperature at 59.45 MHz in polycrystalline PEO. The signal has been manipulated so that the echo maximum appears at $t = 0$.

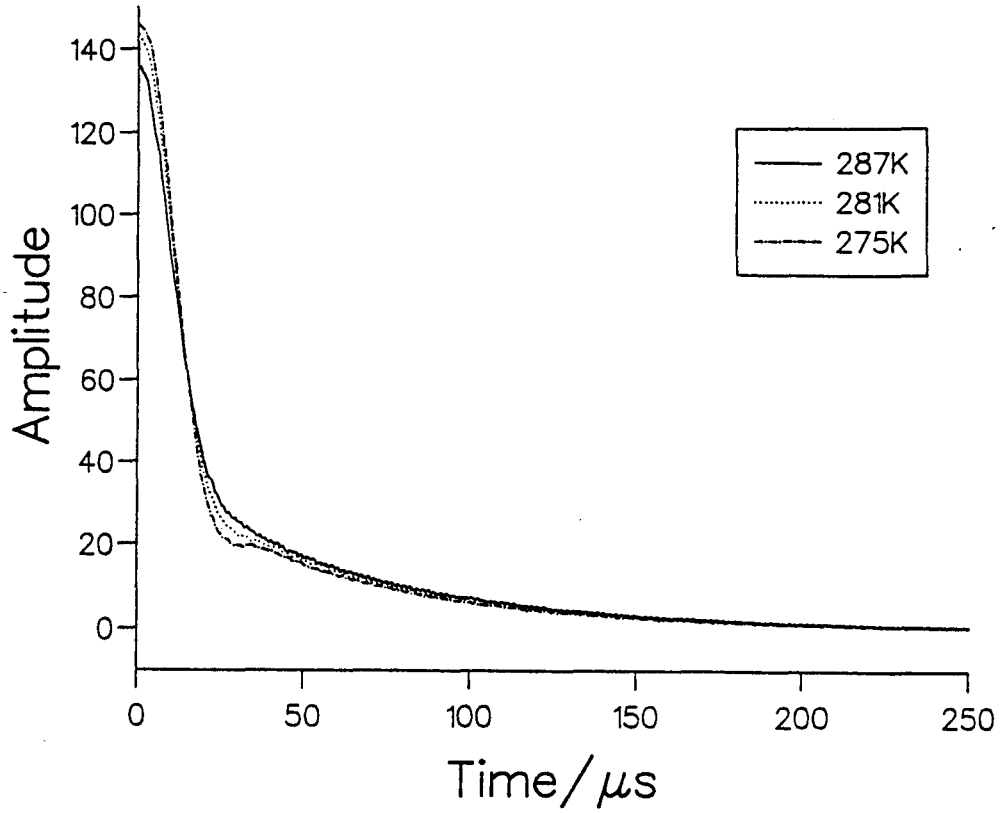

Figure 8.3 Experimental ^1H spin echoes measured as a function of temperature at 59.45 MHz in polycrystalline PEO. The signal has been manipulated so that the echo maximum appears at t = 0.

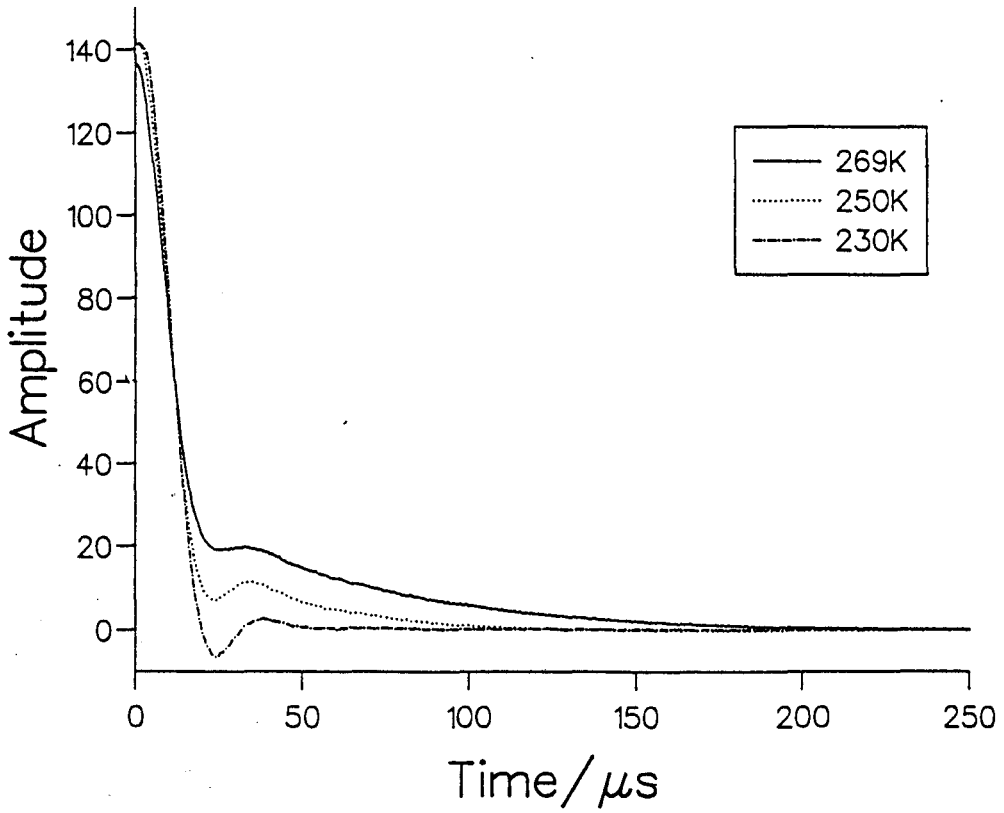

Figure 8.4 Experimental ^1H spin echoes measured as a function of temperature at 59.45 MHz in polycrystalline PEO. The signal has been manipulated so that the echo maximum appears at t = 0.

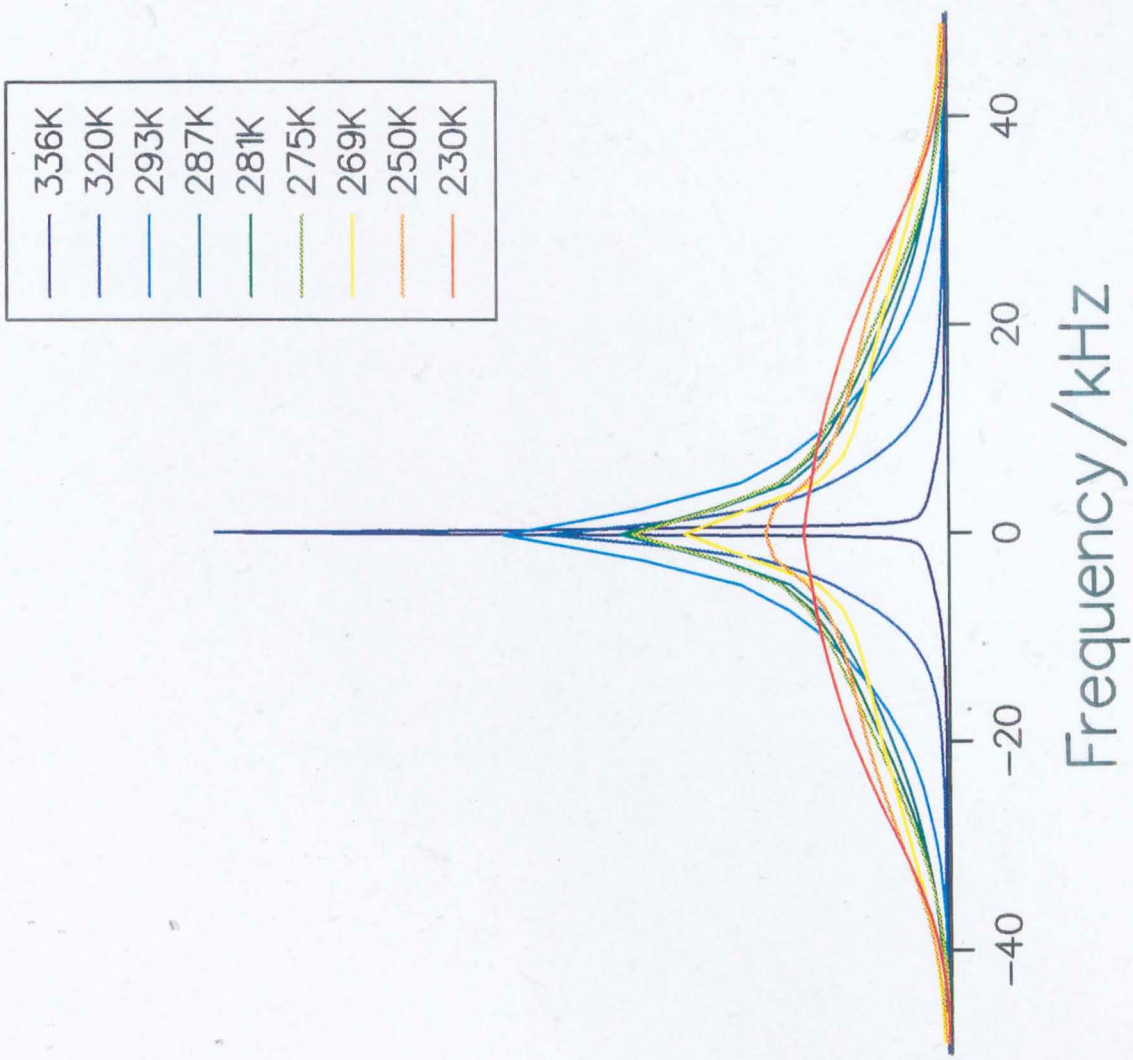

Figure 8.5 Experimental ^1H frequency domain lineshapes measured as a function of temperature, at 59.45 MHz, in polycrystalline PEO.

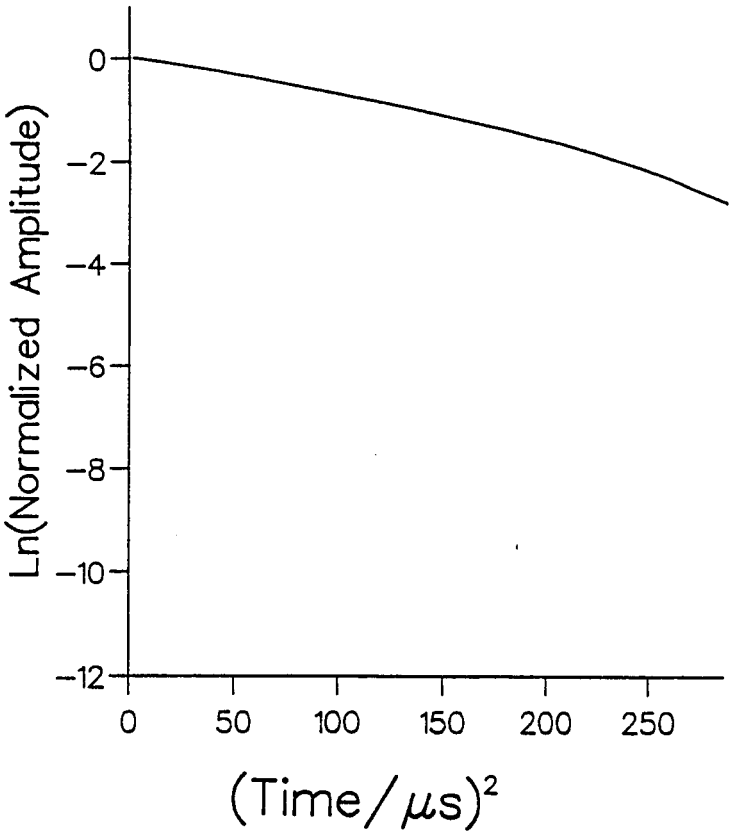

Figure 8.6 The time dependence of the echo amplitude of the ^1H spin echo measured at 59.45 MHz and 230 K in polycrystalline PEO.

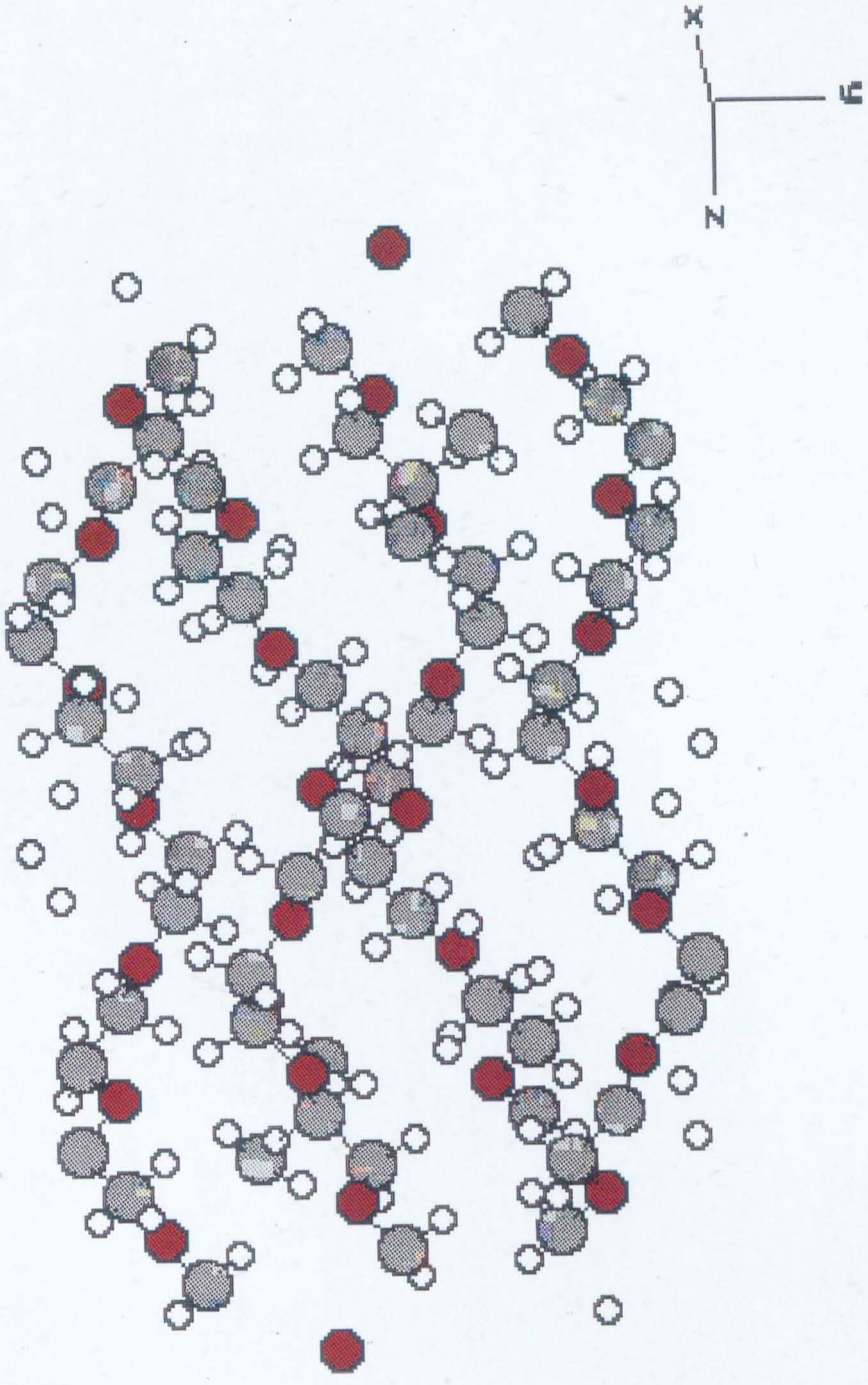

Figure 8.7 The crystal structure of polyethylene oxide. ^{12}C is represented by grey, ^{16}O as red and ^{1}H as white.

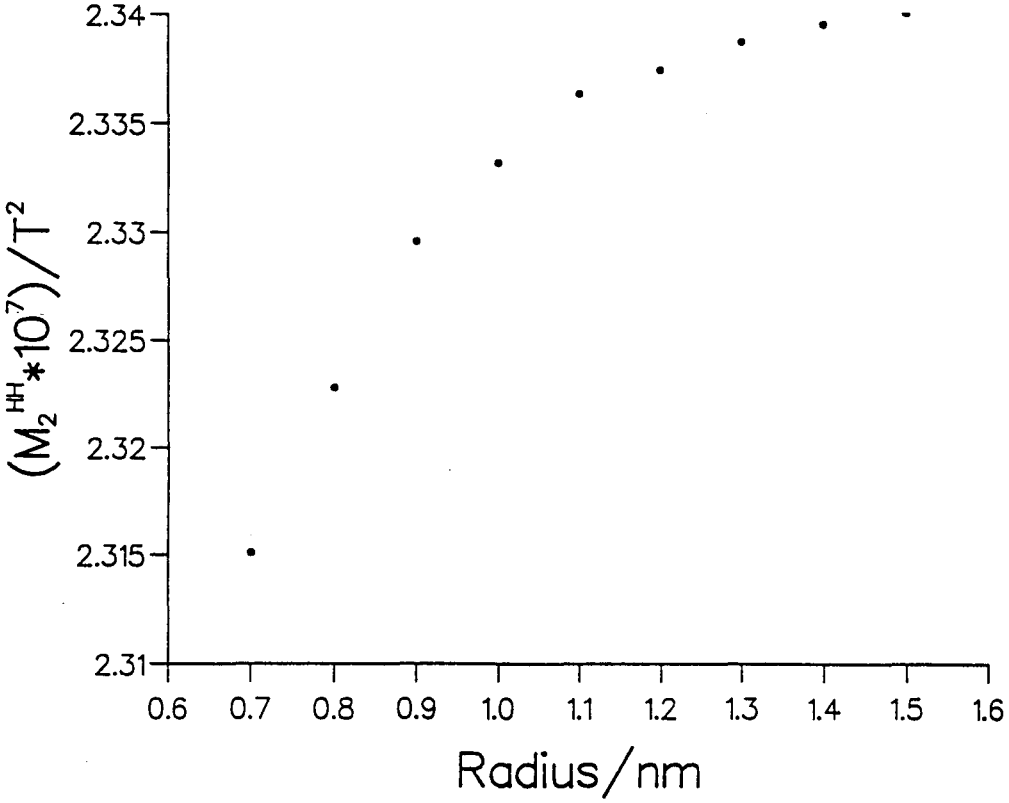

Figure 8.8 The ^1H homonuclear rigid lattice second moment calculated from the proposed crystal structure of PEO, as a function of the radius of a sphere, centred on the reference spin, containing all nuclei involved in the lattice summation.

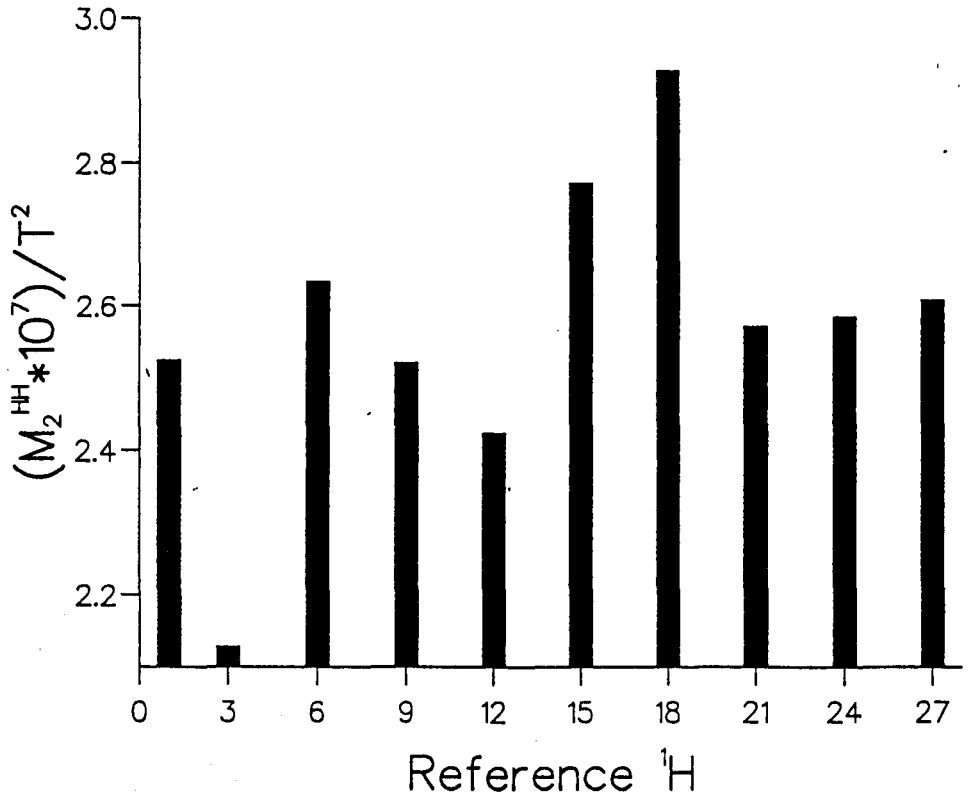

Figure 8.9 The ^1H homonuclear rigid lattice second moment calculated from the proposed crystal structure of PEO, using all ^1H nuclei within 1.5 nm of the reference spin, for 10 crystallographically unique reference nuclei in the PEO chain.

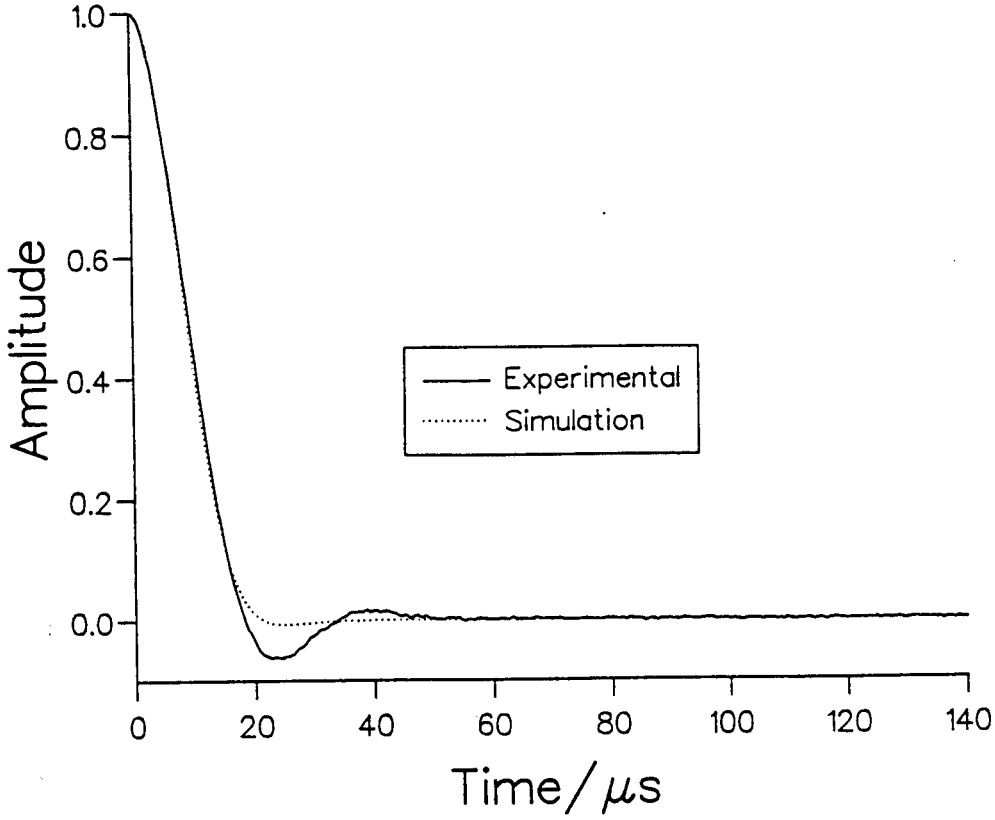

Figure 8.10 The experimental ^1H spin echo measured at 59.45 MHz and 230 K in polycrystalline PEO, compared with a simulation based on an explicit calculation of the f.i.d for a system of isotropically orientated isolated CH_2 groups with $r_{HH} = 0.178$ nm, and an empirical decay function constructed using an intersystem second moment of 12.4×10^{-8} T^2.

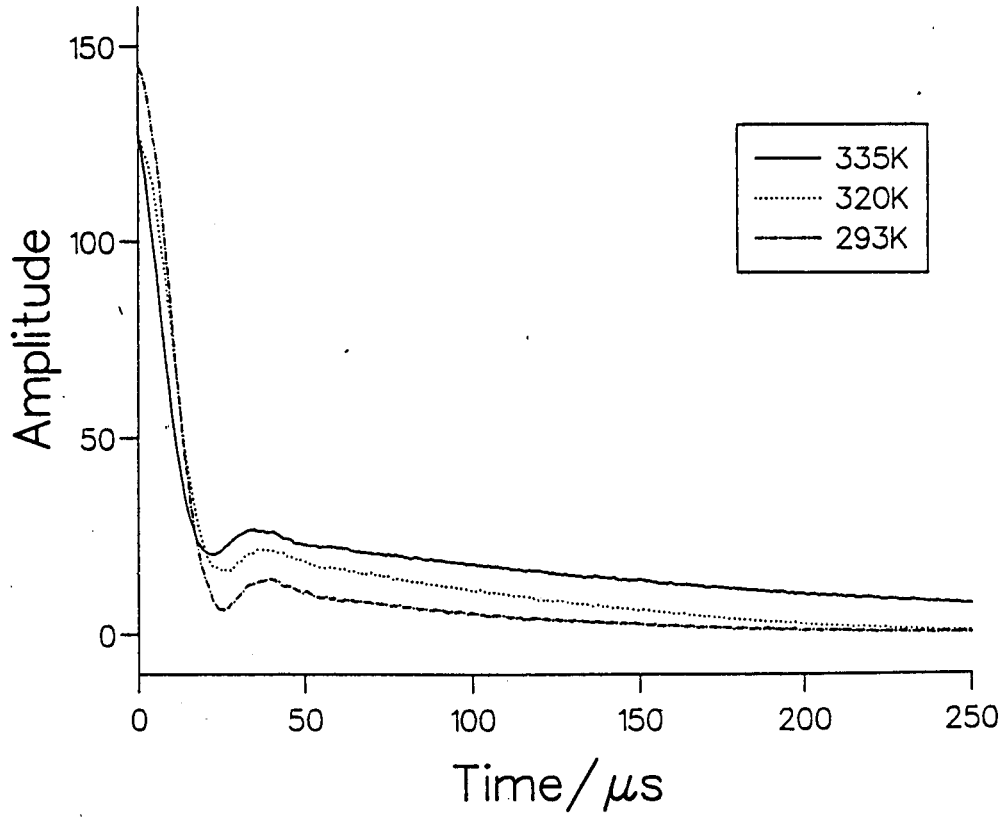

Figure 8.11 Experimental ^1H spin echoes measured as a function of temperature at 59.45 MHz in the 3.5:1 PEO/$LiCF_3SO_3$ system. The signal has been manipulated so that the echo maximum appears at t = 0.

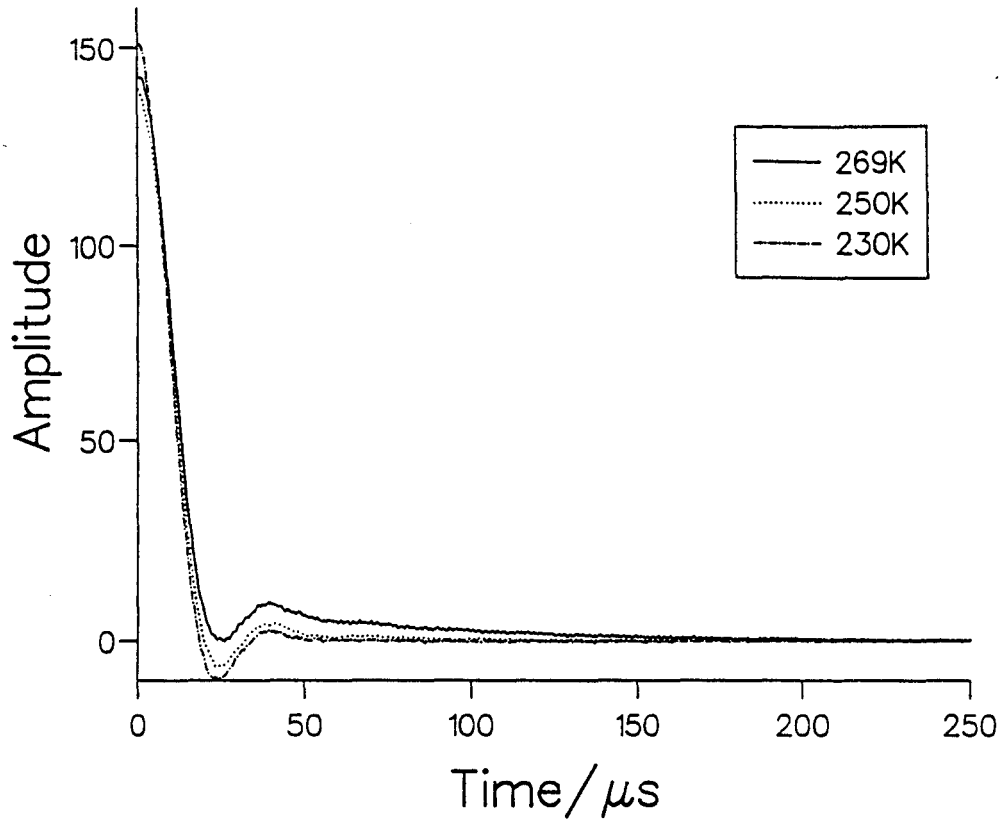

Figure 8.12 Experimental ^1H spin echoes measured as a function of temperature at 59.45 MHz in the 3.5:1 PEO/$LiCF_3SO_3$ system. The signal has been manipulated so that the echo maximum appears at t = 0.

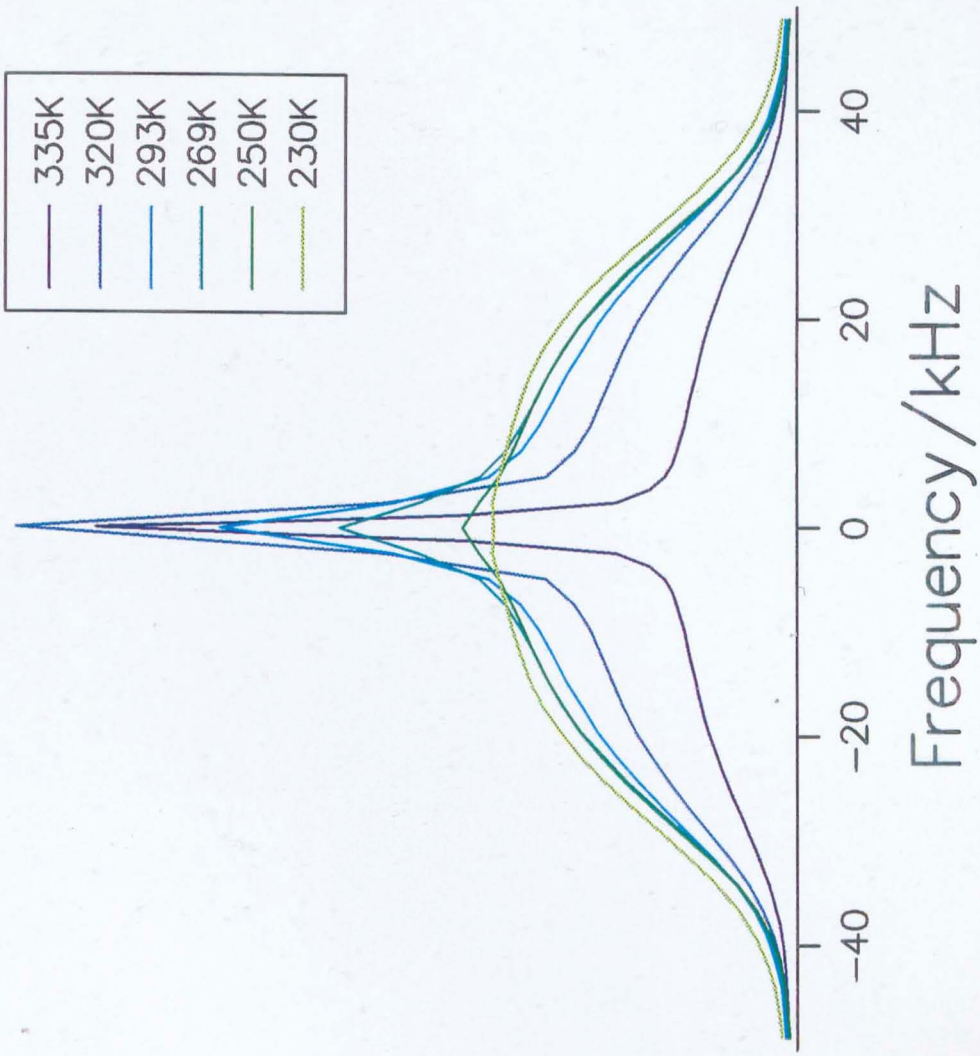

Figure 8.13 Experimental ^1H frequency domain lineshapes measured as a function of temperature at 59.45 MHz in the 3.5:1 PEO/$LiCF_3SO_3$ system.

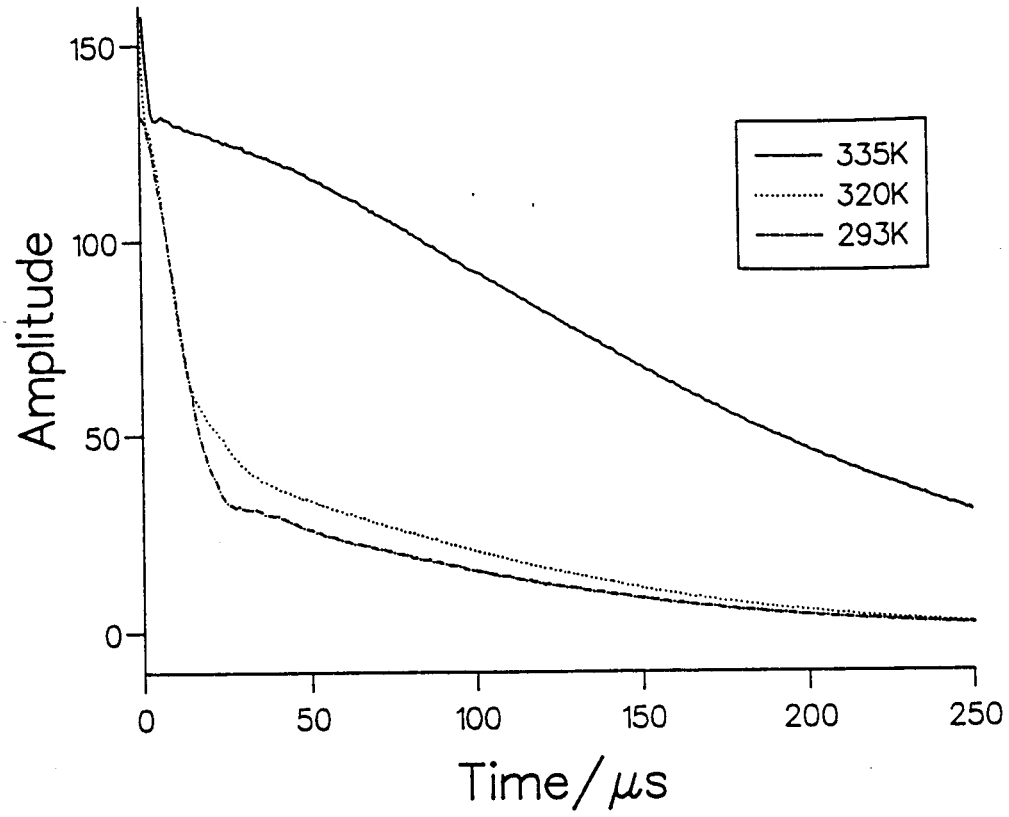

Figure 8.14 Experimental ^1H spin echoes measured as a function of temperature at 59.45 MHz in the 9:1 PEO/$LiCF_3SO_3$ system. The signal has been manipulated so that the echo maximum appears at t = 0.

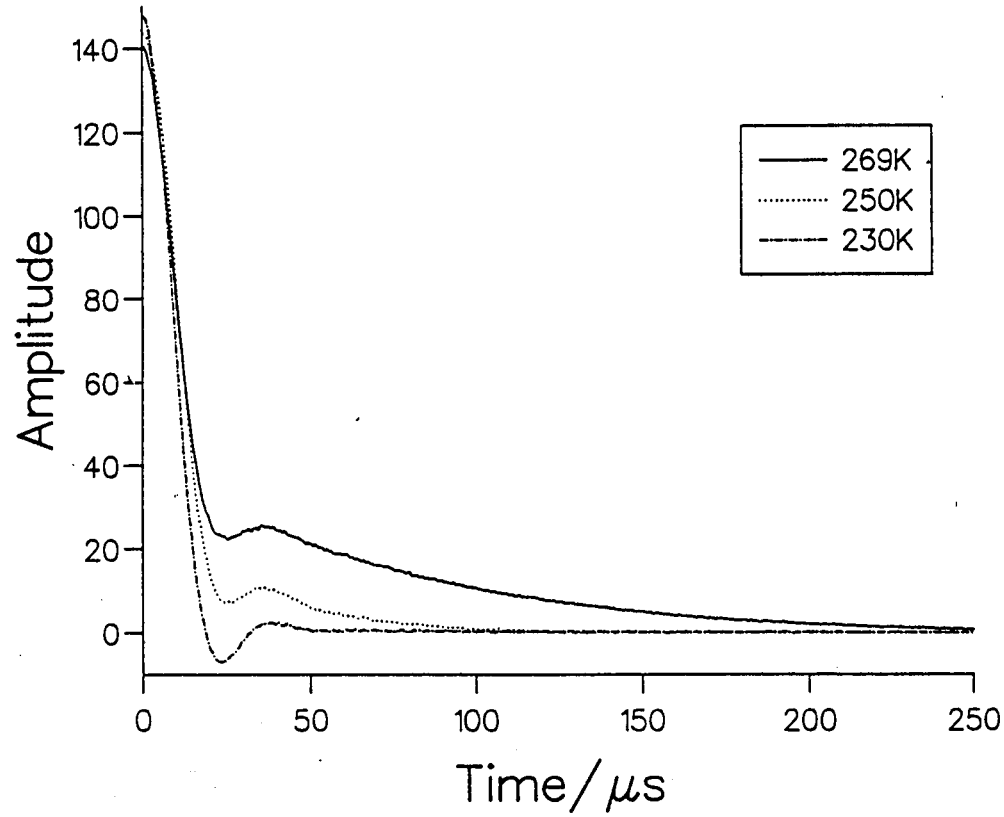

Figure 8.15 Experimental ^1H spin echoes measured as a function of temperature at 59.45 MHz in the 9:1 PEO/$LiCF_3SO_3$ system. The signal has been manipulated so that the echo maximum appears at t = 0.

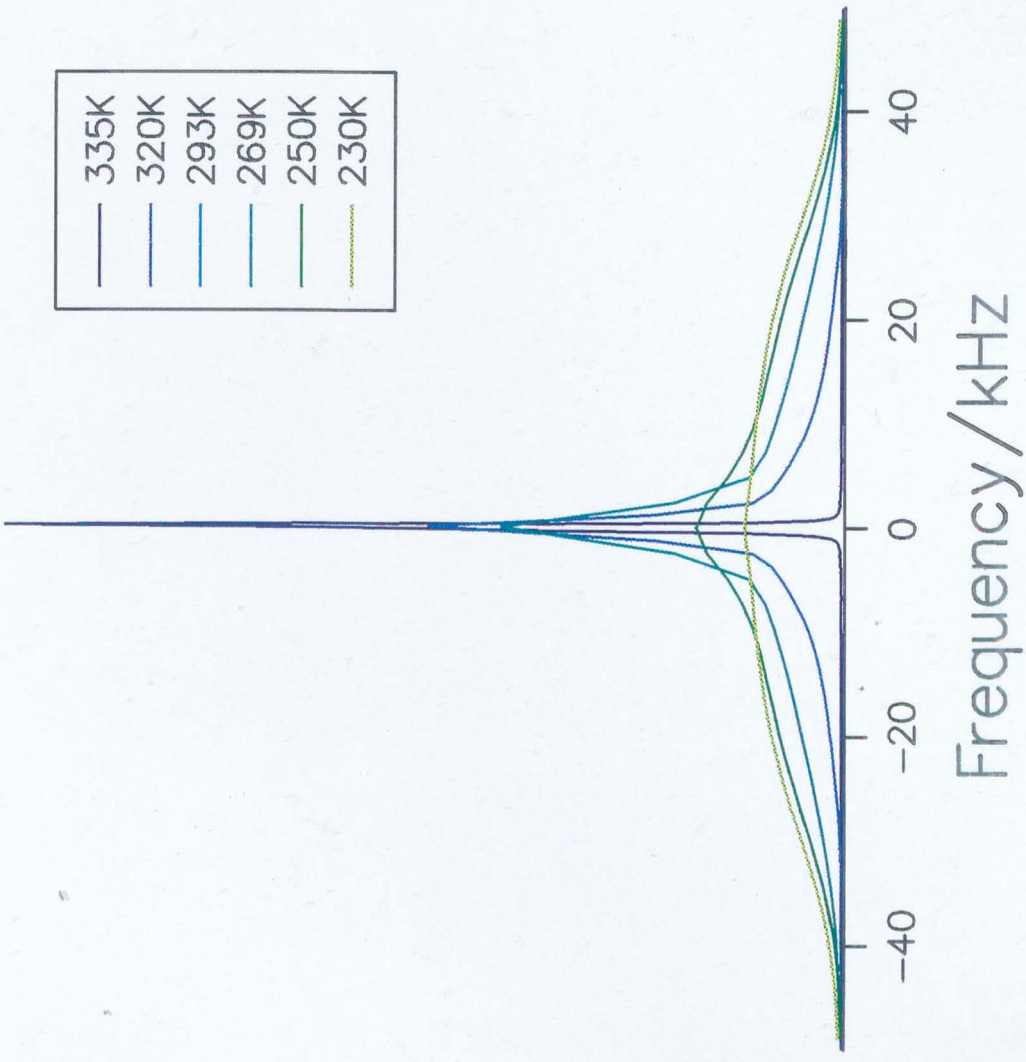

Figure 8.16 Experimental ^1H frequency domain lineshapes measured as a function of temperature at 59.45 MHz in the 9:1 PEO/$LiCF_3SO_3$ system.

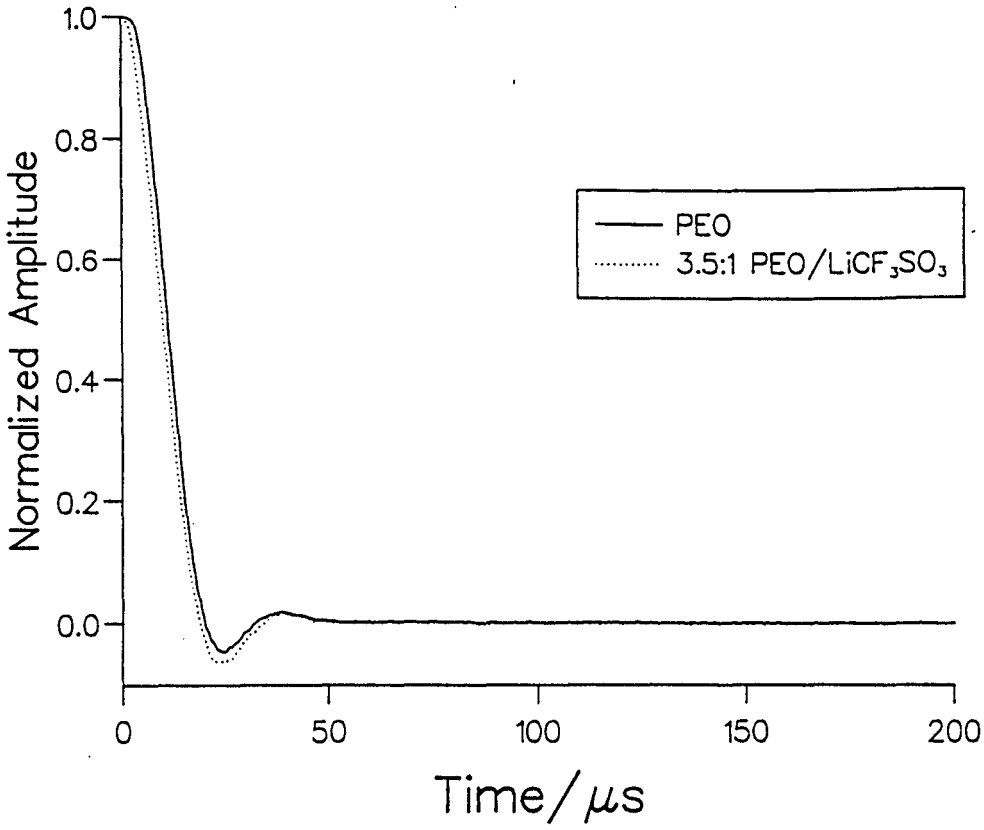

Figure 8.17 Experimental ^1H spin echoes measured at 59.45 MHz and 230 K, in polycrystalline PEO and the 3.5:1 PEO/$LiCF_3SO_3$ system respectively.

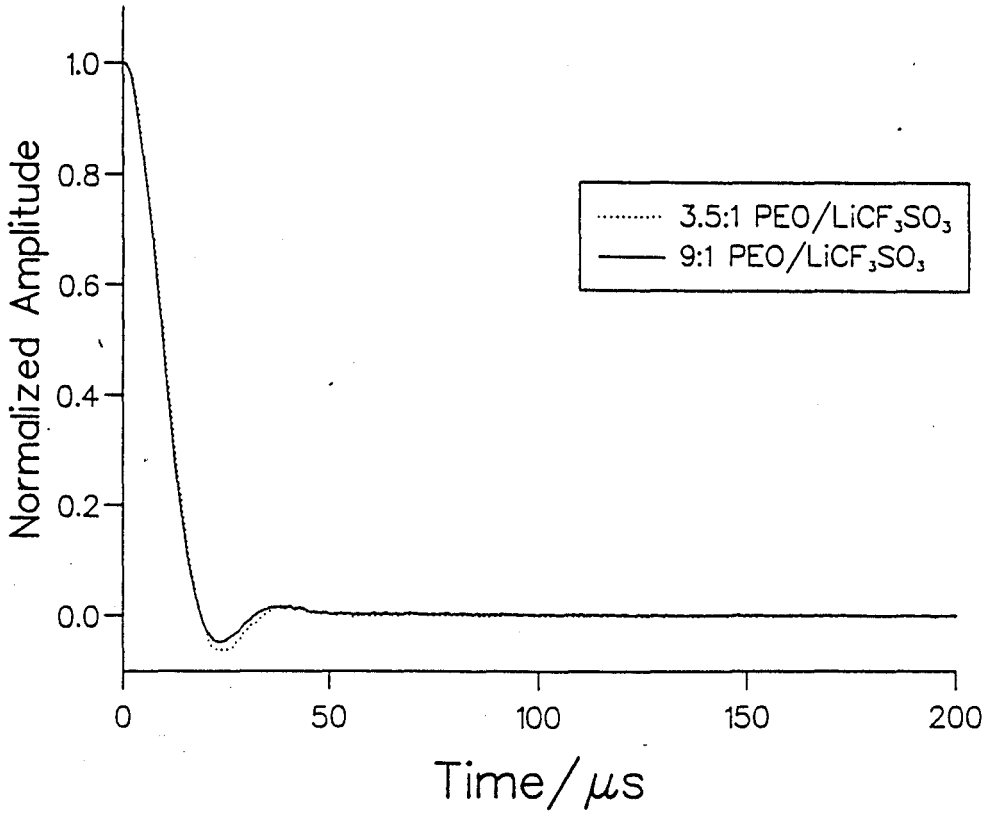

Figure 8.18 Experimental ^1H spin echoes measured at 59.45 MHz and 230 K, in the 3.5:1 and 9:1 PEO/$LiCF_3SO_3$ systems respectively.

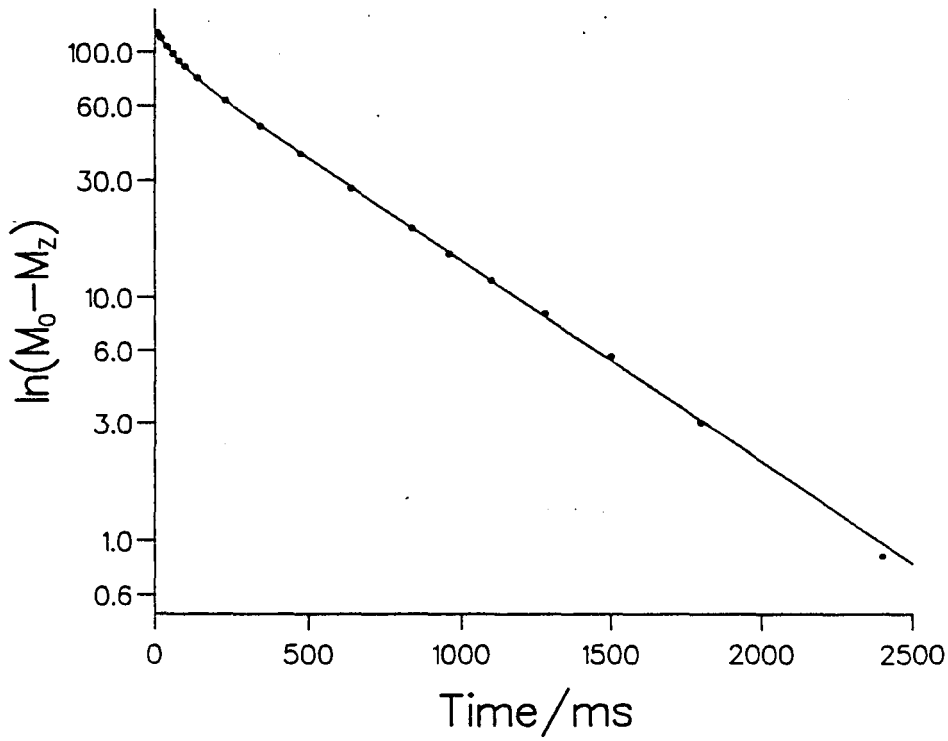

Figure 8.19 The ^1H nuclear magnetization recovery measured at 59.45 MHz and 290 K, in polycrystalline PEO.

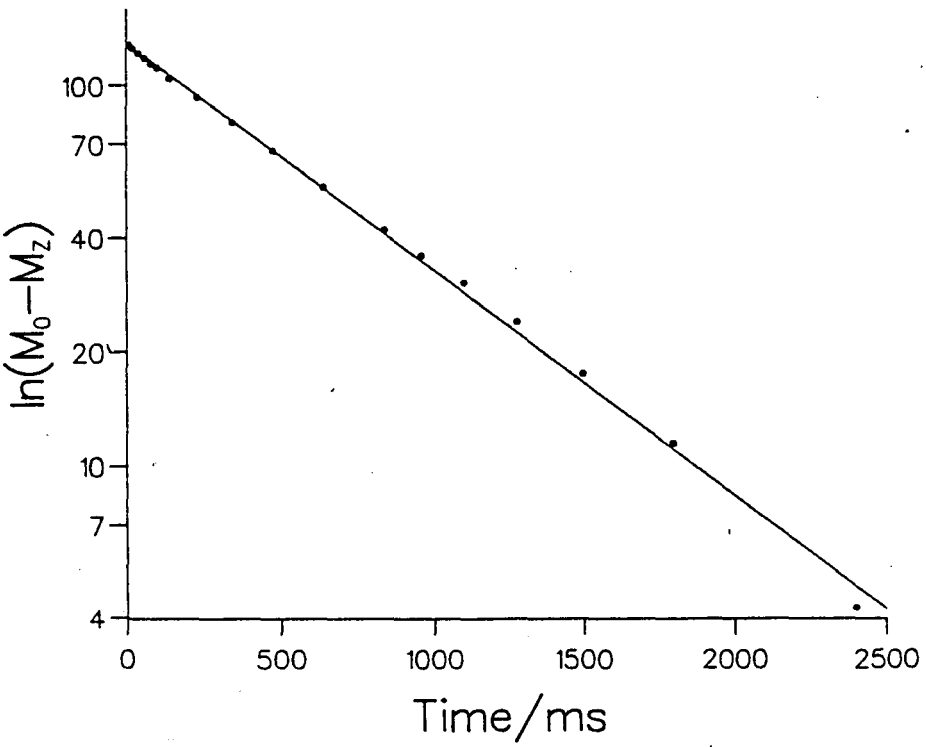

Figure 8.20 The ^1H nuclear magnetization recovery measured at 59.45 MHz and 290 K, in the 3.5:1 PEO/$LiCF_3SO_3$ system.

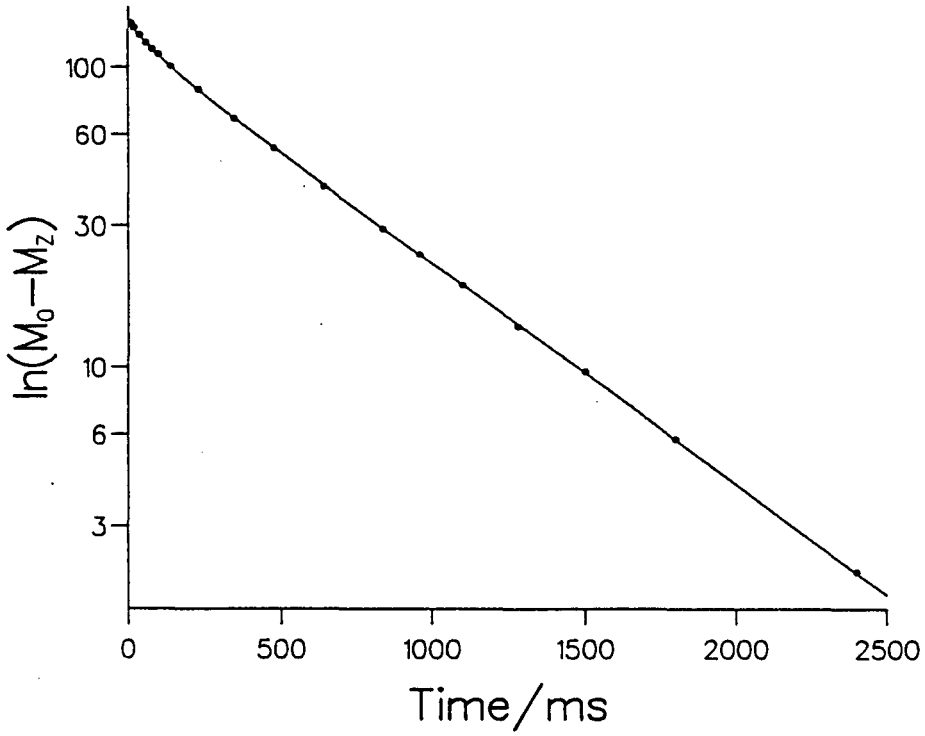

Figure 8.21 The ^1H nuclear magnetization recovery measured at 59.45 MHz and 290 K, in the 9:1 PEO/$LiCF_3SO_3$ system.

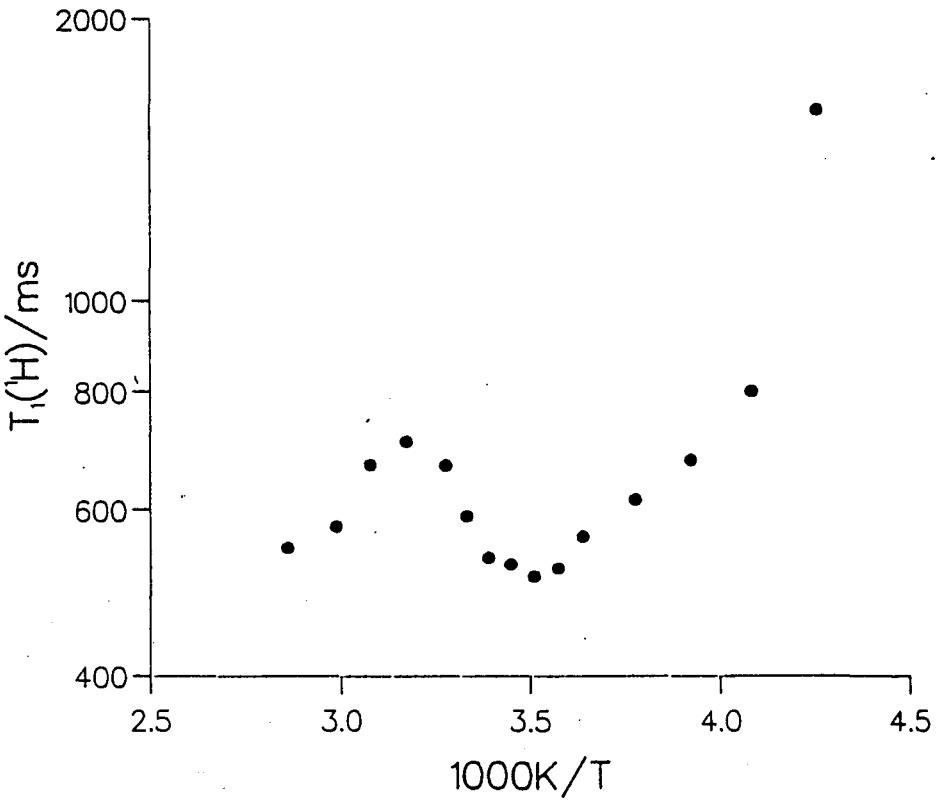

Figure 8.22 The temperature dependence of the experimental ^1H spin-lattice relaxation times, measured at 59.45 MHz, in polycrystalline PEO, plotted in the form of ln ($T_1(^1H)$) versus reciprocal temperature.

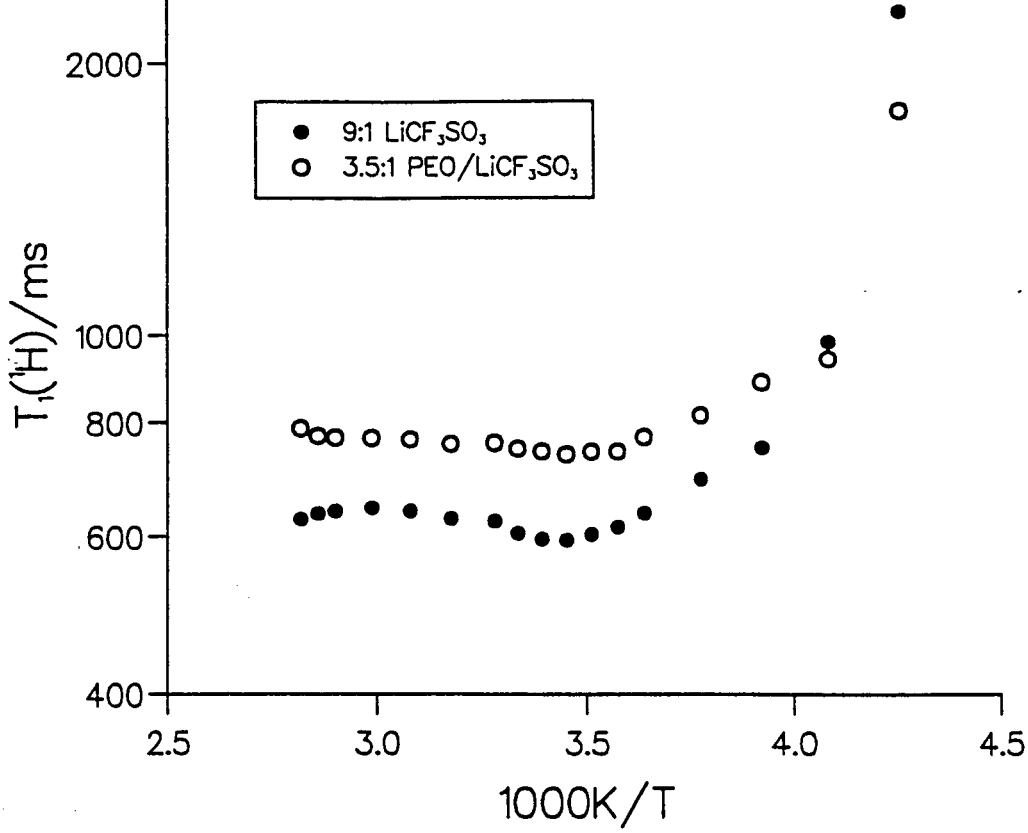

Figure 8.23 The temperature dependence of the experimental ^1H spin-lattice relaxation times in the 3.5:1 and 9:1 PEO/$LiCF_3SO_3$ systems, plotted in the form of $\ln(T_1(^1H))$ versus reciprocal temperature.

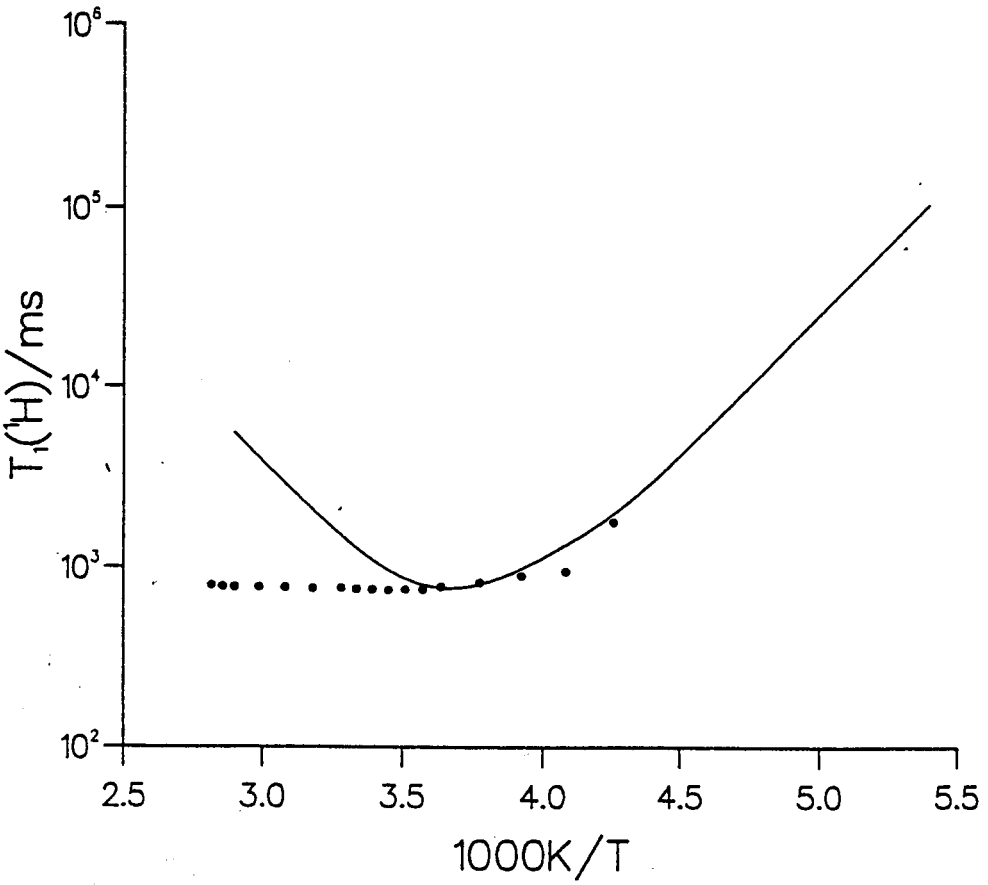

Figure 8.24 The temperature dependence of the experimental ^1H spin-lattice relaxation times measured at 59.45 MHz, in the 3.5:1 PEO/$LiCF_3SO_3$ system, compared with that calclated using a model based on a ^1H-^{19}F dipolar coupled cross-relaxation mechanism; as discussed thoroughly in Chapter 6 in the context of the ^{19}F spin-lattice relaxation results.